

AN EVALUATION OF PARTIAL DIFFERENTIAL EQUATIONS BASED DIGITAL INPAINTING ALGORITHMS

BY

AHMED AL-JABERI



School of Computing

The University of Buckingham / United Kingdom

A Thesis

Submitted for the Degree of Doctor of Philosophy in Mathematics
and Computation

Science to the School of Computing in the University of
Buckingham

February 2019

ABSTRACT

Partial Differential equations (PDEs) have been used to model various phenomena/tasks in different scientific and engineering endeavours. This thesis is devoted to modelling image inpainting by numerical implementations of certain PDEs. The main objectives of image inpainting include reconstructing damaged parts and filling-in regions in which data/colour information are missing. Different automatic and semi-automatic approaches to image inpainting have been developed including PDE-based, texture synthesis-based, exemplar-based, and hybrid approaches. Various challenges remain unresolved in reconstructing large size missing regions and/or missing areas with highly textured surroundings. Our main aim is to address such challenges by developing new advanced schemes with particular focus on using PDEs of different orders to preserve continuity of textural and geometric information in the surrounding of missing regions.

We first investigated the problem of partial colour restoration in an image region whose greyscale channel is intact. A PDE-based solution is known that is modelled as minimising total variation of gradients in the different colour channels. We extend the applicability of this model to partial inpainting in other 3-channels colour spaces (such as RGB where information is missing in any of the two colours), simply by exploiting the known linear/affine relationships between different colouring models in the derivation of a modified PDE solution obtained by using the Euler-Lagrange minimisation of the corresponding gradient Total Variation (TV). We also developed two TV models on the relations between greyscale and colour channels using the Laplacian operator and the directional derivatives of gradients. The corresponding Euler-Lagrange minimisation yields two new PDEs of different orders for partial colourisation. We implemented these solutions in both spatial and frequency domains. We measure the success of these models by evaluating known image quality measures in inpainted regions for sufficiently large datasets and scenarios. The results reveal that our schemes compare well with existing algorithms, but inpainting large regions remains a challenge.

Secondly, we investigate the Total Inpainting (TI) problem where all colour channels are missing in an image region. Reviewing and implementing existing PDE-based total inpainting methods reveal that high order PDEs, applied to each colour channel

Abstract

separately, perform well but are influenced by the size of the region and the quantity of texture surrounding it. Here we developed a TI scheme that benefits from our partial inpainting approach and apply two PDE methods to recover the missing regions in the image. First, we extract the (Y, Cb, Cr) of the image outside the missing region, apply the above PDE methods for reconstructing the missing regions in the luminance channel (Y), and then use the colourisation method to recover the missing (Cb, Cr) colours in the region. We shall demonstrate that compared to existing TI algorithms, our proposed method (using 2 PDE methods) performs well when tested on large datasets of natural and face images. Furthermore, this helps understanding of the impact of the texture in the surrounding areas on inpainting and opens new research directions.

Thirdly, we investigate existing Exemplar-Based Inpainting (EBI) methods that do not use PDEs but simultaneously propagate the texture and structure into the missing region by finding similar patches within the rest of image and copying them into the boundary of the missing region. The order of patch propagation is determined by a priority function, and the similarity is determined by matching criteria. We shall exploit recently emerging Topological Data Analysis (TDA) tools to create innovative EBI schemes, referred to as TEBI. TDA studies shapes of data/objects to quantify image texture in terms of connectivity and closeness properties of certain data landmarks. Such quantifications help determine the appropriate size of patch propagation and will be used to modify the patch propagation priority function using the geometrical properties of curvature of isophotes, and to improve the matching criteria of patches by calculating the correlation coefficients from the spatial, gradient and Laplacian domains. The performance of this TEBI method will be tested by applying it to natural dataset images, resulting in improved inpainting when compared with other EBI methods.

Fourthly, the recent hybrid-based inpainting techniques are reviewed and a number of highly performing innovative hybrid techniques that combine the use of high order PDE methods with the TEBI method for the simultaneous rebuilding of the missing texture and structure regions in an image are proposed. Such a hybrid scheme first decomposes the image into texture and structure components, and then the missing regions in these components are recovered by TEBI and PDE based methods respectively. The performance of our hybrid schemes will be compared with two existing hybrid algorithms.

Fifthly, we turn our attention to inpainting large missing regions, and develop an innovative inpainting scheme that uses the concept of *seam carving* to reduce this

Abstract

problem to that of inpainting a smaller size missing region that can be dealt with efficiently using the inpainting schemes developed above. Seam carving resizes images based on content-awareness of the image for both reduction and expansion without affecting those image regions that have rich information. The missing region of the seam-carved version will be recovered by the TEBI method, original image size is restored by adding the removed seams and the missing parts of the added seams are then repaired using a high order PDE inpainting scheme. The benefits of this approach in dealing with large missing regions are demonstrated.

The extensive performance testing of the developed inpainting methods shows that these methods significantly outperform existing inpainting methods for such a challenging task. However, the performance is still not acceptable in recovering large missing regions in high texture and structure images, and hence we shall identify remaining challenges to be investigated in the future. We shall also extend our work by investigating recently developed deep learning based image/video colourisation, with the aim of overcoming its limitations and shortcoming. Finally, we should also describe our on-going research into using TDA to detect recently growing serious “malicious” use of inpainting to create Fake images/videos.

Dedicated to
My father's soul and my family

ACKNOWLEDGEMENTS

ALLAH THE MOST GRACIOUS AND MERCIFUL: Who gave me this opportunity for doing research at this level. In addition, there are many people that I have to thank because, without them, I would not be the PhD student that I am today.

My family: My heartiest and warm thanks go to my family, for their support, patience and understanding throughout the duration of my PhD time. I begin with my Mother who has not stopped praying for this work to be completed and I would like to dedicate this work and all my success to my Father, who passed away before I start this work. My wife who has been there for me every step of the way. I end with my sisters, who have been my continuous source of hope and determination to continue, despite the difficult times I have encountered.

My supervisors: I would like to express my sincerest gratitude towards my Supervisor Professor Sabah Jassim for his support, patience, valuable advice, suggestions, convincing arguments, and more during the life of this thesis; I wish him all the best for the future. I would also like to thank my Supervisor Dr. Nasser AL-Jawad for his valuable comments, useful discussions, and encouragement from the beginning until the end.

Staff and Colleague: I am highly indebted and thoroughly grateful to staff at Applied Computing Department and my colleagues. Special thanks go to Aras Asaad, PhD student in the School for his discussion and collaboration to propose and work together, I wish all the best for him in the future. In addition, I would also like to thank my personal tutor (Mr. Hongbo Du) for being a very good listener and for his continuous support and encouragement.

My Sponsor: I would like to express my sincere appreciation and gratitude to the Ministry of Higher Education and Scientific Research in Iraq, to my University in Basra and to the Iraqi Culture Attaché in London for sponsoring my PhD program of study.

ABBREVIATIONS

Anupam	Modified EBI method that introduced in (Anupam et al. 2010).
BP	Belief Propagation approach
BV	Bounded Variation space
CCs	Connected Components
CDD	Curvature-Driven Diffusion model
CMY	(Cyan, Magenta, and Yellow) colour model
CMYK	(Cyan, Magenta, Yellow, and Black) colour model
Criminisi	EBI method that introduced in (Criminisi et al. 2004).
CSQM	Coherence and Structure Quality Measurement
CSRBF	Compactly Supported Radial Basis Function
Deng	Modified EBI method that introduced in (Deng et al. 2015).
DWT	Discrete Wavelet Transform
DFT	Discrete Fourier Transform
EBI	Exemplar-based Inpainting
FDM	Finite-Difference Method
FT	Fourier Transform
HIS	(Hue, Intensity, and Saturation) colour model
HH	High-High (refers to a wavelet subband)
HL	High -Low (refers to a wavelet subband)
$\mathcal{H}^1(\Gamma)$	one-dimensional Hausdorff space
$H_0^1(\Omega)$	Sobolev space
HT	High Texture
HSV	(Hue, Saturation, and Value) colour model
LBP	Local Binary Pattern
LH	Low- High (refers to a wavelet subband)
LL	Low-Low (refers to a wavelet subband)
LT	Low Texture
mCH	modified Cahn-Hilliard model
MESM	Mumford-Shah-Euler Model
MSM	Mumford-Shah Model
MSE	Mean Squared Error
MSSIM	Mean of Structural Similarity

NCD	Normalised Colour Distance
NCC	Normalised Correlation Coefficients
NTSC	(luminance, chrominance, and chrominance) colour model
PDE	Partial Differential Equation
PDE-BI	Partial Differential Equation-Based Inpainting algorithm
PSNR	Peak Signal to Noise Ratio
QCDD	Quick Curvature-Driven Diffusion model
RGB	(Red, Green, Blue) colour space
SC	Seam Carving approach
SSIM	Structural Similarity Index
SVM	Support Vector Machine
TDA	Topological Data Analysis
TEBI	Topological Exemplar-Based Inpainting Method
TK	Tikhonov regularisation
TI	Total Inpainting
TV	Total Variation regularisation
ULBP	Uniform LBP
WT	Wavelet Transform
XYZ	(chrominance, luminance, and chrominance) colour model
YCbCr	(luminance, chrominance, and chrominance) colour model
YUV	(luminance, chrominance, and chrominance) colour model

TABLE OF CONTENTS

ABSTRACT	i
ACKNOWLEDGEMENTS	iv
ABBREVIATIONS	v
TABLE OF CONTENTS	iv
LIST OF FIGURES	iv
LIST OF TABLES	iv
DECLARATION	iv
1 Chapter 1. INTRODUCTION	1
1.1 OVERVIEW OF THE RESEARCH.....	1
1.2 THE PROBLEM OF IMAGE INPAINTING	5
1.2.1 Digital Image.....	5
1.2.2 Image Inpainting.....	6
1.2.3 Applications of Inpainting.....	7
1.3 RESEARCH QUESTIONS.....	9
1.4 AIMS AND OBJECTIVES OF THIS RESEARCH PROJECT	10
1.5 THESIS MAIN CONTRIBUTIONS	11
1.6 PUBLICATIONS AND PRESENTATIONS.....	15
1.6.1 Publications	15
1.6.2 Presentations	16
1.7 THESIS OUTLINE	17
2 Chapter 2. MATHEMATICAL BACKGROUNDS	19
2.1 CLASSIFICATION OF INPAINTING METHODS	19
2.2 INPAINTING DOMAINS	21
2.2.1 Frequency Domain	21
2.3 FUNCTIONS OF BOUNDED VARIATION (BV)	25
2.3.1 Special Differential Operators	26
2.3.2 Space of functions with Bounded Total Variation	26
2.3.3 Calculus of Variations – A brief introduction.....	27
2.4 MINIMISATION PROBLEMS	28
2.4.1 Euler-Lagrange Equation	29
2.4.1.1 Lagrange Multipliers (Bertsekas 2014)	30
2.4.2 The Method of Steepest Descent (Gradient Descent) (Kelley 1999).....	31
2.4.2.1 Unique Solution (W. Rudin 1976)	32
2.5 NUMERICAL METHODS OF PDE-BASED INPAINTING MODELS.....	33
2.5.1 Finite Difference	34
2.5.2 Finite Difference Method	36
2.6 IMAGE INPAINTING QUALITY ASSESSMENTS	39
2.6.1 Statistical Quality Measurements	39
• Full-Reference Image Quality Assessment	39
2.6.1.1 MSE and PSNR.....	40
2.6.1.2 Structural Similarity Index (SSIM)	40
• No Reference Image Quality Assessment	41
2.6.1.3 Entropy	42
2.6.1.4 Mean of Structural Similarity (MSSIM)	42
2.6.1.5 Coherence and Structure Quality Measurement (CSQM).....	43

2.6.2	Topological Data Analysis for Image Quality Assessments	44
2.6.2.1	Local Binary Patterns (LBP)	45
2.6.2.2	Simplicial Complex Construction	47
2.7	SUMMARY AND CONCLUSION.....	48
3	Chapter 3. COLOURISING GREYSCALE IMAGES BASED ON PDE ALGORITHMS	49
3.1	GENERAL COLOURISATION CONCEPTS	49
3.2	LITERATURE OVERVIEW.....	51
3.3	BASICS OF SEMI-AUTOMATIC GREYSCALE IMAGE COLOURISATION.....	57
3.3.1	Image Colour Models	58
3.4	GEOMETRIC CONSIDERATION OF THE COLOURISATION PROBLEM	60
3.4.1	The Mathematics of Sapiro's Colourisation Scheme	61
3.4.2	Further Variation -based Formulation of Image Colourisation	66
3.4.2.1	Minimisation of Directional Derivative of Gradient in Colour Channels	66
3.4.2.2	Minimisation of the Laplacian in Colour Channels.....	69
3.4.2.3	Summary of the above colourisation algorithms.....	72
3.5	EXPERIMENTAL RESULTS	72
3.5.1	Using Non-Segmented Images	74
3.5.2	Using Pre-Segmented Images.....	74
3.6	IMAGE QUALITY ASSESSMENTS.....	76
3.6.1	Database Description	77
3.6.2	Experiment 1: Results of Berkeley Segmentation Database	78
3.6.3	Results Analysis	81
3.6.4	Experiment 2: Examples of Semi-Automatic Image Colourisation Algorithms	82
3.7	SUMMARY AND CONCLUSION.....	84
4	Chapter 4. PDE BASED FULL INPAINTING METHODS	85
4.1	GENERAL CONCEPTS AND MATHEMATICS OF PDE-BI METHODS	86
4.1.1	Variational Methods.....	86
4.1.2	Non-Variational Methods.....	88
4.1.3	Literature Overview.....	88
4.2	SECOND-ORDER PDE-BI METHODS.....	90
4.2.1	Isotropic Diffusion (Tikhonov Regularisation Technique)	90
4.2.2	Harmonic Extension Equation	92
4.2.3	Anisotropic Diffusion (TV Regularisation Technique).....	93
4.2.4	Mumford-Shah Model (MSM).....	95
4.3	HIGHER-ORDER PDE-BI METHODS	97
4.3.1	Mumford-Shah-Euler Model (MESM)	97
4.3.2	Bertalmio Approach (Transport Model).....	99
4.3.3	Modified Cahn-Hilliard Model (mCH).....	102
4.3.4	Fourth-Order Total Variation Model	103
4.4	EXAMPLES OF PDE-BI METHODS IN SPATIAL DOMAIN.....	104
4.4.1	Second-Versus Higher-Order PDE Methods in Inpainting.....	108
4.5	INPAINTING BASED ON PDE AND COLOURISATION METHODS IN SPATIAL DOMAIN	109
4.6	PDE-BI METHOD IN THE FREQUENCY DOMAIN	110
4.7	IMAGE QUALITY ASSESSMENT POST INPAINTING.....	114
4.7.1	Databases Description.....	114
4.7.2	Statistical Measurements for Image Quality	116
4.7.2.1	Experiment 1: Results of using PDE on the natural dataset.....	116
4.7.2.2	Experiment 2: Results of using PDE on the face dataset.....	121
4.7.2.3	Experiment 3: Results of using PDE and colourisation methods.....	128
4.7.2.4	Results Analysis.....	128
4.7.3	TDA for Image Quality Assessment	132
4.7.3.1	Results Analysis.....	140
4.7.4	TDA for PDEs Performance.....	141
4.7.4.1	Results Analysis.....	146

4.8	SUMMARY AND CONCLUSION.....	147
5	Chapter 5. TOPOLOGICAL EXEMPLAR-BASED INPAINTING	149
5.1	INTRODUCTION	149
5.2	EXISTING EXEMPLAR-BASED INPAINTING (EBI).....	151
5.3	LITERATURE REVIEW.....	152
5.4	TOPOLOGICAL EXEMPLAR-BASED INPAINTING METHOD (TEBI)	156
5.4.1	Topological Image analysis.....	157
5.4.1.1	Experimental Dataset and Protocols.....	157
5.4.1.2	Classification Results.....	159
5.4.1.3	Determination of Patch Size	161
5.4.2	Patch Filling Function	162
5.4.2.1	Innovative Adaptive Priority Function	163
5.4.3	Matching Criteria.....	166
5.5	EXPERIMENTAL RESULTS	167
5.6	IMAGE QUALITY ASSESSMENT	170
5.6.1	Statistical measurements for image quality.....	172
5.6.1.1	Results Analysis.....	174
5.6.2	Topological Data analysis for image quality	175
5.6.2.1	Results Analysis.....	179
5.7	SUMMARY AND CONCLUSION.....	180
6	Chapter 6. HYBRID IMAGE INPAINTING TECHNIQUE	182
6.1	HYBRID INPAINTING TECHNIQUES - A LITERATURE REVIEW	183
6.2	HYBRID INPAINTING TECHNIQUE IN THE SPATIAL DOMAIN.....	186
6.2.1	Image decomposition methods.....	186
6.2.2	Inpainting methods for reconstructing the texture and structure images	190
6.2.3	Experimental results in the spatial domain.....	193
6.3	HYBRID INPAINTING TECHNIQUE IN THE FREQUENCY DOMAIN	196
6.4	PERFORMANCE OF THE HYBRID SCHEME IN TERMS OF IMAGE QUALITY.....	200
6.4.1	Statistical image quality measures	200
6.4.1.1	Results analysis.....	205
6.4.2	Topological Data Analysis for image quality.....	207
6.4.2.1	Results analysis	210
6.5	SUMMARY AND CONCLUSION.....	211
7	Chapter 7. INPAINTING LARGE MISSING REGIONS BASED ON SEAM CARVING	213
7.1	INPAINTING RELATIVELY LARGE MISSING REGIONS - INTRODUCTION.....	213
7.2	SEAM CARVING – INTRODUCTION AND IMPLEMENTATION.....	217
7.3	SEAM-CARVED APPROACH TO INPAINTING.....	221
7.4	EXPERIMENTAL RESULTS	221
7.5	IMAGE QUALITY ASSESSMENT	225
7.5.1	Statistical measurements for image quality	226
7.5.1.1	Quality measures for removing large regions.....	228
7.5.1.2	Quality measures for reconstructing large missing regions.....	229
7.5.1.3	Results analysis	229
7.5.2	Topological Data analysis for image quality	231
7.6	SUMMARY AND CONCLUSION.....	233
8	Chapter 8. CONCLUSIONS AND FUTURE RESEARCH.....	235
8.1	WORK SUMMARY	235
8.2	ONGOING AND FUTURE RESEARCH DIRECTIONS	240
	References	242
	Appendix.....	270
A.	EVALUATION OF PERFORMANCE OF PDE ALGORITHMS	270

B.	EVALUATION OF PERFORMANCE OF EBI METHODS	280
C.	EVALUATION OF PERFORMANCE OF HYBRID TECHNIQUES	285
D.	EVALUATION OF PERFORMANCE OF PROPOSED TECHNIQUE BASED ON SEAM CARVING	290

LIST OF FIGURES

Figure 1-1: The digital grayscale image.	6
Figure 1-2: The inpainting task. It is taken from (Sc et al. 2011).	7
Figure 2-1: Inpainting processing in the frequency domain.	21
Figure 2-2: Process of the Haar wavelet transform for the 1 st level.	24
Figure 2-3: Pyramid of wavelet transform for 1st, 2nd and 3rd levels.	25
Figure 2-4: The level curves of a poorly scaled problem.	31
Figure 2-5: A straight line segment connecting two points in a set.	32
Figure 2-6: A straight line segment connecting two points at a function.	32
Figure 2-7: Finite difference of $U(x)$	34
Figure 2-8: The representative mesh point $P(ih, jk)$	35
Figure 2-9: General idea of the finite-difference method	36
Figure 2-10: The finite-difference grid of heat equation.	38
Figure 2-11: Heat inpainting process	38
Figure 2-12: Image quality assessment approaches: Full Reference.	39
Figure 2-13: Image quality assessment approaches: No-Reference.	41
Figure 2-14: Local binary operator.	45
Figure 2-15: The 58 different uniform patterns in $(8, 1)$	46
Figure 2-16: Simplicial complex construction for the quality of image inpainting.	48
Figure 3-1: Schema of semiautomatic colourisation steps.	57
Figure 3-2: Example of a colourisation software layout.	58
Figure 3-3: Illustration of colour spaces.	60
Figure 3-4: Sapiro colourisation algorithm.	65
Figure 3-5: Sapiro colourisation algorithm.	65
Figure 3-6: PDE colourisation algorithms.	72
Figure 3-7: Flowchart of an algorithm for inpainting the colours	72
Figure 3-8: Colourising missing colour regions.	73
Figure 3-9: Colourising whole grayscale image.	73
Figure 3-10: Adding colour to non-segmented images.	74
Figure 3-11: An image has segmented.	75
Figure 3-12: Colourising segmented image in the spatial domain.	75
Figure 3-13: Colourising segmented image in frequency domain.	75
Figure 3-14: Examples of colourising grayscale images.	76
Figure 3-15: Example of eight out of 300 training natural images.	77
Figure 3-16: Masked colour natural image in the RGB colour space.	79
Figure 3-17: Masked colour natural image in the YCbCr colour space.	79
Figure 3-18: Examples of five out of 80 colourisation	79
Figure 3-19: A comparison of colourisation quality achieved.	83
Figure 4-1: Steps of inpainting based PDE method.	86
Figure 4-2: Inpainting based isotropic model	91
Figure 4-3: Isotropic and anisotropic process.	94

List of Figures

Figure4-4: Explanation of Bertalmio module.	100
Figure4-5: Recovering hole in an image.....	105
Figure4-6: Recovering large hole in an image.	105
Figure4-7: Removing text using a PDE inpainting method.....	106
Figure4-8: Removing scratches PDEs inpainting methods.	106
Figure4-9: Removing bold text using PDEs inpainting methods.	106
Figure4-10: Removing bold text by PDEs inpainting methods.	107
Figure 4-11: Recovering missing regions using PDE-based inpainting and colourisation methods in the spatial domain.....	109
Figure 4-12: Recovering missing regions using PDE-based inpainting and colourisation methods in the spatial domain.....	110
Figure4-13: Inpainting based-PDE method in 1st and 2 nd level Haar.....	112
Figure4-14: Removing scratches using PDE inpainting methods in the frequency domain.....	113
Figure4-15: Removing scratches using PDE inpainting methods in the frequency domain.....	113
Figure4-16: Example of eight out of 300 training natural images.....	115
Figure4-17: Example of eight out of 114 training face images.	115
Figure4-18: The same natural image with five different inpainting domains.....	117
Figure4-19: Removing scratches using PDE-BI methods in the spatial domain.....	118
Figure4-20: Removing scratches using PDE-BI methods in the spatial domain.....	118
Figure4-21: Recovering missing regions using PDE-BI methods in the spatial domain.	118
Figure4-22: Recovering missing regions using PDE-BI methods in the wavelet domain.	119
Figure4-23: The same face image with five different inpainting domains.	122
Figure4-24: Scratch removal using the harmonic model in the spatial domain.....	123
Figure4-25: Scratch removal using the mCH model in the spatial domain.	123
Figure4-26: Text removal using the harmonic model in the spatial domain.	123
Figure4-27: Scratches removal using the transport model in the spatial domain.	124
Figure4-28: Object removal using the transport model in the spatial domain.....	124
Figure4-29: Scratches removal using PDE-BI methods in the frequency domain.	125
Figure4-30: Object removal using PDE-BI methods in the frequency domain.....	125
Figure4-31: Example to the MSE of image..	130
Figure4-32: First row; an example of two images	131
Figure4-33: LBP and simplicial complexes of the original and inpainted image.....	132
Figure 4-34: Example of drawing SC for two images that have same value of PSNR.	133
Figure4-35: Evaluation of performance of PDE-BI methods	135
Figure4-36: Evaluation of performance of PDE-BI methods	136
Figure4-37: Evaluation of performance of PDE-BI methods	138
Figure4-38: Evaluation of performance of PDE-BI methods	139
Figure4-39: Object removal using PDE-BI methods.....	142
Figure4-40: Evaluation of performance of PDE-BI methods.	143
Figure4-41: Object removal using PDE-BI methods.....	143
Figure4-42: Evaluation of performance of PDE-BI methods.	144

List of Figures

Figure4-43: Object removal using PDE-BI methods.....	144
Figure4-44: Evaluation of performance of PDE-BI methods.	145
Figure4-45: Object removal using PDE-BI methods.....	145
Figure4-46: Evaluation of performance of PDE-BI methods.....	146
Figure5-1: The EBI procedures for recovering the missing region.....	152
Figure5-2: Flowchart of the proposed topological EBI method.	156
Figure5-3: Samples of low texture images selected from google image.	158
Figure5-4: Texture classification results using SVM classifier.....	160
Figure5-5: Texture classification results using an SVM classifier.	160
Figure5-6: Removing Objects.....	168
Figure5-7: Region reconstruction using EBI.	168
Figure5-8: Region reconstruction using EBI.	169
Figure5-9: Region reconstruction using EBI.	169
Figure5-10: Example of eight out of 100 training low-information natural images....	171
Figure5-11: Example of eight out of 100 training high-information natural images...171	
Figure5-12: The same natural image with five different inpainting domains.....	172
Figure5-13: Evaluation of performance of EBI techniques.	177
Figure5-14: Evaluation of performance of EBI techniques.	178
Figure6-1: Image denoising example.....	188
Figure 6-2: Comparison of three denoising models.....	189
Figure6-3: Image decomposition example.....	189
Figure6-4: Comparison of three decomposing models:.....	190
Figure6-5: Flowchart Hybrid technique in the spatial domain.	191
Figure6-6: Recovering missing texture region.....	192
Figure6-7: Hybrid inpainting process.	194
Figure6-8: Recovering the missing region using the hybrid technique.	194
Figure6-9: Object removal by hybrid technique.....	195
Figure6-10: Comparison of the proposed hybrid technique.....	195
Figure6-11: The representative value of the wavelet transform.....	198
Figure6-12: Hybrid-Based Inpainting technique.	199
Figure6-13: Inpainting based-hybrid technique in 2 nd and 3 rd level wavelet.....	200
Figure 6-14: The same natural image with five different inpainting domains.....	202
Figure6-15: Recovering missing regions in the spatial domain.....	202
Figure6-16: Recovering missing regions in the spatial domain.....	203
Figure6-17: Recovering missing regions in the frequency domain.	203
Figure6-18: Recovering missing regions in the frequency domain.	203
Figure6-19: Evaluation of performance of hybrid techniques using TDA approach at 8 iterations in G6.....	208
Figure6-20: Evaluation of performance of hybrid techniques using TDA approach at 8 iterations in G5.....	209
Figure 7-1: Failure of wavelet-based Hybrid inpainting for large missing region.	216
Figure7-2: Different energy functions for the natural image.....	218
Figure7-3: The flowchart of the seam carving approach.....	219
Figure7-4: Seam carving process.....	219
Figure7-5: Seam carving process.....	220

List of Figures

Figure7-6: Inpainting-based seam-carving approach.....	221
Figure7-7: Large object removal examples.....	222
Figure7-8: Recovering large missing regions examples.....	224
Figure7-9: The same natural image with five different inpainting domains.....	226
Figure 7-10: Recovering large missing regions examples.....	227
Figure7-11: Evaluation of performance of the proposed inpainting technique using TDA approach at 8 iterations in G5.....	232
Figure7-12: Evaluation of performance of the proposed inpainting technique using the TDA approach at 8 iterations in G1.....	232
Figure A-1: Evaluation of performance of PDE algorithms using TDA approach at 8 iterations in G1.....	270
Figure A-2: Evaluation of performance of PDE algorithms using TDA approach at 8 iterations in G2.....	271
Figure A-3: Evaluation of performance of PDE algorithms using TDA approach at 8 iterations in G4.....	272
Figure A-4: Evaluation of performance of PDE algorithms using TDA approach at 8 iterations in G5.....	273
Figure A-5: Evaluation of performance of PDE algorithms using TDA approach at 8 iterations in G7.....	274
Figure A-6: Evaluation of performance of PDE algorithms using TDA approach at 8 iterations in G1.....	275
Figure A-7: Evaluation of performance of PDE algorithms using TDA approach at 8 iterations in G2.....	276
Figure A-8: Evaluation of performance of PDE algorithms using TDA approach at 8 iterations in G4.....	277
Figure A-9: Evaluation of performance of PDE algorithms using TDA approach at 8 iterations in G5.....	278
Figure A-10: Evaluation of performance of PDE algorithms using TDA approach at 8 iterations in G7.....	279
Figure B-1: Evaluation of performance of EBI techniques using TDA approach at 8 iterations in G1.....	280
Figure B-2: Evaluation of performance of EBI techniques using TDA approach at 8 iterations in G2.....	281
Figure B-3: Evaluation of performance of EBI techniques using TDA approach at 8 iterations in G3.....	282
Figure B-4: Evaluation of performance of EBI techniques using TDA approach at 8 iterations in G5.....	283
Figure B-5: Evaluation of performance of EBI techniques using TDA approach at 8 iterations in G6.....	284
Figure C-1: Evaluation of performance of hybrid techniques using TDA approach at 8 iterations in G1.....	285
Figure C-2: Evaluation of performance of hybrid techniques using TDA approach at 8 iterations in G2.....	286
Figure C-3: Evaluation of performance of hybrid techniques using TDA approach at 8 iterations in G3.....	287

List of Figures

Figure C-4: Evaluation of performance of hybrid techniques using TDA approach at 8 iterations in G4.....	288
Figure C-5: Evaluation of performance of hybrid techniques using TDA approach at 8 iterations in G7.....	289
Figure D-1: Evaluation of performance of the proposed technique using the TDA approach at 8 iterations in G2	290
Figure D-2: Evaluation of performance of the proposed technique using the TDA approach at 8 iterations in G3.	291
Figure D-3: Evaluation of performance of the proposed technique using the TDA approach at 8 iterations in G4.	291
Figure D-4: Evaluation of performance of the proposed technique using the TDA approach at 8 iterations in G6.	292
Figure D-5: Evaluation of performance of the proposed technique using the TDA approach at 8 iterations in G7.	292

LIST OF TABLES

Table 3-1: Values of conversion parameters from different colour spaces to RGB space. .	64
Table 3-2: The average of PSNR, SSIM and NCD values from original and inpainted images in the spatial domain for 8 different colour spaces. Poisson, Curvature and 4 th -order methods have been used to obtain these error values.	80
Table 3-3: The average of PSNR, SSIM and NCD values from original and inpainted images, in the frequency domain for 8 different colour spaces. Poisson, Curvature and 4 th -order PDE methods have used to obtain these values.....	81
Table 3-4: Results of colourisation quality for all three algorithms, PSNR, SSIM, and NCD.	83
Table 4-1: The average values of MSE and PSNR of inpainted images of PDE methods in different levels of DWT.	112
Table 4-2: The average values of MSE, PSNR, SSIM, and entropy are shown for image inpainting using Harmonic Transport, MES and mCH models in the spatial domain.	120
Table 4-3: The average values of MSE, PSNR, SSIM, and entropy are shown for image inpainting using harmonic transport, MES and mCH models in the frequency domain.	121
Table 4-4: The average values of MSE, PSNR, SSIM, and entropy are demonstrated for image inpainting using harmonic, transport, MES and mCH models in the spatial domain.	126
Table 4-5: The average values of MSE, PSNR, SSIM, and entropy are demonstrated for image inpainting using harmonic, transport, MES and mCH models in the frequency domain.	127
Table 4-6: The average values of MSE, PSNR, SSIM, and entropy are demonstrated for image inpainting using only harmonic, MES and mCH models and these models with colourisation method in the spatial domain.....	128
Table 5-1: Description of the priority functions tested in this study.	163
Table 5-2: comparing priority function, matching criteria and patch size in Criminisi, Anupam, Deng and TEBI.....	168
Table 5-3: Inpainted image quality assessment comparison using MSE, PSNR, SSIM, CSQM and Entropy for low information dataset images.	173
Table 5-4: Inpainted image quality assessment comparison using MSE, PSNR, SSIM, CSQM and Entropy for high information dataset images.	173
Table 6-1: The average values of MSE, PSNR and SSIM are shown for image inpainting using Bertalmio, TEBI techniques and our proposed hybrid techniques in the spatial domain.	204
Table 6-2: The average values of MSE, PSNR and SSIM are shown for image inpainting using Bertalmio, TEBI techniques and our proposed hybrid techniques in the frequency domain.	205
Table 7-1: Ratios of missing regions size to whole images in figure 7-7 before and after seam-carving.	223
Table 7-2: The size of the missing regions to the whole images in figure 7-8 before and after reduction using the seam-carving method.	224
Table 7-3: The size of the missing regions to the whole images in figure 7-9 before and after reduced using the seam-carving approach.	227
Table 7-4: Inpainted image quality assessment comparison using E, MSSIM, and CSQM.	228
Table 7-5: Inpainted image quality assessment comparison using MSE, PSNR, SSIM, CSQM and Entropy.....	229

DECLARATION

This work has not previously been submitted for a degree or diploma in the University of Buckingham or any other university. To the best of my knowledge and belief, the thesis contains no material previously published or written by another person except where due reference is made in the thesis itself.

Ahmed Al-Jaberi

Chapter 1 INTRODUCTION

Image inpainting is a process that has been investigated for a long time as the concept of reconstructing old photos that have degraded over time or modifying a photo to remove unwanted objects/persons from it. However, a variety of malicious as well as genuine use of image inpainting started to grow fast as a result of the recent rapid advances in technology that have led to exponential growth of deployment of cheaply available computing devices (mobiles) of high computational power endowed with free software that enable fast transmission of high-resolution digital images/videos. Indeed, the concept of inpainting has expanded in many directions that go well beyond repairing images. As an instant of missing data, interpolation has long been recognised as the underlying tool of inpainting. Consequently, calculus of variation and numerical solutions of partial differential equations have been the natural source of solutions for the filling missing data version of image inpainting. The main aim of this thesis is to investigate the use of Partial Differential Equation (PDE) for dealing with the emergent aspects and application of inpainting with focus on developing innovative efficient inpainting tools, testing the performance of these tools in terms of various image quality measures as well as detection of malicious image modifications by inpainting.

The aim of this introductory chapter is to describe the general idea of image inpainting and its challenges in image inpainting. First there is an overview of emerging inpainting research challenges, briefly highlighting related approaches and directions of research, if any, that have been adopted in the literature and the bases of our innovation to improve and complement these efforts. Then the main modern applications that form our motivations for doing this research are described, and the overall objectives of the research reported in this thesis are stated. This will be followed by brief descriptions of the main contributions of this thesis including the list of publications produced so far, and of the thesis organisational structure.

1.1 Overview of the Research

In image processing and analysis, the success of most applications depends on the quality of the image signal. The quality of digital images is a variety of

Chapter 1: Introduction

actions/decisions that occur during recording, digitisation, compression, and in transit over channels that are subject to signal interference. At each of these stages, factors influencing the image quality include camera properties, lighting and environmental conditions, compression rates and communication channel capacity and their effects are manifested by the appearance of different types of noise and artefacts as well as blurring and other type's degradations. In contrast, printed photographs, portraits, and pre-digital age recorded films may over time degrade, fade and suffer from loss of image data in irregular strokes-like regions and torn material as a result of storage/display related conditions or sabotage. The most common feature in these cases, is the presence of regions with missing/incomplete image data/information. Repairing such images/photos/paintings and restoring missing data/ information to its "original state" is referred to as image inpainting.

A well-established example of inpainting application is the regular restoration of old paintings kept in museums carried out by skilled artists. Since the early days of the discovery of photography, inpainting has been used, albeit sparingly, to remove undesired objects/persons or superposing photos of unrelated objects/persons onto an existing photo. The advent of digital imaging created not only new applications in a variety of human activities but the digitisation process and other basic image processing tasks such as compression result in a variety of image degradations that need to be dealt with to ensure adequate image quality. To some extent, most image degradations result in spurious local features not blending well with their surroundings, and inpainting-related procedures may be useful for quality enhancements.

There are different types of missing image information such as missing colour, and missing regions caused by, e.g. noise, blur, degradation, etc. In the digital world, image inpainting (also known as interpolation image/video) refers to the application of advanced algorithms to supersede lost or damaged data from an image portion. The aim of inpainting is to blend the modification within the undegraded surrounding and success is measured by how difficult the repair can be detected visibly or by image analysis.

In recent years, the above two main approaches have been modified and improved in various directions, and in general image inpainting approaches are classified into several categories (Vadhel & Limbasiya 2016), (Nileshbhai Patel 2016), and (Suthar et al. 2014):

Chapter 1: Introduction

1. PDE based Inpainting.
2. Texture Synthesis based Inpainting.
3. Exemplar-based Inpainting (EBI).
4. Semi-automatic and Fast Inpainting.
5. Hybrid Inpainting.

Each of these approaches recovers the damaged regions in accordance to certain requirements of expectation of the repaired image content, and hence have own limitations and shortcomings. Next, the main ideas in these approaches are briefly explained. There are different inpainting techniques, the most prominent inpainting techniques are variational/PDE-based inpainting and exemplar-based inpainting techniques. The variational/PDE based approaches justified by the expectation that image information flow along image features are interrupted through the missing region and accordingly have been used to restore relatively small missing image regions, (Sc et al. 2011). In this case, the small missing region is reconstructed pixel by pixel based on propagating the information from the immediate boundary pixels of the missing area. The larger the missing region is, the less likely image features flow continuously/smoothly along their paths for long spatial periods. Moreover, image features may not flow in the same directions of the way numerical solutions of PDE propagate information. The exemplar-based inpainting approach, complements the idea of using flow of information along image features with the idea that in most images there are a lot of similarities between image blocks, and reconstruct the missing regions block by block using block similarities in the surrounding regions (Criminisi et al. 2004). The exemplar-based techniques have been used for reconstructing relatively large missing regions, and it fill-in the missing region with information in such a way that isophote lines arriving at the regions' boundaries are completed inside the region. This technique does not require to specify where the new information comes from the borders, but its success relies on compatibility of information between the missing region and its surrounding regions in terms of simple textures and structures.

The texture synthesis approach recovers the missing texture region in the image by searching for similar missing pixels neighbour around the missing region and copy its pixel value to the missing pixel. This algorithm performs reasonably well, but it is very slow due to the extensive searching (Efros & Leung 1999).

Chapter 1: Introduction

Whereas, hybrid inpainting is combined of two inpainting methods which are texture-based synthesis and PDE-based inpainting methods for filling the missing regions. The first step of this approach is to divide the image into texture and structure regions. Then these regions are reconstructed with corresponding methods which they need a relatively long time (Rane et al. 2003).

The semi-automatic inpainting approach is a two-stage process. In the first stage, the user provides essential missing information manually by sketching object boundaries from the surrounding areas to the missing area. The patch-based texture synthesis method is utilised to produce the texture (Telea 2018) in the second stage. This approach takes a long time in proportion to the inpainting region size.

The challenges of applying these inpainting approaches to recover the missing regions are the large size of the missing regions and the complexity of texture and structure in the surrounding of the missing regions. The main premise of our optimism comes from the fact that images convey significant amount of information that can be modelled in much more sophisticated and well-understood ways than that exploited by the current models of texture similarity and distribution as well as variational relation between different channels of image colour spaces. Moreover, the wealth of innovative techniques developed over the years in the field of image processing and image analysis provide a rich source of mathematically based procedures that one can exploit in dealing with these challenges. For example, the properties of variation in image information, across different colour channels, captured by gradient, Laplacian and other transformations can be used to propose new methods for adding colour to grayscale images. The use of different order PDE-based inpainting techniques is an obvious candidate approach for investigating inpainting missing regions of larger size than that dealt with in the literature. Compression, or related, techniques provide another source of methods to deal with the challenge of missing region size. For example, the concept of seam carving that results in compressing/resizing images horizontally and/or vertically with minimal loss of important image information is a natural approach to improve the performance of existing inpainting schemes, such as the EBI, for recovering large missing regions. Together, these various ideas will be investigated and used to introduce more ways of building hybrid inpainting techniques.

In order to measure the success of any inpainting solutions, it is natural to simulate loss of various types of image on publicly available image dataset and compare the quality

Chapter 1: Introduction

of the inpainted images with those of the original images. Unfortunately, commonly used image quality measures, such as MSE, PSNR, NCD, SSIM, MSSIM, CSQM and Entropy are not adequately capable of assessing the success of various image inpainting techniques. The recent work, conducted at Buckingham, on the extension/realisation of the emerging new Topological Data Analysis (TDA) approach to image analysis seem to provide an innovative image quality assessment tool. Indeed, the fact that the TDA approach model image texture at different filtration/proximity thresholds is an obvious mathematically rich candidate for incorporation into our assessment test of the success of inpainting techniques. In particular, the performance of innovative techniques of image inpainting is developed and tested to overcome their limitations and to reconstruct the large missing regions in natural and face images that lead to improvements in the accuracy. In addition, the topological data analysis approach could help to refine block similarity concept used in the EBI-based inpainting technique, to allow recovering large missing regions with complex texture and structure around them.

1.2 The Problem of Image Inpainting

This section is devoted to the mathematical definition of the problem under investigation (image inpainting) and we shall highlight the need for this research by giving an overview of the various modern applications that have expanded over the last few years beyond the obvious image restoration. In order to describe the concept of image inpainting, we shall first describe basic mathematics of digital images. This is done for the benefit of readers who have little or no background in Image processing and can be skipped by others.

1.2.1 Digital Image

A digital image is obtained from an analogue image (representing the photograph of a scene, object or phenomena in the continuous world) by sampling and quantization. Basically, this means that the digital camera superimposes a regular grid on an analogue image and assigns a value to each grid element e.g. the mean brightness in this area element. cf. (Aubert & Kornprobst 2006). Mathematically, a digital image f is a rectangular array/matrix structure where each element at position (i, j) of the structure function pixel is assigned an intensity values $f(i, j)$. In grayscale images, the value $f_{i,j}$ is a single number, a scalar value normally ranging between 0 (black) and 255 (white). For colour images each $f_{i,j}$ is a vector of three colour values, e.g., (r, g, b), where each

Chapter 1: Introduction

channel r , g and b represents the red, green, and blue component of the colour and ranges, each $f_{i,j}$ is a vector of three values,

$$f_{i,j} = (r_{i,j}, g_{i,j}, b_{i,j}),$$

that denotes the intensity of red, green, and blue channels at the point (i,j) . As in the case of greyscale images, the values in these channels are also integers in the range from 0 to 255. A digital image can also be defined mathematically as a two-dimensional image function defined on a flat rectangle called the image domain. This function is single-valued in case of the grayscale image while it is 3-dimensional vector-valued in the case of a colour image. The pixel value $f(x,y)$ denotes the gray value, i.e., colour value, of the image at the pixel position (x,y) of the image domain. Figure 1-1 describes the digital image and its image function (a matrix) for the case of a grey value image.



Figure 1-1: The digital grayscale image with a small red square in (a), a red region to the data matrix in (b).

Now, an image function (a matrix) is known as a mathematical object on which a variety of mathematical operations can act. These mathematical operations are often used analyse or extract different types of information for image processing purposes, including statistical methods, morphological operations, and other filtering. We are especially concerned with operations that use PDE and variational methods image inpainting and filling missing regions.

1.2.2 Image Inpainting

This section is devoted to the mathematical definition of the problem under investigation (image inpainting) and we shall highlight the need for this research by giving an overview of the various modern applications that have expanded over the last few years beyond the obvious image restoration. Inpainting is the process of

Chapter 1: Introduction

reconstructing the missing regions of the damaged images based on information which that obtained from the surrounding regions, this process is called image inpainting, and it considers an important task in image processing.

Let f represents a given image which that defined on an image domain Ω . Generally speaking, the task is to reconstruct the missing region of damaged image u in the damaged domain $D \subset \Omega$, called inpainting domain (or a gap/hole), see Figure 1-2.

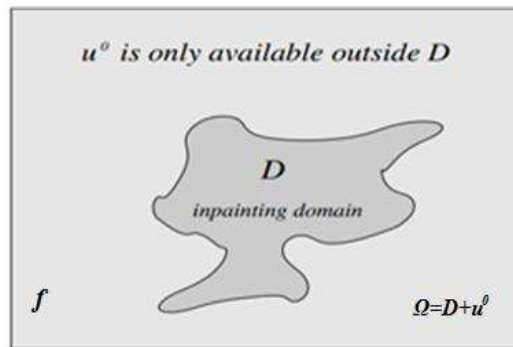


Figure 1-2: The inpainting task. It is taken from (Sc et al. 2011).

The task of reconstructing the missing region of the damaged image has been called term inpainting by the art restoration workers, see in (Ekeland & Temam 1976). The framework of digital restoration has introduced for the first time by Bertalmio et al. in (Bertalmio et al. 2000). Therein the authors in (Bertalmio et al. 2000) introduced a new PDE which intends to mimic the restoration work of museum artists. This equation will be discussed in more detail in section 4.3.2. The next section gives some applications for image inpainting.

1.2.3 Applications of Inpainting

There are several applications which use the concept of inpainting in image processing for a variety of reasons. One important application of digital inpainting is automatic text removal and object removal in images and films for special effects; different mathematical models have been used to remove the objects and to recover the missing regions based on the PDE methods described by (Bertalmio et al. 2000), (Chan & Shen 2002), and (Cocquerez et al. 2003). These PDE methods have been proposed based on total variation, isophote, curvature driven diffusion and so on, and these methods propagated the information in the missing regions based on the information in the surrounding areas. Furthermore, these PDE methods can also be used to remove the dates, texts, subtitles, or publicity from an image (Bertalmio et al. 2000), (Chan & Shen 2002), (Ballester et al. 2001), and (T. Chan and J.Shen 2001), by propagating

Chapter 1: Introduction

information from the surrounding areas into the missing regions. In addition, old or damaged images and films can be restored by detecting missing regions and reconstructing the information without causing distortion to those areas of the frames (images) that are not affected. Different statistical detector models have been used and then the detected missing regions have been reconstructed (Kokaram et al. 1995a) and (Kokaram et al. 1995b). In lossy perceptual image coding and compression based on the edge information, where the edge has played a crucial role in vision and image analysis, in image coding, the performance of a scheme is very much determined by its reaction to edges. The inpainting based PDE approach has been used for (lossy) image coding and compression based on the edge information (Chan & Shen 2002) and (Saha & Vemuri 2000). Moreover, PDE-based inpainting methods have been used for adding colour to grayscale images; these methods have been proposed based on the geometric relations between the channels in the colour space (Sapiro 2005). Furthermore, disocclusion is required (using the variational model to reconstruct the missing region based on the geometry of objects in the image), the numerical solutions of PDE methods recovers the missing regions. (Nitzberg et al. 1993), and (Masnou & Morel 1998). In the context of error control and concealment of it in video communication, where the inpainting methods attempt to recover the lost information by estimation and interpolation without depending on additional information from the encoder, these inpainting methods are called interactive error concealment methods (interpolation and statistical methods) (Yao Wang & Qin-Fan Zhu 1998). For image super-resolution, the inpainting based PDE method have been used to reconstruct high-resolution images. This method for super-resolution is based on a total variation prior and variational distribution approximations (Babacan et al. 2008). For image zooming (Chan & Shen 2002), and (Malgouyres & Guichard 2001), digital zoom-in has wide applications in digital image processing, image super-resolution, data compression, etc. Zoom-out is a process entailing loss of detail, including in the framework of wavelets and multi-resolution analysis. The inpainting method has been used to zoom-in which is the inverse of zoom-out and thus belongs to the general category of image restoration problems. A digital zoom-in model almost identical to the continuous TV inpainting model is constructed based on the self-contained digitised PDE method developed by authors in (Chan & Shen 2002). On the other hand, the inpainting methods can be used for malicious purposes such as fake news and images. The development of the software for use in phones and computers in recent years has facilitated dealing with digital

images. This software is available to anyone who can use it. As a result the world has become susceptible to fake news and so it is increasingly important for researchers to acquire understanding of how these inpainting methods are working so that they can try to reverse the inpainting process to detect the forged images, this field of work is now called image forgery detection for object removal by image inpainting methods (Muhammad et al. 2012), (Liang et al. 2015) and (Yang et al. 2017). These algorithms have been used to detect forged images and identify the manipulated regions in them.

1.3 Research Questions

The main focus of this work is investigating the numerical solutions of certain PDEs that have applications in image processing such as image inpainting. The questions arising from this are:

1. Can high order PDE methods do better than second order PDE methods for recovering missing region?

The high order PDE methods essentially expected to recover missing regions of images better than second order PDE methods because they use relatively more information from the borders during the recovery process. Therefore, it's interesting to know what the effect of the high order of PDE methods.

2. Can high order PDE methods be used to recover small missing regions with complex texture in the surrounding areas?

PDE methods generally recover non-textured missing regions in an image, so the effects of PDE order in recovering small missing regions with high texture in the surrounding areas need to be investigated in terms of the connection of edges over large distances (i.e. Connectivity Principle).

3. Can high order PDE methods be used to recover large missing regions with simple texture and structure in the surrounding areas?

PDE methods usually recover small missing regions in an image, so the effects of PDE order in recovering large missing regions in terms of the smooth propagation of level lines into the damaged domain (i.e. Curvature Preservation) need to be investigated and studied.

4. Are the statistical measurements good for image quality measurement? If not, are there other measurements which can be used to check the qualities of inpainted images?

Some of these statistical measurements (MSE and PSNR) have limitations revealed by their failures to give results which correspond to visual quality assessments. An application that tests the change in the image structure needs to be investigated and compared with the traditional image quality assessment methods.

5. Does the size of patch propagation in the EBI method affect the results?

The EBI method propagates the information in the missing region with a typical fixed size of patch propagation 9×9 . Investigating the effects of changing the size of patch propagation in the missing regions is needed to be tested.

1.4 Aims and Objectives of this Research project

This thesis primarily aims to investigate and develop mathematically inspired and justified techniques that improve the treatment of the different missing regions in a variety of images. In summary, the main objectives are:

- In partial missing regions, studying the geometric relations between the channels in the colour spaces such as RGB, and seven other spaces and exploiting these relations to propose a colourisation formula for adding colour to greyscale images in both spatial and frequency domains.
- In total missing regions, analyses and evaluations of the performances of inpainting-based PDE methods of various orders in recovering the missing regions in the image. This will help to choose the best PDE method that will be used with other inpainting techniques to recover texture and structure in images in both spatial and frequency domains.
- Carrying out theoretical and empirical analyses of current inpainting methods (i.e. PDE methods), which aim to evaluate their performance in reconstructing the contents of missing regions of various sizes and with various quantities of texture and structure in the surrounding areas.
- Developing an innovative hybrid technique that uses high order-PDE and Topological EBI methods to recover small missing regions with high texture and structure in the surrounding areas.

Chapter 1: Introduction

- Developing a novel technique to recover large missing regions with high texture and structure in the surrounding areas using a seam-carving approach.
- Rigorous evaluation of the quality of image inpainting obtained using different inpainting methods based on the proposed TDA approach that is used to check the performances of these inpainting algorithms.
- Investigation of the performances of EBI method with different-size patch propagations in recovering missing regions of different sizes. The TDA approach is used to improve the EBI method, and is applied to adaptively determine the patch size based on the quantity of texture in the surrounding areas.

Our approaches to meet these objectives rely in many ways on the wealth of mathematical techniques and concepts developed over the last few decades in the field of image processing and analysis.

1.5 Thesis Main Contributions

Our extensive investigations and experimental work have led to a number of advances in meeting the main objectives and modifying existing inpainting schemes with improved capability in restoring missing image regions in different scenarios. Our review of the different existing inpainting schemes revealed that their deployment under different circumstances in various applications continues to entail many challenges. Many studies have been conducted to handle textured large missing regions in natural images of high quality. Three main shortcoming issues are identified that face these algorithms, which arise when the missing region is large, when there is a high quantity of texture around the missing region and when the surrounding areas of the missing regions contain geometrically complex features. New algorithms are developed to remedy the above shortcomings. The implementations of these new algorithms reconstruct the textured large missing regions in natural images, based on the contents of the areas surrounding missing regions. Therefore, this thesis claims the following major contributions:

1. In (Sapiro 2005), G. Sapiro proposed a PDE-based colourisation technique that deals with the loss of 2 specific colour channels in a region where the 3 channel is available. The author has shown that the (scalar) luminance channel faithfully represents the geometry of the whole (directional) colour image. The performance

Chapter 1: Introduction

of this technique was good in adding colour to the greyscale image. However, it has a problem at edges where the colours overlap with each other.

- To overcome this problem, new colourisation formulas are deduced to reduce the effect of the colour overlapping at object edges, which are tested on non-segmented images and pre-segmented images.
- These formulas are implemented on 8 different colour spaces, both in the spatial and frequency image domains.

The performance of this technique was tested on 80 publicly available natural images, and compared with those of three existing algorithms introduced in (Sapiro 2005), (Levin et al. 2004), and (Popowicz & Smolka 2014). The evaluation was based on statistical measurements such as MSE, PSNR, NCD, and SSIM. The results confirmed that our technique successfully propagates the missing colours into the greyscale regions of the images.

2. Our next contribution focused on the more general colourisation problem to the case of missing all colour in a region, i.e. colour information is only available outside and on the border of the region. Existing PDE-based inpainting algorithms can be divided into two groups: inpainting algorithms based on energy function, and inpainting algorithms based on PDEs directly. Inpainting-based PDE algorithms have first been developed, in this thesis, for the reconstructions of small missing regions without texture. Our contributions, in this respect, relate the overcoming these limitations and can be summarised as follows:

- Several PDE algorithms of 2nd and higher orders have been studied to reconstruct the small missing regions.
- We propose to use PDE algorithms to recover missing regions in Y channel, then PDE-based colourisation methods have been applied to reconstruct the missing regions in Cb and Cr channels.
- The performance of inpainting-based PDE algorithms is evaluated by statistical measurements and topological data analysis-based quality measure.
- The performance of 2nd and higher order PDE methods have been tested on the connection of edges over large distances (i.e. Connectivity Principle) and the smooth propagation of level lines into the damaged domain (i.e. Curvature Preservation).

Chapter 1: Introduction

- The performance of these algorithms has been assessed by studying their iterations and their convergence properties.
- Also, these PDE algorithms have been applied to natural and face images datasets in the frequency domain, and their results are compared with the results of the spatial domain. MSE, PSNR E, MSSIM and CSQM are used to evaluate these techniques in both the spatial and frequency domains. TDA scheme is used to check the quality of image inpainting and to check the efficacy of the PDE algorithms.
- The PDE algorithms have tested on the natural images in both the spatial and frequency domains. The results of these algorithms in the spatial domain have compared the results of them in the frequency domain.

To sum up, these PDE algorithms have been applied to several natural images and shown to successfully reconstruct small non-textured missing regions with edges and corners, but there is still challenging existing with textured missing regions. Therefore, we attempted to handle this challenge as our next contribution.

3. As mentioned before, inpainting-based PDE algorithms cannot reconstruct textured missing regions. Our review of existing schemes to deal with this issue revealed two interesting schemes: an EBI method (Jassim et al. 2018) and high order PDE algorithm (Esedoglu & Shen 2002). A novel hybrid inpainting technique is developed which is inspired by (Bertalmio et al. 2000). The basic idea is to divide the image into texture and structure components. The missing regions of these components are restored separately by EBI and PDE-based methods respectively.

The specific contributions of this work can be summarised as follows:

- Three types of decomposing methods have been tested to divide the image into texture and structure components (Rudin et al. 1992).
- Different order PDE-based algorithms such as Mumford-Shah (Esedoglu & Shen 2002), and Cahn-Hilliard (A. L. Bertozzi et al. 2007), have been used to reconstruct missing regions in the structure component.
- An EBI method has been applied to reconstruct the missing regions in the texture image component; the use of different block sizes, based on the quantities of the texture in the surrounding of the missing regions is proposed.

- The hybrid technique has been applied to natural dataset images in both the spatial and frequency domains, its results in the spatial domain has compared with its results in the frequency domain.

To conclude, the proposed technique has been applied to a sufficiently large dataset of natural images, and their performances have been compared with those resulting from the use of the algorithm in (Bertalmio et al. 2000). Statistical measurements and TDA approach are used to evaluate the results of the mentioned techniques. This technique successfully reconstructed the small textured missing regions with edges and corners, but it still has the challenge to recover the large missing regions with high structure and texture. Therefore, the next step will deal with this issue by applying the EBI algorithm.

4. An EBI technique was proposed in (Criminisi et al. 2004) for reconstructing large missing regions with simple textures and structures. It is somewhat limited to recovering missing regions with rich textures and structures. To overcome this drawback, an innovative topological exemplar-based inpainting (TEBI) technique is developed whereby the assessment of the similarity of patches includes the application of topological parameters gained by topological data analysis scheme (Jassim et al. 2018). Furthermore, the ideas in (Anupam et al. 2010), (Hesabi & Mahdavi-Amiri 2012), (Deng et al. 2015), and (Asaad & Jassim 2017) are improved by using geometrical structure features of the images. Below are the main achievements in this part:

- The size of the patch (a window to be searched for its match in the whole image) is determined based on the quantity of the texture in the surrounding of the missing region via Topological Data Analysis (TDA) scheme.
- The filling priority of the patch is determined by the geometrical properties of curvature of isophotes.
- Introducing new patch-matching scheme, which can be divided into two stages;
 - 1- Calculating the sum -of -squared distance (SSD) for Laplacian, gradient and spatial domains of the image and selecting the nearest 30 patches.
 - 2- Measuring the normalised cross-correlation coefficient of the 30 patches defined in stage one to select the nearest patch.

Chapter 1: Introduction

The proposed approach is implemented on 200 natural images that contain missing regions of different sizes and random locations in the same images. The results have been compared with the results of algorithms introduced in (Criminisi et al. 2004), (Anupam et al. 2010), and (Abdollahifard & Kalantari 2016), and evaluated based on statistical measurements such as MSE, PSNR and SSIM. Also, this proposed approach has been applied to natural images in the frequency domain, and its result is compared with the results of the spatial domain. MSE, PSNR E, MSSIM and CSQM are used to evaluate these techniques in both the spatial and frequency domains. This proposed approach successfully reconstructed the large missing regions with rich texture and structure however it still has a shortcoming with the largest missing regions which is solved in the next step.

5. All inpainting algorithms, including the above ones, have limitations with large missing regions. A novel technique for reconstructing large missing regions in images has been developed consisting of EBI and PDEs algorithms successively with the seam carving approach (Avidan & Shamir 2007), as explained below:

- The seam carving approach helped to shrink the missing region in the image.
- A TEBI algorithm has been applied for reconstructing shrunken missing regions.
- The carved seams carving has been reinstated to restore the original missing region size in the image.
- Three different high-order PDE algorithms have then been used for restoring image information along the seams within the missing regions in the image.

Lastly, the performance of the proposed technique has been tested on different natural images. The results have been compared with the results of the algorithm in (Criminisi et al. 2004) by using statistical measurements and TDA approach. The proposed technique achieved reconstructing the largest texture and structure missing regions.

1.6 Publications and Presentations

1.6.1 Publications

1. A. Al-Jabari, S. Jassim, and N. Al-Jawad. ‘‘ Colourising monochrome images’’. SPIE Commercial + Scientific Sensing and Imaging, 2018, Orlando, Florida, United States. Proceedings Volume 10668, Mobile Multimedia/Image

Chapter 1: Introduction

- Processing, Security, and Applications 2018; 1066806 (2018).
<https://doi.org/10.1117/12.2309938>.
2. A. Al-Jaberi, A. Asaad, S. Jassim, and N. Al-Jawad. “Topological data analysis to improve exemplar-based inpainting”. SPIE Commercial + Scientific Sensing and Imaging, 2018, Orlando, Florida, United States. Proceedings Volume 10668, Mobile Multimedia/Image Processing, Security, and Applications 2018; 1066805 (2018). <https://doi.org/10.1117/12.2309931>.
 3. A. Al-Jabari, S. A. Jassim, and N. Al-Jawad. “Inpainting Large Missing Region-Based on Seam Carving Approach”, Intelligent Systems with Computer Vision and Data Analytics, EAI, ID 2280, November (2018). <http://dx.doi.org/10.4108/eai.29-11-2018.156000>.
 4. A. Asaad, A. Al-Jabari, N. Al-Jawad, S. A. Jassim. “Topological Data Analysis for evaluating PDE-based inpainting methods” (will be submitted)
 5. A. Al-Jaberi, A. Asaad, S. Jassim, and N. Al-Jawad. “Topological data analysis for forgery detection of image inpainting” (will be submitted)

1.6.2 Presentations

1. Presentation of (Colourising greyscale images based on PDE methods) in EGL 2017 Workshop on Applied and Numerical Mathematics, in University of Greenwich, London, on 8th – 9th June 2017,

<https://www.gre.ac.uk/ach/services/events/EGLmathsworkshop>.
2. Presentation of (Inpainting monochrome images) in SPIE Commercial + Scientific Sensing and Imaging Conference, Orlando, Florida, United States, on 15th – 19th April 2018,

<https://www.spiedigitallibrary.org/conference-proceedings-of-spie/10668/1066806/Colourising-monochrome-images/10.1117/12.2309938>.
3. Presentation of (Inpainting Large Missing Region-Based on Seam Carving Approach) in EGL 2018 Workshop on Optimisation, Applied and Numerical Mathematics, in University of Essex, on 6th – 7th June 2018,

<https://www.essex.ac.uk/events/2018/06/06/egl-2018-workshop-on-optimisation,-applied-and-numerical-mathematics>.

1.7 Thesis Outline

The contents of this report are organised as follows:

- **Chapter 2** presents the mathematical preliminaries of inpainting algorithms such as some definitions and theories which that consider important for the understanding these algorithms.
- **Chapter 3** presents the process of converting grayscale images to a colour image, the process of adding colour to the grayscale images, is called colourisation term. There are several colourisation techniques, these techniques divided into two groups. Also, this chapter reviews recently devised colourisation techniques and then clarifies the differences between them. Colourisation-based PDE algorithm is described, and an improvement of this algorithm is introduced. The efficiency of this algorithm is checked by comparing it with the other three colourisation algorithms. This comparison is done by using statistical measurements. Conclusion and the future work is introduced.
- **Chapter 4** provides a detailed review of existing PDEs algorithms in inpainting and discusses relevant work on inpainting missing regions and handling the edges and corners in missing regions in both the spatial and frequency domains and evaluating the perceptual quality of these image inpainting algorithms. The efficiency of high-order PDEs algorithms is investigated in handling edges and corners in small missing regions.
- **Chapter 5** introduces a novel EBI algorithm for restoring textured missing regions in the image. This algorithm removes an unwanted object and recovers missing regions in the old images as well. It includes a new mechanism to identify the size of a patch based on a quantity of texture in missing regions, the filling priority definition based on the geometrical properties of curvature of isophotes. Furthermore, the patch-matching scheme uses two stages of selecting the nearest patch. Lastly the usefulness of different missing regions EBI in structure and texture finish stage of nature image inpainting algorithm with practical examples are demonstrated.
- **Chapter 6** presents previous studies on hybrid inpainting techniques and describes the image decomposition into a texture and structure components which that inpainting by EBI and PDEs algorithms respectively. Three kinds

Chapter 1: Introduction

of PDEs algorithms are used for the inpainting of structure components. Hybrid technique deals with textured missing regions, the results of this technique have compared with each other. These techniques have been applied on natural dataset images in both the spatial and frequency domains.

- **Chapter 7** introduces a novel technique to handling for large missing regions into images which that use EBI and PDEs algorithms successively. Also, this technique has applied to images after reshaping large missing region, where they use seam carving to reshape missing regions.
- **Chapter 8** provides a general discussion of our contributions of this research to summarize the conclusions, followed by a list of open directions for future research issues.

The Appendices include some experimental results of each inpainting algorithm that used in this thesis.

Chapter 2 MATHEMATICAL BACKGROUNDS

The field of image inpainting has evolved and expanded rapidly in the last two decades, and it has become useful in different image processing and computer vision applications. This chapter outlines mathematical definitions and theorems underpinning the current dominantly PDE-based inpainting techniques (i.e. variational models of image inpainting). The importance in image enhancements and restoration of missing information is stressed, and the domains of inpainting are illustrated. Image quality measures are introduced in assessing the success and limitations of such schemes.

The chapter is divided into seven main sections. Section 2.1 provides a brief overview of inpainting methods and describes the various ways of classification of these methods. Section 2.2 illustrates the domains used in this thesis. Section 2.3 describes the space of functions of bounded variation which are commonly used in image analysis, highlighting types of functions relevant to our research project. Section 2.4 presents the minimisation formulas that model many problems in computer vision. We also outline the process of solving these minimisation problems especially for restoring the information in missing regions. In section 2.5, an overview of numerical methods is provided for solving PDEs in order to restore missing information in images. Section 2.6 reviews the commonly used statistical-based image quality measures and introduces the TDA approach for assessing the performances of inpainting schemes. Section 2.7 gives a brief summary of this chapter.

2.1 Classification of Inpainting Methods

Inpainting techniques can be categorised in many ways, for example, as mathematical and statistical techniques in terms of their corresponding theoretical models, mathematical inpainting methods used PDEs and variational methods for recovering missing information in image regions (Chan & Shen 2005), (Rudin et al. 1992). Statistical techniques are used in the context of image interpolation (Kokaram et al. 1995b), image replacement (Igehy & Pereira 1997), error concealment (Jung et al. 1994), and image coding (Le Floch & Labit 1996). More precisely, in statistical class, the methods assume that the image consists of mainly homogeneous regions, separated

Chapter 2: Backgrounds

by discontinuities, i.e., edges. Inpainting methods for (lossy) image coding and compression based on the edge information (the geometric structure of the discontinuities and the amplitudes at the edges) are introduced.

Inpainting techniques can also be classified in terms of the size of missing regions, the EBI and hybrid methods (Jiyong Wu & Qiuqi Ruan 2008), (Bertalmio et al. 2003), (Kim & Cai 2015), (Criminisi et al. 2004), (Cheng et al. 2005) are used to recover large missing regions in the images, while the PDE inpainting methods (Recktenwald 2011), (Wei Guo & Li-Hong Qiao 2007), (Shen & Chan 2002) are used to propagate information into small missing regions (i.e. scribbles, texts and dates).

Another important base for classifying inpainting schemes is in terms of texture quantity in the surrounding areas of missing region. Such schemes can be divided into texture synthesis-based and PDE-based inpainting methods. The texture synthesis based methods of (Efros & Leung 1999), (Wei & Levoy 2000) are used to recover highly-textured missing regions, while PDE methods (Chan & Shen 2001), (Shen & Chan 2002), (Burger et al. 2009) are used to recover non-textured missing regions in the image.

Guided by the stated aims of this research which is focused on mathematically-inspired approaches, in this thesis, the classification of inpainting methods as being non-Exemplar Based Inpainting (nEBI) and EBI based on information propagation process is adopted. The first type, nEBI methods uses Partial Differential Equations (PDEs) to propagate the information pixel by pixel from the surrounding (or neighbouring areas of the missing region) to the missing region, (e.g. see (Burger et al. 2009), (Esedoglu & Shen 2002), (Schönlieb et al. 2010)). While the EBI methods have been proposed to recover the large missing regions based on propagating the information block by block from the rest of the image to the missing region (e.g. see (Criminisi et al. 2004), (Cheng et al. 2005), (Jassim et al. 2018), (Sangeeth et al. 2011)).

The above terms of classifications are based on the underpinning theories, the actual method of image propagation, the models of missing colour/texture information, and the size of the missing regions. Since digital images can be represented in different domains that can be derived from their intensity matrix by different discrete mathematical transformation. Accordingly, one may classify inpainting methods in terms of domain of operation. For some transforms, one may be able to implement some or all the above-mentioned inpainting schemes in the corresponding domain. It is

worth noting, that recently inpainting techniques have been proposed to deal with situations where there are missing intensity data and/or missing transformed data, (see e.g. (Chan et al. 2006) and (Tavakoli et al. 2018)). In this thesis, we only consider the case where the only missing data are intensity in some regions but interested in using properties of some transforms to deal with challenges like missing data in large regions.

2.2 Inpainting Domains

The intensity matrix representation of a digital image is referred to as its *spatial domain*, where each entry represents digitisation of the reflected light at the corresponding position in the photographed space/scene, (see section 1.2.1). Discrete Fourier transforms, and other wave-forms transforms provide other digital image domains, referred to as frequency domains because these transforms analyse the images into different frequency ranges.

Inpainting in the spatial domain, simply fills a missing region with intensity values obtained from any of the schemes mentioned above. Whereas in the frequency domain, inpainting requires the use of a discrete invertible frequency transform, as well as an inpainting scheme in the frequency domain Figure 2-1, which is a block diagram illustration of the way such schemes work.

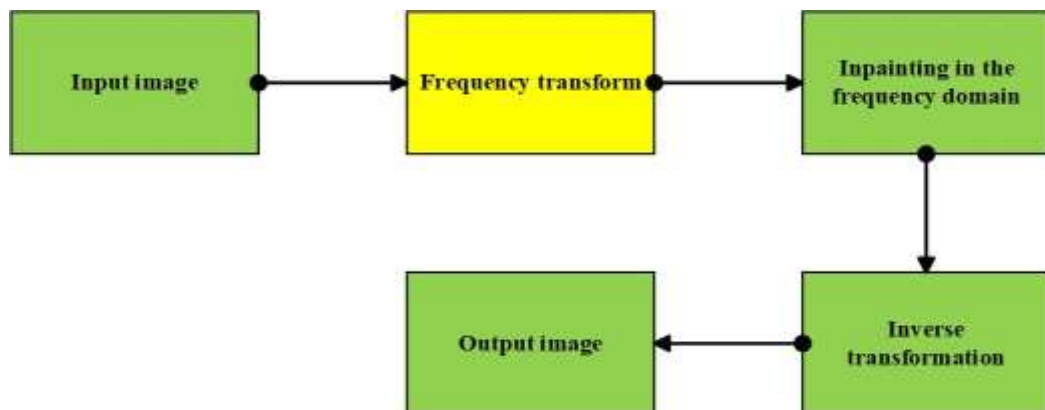


Figure 2-1: Inpainting processing in the frequency domain.

2.2.1 Frequency Domain

The two most commonly used frequency transforms are the Fourier Transform (FT) and the Wavelet Transform (WT). For digital images, their discrete versions DFT and DWT are used to analyse any digital signal/image into different frequency ranges. In both cases, transformed coefficients in the high-frequency range correspond to edges and other image discontinuities in an image, while coefficients in low-frequency range

Chapter 2: Backgrounds

are associated with smooth regions. Our interest in implementing inpainting schemes in the frequency domain for the restoration of missing intensity data stems from the importance of knowledge texture for inpainting. In this thesis, we shall confine our work to prove this principle for the wavelet domain.

The DFT decomposes an image/signal by projecting it onto sine and cosine waveforms of different frequencies over the entire image. At any frequency, the output Fourier coefficient is a complex number whose value depends on every pixel in the image. In contrast, Wavelet transform decomposes images/signals using other waveform functions that have similar properties to circular functions, but whose energy is centrally concentrated in a relatively small interval but decays away from it. Both DFT and DWT are used in a wide range of applications, such as image analysis, image filtering, image reconstruction and image compression. The finiteness of wavelet support implies that, unlike the DFT, the DWT is capable of discovering localised features at various scales, and its multi-resolution way of analysing images/signals is a very important characteristic. This significantly benefits inpainting by providing an obvious way of dealing with the challenge of restructuring large missing regions. It also helps to provide a better global structure estimation of a damaged region in addition to its better shape- and texture-preserving properties. The multi-resolution property is a consequence of the fact that appropriately chosen wavelet functions, referred to as mother wavelets, can be used to construct a nested sequence of subspaces of the Banach space of all continuous bounded real-valued functions where the subspaces are generated simply by scaling and shifting the mother wavelet function. This sequence together with their dual subspaces facilitates the exact reconstruction of the original images/signals.

The DWT of a 1D-signal is computed by convolution with the generated bases of the nested sequence and their dual, and the output coefficients represent the projection of the signal onto the chosen bases (i.e. the mother wavelets, its successive scaled and shifted versions plus their corresponding dual vectors). This implies that the DWT acts as a filtering procedure using a wavelet filter bank. Many filter banks have been developed and used over the last few decades. The DWT is usually applied first on the rows of an image and then on the resulting columns in accordance with a number of decomposition schemes, the most common of which is the pyramid scheme. In the rest of this section, this process is described by an example.

Chapter 2: Backgrounds

A DWT decomposes a signal into low and high-frequency sub-bands, each of which can be transformed repeatedly, providing multiple-resolution representations of the signal at different spatial scales and different ranges of frequencies. The DWT of any signal is a representation of the signal in terms of a family of orthonormal wavelet bases obtained from a single wavelet function, called a mother wavelet, through repeated translation. There are different wavelet transform filters that have been designed and used for various signal- and image-processing applications. The famed wavelet filter is Daubechies (db) (Daubechies 1990) and its family of filters including db2, db4, db6, and db8 of length 2, 4, 6 and 8 respectively. The Daubechies 1 (db1) filter, which is simply the original Haar filter, is a piecewise constant function and can be defined as:

$$h(t) = \begin{cases} 1 & 0 \leq t < 0.5 \\ -1 & 0.5 \leq t < 1 \\ 0 & \textit{otherwise} \end{cases} \quad (2.1)$$

The separable property of the DWT makes the implementation of the 2-dimensional wavelet transform (DWT) of images equivalent to a successful implementation of the 1-dimensional DWT in two orthogonal directions. It is usual to apply the DWT firstly in the horizontal direction across the rows of the input image into low and high-frequency sub-bands. The low-frequency sub-band is commonly referred to as the approximation sub-band which represents low-frequencies, while the high sub-band, called the details-sub-band represents the high frequencies in the horizontal direction. Lastly, each one of these sub-bands has been vertically decomposed into two low and high sub-bands. Therefore, the image is decomposed into 4-subbands: low-frequency sub-band (LL) and high-frequency sub-bands (LH, HL, and HH). The LL sub-band represents the low-frequencies in both horizontal and vertical directions; LH, HL, and HH sub-bands represent the high frequencies (indicating significant features such as edges) in the vertical direction, in the horizontal direction and in the diagonal direction, respectively. Figure 2-2 clarifies the analysis of the image by using the Haar wavelet transform.

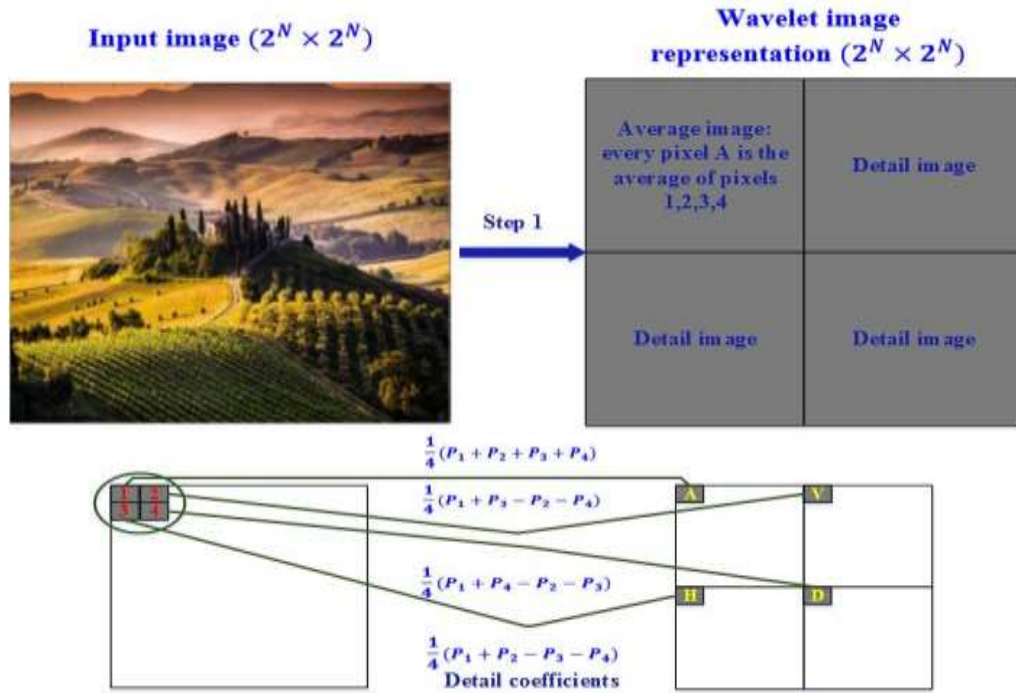


Figure 2-2: Process of the Haar wavelet transform for the 1st level.

In Figure 2-2, the Haar wavelet function decomposed the signal into an approximation sub-band containing the low-frequencies by averaging the coefficient and a detail sub-band containing the high frequencies by differencing the coefficients. As mentioned above, when the DWT is applied on an image, it produces 4 sub-images with half the resolution of the original image. The first output of the `dwt2` transform is the approximation coefficients where each output pixel is an average of a 2×2 window. The other outputs (2nd, 3rd and 4th) are detail windows that take two pixels within the window and subtract their sum from that of two other pixels in the window.

The recursive decomposition is performed only on the approximation coefficients, and Figure 2-3 is an example of level three of the pyramid decomposition scheme. Numerous wavelet filter banks can implement in a variety of decomposition schemes. The Haar wavelet filter has been selected for use throughout this thesis due to its simplicity.

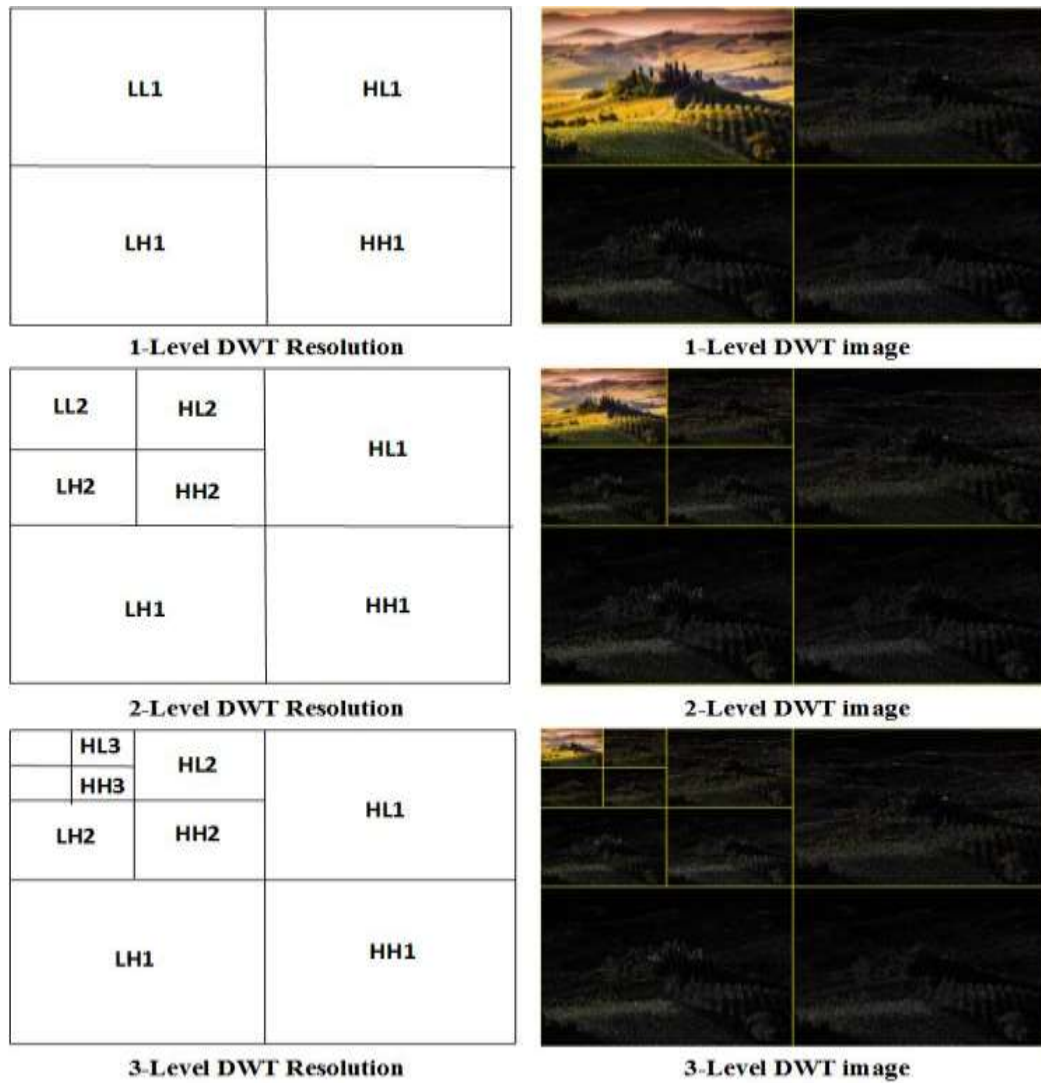


Figure 2-3: Pyramid of wavelet transform for 1st, 2nd and 3rd levels.

2.3 Functions of Bounded Variation (BV)

In most computer vision problems, the ability to model discontinuous image features is significant importance and this particularly relevant to inpainting. Image inpainting is fundamentally an ill-posed optimised interpolation problem, and missing data regions can be predicted by modelling discontinuities in terms of some bounded functions $u(x, y)$. The space BV of functions of bounded variation endowed with the so-called *total variation* norm is well adapted for this purpose. This norm is used to control the regularisation term during the iterative solution of optimisation tasks. For the sake of self-containment and clarity, the basic definitions in dealing with these issues are given.

2.3.1 Special Differential Operators

In this work, the following definitions and theorems are needed for functions of two variables. Generalisations to functions of more variables are straightforward and can be found in (W. Rudin 1976).

Definition 1 (Differentiable): A function $f(x, y)$, is differentiable at the point (x_0, y_0) if

$$\lim_{(h,k) \rightarrow (0,0)} \frac{f(x_0+h, y_0+k) - f(x_0, y_0) - h \frac{\partial f}{\partial x}(x_0, y_0) - k \frac{\partial f}{\partial y}(x_0, y_0)}{\sqrt{h^2 + k^2}} = 0. \quad (2.2)$$

This implies that the first partial derivatives of f exist and that f is continuous at (x_0, y_0) .

Definition 2: The special differential operators for the function $f(x, y)$ are defined as follows:

- The gradient vector of $f(x, y)$ is defined as $\nabla f(x, y) = \left(\frac{\partial f}{\partial x}, \frac{\partial f}{\partial y} \right)$.
- The Laplacian of $f(x, y)$ is defined as $\Delta f(x, y) = \frac{\partial^2 f}{\partial x^2} + \frac{\partial^2 f}{\partial y^2}$.
- The divergence of $f(x, y)$ is defined as $\nabla \cdot f(x, y) = \frac{\partial f}{\partial x} i + \frac{\partial f}{\partial y} j$.

and the perpendicular gradient vector $\nabla^\perp f$ by

$$\nabla^\perp f(x, y) = \left(-\frac{\partial f}{\partial y}, \frac{\partial f}{\partial x} \right)$$

The relationship between the level curves of f and the gradient vector ∇f is stated in the theorem 3.

2.3.2 Spaces of functions with Bounded Total Variation

Let $\Omega \subseteq R^n$ be a bounded open set, $u: \Omega \rightarrow R^n$ (an image representation), is a function of bounded variation in $L^1(\Omega)$ if the distributional derivative of u is representable by a finite measure in Ω , that is, if.

$$\int_{\Omega} u \frac{\partial \phi}{\partial x_i} dx = \int_{\Omega} \phi dD_i u \quad \forall \phi \in C_c^\infty(\Omega), \quad i = 1, 2, \quad (2.3)$$

in R^2 , $Du = (D_1 u, D_2 u)$ in Ω . The vector space of all functions of bounded variation in Ω is denoted by $BV(\Omega)$. Further, the space $BV(\Omega)$ can be characterised by the total variation of Du . For this, the so-called variation $V(u, \Omega)$ of a function $u \in L^1(\Omega)$ is firstly defined.

Definition 4 (Variation): Let $u \in L^1(\Omega)$, the variation $V(u, \Omega)$ of u in Ω is defined by

$$V(u, \Omega) = \sup \left\{ \int_{\Omega} u \operatorname{div} \phi \, dx : \phi \in C_c^1(\Omega), |\phi|_{L^1(\Omega)} \leq 1 \, \forall x \in \Omega \right\}. \quad (2.4)$$

A simple integration by parts proves that total variation defined on the L^1 -norm of the gradient in Ω

$$\|u\|_{TV(\Omega)} = V(u, \Omega) = \int_{\Omega} |\nabla u| dx, \quad \forall u \in C^1(\Omega) \quad (2.5)$$

if $u \in C_0^1(\Omega)$. In (2.3) represents the bounded space defined on the space of functions with bounded total variation $BV(\Omega)$. The definition of this space is

$$BV(\Omega) = \{u \in L^1(\Omega): \|u\|_{TV} < \infty\}. \quad (2.6)$$

$BV(\Omega)$ is a Banach space endowed with the norm

$$\|u\|_{BV(\Omega)} = \|u\|_{L^1(\Omega)} + \|u\|_{TV(\Omega)}. \quad (2.7)$$

Thus BV -functions are the L^1 functions with bounded TV -norm, and discontinuous functions are included in this space. The advantage of the TV -norm is that it allows for discontinuities, while avoiding irregular oscillations, such as noise. Nevertheless, it is used to remove the noise in an image whilst preserving important details such as edges (Rudin et al. 1992).

In contrast, the L^2 norm of the bounded variation, the regularisation term of the magnitude of the image gradient is used in the L^2 norm (i.e. the Tikhonov (TK) regularisation method (Tikhonov 2014) which is defined on the L^2 norm). The norm of $BV(\Omega)$ is given as follows:

$$\|u\|_{BV(\Omega)}^2 = \|u\|_{L^2(\Omega)}^2 + \|u\|_{TK(\Omega)}^2 \quad (2.8)$$

The TK regularisation technique successfully removes image noise but results in blurring important image features/structures like edges and jumps in the denoised image (Liu et al. 2014).

2.3.3 Calculus of Variations – A brief introduction

In this section, the mathematical background that leads to the variational-based inpainting method is briefly reviewed. Calculus of variation is concerned with functionals (i.e. functions whose codomains are functions).

A functional on a real vector space V , F is a mapping on V onto the set of real-valued functions defined on V . The functional derivative is the derivative of a functional with respect to a function and is a generalisation of the function derivative. It tells us how the functional changes when the function changes by a small amount. In this work, the space V can be restricted to be a Banach space. A functional on a Banach space is a scalar-valued mapping which is continuous, but not necessarily linear.

Let V be a Banach space and let $F : V \rightarrow R$ be a functional. The definition of the functional derivative at x in the direction of y is then

$$F'(x)y = \lim_{\epsilon \rightarrow 0} \frac{F(x + \epsilon y) - F(x)}{\epsilon} \quad (2.9)$$

F is (Fréchet) differentiable at x if

Chapter 2: Backgrounds

$$F(x + y) = F(x) + F'(x)y + O(\|y\|_V) \quad \text{as } \|y\|_V \rightarrow 0 \quad (2.10)$$

$F'(x)$ is a bounded linear functional. Analogous to the ordinary calculus. x is a critical point of F if $F'(x) = 0$, i.e.

$$F'(x)y = 0, \quad \forall y \in X \quad (2.11)$$

where $X \subset R^n$ is a nonempty set subset of the vector space R^n . This critical point condition is called the Euler-Lagrange equation for the functional F .

Calculus of variations is essentially a generalisation of ordinary calculus, (Hadamard 2003), It seeks to find the path, curve, surface, etc. of a functional that has a stationary value. Therefore, calculus of variations is a field which deals with finding extrema's (i.e. usually in physical problems, a minimum or maximum). Mathematically, this involves finding stationary values of an energy functional form:

$$I = \int_a^b F(t, y(t), y'(t)) dx, \quad (2.12)$$

I has an extremum only if the Euler-Lagrange differential equation is satisfied.

2.4 Minimisation Problems

Before going deeper into the minimisation problems, a few more definitions are needed.

Definition 4 (Hadamard 2003): Let X and Y be a normed space, $T: X \rightarrow Y$ a (linear or nonlinear) mapping. The equation

$$Tu = f \quad (2.13)$$

is called well-posed if the following three conditions hold:

1. Existence: For every $f \in Y$ there is (at least one) $u \in X$ such that $Tu = f$.
2. Uniqueness: For every $f \in Y$ there is at most one $u \in X$ with $Tu = f$.
3. Stability: The solution u depends continuously on f ; that is, for every sequence $(u_n) \rightarrow X$ with $Tu_n \rightarrow Tu$ ($n \rightarrow \infty$), it follows that $u_n \rightarrow u$ ($n \rightarrow \infty$).

If (at least) one of the previous conditions fails, that the problem (2.13) is called ill-posed in the sense of Hadamard.

In image processing problems, ill-posedness leads to instability issues. The right-hand side f to Y is never known exactly, but only up to an error $\epsilon > 0$, which is responsible for instability, and the problem (2.13) is transformed to a perturbed one as follows:

$$f = Tu + \delta \quad (2.14)$$

Various digital processes can be applied to the digitised image f to generate a new digital image u . The Euler-Lagrange differential equation has been applied to solve the problem of finding the minimum or maximum values of the energy functional.

Theorem 1: Each problem in the calculus of variations can be stated in three equivalent forms, which are

Chapter 2: Backgrounds

Variational form:

$$\text{Minimise } E(u) = \iint_{\Omega} F(u) d\Omega$$

Weak form:

$$\frac{\partial E}{\partial u} = \iint_{\Omega} \left(\sum \frac{\partial F}{\partial D_i u} \right) (D_i v) d\Omega = 0 \text{ for all } v$$

Euler equation:

$$\sum D_i^T \left(\frac{\partial F}{\partial D_i u} \right) = 0.$$

When F is a quadratic function of u and its derivatives, the expressions $\partial F / \partial D_i u$ are linear and so is the Euler equation.

2.4.1 Euler-Lagrange Equation

The Euler-Lagrange differential equation is the essential equation of the calculus of variations. It stipulates that if I is defined by an integral of the form (2.14), where $\dot{y} = \frac{\partial y}{\partial t}$, then I has a stationary value if the Euler-Lagrange differential equation

$$\frac{\partial F}{\partial x} - \frac{\partial}{\partial x} \left(\frac{\partial F}{\partial \dot{y}} \right) = 0 \quad (2.15)$$

is satisfied.

For two independent variables, formula (2.16) shows the double integral to be minimised over a fixed domain D of the plane, with respect to functions $y = y(t, h)$.

$$I = \iint_D F(t, h, y, y'_t, y'_h) dx, \quad (2.16)$$

The Euler Lagrange equation for the minimisation of (2.16) the equation is

$$\frac{\partial F}{\partial y} - \frac{\partial}{\partial t} \left(\frac{\partial F}{\partial y'_t} \right) - \frac{\partial}{\partial h} \left(\frac{\partial F}{\partial y'_h} \right) = 0 \quad (2.17)$$

Definition 5 (Local minimum values): A function f has a local minimum value $f(x_1)$ at the point x_1 in its domain provided there exists a number $h > 0$ such that $f(x) \geq f(x_1)$ whenever x is in the domain of f and $|x - x_1| < h$. A function f can have many local minima.

Definition 6 (Absolute minimum values): A function f has an absolute minimum value $f(x_1)$ at the point x_1 in its domain, if $f(x) \geq f(x_1)$ holds for every x in the domain. This means that a function can have at most one absolute maximum or minimum value, though this value can be assumed at many points. When the global minimum of a function $f(x)$ is to be found, we need to find x such that $f(x)$ has the smallest possible value. The unconstrained minimisation problem is formulated as

$$\min_x f(x), \quad (2.18)$$

Chapter 2: Backgrounds

where $x \in R^n$ is a real vector with $n \geq 1$ components and $f : R^n \rightarrow R$ is a smooth function. Sometimes a constraint must be fulfilled at the minimum. We can for example look for the minimum only at points where another function $g(x) = 0$. The constrained minimisation problem is formulated as

$$\min_x f(x) \text{ subject to } g(x) = 0, \quad (2.19)$$

where x and f are defined as above and $g : R^n \rightarrow R$ is a smooth function. To find local extrema values of the function f , the Lagrange multipliers method can be used.

2.4.1.1 Lagrange Multipliers (Bertsekas 2014)

The method of Lagrange multipliers is a strategy for finding local extrema of minimisation function $f(x_1, \dots, x_n)$ subject to a constraint $g(x_1, \dots, x_n) = 0$, where f and g must be functions with continuous first partial derivatives in the open set containing $g(x_1, \dots, x_n) = 0$ and $\nabla g \neq 0$ at any point in the open set.

A new variable (λ) called a Lagrange multiplier is introduced, and study the Lagrange function that defined by

$$L(x_1, \dots, x_n, \lambda) = f(x_1, \dots, x_n) + \lambda g(x_1, \dots, x_n), \quad (2.20)$$

Where the Lagrange multiplier λ is a constant coefficient (i.e. λ is the change in the optimal value of the objective function $f(x_1, \dots, x_n)$ due to the relaxation of a given constraint $g(x_1, \dots, x_n)$).

If $f(x_1)$ is a maximum of $f(x_1)$ for the original constrained problem, then there exists λ_0 such that (x_1, λ_1) is a stationary point for the Lagrange function (stationary points are those points where the first partial derivatives of $L = 0$). However, not all stationary points yield a solution of the original problem, as the method of Lagrange multipliers yields only a necessary condition for optimality in constrained problems.

This method of Lagrange multipliers is used to solve $\nabla L(x_1, \dots, x_n, \lambda) = 0$. Note that $\nabla_{\lambda} L(x_1, \dots, x_n, \lambda) = 0$ implies $g(x_1, \dots, x_n) = 0$. To summarise

$$\nabla L(x_1, \dots, x_n, \lambda) = \begin{cases} \nabla f(x_1, \dots, x_n) = -\lambda \nabla g(x_1, \dots, x_n) \\ g(x_1, \dots, x_n) = 0 \end{cases} \quad (2.21)$$

This $\nabla f = -\lambda \nabla g$ implies that the extrema ∇f and ∇g are parallel.

$$\nabla f = \lambda_1 \nabla g_1 + \dots + \lambda_n \nabla g_n \quad (2.22)$$

is required at the extrema. To solve equation (2.21), which amounts to solving n equations in n unknowns.

To sum up, Lagrange multipliers method is just a strategy that finds the local maxima and minima of the gradient of function points in the same direction as the gradients of

Chapter 2: Backgrounds

its constraints, while also satisfying those constraints. The method of Lagrange multipliers is used to solve the constraint optimisation problems

Similarly, if $F(u) : V \rightarrow R$ and $G(u) : V \rightarrow R$ are C^1 -functionals on a Banach space, we can minimise $F(u)$ on the constrained set $C = \{u \in V : G(u) = 0\}$. The Lagrange functional is defined by

$$L(u, \lambda) = F(u) + \int_{\Omega} \lambda G(u) dx, \quad (2.23)$$

where $u: \Omega \rightarrow R$ and $\lambda: \Omega \rightarrow R$ are functions, then the solution of a minimisation problem (2.23) is found by iterative algorithms.

2.4.2 The Method of Steepest Descent (Gradient Descent) (Kelley 1999)

The steepest descent method is an optimisation method for finding the local maximum or minimum of the function $f(x)$. The method of steepest descent is also called the gradient descent method, this method starts at x^0 and, as many times as needed, moves from x^n to x^{n+1} by minimising along the line extending from x^n in the direction of $-\nabla f(x^n)$, the local downhill gradient. Formally, this can be done several times by the algorithm

$$x^{n+1} = x^n + \Delta t \nabla f(x^n); n = 0; 1; 2, \quad (2.24),$$

where Δt is small enough, x^n gets closer to the minimum as n increases. At a minimum x^* the gradient $\nabla f(x^*)$ equals zero and the iterative algorithm has converged. A drawback of the method is that many iterations may be needed before convergence. In general, the convergence rate is only linear. The convergence can be improved by calculating the optimal Δt in each step, as see in Figure 2-4. This will take more computational time and the conjugate gradients method is often a better alternative.

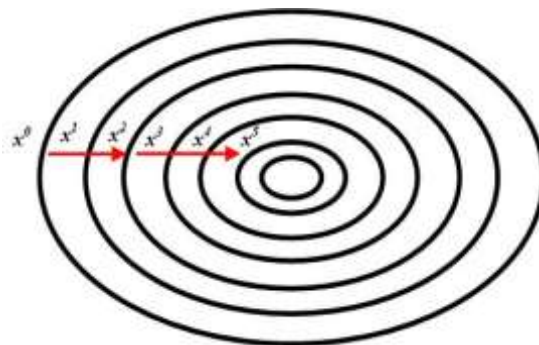


Figure 2-4: The level curves of a poorly scaled problem. The vector points in the steepest descent direction.

The steepest descent method is expressed *via* the diffusion equation. Numerical methods can be used to solve the equation (2.23). The gradient descent is simply an iterative method for finding the minimum of a function in an iterative way.

Chapter 2: Backgrounds

2.4.2.1 Unique Solution (W. Rudin 1976)

A minimisation problem can have several local minima. The aim is in finding the global minima which represents the best of all such local minima. Sometimes, the problem is that even if the iterations have converged (i.e. each iteration represents the solution of the problem), a global minimum solution is difficult to determine, so we will visually determine it on the image.

Theorem 2: Any local minimiser x^* is a global minimiser of differentiable f if function f is convex. Then any stationary point x^* is a global minimum. Therefore, the concept of convex needs to be defined (W. Rudin 1976).

Definition 7 (Convex set) (W. Rudin 1976): A set S in a vector space over R^n is called a convex set if the line segment connecting any pair of points of S lies entirely in S . Formally, for any two points $x \in S$ and $y \in S$, we have.

$$\alpha x + (1 - \alpha)y \in S, \quad \forall \alpha \in [0, 1] \quad (2.25)$$

This definition is illustrated in Figure 2-5.



Figure 2-5: A straight line segment connecting two points in a set. The left is a convex set. The right is a non-convex set.

Definition 8 (Convex function) (W. Rudin 1976): A function $f: M \rightarrow R$ defined on a nonempty subset M of R^n and taking real values is called convex, if

- the domain M of the function f is convex set;
- for any $x, y \in M$ and every $\alpha \in [0, 1]$ one has

$$f(\alpha x + (1 - \alpha)y) \leq \alpha f(x) + (1 - \alpha)f(y), \quad (2.26)$$

Then the graph of f lies below the straight line connecting $(x, f(x))$ to $(y, f(y))$ in the space R^n . Figure 2-6 is clarified the definition of convex function.

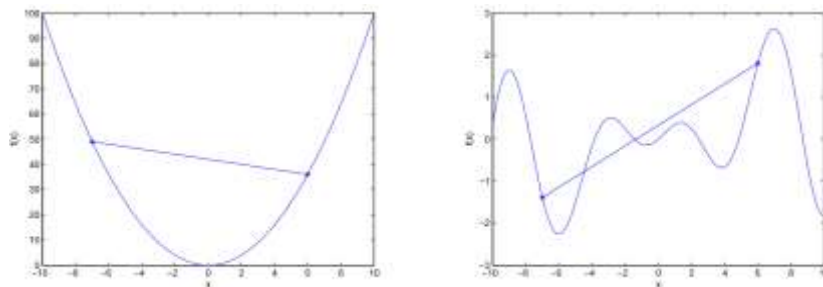


Figure 2-6: A straight line segment connecting two points at a function. The left is a convex function. The right is a non-convex function.

Chapter 2: Backgrounds

The main point necessary to the proof of well-posedness, the convexity of the regularisation functional, will also be necessary to establish the well-posedness of different types of regularisation operators (Oman 1995).

The solution of the Euler-Lagrange equation which follows from the minimisation problem leads to the PDE. Therefore, the numerical method has been applied to solve the PDE. The next section shows the numerical methods which have been used to apply the PDE-based inpainting models.

2.5 Numerical Methods of PDE-based Inpainting Models

Fast numerical methods for PDE-inpainting models continue to be an active research area. Researchers from different fields have been bringing many fresh ideas to the problem, which has led to many exciting results. Carola in (Schonlieb 2015) has studied the numerical solution of PDE-based inpainting models and also discussed the numerical solutions of high order PDE models. Some categories to be particularly mentioned are the finite difference (Smith 1985), finite element (Schönlieb 2009), and dual/primal-dual (Chambolle & Pock 2010) methods. Many of these methods have a long history with a great deal of general theories developed. But when it comes to their application to the PDE-based inpainting models, many further properties and specialised refinements can be exploited to obtain even faster methods. The finite-Difference Method (FDM) is one of the numerous numerical methods that used to solve linear and nonlinear PDEs (Smith 1985). The FDM was published as early as 1910 by L. F. Richardson. FDM is the dominant approach that is used to find the numerical solutions of partial differential equations which that describe different problems because it is easy to implement, and its solutions are easily verified as well. More recently, numerical solutions to the heat equation have been proposed in (Recktenwald 2011) based on using finite difference techniques which applied the explicit, and Crank-Nicolson implicit methods to find the approximate solution. The solution entails a series of steps. Firstly, the PDE is converted into a discrete difference equation by finite difference derived from a Taylor series expansion. Secondly, the discrete mesh of the difference equation is constructed using initial and boundary conditions. Finally, the discrete difference equation is solved.

In this thesis, the finite difference method has been applied to implement the PDE-based inpainting models. Therefore, the next section introduces the finite difference methods with all details and with some examples.

2.5.1 Finite Difference

(Smith 1985):

Let $U(x)$ represent a function of one variable that, unless otherwise stated, will always be assumed to be smooth, meaning that we can differentiate the function several times and each derivative is a well-defined bounded function over an interval containing a particular point of interest \bar{x} . Three forms are commonly considered, which are forward, backward, and central differences. Then by Taylor's theorem,

$$U(x + h) = U(x) + hU'(x) + \frac{1}{2}h^2 U''(x) + \frac{1}{6}h^3 U'''(x) + \dots \quad (2.28)$$

and

$$U(x - h) = U(x) - hU'(x) + \frac{1}{2}h^2 U''(x) - \frac{1}{6}h^3 U'''(x) + \dots \quad (2.29)$$

Collecting equations (2.28) and (2.29) will give

$$U(x + h) + U(x - h) = 2U(x) + h^2 U''(x) + O(h^4), \quad (2.30)$$

where $O(h^4)$ denotes terms containing 4th and higher powers of h . We are supposing these terms $O(h^4)$ are trivial in comparison with lower powers of h ; it follows that,

$$U''(x) = \left(\frac{\partial^2 U}{\partial x^2} \right)_{x=x} \approx \frac{1}{h^2} \{U(x + h) - 2U(x) + U(x - h)\}, \quad (2.31)$$

with a leading error on the right-hand side of order h^2 . Figure 2-7 clarifies the following formulas; the forward-difference formula clearly approximates the slope of the tangent at P by the slope of the chord PB ,

$$U'(x) \approx \frac{1}{h} \{U(x + h) - U(x)\}, \quad (2.32)$$

or the slope of the chord AP represents the backward-difference formula

$$U'(x) \approx \frac{1}{h} \{U(x) - U(x - h)\}, \quad (2.33)$$

whilst the slope of the chord AB denotes the centred-difference formula

$$U'(x) \approx \frac{1}{h} \{U(x + h) - U(x - h)\}, \quad (2.34)$$

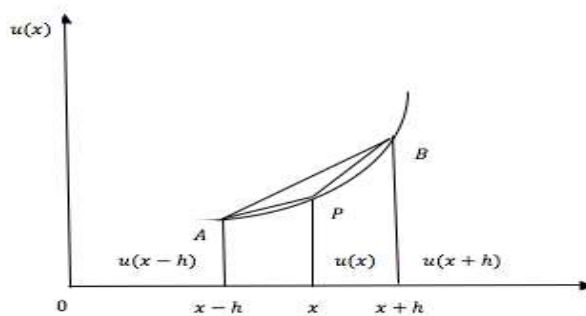


Figure 2-7: Finite difference of $U(x)$.

Chapter 2: Backgrounds

The formulas (2.32) and (2.33) can be written instantly from equations (2.28) and (2.29) respectively and assuming 2nd and higher powers of h are trivial. Whereas, the formula (2.34) can be obtained by subtracting equation (2.28) from equation (2.29) and ignoring terms of order h^3 . This shows that $O(h)$ denotes the error for forward and backward-difference formulas, while the $O(h^2)$ indicates the error for a centred-difference formula. The finite difference of a function of more than one variable is illustrated in the following definition.

Definition 8 (Smith 1985): Let U be a function of the independent variables x and t . Partition the $x - t$ plane into sets of equal rectangles of sides $\Delta x, \Delta t$, by equally spaced grid lines parallel to Oy , defined by $x_i = ih, i = 0, \pm 1, \pm 2, \dots$, and equally spaced grid lines parallel to Ox , defined by $t_j = jk, j = 0, \pm 1, \pm 2, \dots$, as clarified in the Figure 2-8. Denote the value of U at the representative mesh point $P(ih, jk)$ by

$$U_P = U(ih, jk) = U_{i,j}.$$

Then by equation (2.31),

$$\left(\frac{\partial^2 U}{\partial x^2}\right)_P = \left(\frac{\partial^2 U}{\partial x^2}\right)_{i,j} \approx \frac{U\{(i+1)h, jk\} - 2U\{i\Delta x, j\Delta t\} + U\{(i-1)h, j\Delta t\}}{(h)^2}$$

i.e.

$$\frac{\partial^2 U}{\partial x^2} \approx \frac{U_{i+1,j} - 2U_{i,j} + U_{i-1,j}}{(h)^2}, \quad (2.35)$$

with an error of order $(\Delta x)^2$. The forward-difference approximation for $\frac{\partial U}{\partial t}$ at P is

$$\frac{\partial U}{\partial t} \approx \frac{U_{i,j+1} - U_{i,j}}{k}, \quad (2.36)$$

with an error of order $O(\Delta t)$. Therefore, the backward-difference approximation for $\frac{\partial U}{\partial x}$ at P is

$$\frac{\partial U}{\partial x} \approx \frac{U_{i,j} - U_{i-1,j}}{h}, \quad (2.37)$$

with an error of order $O(h)$.

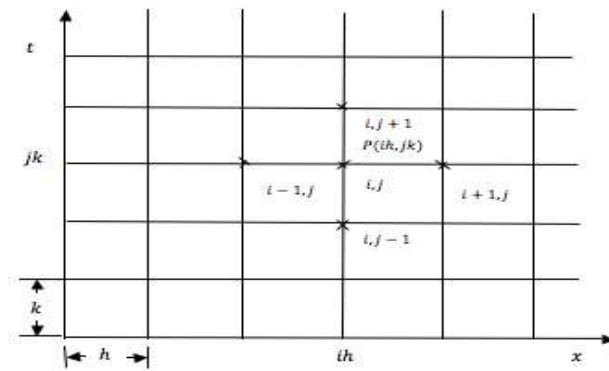


Figure 2-8: The representative mesh point $P(ih, jk)$.

2.5.2 Explicit Finite Difference Method

It is a numerical method for solving differential equations by approximating them with difference equations, in which finite differences approximate the derivatives. FDM is thus a discrete method. The first step is to replace each partial derivative by a finite difference, leading to a differences formula. The second step will be to construct the grid (i.e. discrete space (image)) of spatial and time variables of this equation. Note that, the initial condition of this problem represents the initial state of the missing region in the image (always zero), and the boundary conditions represent the values at the boundary of the missing region. So, every value of the second row is determined from the values in the first row by using the finite difference equation, and so on for the other rows. Derivatives are replaced with difference formulas which only contain the discrete values located on the grid. A general idea of this method is illustrated in Figure 2-9.

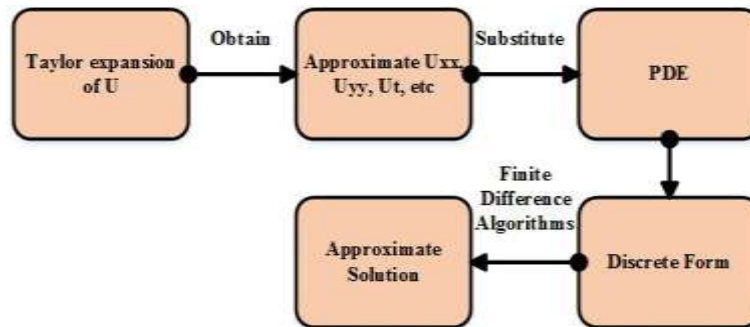


Figure 2-9: General idea of the finite-difference method

In the next examples, the explicit finite-difference method is used to find the solution of 2-D heat equation.

Example.1: Solve the $U_t = U_{xx} + U_{yy}$ on the 2-D domain case (black missing region), the size of this missing region is 60×80 .

$$u_t = u_{xx} + u_{yy} \tag{2.38}$$

The numerical solution of equation (2.38) with Neumann boundary condition reconstructs the missing region based on the information obtainable from the surrounding region. The explicit finite difference method has been used to find the numerical solution. The partial derivative in the equation (2.38) converts to a finite difference formula:

$$\frac{u_{i,j}^{n+1} - u_{i,j}^n}{k} = \frac{u_{i+1,j}^n - 2u_{i,j}^n + u_{i-1,j}^n}{h^2} + \frac{u_{i,j+1}^n - 2u_{i,j}^n + u_{i,j-1}^n}{h^2} \tag{2.39}$$

The solutions of the heat equation are obtained via a stably-conditioned explicit finite difference equation. To build the mesh, we need to determine the sizes of the spatial grid and time steps. The spatial grid in an image is represented based on its height and

Chapter 2: Backgrounds

width (M, N) , and the spatial stepping size is 1, which represents the distance between the any pixel and its neighbours, which is $h = 1$. The time stepping size is chosen to achieve the stability requirement of the finite difference solutions, which may be expressed as $\frac{k}{h^2} \leq 0.5$. The time stepping size is determined as $k = 0.1$.

Equation (2.39) can be rewritten as follows:

$$u_{i,j}^{n+1} = u_{i,j}^n + \frac{k}{h^2} \left((u_{i+1,j}^n + u_{i-1,j}^n - 4u_{i,j}^n + u_{i,j+1}^n + u_{i,j-1}^n) \right) \quad (2.40)$$

where $2 \leq i \leq M - 1$ and $2 \leq j \leq N - 1$. The Neumann boundary condition can be written as follows:

$$\begin{aligned} u_x(x, 1, t) &= u_{2,x} - u_{1,x}, u_x(x, N, t) = u_{N-1,x} - u_{N,x}, u_x(1, y, t) = u_{y,2} - u_{y,1}, u_x(M, y, t) \\ &= u_{y,M-1} - u_{y,M} \end{aligned}$$

and the initial condition is $u(x, y, 0) = 0$. The finite difference method can be used to rewrite these boundary conditions, as follows

$$u_x(j, 1, t) = \frac{u_{2,j}^n - u_{1,j}^n}{h}, u_x(j, N, t) = \frac{u_{N-1,j}^n - u_{N,j}^n}{h}, u_y(1, i, t) = \frac{u_{i,2}^n - u_{i,1}^n}{h}, u_y(M, i, t) = \frac{u_{i,M-1}^n - u_{i,M}^n}{h},$$

The numerical solution of equation (2.38) with the Neumann boundary conditions recovers the missing region in the image. Neumann boundary conditions give the normal derivatives on a surface, $\partial u / \partial n$, is prescribed on the boundary. Which means govern information flux from a surface (i.e. through the edges of a surface). Neumann boundary conditions are applied on all the boundaries in image inpainting problem which encourage to recover the edges in the missing regions. After determining the values of all pixels in the whole direction of the border, the equation (2.40) is used to calculate the pixels' values and starts from the pixel in position $(i=2, j=2)$ based on the information on the border (i.e. row 1 and n and column 1 and m) for the whole image. In the next stage, this process is repeated based on the border information and the information from the first stage, until the last value of the time $t=1000$. The equation (2.40) with Neumann boundary conditions are applied to each pixel in each (R, G, B) channel of the image; in the end, it recovers the missing regions in the image. Figure 2-10 clarifies the filling in of a missing region based on the boundaries (Neumann).

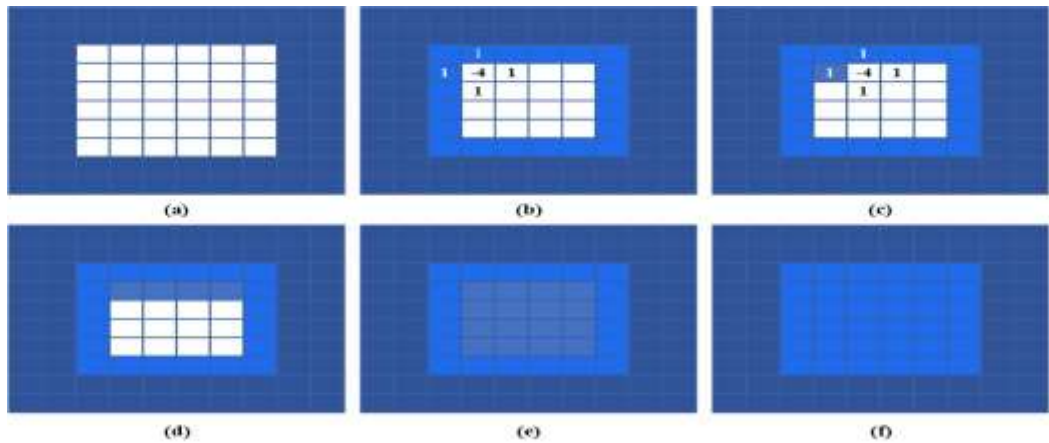


Figure 2-10: The finite-difference grid of heat equation.

Figure 2-10 is shown the procedures of using the finite-difference method to solve heat equation. In Figure 2-10b, calculating the values of the border of missing region based on the boundary condition and applying finite difference formula on the first pixels, and solving finite difference formula on the first pixels and applying finite difference formula on the second pixels in Figure 2-10c, then solving the finite difference formula until last pixel in the first row in Figure 2-10d. Applying the same process for the other rows from the missing region in Figure 2-10e. Finally, repeating the same process for 10000 times (i.e. until get to the converged solutions), as seen in Figure 2-10f.

Figure 2-11 clarifies how to the black missing region in the grayscale image by using heat inpainting model. For more information about the heat model can be found in Chapter 4.

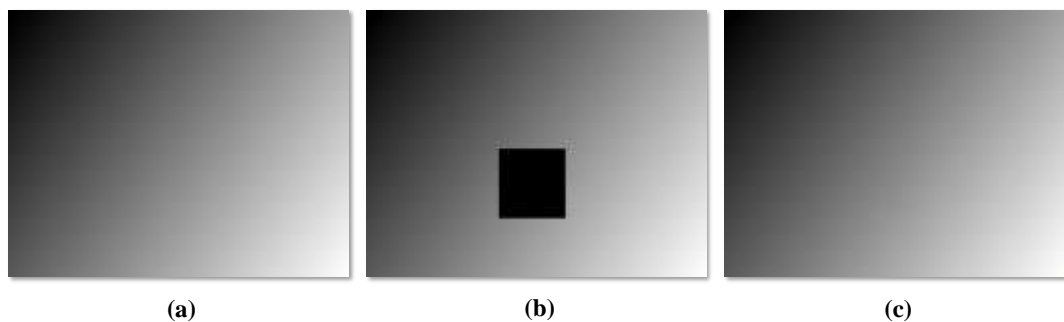


Figure 2-11: Heat inpainting process: (a) original image, (b) masked image, (c) inpainted image.

The next section shows the existing statistical quality measurements and explains all their drawbacks. Therefore, to overcome the drawbacks of these statistical measurements, a TDA approach is proposed to evaluate the quality of image inpainting.

2.6 Image Inpainting Quality Assessments

The results of the proposed inpainting methods should be assessed in terms of the performance and the quality. Therefore, different quality image measurements proposed in the literature are studied. The most common methods are the statistical measurements which are used to evaluate the results.

In this thesis, image inpainting methods are assessed both with and without use of reference images. There are several studies in the literature on the quality of image inpainting without using reference images; however, these studies are still a complicated task. The next subsection presents the statistical quality measurements of image inpainting.

2.6.1 Statistical Quality Measurements

Statistical quality measurements are computed directly from resulting images. According to the availability of the original image the measurements can be classified as Full Reference (FR), No Reference (NR) and Reduced Reference (RR) (Wang & Bovik 2006). In this thesis, the quality assessment of image inpainting in case of FR and NR is studied by using different statistical measurements. In the next section the well-known methods of FR, and NR are explained.

- **Full-Reference Image Quality Assessment**

Full-reference (FR) measurements (see Figure 2-12) perform a direct comparison between the image under test and a reference or "original" image in a properly defined image space.

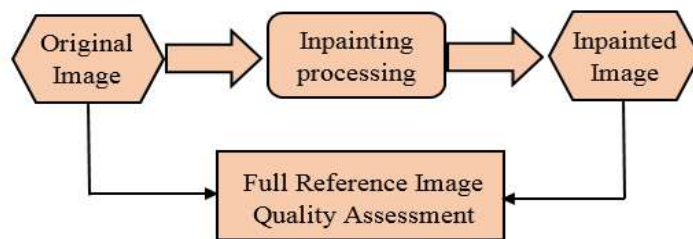


Figure 2-12: Image quality assessment approaches: Full Reference.

To check the quality of an inpainted image when a reference image exists, the inpainting algorithms are applied on datasets of natural images, thereby adding different missing regions (i.e. scratches, text, and object). The quality of the results and the efficiency of these algorithms is checked by applying statistical measurements on the inpainted image and original images.

Chapter 2: Backgrounds

The MSE, PSNR, and SSIM measures are used to evaluate the image inpainting qualities when a full set of reference images is available.

2.6.1.1 MSE and PSNR

The Mean Squared Error (MSE) and the Peak Signal to Noise Ratio (PSNR) are widely used, as they are easy to implement and thus convenient to use for optimisation purposes (Pedersen & Marius 2012). The MSE computes the cumulative squared error between two images: one reference (i.e. original) image and a modified version of it. The MSE (Popowicz & Smolka 2015) is calculated between colour original O and inpainted images I as follows:

$$\text{MSE} = \frac{1}{(NMQ)} \sum_{q=1}^Q \sum_{n=1}^N \sum_{m=1}^M [O_q(n, m) - I_q(n, m)]^2 \quad (2.41)$$

Where $Q=3$, the number of channels in a colour image, and N and M represent the size of the image (i.e. the number of rows and columns in the channel image). A lower value for the MSE indicates a lower error, and thus better quality of the inpainted image. The PSNR computes the peak signal to noise ratio between two images and gives a value in decibels (db) as a result. The first step in computing the PSNR is to obtain the MSE value for the two images. Then, the PSNR is defined as:

$$\text{PSNR} = 10 \log_{10} \left(\frac{255^2}{\text{MSE}} \right) \quad (2.42)$$

The higher the value obtained for PSNR, the better the quality of the inpainted image. The relationship between PSNR and MSE is an inverse correlation.

2.6.1.2 Structural Similarity Index (SSIM)

The colour version of the Structural Similarity Index (SSIM) was proposed by Wang et al. in (Wang et al. 2004). SSIM considers quality degradations in the images as perceived changes in the variation of structural information between the original and inpainted images. The idea behind this measurement is to perform separate comparisons of the luminance (l), contrast (c) and structure (s) information between local windows in the original and inpainted images and then combine the results of these comparisons to obtain the value for the SSIM. The SSIM is a weighted combination of three comparative measurements between the original and inpainted images:

$$\text{SSIM}(O, I) = [l(O, I)^\alpha \cdot c(O, I)^\beta \cdot s(O, I)^\gamma] \quad (2.43)$$

Where l, c and s represents the luminance, contrast and structure comparison measurements respectively. Where

$$l(O, I) = \frac{2\mu_O \mu_I + c_1}{\mu_O^2 + \mu_I^2 + c_1}, \quad c(O, I) = \frac{2\sigma_O \sigma_I + c_2}{\sigma_O^2 + \sigma_I^2 + c_2}, \quad \text{and} \quad s(O, I) = \frac{2\sigma_{OI} + c_3}{\sigma_O \sigma_I + c_3}$$

where $c_3 = c_2/2$, and $\alpha = \beta = \gamma = 1$, then the formula of SSIM (2.43) is simplified as follows:

$$SSIM(O, I) = \frac{(2\mu_O \mu_I + c_1)(2\sigma_{OI} + c_2)}{(\mu_O^2 + \mu_I^2 + c_1)(\sigma_O^2 + \sigma_I^2 + c_2)} \quad (2.44)$$

where (μ_O, σ_O) and (μ_I, σ_I) denote the mean and standard deviation of patches in the images O and I, respectively; σ_{OI} : the covariance of O and I; $c_1 = (k_1 h)^2$, $c_2 = (k_2 h)^2$ such that $h = 2^{\text{bits per pixel}} - 1$, $k_1 = 0.01$ and $k_2 = 0.03$.

In our work, SSIM is calculated on a window size of 8×8 , and then the results from the R, G, and B channels are averaged. The resultant of SSIM index is a decimal value between -1 and 1. The value 1 is only reachable in the case of original and inpainted identical images.

- **No Reference Image Quality Assessment**

No-reference (NR) measurements (see Figure 2-13) are also called blind measurements and assume that IQ can be determined without a direct comparison between the original and the inpainted images.

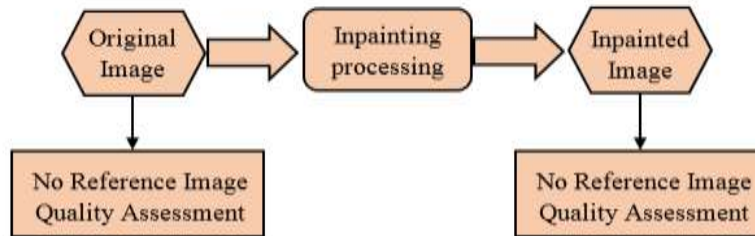


Figure 2-13: Image quality assessment approaches: No-Reference.

Theoretically, it is possible to measure the quality of any visual contents. In practice, some information about the application domain, requirements and users' preferences are required to contextualise the quality measurements. NR measurements are designed to identify and quantify the presence of specific processing distortions that may exist in the evaluated image. To estimate the presence of a defect or artefact produced by some imaging processing on the image, we need to characterise the properties of the artefact as well as the effects that it produces on the low-level components of the image (edges, homogeneous areas, etc.). In the case not existing reference image, Entropy, MSSIM and CSQM are used to check the quality of the inpainted image.

2.6.1.3 Entropy

Entropy is defined as the quantitative measurements of disorder or randomness in the image, the entropy of an inpainted image is defined as:

$$E = - \sum_{i=1}^n \sum_{j=1}^m P_{I_{i,j}} \log_2 P_{I_{i,j}} \quad (2.45)$$

Where $P_{I_{i,j}}$ is the probability of pixel intensities (i.e. the distribution of element values), and \log_2 is the base 2 logarithm. In other words, high entropy refers to less information about uncertainty in the image and in contrast low entropy means there is more information about uncertainty in the image. This measurement is applied on the inpainted regions that are obtained using different inpainting methods.

2.6.1.4 Mean of Structural Similarity (MSSIM)

The mean of structural similarity (MSSIM) is a function to measure an appropriateness degree between the inpainted region Ω and the rest of image $\Phi = I - \Omega$, the size of inpainted region Ω is $n \times m$. The MSSIM is defined as follows:

$$MSSIM = \frac{1}{mn} \sum_{i=1}^n \sum_{j=1}^m \max\{SIM(\Psi_p, \Psi_q)\} \quad (2.46)$$

Where $p \in \Omega$ and $\forall \Psi_q \in \Phi$. The idea of similarity measurement combining structure and colour information (Shi et al. 2009) is used in this thesis. The similarity function is then defined as follows:

$$SIM(\Psi_p, \Psi_q) = (1 - h) SS(\Psi_p, \Psi_q) + h HS(\Psi_p, \Psi_q) \quad (2.47)$$

where, h is a positive constant within the range $[0, 1]$ defining the relative importance between structure similarity (SS) and hue similarity (HS), corresponding to the colour information. The structure and hue similarity indexes are defined by equations (2.48) and (2.49), respectively:

$$SS(\Psi_p, \Psi_q) = \frac{2\sigma_{pq} + d_1}{\sigma_p + \sigma_q + d_1} \quad (2.48)$$

$$HS(\Psi_p, \Psi_q) = \frac{2\mu_p\mu_q + d_2}{\mu_p^2 + \mu_q^2 + d_2} \quad (2.49)$$

where (μ_p, σ_p) and (μ_q, σ_q) denote the mean and standard deviation set of patches Ψ_p and Ψ_q , respectively; σ_{pq} denotes the cross correlation between Ψ_p and Ψ_q . Where d_1 and d_2 are small positive constant. In our experiments, constants are set as in (Shi et al. 2009), i.e. $h = 0.1667$; $d_1 = d_2 = 6.5025$. MSSIM is applied on the inpainted regions in the image and identifying the coherence extent of the inpainted regions with the rest of the image.

2.6.1.5 Coherence and Structure Quality Measurement (CSQM)

The last image quality measurement has used to evaluate the image inpainting is coherence and structure quality measurement (CSQM). The idea of CSQM introduced in (A. DANG Thanh Trung, B. Azeddine BEGHADADI 2013) is exploited based on the coherence of inpainted regions with the rest of image, and the salient features (i.e. structures or contours) should be more associated to the rest of image. The inpainted image quality index CSQM is defined as expressed as follows:

$$CSQM = \frac{\sum_{i=1}^n \sum_{j=1}^m C(p)^\alpha S(p)^\beta}{\|\Omega\|} \quad (2.50)$$

where $C(p)$ and $S(p)$ are respectively the coherence and structure terms defined below. Two positive parameters α and β are associated with the aforementioned terms in order to be able to adjust their influence on the quality index (in our implementation, are set as in (A. DANG Thanh Trung, B. Azeddine BEGHADADI 2013), $\alpha = \beta = 1$). The coherence term is an objective function to evaluate the similarity between two patches that measurements an appropriateness degree between the inpainted patch and the rest of image. Coherence term is a mean of structural similarity that introduced before,

$$C(p) = \max\{SIM(\Psi p, \Psi q)\} \quad (2.51)$$

While the structure term which interested with the contours and other relevant structures in the inpainted regions attract more human gaze than the other components. For that reason, the structure term that using the information provided by a saliency map identified as follows:

$$S(p) = \frac{SM(p)}{\max_I\{SM\}} \quad (2.52)$$

For all $p \in \Phi$, where SM is the saliency map of inpainted image. There several models have been proposed to find the saliency of image. A simple formulation of the aforementioned saliency map SM , can be expressed as follows:

$$SM = \|I_\mu - I_G\| \quad (2.53)$$

where I_μ and I_G are the arithmetic mean pixel value and the Gaussian blurred version of the inpainted image, respectively.

The high values of MSSIM and CSQM represents a better result. The comparison of the results is applied by using Entropy, MSSIM and CSQM to evaluate the performance of inpainting methods and assess their image quality results. These measurements are used to study the quality of inpainted regions when the objects are removed from these images and then recovered (cf. Chapter 7).

In the next subsection, the Topological Data Analysis (TDA) approach is introduced and proposed as a method for the evaluation of the image inpainting.

2.6.2 Topological Data Analysis for Image Quality Assessments

Machine learning and data analysis tasks such as classification and recognition require distinct patterns/features that need to be extracted from the object of interest in any domain. Traditional data analysis techniques rely on extracting features from data points (objects) of interest then computing pairwise symmetries between them. Recent challenges in Big Data applications revealed that nowadays data is more complex and noisier than the past and classical approaches fail to extract understandable insights from them. But more interestingly last decade has seen many attempts to show that data has a shape (Carlsson 2009), (Lum et al. 2013) and (Edelsbrunner 2012). The branch of mathematics studies shapes of data (objects) is known as topology. Once the shape of the data (e.g. Images or data records) constructed, then topology has rich tools to study the connectivity and closeness properties of that shape/object, using a finite combinatorial process known as Simplicial Complex (SC). Roughly speaking simplicial complexes are made up of zero-dimensional simplices (i.e. vertices), then building one-dimensional simplices (i.e. edges between the vertices) from them, then 2nd dimensional simplices (i.e. triangles) from zero and one-dimensional simplices and then higher dimensional simplices are constructed similarly. Finally, one gets a SC by gluing these simplices ‘nicely’ together along their edges and faces. There are many types of SCs, but here we are using what is known Vietoris-Rips (Rips) SCs as it is easy to construct and compute in comparison with other types of SCs. Traditional construction of Rips SCs are based on selecting a single distance threshold and calculating corresponding topological invariants such as betti numbers (β_n for $n = 0,1,2$), Euler characteristics, cliques and other topological invariants. Instead of a single threshold, recent paradigm that relies on capturing the persistency of topological invariants across an increasing sequence of distance thresholds is known as topological data analysis (TDA).

The popular mathematical theory used to characterise topological features is known as homology theory. More precisely, the rank of the n -th homology group equals to what is known as betti numbers β_n , where β_0 is equal to the number of connected components (CCs), β_1 is the number of holes and β_2 is the number of cavities in the constructed Rips SC. Instead of computing aforementioned topological invariants at a single distance threshold, TDA depends on calculating the persistency of these invariants across an increasing series of distance thresholds using what is known as

Chapter 2: Backgrounds

persistent homology (Edelsbrunner 2012) and (Ghrist 2008). TDA applications in growing fast and beyond the scope of this thesis to discuss it, but recent applications include image tampering detection (Asaad & Jassim 2017), fingerprint classification (Giansiracusa et al. 2017), steganalysis (Ahonen et al. 2006), brain artery (Bendich et al. 2016), classification of hepatic lesions(Adcock et al. 2014), gait recognition(Lamar-León et al. 2012), and many more.

The first step in building a SC is to consider landmark points (i.e. zero-dimensional simplices) in order to be able to build on them higher dimensional simplices such as edges, triangles and tetrahedrons. For this task, the approach suggested by A. Asaad and S. Jassim in (Asaad et al. 2017) is followed which is the use of uniform Local Binary Patterns as a tool to systematically choose landmark points from images of interest to build topological objects. The next section is dedicated to briefly describe local binary patterns LBP as a landmark selection procedure in our SC construction.

2.6.2.1 Local Binary Patterns (LBP)

Ojala *et al.* in (Ojala et al. 1996) first introduced LBP as an image texture descriptor. After that many versions of LBP have been proposed by other researchers for different pattern recognition tasks. In this thesis, the original idea proposed by Ojala *et al.* in (Ojala et al. 1996) is followed. Given any image, LBP replaces each pixel of the image with an 8-bit binary code, which encapsulates texture and local structure, determined by its 8 neighbouring pixels in a 3×3 window surrounding it in clockwise order, see Figure 2-14. The process works as follow: starting from the top-left corner of the window; subtract central pixel from its 8 neighbouring pixels, assign 0 if the result is negative, and 1 otherwise. Mathematically this process can be written as follow:

$$LBP(x_c, y_c) = \sum_{i=1}^7 \alpha(P_i - P_c)2^i \quad (2.54)$$

Where P_i is the neighboring grey value pixels, P_c is the center grey value pixel, and the function $\alpha(x)$ is as follow:

$$\alpha(x) = \begin{cases} 1 & \text{if } x \geq 0 \\ 0 & \text{if } x < 0 \end{cases} \quad (2.55)$$

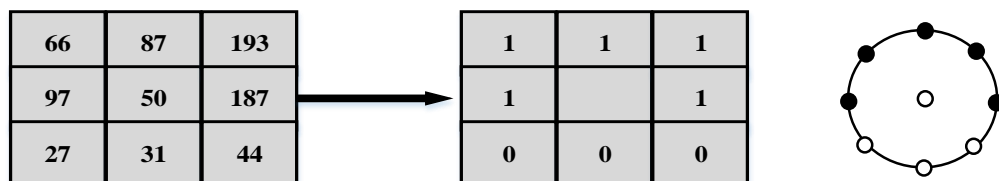


Figure 2-14: Local binary operator. Left matrix is a block of size 3×3 taken from an image. The second matrix is the corresponding binary code.

Chapter 2: Backgrounds

Uniform LBP (ULBP) refers to 8-bit circular bytes that have no more than 2 circular transitions. For the sake of clarity, examples of ULBPs are 11110000 (2 transitions), 11111111 (0-transitions) and examples of non-uniform LBP are 10101010 (8-transitions), 110011110 (4 transitions). This means that ULBP of any monochrome image consists of 58 unique uniform geometries, see Figure 2-15. It has been shown that ULBP codes constitute 90% of LBP codes in natural images (Ahonen et al. 2006). From Figure 2-15, it is easy to see that there seven groups (of 8 binary codes) of ULBP according to the number of 0's and 1's in their binary codes, excluding the cases 00000000 and 11111111. Each of these groups is related to certain types of image textures. We shall refer to ULBP codes that have t consecutive 1's as geometry- t . Our experimental investigation contains the set of pixels in all geometries as potential landmark candidates to build SC.

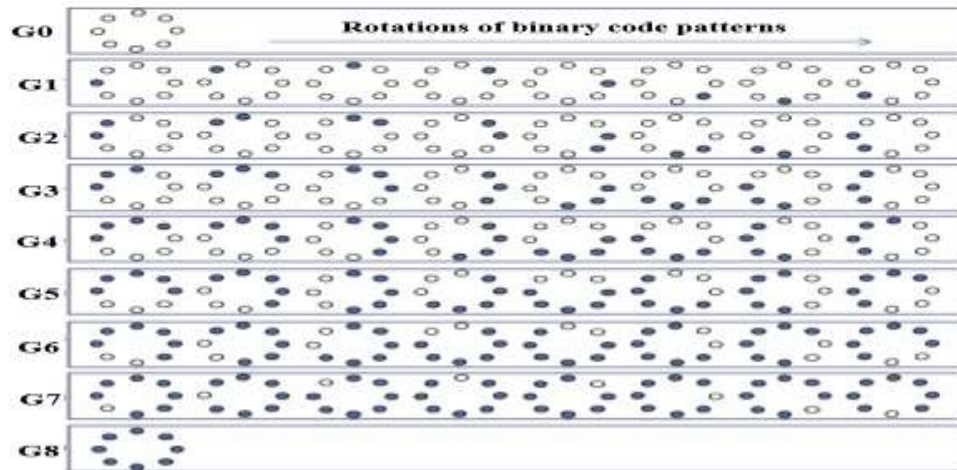


Figure 2-15: The 58 different uniform patterns in (8, 1)

Regarding uniform LBP patterns classifications based on the number of ones included in the pattern in the natural images database which described in (Ojala et al. 2002); these geometries may be characterised as follows:

- 1- The patterns in G0 describe the flat area in the image.
- 2- The patterns in G8 shows the spot area in the image.
- 3- The patterns in G2 and G4 represent the edges in the image.
- 4- The patterns in G3 and G5 describe the corners in the image.
- 5- The patterns in G6 describe the line ends in the image.

While the uniform LBP patterns classifications based on the number of ones included in the pattern in the face images database which described in(Chan 2007); these geometries are described as:

- 1- Flat area: When there is G0 (i.e. no ones) in the pattern.
- 2- Spot area: When G8 (i.e. 8 ones) is available.
- 3- Edges: When G5 (i.e. 5 ones) is available.
- 4- End Lines: When G1 or G7 (i.e. 1 or 7 ones) is or are available.
- 5- Corners: When G2, G3, G4, and G6 (i.e. 2, 3, 4 and 6 ones) are available.

After selecting the landmark points, a sequence of distance thresholds and a constructed inclusion series of SCs are selected. These geometries are studied on the inpainted images in the later chapters. Thus the next section is dedicated to explaining the process of this construction.

2.6.2.2 Simplicial Complex Construction

For each class of geometry- t in ULBP, its corresponding positions are extracted in the inpainted region of the given image. As a result, we end up with a set of image pixel positions of the 8 sets of t -ones ULBP codes. First, the known Euclidean distance is calculated between all pairs of points in the set, and then an increasing 8 sequence of T -dependent Rips complexes is constructed, one for each rotation of the geometry- t codes. For $T = 0$, only 0-dimensional simplices are obtained, i.e. the points. Then T is gradually increased and computed β_0 at each T .

Robert Ghrist in (Ghrist 2008) illustrated that there is no optimal method to select the best threshold that best captures the topology of data sets. A fixed number of distance thresholds are used, as follows:

$$T_1 = 0, T_2 = 5, T_3 = 10, T_4 = 15, T_5 = 20, T_6 = 25.$$

The reason behind using a fixed number of distance thresholds is that beyond certain distance thresholds, the computed number of CC will lose its power to discriminate inpainted regions with non-inpainted ones or even different types of images inpainted through PDE-based inpainting algorithms (see Chapter 4). The diagram Figure 2-16 below summarises the process of selecting Landmarks from images of interest and consequently building SCs.

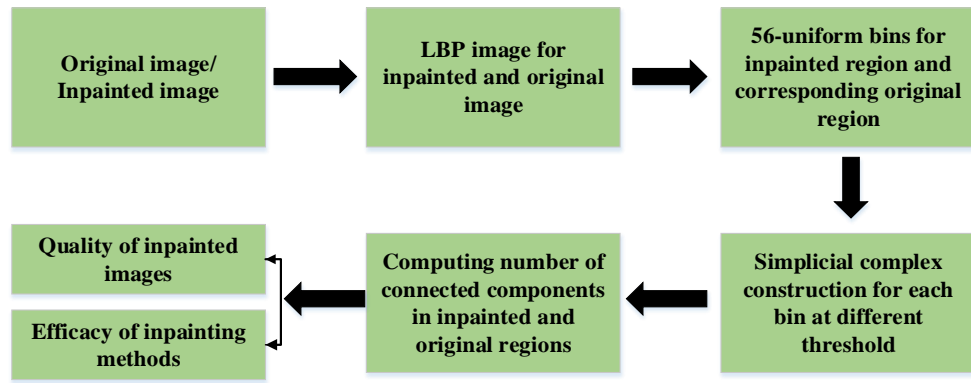


Figure 2-16: Simplicial complex construction for the quality of image inpainting.

Aforementioned procedure of building topological shapes from images are used in the rest of the thesis as an image quality assessment tool. This approach is motivated by the work of A. Asaad and S. Jassim in (Asaad et al. 2017), as they used the TDA approach to assess the quality of degraded images. In particular, they focused on discriminating face images degraded by shadows and blurring. The topological invariant which is used across this thesis is the zero homology groups, which correspond to the number of CC this is due to its ease of computation. More specifically, the number of CC is calculated for both the inpainted and original regions. The closer the number of CC of the inpainted region to the number of CC of original region, the better is the quality of the inpainted region, and consequently the better inpainting algorithm. The TDA is used to evaluate the image inpainting quality in the case full reference is available.

2.7 Summary and Conclusion

The task of inpainting can be described as a minimisation problem; the total variation has been used in the minimisation problem. A PDE method is produced by solving the minimisation problem *via* the Euler-Lagrange equation. The numerical solutions of PDEs are used to reconstruct the missing regions in images. In this chapter, mathematical definitions and theories are introduced for variational formulas used for adding colour to grayscale images and recovering missing regions in colour images. The numerical method which has been used to solve these PDE-based inpainting methods in both spatial and frequency domains is also introduced. The statistical and topological measurements for image quality assessments and for checking the performance of inpainting methods are also introduced.

Chapter 3 PDE BASED PARTIAL INPAINTING METHODS (COLOURISATION)

Colourisation, in general, is a process to convert grayscale images/videos to colour images/videos. The missing colour information may be restricted to a region of the image. There are many research fields in which colourisation algorithms are employed, such as biology, astronomy, medicine, and other disciplines. Several colourisation techniques have been developed in recent years that are either automatic or semi-automatic. Here, we first review recently devised colourisation techniques and highlighted their advantages and disadvantages. We shall then consider PDE-based semi-automatic colourisation techniques, designed to restore colour to a region over which grayscale information is known, and then extends its applicability to the case when one colour channel is known for any colour space including RGB. Statistical-based image quality measures are used to evaluate the quality of coloured images, as an indicator of the performances of PDE techniques. We shall demonstrate experimentally that the PDE algorithms compare well with other algorithms in terms of these measurements.

3.1 General Colourisation Concepts

A colour image consists of three-dimensional information about the colours in the image, usually expressed by three colour channels (e.g. Red, Green and Blue channels). A grayscale image consists of one channel (i.e. luminance or intensity) which means it is one-dimensional information. A colour image contains more useful information than a grayscale image; it is lively and visually appealing to viewers. Colourisation is the process of adding missing colours to grayscale images by a computer algorithm. Its applications range from old black and white images and movies to scientific illustrations (Levin et al. 2004), (Popowicz & Smolka 2014), (Yatziv & Sapiro 2006), and (Zhang et al. 2009). Additionally, colourisation has been shown to be useful in image compression (Takamichi Miyata et al. 2009), (Sukho Lee et al. 2013) and medical images such as MRI, X-ray and CT images, where the indications of some crucial regions within medical images may be of special interest to physicians (Shah et al. 2013), (Popowicz & Smolka 2017).

The 3-dimensional image colour space can be represented by many other 3 channels and the most common ones that can be obtained from RGB by affine/linear transformation. Converting a colour image to grey entails a reduction of information and is quite easy, but the reverse process is not. This is because there can be numerous colours which lead to one grey level, meaning that RGB-based colours are underdetermined by greyscale values (Sapiro 2005).

The colourisation problem lies in the restoration of the missing colour information in image regions or in the colouration of an entire grayscale image. The first case can be divided into 2 categories: (1) The *colourisation region* problem where the missing region has texture (i.e. grayscale) information or (2) the *total inpainting* problem when no information is known in the missing region. Note that, G. Sapiro, (Sapiro 2005), refers to the first category as inpainting the colours, and it is, therefore, reasonable to consider the first category as *partial inpainting* which will be the focus of this chapter. The other cases, including the colouring of entire grayscale images which is the extreme case of colourisation category when the missing region is the entire image, is discussed in the rest of this thesis.

The colourisation problem, as well as the total inpainting problem, has no exact solutions because there is no deterministic relation between the luminance of a grayscale image and exact colours at the image pixels. The solution of this problem aims to restore RGB colours or equivalently restoring any other 3-colour channels. Hence, it can be considered as an optimisation (or approximation) problem in terms of some subjective/automatic quality measures. Existing colourisation techniques are generally divided into semi-automatic and automatic techniques. In the case of semi-automatic techniques, a user should insert colour scribbles within the missing grayscale region. These scribbles enable the algorithms deciding which colours have to be used for in corresponding parts of the image. This procedure may be visualised as mimicking artist painters through colour spilling over the missing areas starting from the inserted scribbles (Levin et al. 2004), (Popowicz & Smolka 2014), (Yatziv & Sapiro 2006), and (Lagodzinski & Smolka 2014).

Automatic colourisation techniques, use a source image to produce the colours and works by transferring colour from a colour image to a target grayscale image, (Xiang et al. 2009). These automatic techniques do not require the user to select and apply individual colours to the target image. Several automatic techniques for adding colours to the grayscale image have been developed, and the Welsh *et al.*, (Zhang et al. 2009),

that use statistical properties is a typical example. In some applications, designing automatic techniques is challenging because of the need for a source image(s) close enough in content to the target image to provide the subset sample patches.

It is difficult to objectively evaluate the definitive colourisation results. The evaluations and comparisons of the colourisation algorithms are done by using standard quality measures only if the colour version of the image (i.e. original image) is available. Some quality measures are used to evaluate the colourisation algorithms such as Peak Signal-to-Noise Ratio (PSNR), Structural Similarity (SSIM), and Normalised Colour Difference(NCD).

In this chapter, we are interested in semi-automatic colourisation techniques and aim to develop an extension to the PDE algorithm developed by Sapiro in (Sapiro 2005) to a range of colour channels. The rest of the chapter is organised as follows: Section 3.2 reviews the literature on both semi-automatic and automatic algorithms. While section 3.3 shows the basics of semi-automatic grayscale image colourisation. Our proposed algorithms are illustrated in detail in section 3.4. The results and evaluations of existing colourisation methods in comparison to our proposed algorithm are presented in sections 3.5 and 3.6. Finally, section 3.7 summarises the work done and identify the next set of challenges.

3.2 Literature Overview

The literature provides many semi-automatic colourisation approaches, and this area has continued to be active in recent years. In 1970, Wilson Markle introduced the term of colourisation to describe adding colour to black and white movies assisted by computer processing (Levin et al. 2004). A well-known commercial semi-automatic software package is given in(Neuraltek 2004), for image colourisation. The main drawback of this work is that it requires a manual segmentation of the image, but automatic segmentation is more desirable, and we shall adopt in this thesis.

Our review revealed two main approaches to adding colour either transferring colour from another similar image or using colour information from other parts of the image itself. Reinhard *et al.*, in (Reinhard et al. 2001), described a theoretically sound approach for the colour manipulation, whereby the target image may take on another image's look and meaning, and for this purpose, it used statistical concepts that describe correlations that may exist between different colour channels. This pioneering work argues that a colour space basis vectors with de-correlated axes is ideal for manipulating

colour images. Noting that RGB images can be transferred by an affine transformation to $\ell\alpha\beta$ which is an orthogonal colour space, (*i.e.* de-correlated axes), the authors of (Reinhard et al. 2001) and (Ruderman et al. 1998) then introduced an automatic colourisation scheme that is based on the idea of colour manipulation only in the chrominance channel, without changing the luminance level. Such a method uses the similarities between a reference colour image and a grayscale one. They then applied simple statistical transformations in each separate, de-correlated colour channel of the target image so that the source and the target have a similar look. This algorithm has succeeded in transferring colour from one image to another image. The concept of using de-correlated colour channels has been used in other algorithms such as in automatic image colourisation algorithm.

Zhao *et al.*, in (Zhao et al. 2007) introduce a similar automatic approach, to the above approach, for colouring biomedical images. The authors converted the RGB into de-correlated $\ell\alpha\beta$ space for both the reference and the target images (*i.e.* grayscale image). Then they calculated the mean and standard deviation of the luminance channel in a moving square 7×7 window. Finally, by comparing these two statistical features in each window, the colours are transferred from parts of the reference image into the corresponding parts of the grayscale image.

Another automatic colourisation method is presented in (Zhen et al. 2012) which uses pattern continuity and spatial consistency in a grayscale image, instead of considering the luminance properties. First, the reference image is converted to YUV colour space and segment it. The Gabor wavelet filter used to extract a 10-dimensional texture feature vectors from each 7×7 block in the Y channel from the reference image and use them as the training set. Finally, the K nearest-neighbour method is used for classifying pixels based on closest training examples in the feature space. This method is used for colouring cartoon images and videos.

The above approaches to automatic colourisation work well for images containing distinguishable features, like in the biomedical image, (see section **Error! Reference source not found.**, below). The drawback is that it is difficult to find matching reference colour images. Therefore the applications of such algorithms are usually limited. The alternative is provided by semi-automatic algorithms. These algorithms are very popular for adding colour to grayscale images or movies. Instead of searching for matching the reference image, the user is asked to add colour scribbles into the colour missing image regions.

Popowicz and Smolka in (Popowicz & Smolka 2014) have introduced a semi-automatic colourisation algorithm using distance maps for each scribble indicated by a user. The distance map function has utilised the concept of *isolines* (also referred to as contour lines), as in geographical maps, consisting pixels of the same intensity level, or other property visualised on the maps. Isolines are imaginary lines representing elevation on a map by connecting points of equal elevation, to provide a good visual representation of the terrain. An isoline is determined in terms of the grayscale intensity difference between the pixels and the nearest seed pixel (the one within a scribble). For each pixel, the computed difference represents the maximum intensity deviation encountered on its shortest path to the seed pixel and ending in a current point. Finally, the colour of a pixel is set to the weighted average of each colour is calculated from the seeds.

Levin *et al.*, in (Levin et al. 2004) proposed a semi-automatic approach for adding colours to the grayscale image by defining a quadratic optimisation formula based on the assumption that the neighbouring pixels in space-time with similar intensities should have similar colours. When the distance between pixels of similar intensities are modelled by a Gaussian weighting function, a quadratic cost function is obtained, and the optimisation problem can be solved efficiently by standard techniques. This has been used in a segmentation procedure in (Arbeláez et al. 2011). This algorithm has given a high-quality colourisation but it is time-consuming, and more importantly, it is sensitive to changes in that it requires the colourisation to be re-computed from scratch after the slightest change to the initially marked pixels. Such an algorithm was also applied in biomedical imaging (Shah et al. 2013), and also for video colourisation (Veeravasaram & Sivaswamy 2012). The drawbacks of this algorithm are that it is time consuming and uses a large number of colour scribble pixels because it applies weighted pixel distances. To avoid these limitations, a similar but modified optimisation formula with gradient geometry of channel colours is used, but without using the weighted pixel distances.

On the other hand, Ding and Deng in (Ding et al. 2012) use automatic scribble generation. The authors propose the selection of proper colours for automatic insertion by reduced operator interaction only. Their algorithm starts by segmenting the image through graph-based image segmentation (Felzenszwalb & Huttenlocher 2004). Next, an automatic scribble generation algorithm has been proposed based on spatial distribution entropy, placing scribbles within the regions of high information density. Finally, colour is added to the scribbles by computing quaternion wavelet phases to

Chapter 3: Colourising Greyscale Images Based on PDE Algorithms

conduct colourisation along equal-phase lines. They reconstruct colour image patches as vector elements using polar representations in quaternion algebra, by which the interrelationships between colour channels are well preserved.

Konushin and Vezhnevets in (Konushin & Vezhnevets 2006) focus on treating the computational burden in semi-automatic colourisation, as these methods are time-consuming. The authors use the idea of coupled map lattices, the evolutionary nature of which allows for fast re-colourisation. This method can be applied for the changing of colours in some regions within colour images.

Sapiro and Yatziv in (Yatziv & Sapiro 2006) propose an algorithm which uses the Dijkstra algorithm (Dijkstra 1959) to find the cost of the shortest path between two image pixels by integrating the squared difference of intensities between pixels on the path. Colour is added to the grayscale image by calculating a weighted average of scribbled colours, where the shortest path analysis provides the weights. Therefore, the authors suggested reducing the number of colours during the final blending. Hence their algorithm does not entail a high computational burden.

Yingge Qu *et al.*, in (Qu et al. 2006) adopted a similar manga colourisation which is based on pattern continuity. In manga drawing, they use hatching and screening techniques to show different effects like structures, shading or reflectance. Then the required regions of the same textures should also have similar colours. The Gabor wavelet transform is utilised to obtain the structure features. This method is mainly limited to a very specific application.

The above algorithms add colour either using reference similar images or propagating colour by inserting colour scribbles, and little consideration is giving to the available information in the actual image and in particular, the areas surrounding the missing region (s). The alternative approaches are based on the natural expectation that image information flow along image features only to be interrupted in the missing region. These are categorised as the variational/PDE based approaches (Chan et al. 2006).

Tony *et al.*, in (Chan et al. 2006) describe the relevance of total variation to colourisation and derive a its numerical solutions, proposed two models of the total variation in wavelet-based inpainting, to deal with challenges which include that the resulting inpainting regions in the pixel domain are usually not geometrically well defined, as well as that degradation is often spatially inhomogeneous and creates

problems with sharp edges. This work and we have used it to build a scheme that minimises the directional derivative of the gradient in the coloured channels.

A similar approach was followed by Jacobson *et al.*, in (Jacobson & Sorkine-Hornung 2012) but uses a minimised Dirichlet energy over an image surface where it becomes a (discrete energy) minimisation problem and produces a 2nd-order PDE with a discrete Laplacian operator. Again, in our work, we benefited by following the same steps to obtain the minimisation problem that been used in (Jacobson & Sorkine-Hornung 2012) and to solve the resulting nonlinear 2nd-order PDE.

Sapiro in (Sapiro 2005) inspired by (Levin et al. 2004) proposed the use of the optimisation formula which leads to pragmatic colourisation results. The general idea of adding colours to the greyscale image based on the solution of PDE, which is derived from the assumption, that the difference between the gradient of luminance and chrominance should be minimal. As the PDE is of Poisson type and can be solved by any Poisson **solver**. The advantages of the algorithm are its simplicity and efficiency. The core idea is thinking of colourisation as an inpainting problem (Sapiro 2005). Chung and Sapiro (Do Hyun Chung & Sapiro 2000) have shown that the (scalar) luminance channel faithfully represents the geometry of the whole (vectorial) colour image (Edges).

The Laplacian operator has also been used in different colourisation methods. The weighted p-Laplacian operator has been introduced for image colourisation in (Lezoray et al. 2008) which relies on graph regularisation; we have used the minimised Laplacian operator of the coloured channels, the nonlinear 4th order PDE, achieved by applying the Euler-Lagrange equation with Fréchet derivative to Laplacian minimisation (Peiyang Chen & Yuandi Wang 2008). To define colour constraints, Sapiro used Cb and Cr components in YCbCr colour space. However, the main problem is that Sapiro's method produces significant colour bleeding near the strong edges which are visually disturbing, so applying this algorithm was suggested in the wavelet domain for handling this shortcoming with sharp edges, but the result was not satisfactory. Where this work with all details is introduced in section 3.4.2.

The authors in (Lagodzinski & Smolka 2014) introduce the morphological distance transformation as a possible way to obtain the distance between seed and any other image pixel. They use the double-scan algorithm, which can cover all the pixels paths and obtains a very good estimation of the Euclidean distance between the image points. The distance is modified by making it as the combination of intensity differences and

topographic distance. Finally, the authors calculated the colour as a weighted average of all scribbled colours.

Jacob and Gupta in (Jacob & Gupta 2009) propose a different design based on the image segmentation and clustering the parts of the image into regions that have the same colours. This segmentation method is called the rainwater simulation, then adding colour scribbles to each segment. Finally, all the pixels in the segment are colourised based on the value of indicated colour scribbles.

Luan *et al.*, in (Luan et al. 2007) enable the incorporation of two similarity measures based on the intensity continuity and the texture features. Instead of using scribbles, the user is required to indicate exemplary regions together with their appropriate colour. This works well with complex natural images where both, smooth regions and complicated, textured regions, are present.

Recently developed colourisation schemes follow the current evolving trend of using Machine Learning for image analysis. These algorithms need an initial learning stage that utilises an auxiliary dataset (also called dictionary) of exemplary colour source images to train a classifier, such as support vector machine (SVM), to discriminate between grayscale patches in terms of some texture feature vectors. Such schemes predict the missing colour from the trained model and the known colour channel in the image. A number of these algorithms are discussed in (Charpiat et al. 2010).

Deep learning techniques have also been used to predict the colour (e.g. see (Zhang et al. 2016), (Cheng et al. 2015) and (Varga & Szirányi 2017)). These algorithms avoid adding scribbles or using colour from reference images and output a high-quality fully-automatic colourisation method using a perfect patch matching technique. These algorithms use an extremely large reference database (that contains sufficient colour images), and colours are added (to the Cb and Cr channels) by a patch matching process that uses similarity between the weights in the greyscale inpainted image and the Y channel of the database colour. However, the performance of these techniques is not always acceptable, as it may add one colour to two regions because the different colour regions have the same weights. Also, these techniques consume a long time to complete the colourisation process. Finally, the authors are trying to make these algorithms available for all applications based on using a large number of different images in the training database.

To know these algorithms, in the next section, the basics of the automatic colourisation algorithm are introduced with examples.

3.3 Basics of Semi-Automatic Greyscale Image Colourisation

Most semi-automatic image colourisation algorithms employ similar steps, as seen in Figure 3-1 which describes a general schema of these algorithms. Several actions in this schema are conducted by a user and a computer system. In the first step, a user selects colour scribbles suitable for the inside of different image objects, where paint, see the screenshot of a colourisation software in Figure 3-2. Note that the palettes of standard colours are not enough to produce natural variation in colour intensity such as the case with the colour of human skin. For this, it will be sensible to use colour blocks from other images.

There are two scenarios for using segmentation algorithms. In the first scenario, grayscale images are manually segmented by using colour scribbles to determine the borders of the objects in the image. In the second scenario, automatic segmentation algorithms are used when dealing with the same kinds of images. This step handles the shortcomings in border definitions, but it is time-consuming. Although the next step of the colourisation differs from method to method, the general idea remains the same. The idea is to propagate colour based on the colour scribbles by calculating distances between the neighbourhood pixels of colour scribbles in the luminance channel.

The selection of the colour for a given pixel is performed using different approaches. In one of them, the weighted average of all indicated colours is calculated, where the distances are used as weights; otherwise, the numerical solution of PDE or optimisation formulas is used to propagate the colour. The final step entails avoiding the leakage of colours from distant scribbles by modifying the weights, so that the smallest distances are promoted, or by modifying the colour scribbles.

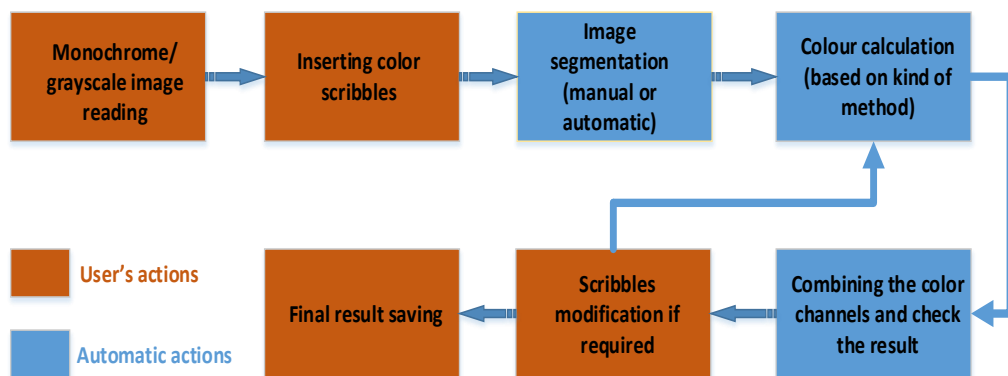


Figure 3-1: Schema of semiautomatic colourisation steps.

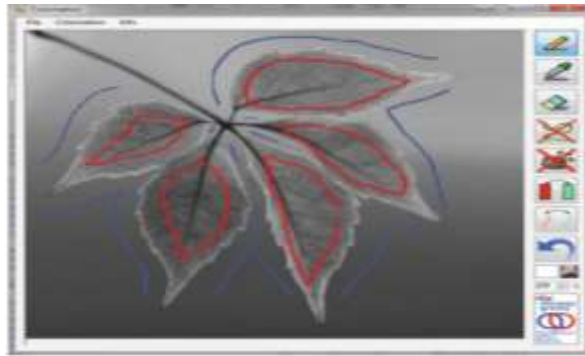


Figure 3-2: Example of a colourisation software layout. Grayscale image with indicated colour scribbles.

3.3.1 Image Colour Models

The literature review reveals that most existing automatic colouring schemes apply inpainting schemes in de-correlated colour channels (e.g. see (Reinhard et al. 2001), (Ruderman et al. 1998), (Zhao et al. 2007), and (Zhen et al. 2012)), and an interesting question arises as to whether these schemes can or cannot be extended to other non-de-correlated colour such as RGB schemes. The structures of image colour space is first briefly reviewed with a focus on the choice of meaningful 3-dimensional colour vectors that generate the entire colour space. It is well known that 3 colours are sufficient to generate all shades of visible colour, and due to the structure of human vision, RGB (Red, Green, and Blue) is the most natural colour model for displaying colour images on electronic devices. In terms of digital image processing, the RGB model is commonly used for colour monitors and a broad class of colour video cameras. The additive nature of the RGB colour image representation means that the obvious correlation exists between the values in the 3 channels. There are several other 3-dimensional additive colour models that use other primary colours can be obtained from the RGB model by linear/affine transformations. This implies that the different channels of such colour models are again correlated.

Besides RGB, colour models in use today are oriented either toward hardware (such as for colour monitors and printers) or toward applications where colour manipulation is a goal (such as in the creation of colour graphics for animation); the additive 3 primary colour CMY (Cyan, Magenta, and Yellow) and CMYK (Cyan, Magenta, Yellow, and Black) models have been used for colour printing; while the HIS (Hue, Intensity, and Saturation) and HSV (Hue, Saturation, and Value) models, which corresponds closely with the way humans describe and interpret colours, so artists prefer to use these colour models.

Chapter 3: Colourising Greyscale Images Based on PDE Algorithms

The colour spaces YCbCr, YUV, NTSC, and YIQ are represented as (luminance, chrominance, and chrominance) channels, which are called De-correlated colour spaces (i.e. separate chrominance from luminance in these spaces). The Y channel represent the grayscale version of the image. The YCbCr model is used widely in digital video and image compression schemes. The YUV model was formerly used in (Australia, Europe, except France) television broadcasts. While, the YIQ model was formerly used in (North America, Japan and elsewhere) television broadcasts. The XYZ (chrominance, luminance, and chrominance) model, which is widely used in scientific work, and colour descriptions in other colour spaces are often related to their representation in this space.

For image inpainting investigation one needs to consider these different colour models in terms of their properties as two categories. In the first category, each colour channel represents all image information (i.e. texture and structure in image beside colour). For example, in RGB, R represents all information and red colour, and the same thing with G and B channels which represent all information for green and blue colours respectively. So, the most common colour spaces in the first group are RGB, CMY and CMYK. While, in the second group of colour spaces, colour information is represented in two channels (i.e. chrominance) and another channel (i.e. luminance) has all texture and structure information, as seen in the colour spaces YCbCr, YUV, NTSC, HSV, HIS, and XYZ. The work in (Sapiro 2005), applied its algorithm on YCbCr colour space, where the idea of this paper built on when having all information in luminance (i.e. Y channel) and they adding colour scribbles to this channel image then trying to propagate this colour in chrominance (i.e. Cb and Cr) channels. In this work, we consider 8 different colour spaces illustrated in Figure 3-3.

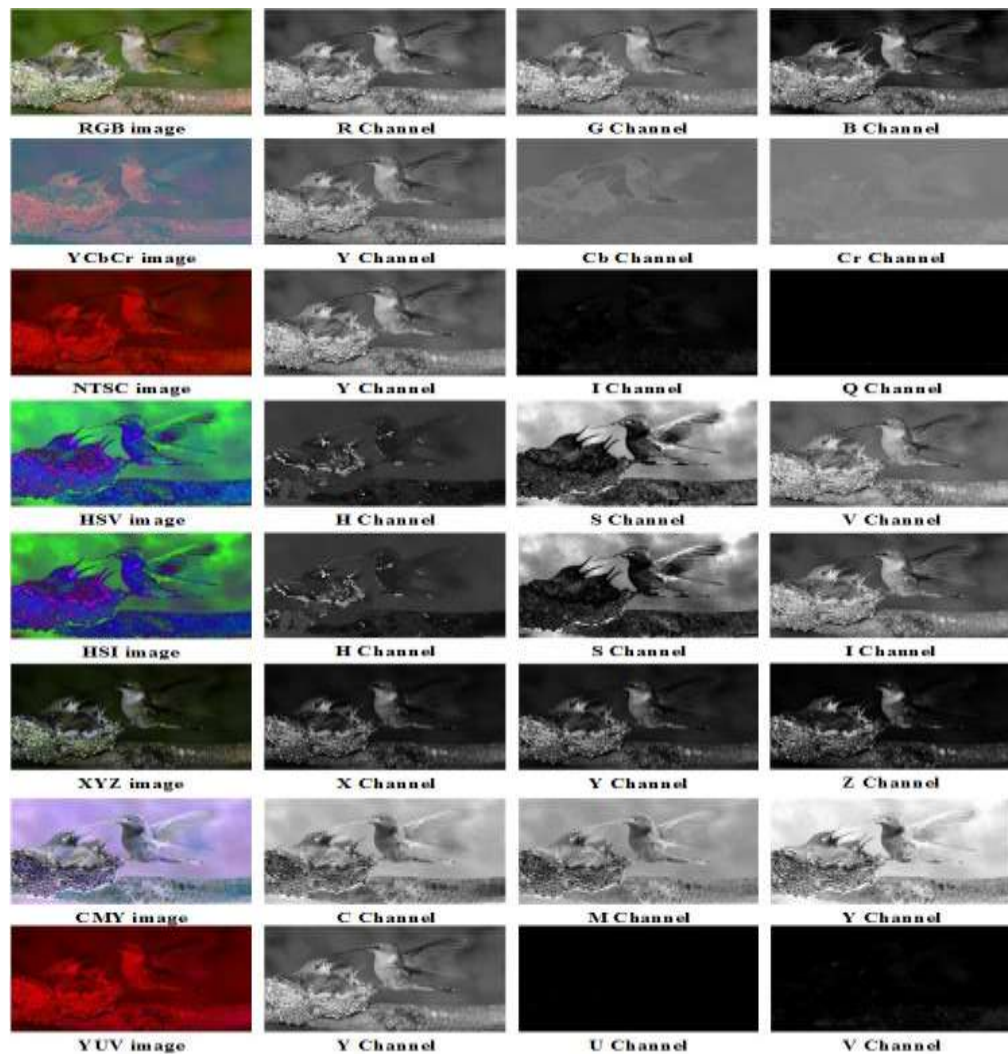


Figure 3-3: Illustration of colour spaces.

The next section describes the PDE based colourising algorithm. There follows applying it in the eight-colour space in both spatial and frequency domains.

3.4 Geometric Consideration of the Colourisation Problem

Understanding the propagation of colour along geometric shapes in images is of great benefit to colourisation. Inspired by work in (Levin et al. 2004), Sapiro in (Sapiro 2005) developed a semi-automatic colourisation technique for YCbCr coloured images based on the fact that the appropriate colour information optimally minimises the total variation between the gradient of the Y channel and the gradient of each of the Cb and Cr channels. Sapiro, used the Euler-Lagrange process to derive a linear 2nd order PDE (Poisson equation), the numerical solutions of which was shown to succeed in adding colour to greyscale images/movies.

Here, we shall first prove that Sapiro’s scheme is extendible to other 3-dimensional colour channels, as a result of a modified version of the Poisson PDE. Furthermore,

inspired by the PDE inpainting algorithms proposed in (Bertalmio et al. 2000) and (Peiyong Chen & Yuandi Wang 2008) that smoothly propagate information from the surrounding areas in the isophotes direction, two functional formulas are investigated, other than the gradient functional, defined in terms of the directional derivative of (1) the gradient and (2) the Laplacian of two colour channels. The Euler-Lagrange process applied to these two functional produces nonlinear 2nd order as well as a nonlinear 4th order PDE's that can be solved numerically to restore colours in a missing region of interest. The effectiveness of the corresponding image inpainting schemes are established, in both the spatial and wavelet domains for 8 different colour spaces. The successes of both schemes for a large number of natural images is demonstrated, showing that they outperform the Poisson formula.

3.4.1 The Mathematics of Sapiro's Colourisation Scheme

For the sake of self-contentment, the mathematical concepts are first described that underpin the colourisation scheme Sapiro, in (Sapiro 2005), in the non-correlated YCbCr image colour space. Let $Y(x, y): \Omega \rightarrow \mathcal{R}^+$, $Cb(x, y): \Omega \rightarrow \mathcal{R}^+$, and $Cr(x, y): \Omega \rightarrow \mathcal{R}^+$ be the functions defining the image Ω in the YCbCr colour space. Assume that Cb and Cr, but not Y, values are missing in a region Ω_c , which is a proper subset of Ω .

The following minimisation in the region problem has been introduced for the reconstructions of the Cb (and Cr) missing colours in Ω_c , from the available Y luminance image channel.

$$\min_{Cb} \int_{\Omega} \sigma |\nabla Y - \nabla Cb| d\Omega, \quad (3.1)$$

Where $\nabla := \left(\frac{\partial}{\partial x}, \frac{\partial}{\partial y} \right)$ is the gradient operator, and $\sigma(\cdot): \mathcal{R} \rightarrow \mathcal{R}$, this function works to determine the type of space that used for the proposed formula, for example, L^1 norm or L^2 norm space.

The basic idea is to force the directional gradient (and therefore the geometry) of Cb to be as the geometry of the given greyscale image Y while preserving the given values of Cb at Ω_c . Note here that though, these given values are considered as hard constraints. This can be particularly useful for editing applications where the user only provides colour hints instead of colour constraints. For ease of the presentation, we continue with the assumption of hard constraints. In (Black et al. 1998), a number of robust selections for σ were discussed for image de-noising, while (Ballester et al. 2001) set σ as the L^1

Chapter 3: Colourising Greyscale Images Based on PDE Algorithms

norm, i.e. $\sigma(\cdot) = |\cdot|$. These choices are based on the work done on total variation in (Rudin et al. 1992), and (Jiying Wu & Qiuqi Ruan 2008). Naturally, the most common, though not strong, chosen is the L^2 norm, $\sigma(\cdot) = \cdot$ which leads via simple calculus of variation (Euler-Lagrange equation) to the following Proposition on the necessary condition to minimise (3.1):

Proposition 3.1: Given a YCbCr colour image f , then in any sub-image of f :

$$\Delta Y = \Delta Cb = \Delta Cr \quad (3.2)$$

where Δ is defined as the Laplacian operator given by $\Delta := \left(\frac{\partial^2}{\partial x^2} + \frac{\partial^2}{\partial y^2} \right)$.

Proof (Sapiro 2005): To prove this, one can rewrite equation (3.1) as follow:

$$I(W) = \min_{cb} \int_{\Omega} \|\nabla W\|^2 d\Omega, \text{ where } W = Y - Cb$$

Since

$$\|\nabla W\|^2 = \nabla W \cdot \nabla W = \left(\frac{\partial W}{\partial x}, \frac{\partial W}{\partial y} \right) \cdot \left(\frac{\partial W}{\partial x}, \frac{\partial W}{\partial y} \right) = \left(\frac{\partial W}{\partial x} \right)^2 + \left(\frac{\partial W}{\partial y} \right)^2,$$

then one we need to find the Euler- Lagrange equation for the following functional

$$I(W) = \min_{cb} \int_{x_1}^{x_2} \int_{y_1}^{y_2} \left[\left(\frac{\partial W}{\partial x} \right)^2 + \left(\frac{\partial W}{\partial y} \right)^2 \right] dx dy,$$

For simplicity, write the Integrand quantity as $G = W_x^2 + W_y^2$. Thus,

$$\frac{\partial G}{\partial W} = 0, \quad \frac{\partial G}{\partial W_x} = 2W_x = 2 \frac{\partial W}{\partial x}, \quad \frac{\partial}{\partial x} \left(\frac{\partial G}{\partial W_x} \right) = 2 \frac{\partial^2 W}{\partial x^2},$$

$$\frac{\partial G}{\partial W_y} = 2W_y = 2 \frac{\partial W}{\partial y}, \quad \frac{\partial}{\partial y} \left(\frac{\partial G}{\partial W_y} \right) = 2 \frac{\partial^2 W}{\partial y^2}.$$

Therefore, the Euler-Lagrange equation for this functional is (Tang 2007),

$$\frac{\partial G}{\partial W} - \frac{\partial}{\partial x} \left(\frac{\partial G}{\partial W_x} \right) - \frac{\partial}{\partial y} \left(\frac{\partial G}{\partial W_y} \right) = 0.$$

which yields the Laplace equation is

$$\frac{\partial^2 W}{\partial x^2} + \frac{\partial^2 W}{\partial y^2} = 0.$$

The proof of the Proposition is complete by the fact that:

$$\Delta W = 0, \Rightarrow \Delta(Y - Cb) = 0 \Rightarrow \Delta Y = \Delta Cb.$$

Similarly, one can prove that $\Delta Y = \Delta Cr$.

Numerical Solution of Equation (3.2).

Equation (3.2) is a linear elliptic equation which known as Poisson’s equation. The boundary conditions will be on Ω_c , and the equation (3.2) is written as follows:

$$\nabla^2 Cb = \mathcal{F} \tag{3.3}$$

Where $\mathcal{F} = \Delta Y$, is the Laplacian of the Y channel data (i.e. luminance, and this data is known). In Cartesian space, equation (3.3) can be written as:

$$\left(\frac{\partial^2}{\partial x^2} + \frac{\partial^2}{\partial y^2}\right) Cb(x, y) = \mathcal{F}(x, y) \tag{3.4}$$

To discretise equation (3.4), the five-point finite difference method is used, as follows:

1. Rewrites (3.4) in discrete space by a finite difference as follows:

$$\nabla^2 u = \frac{u_{i+1,j} - u_{i,j} + u_{i-1,j}}{\Delta x^2} + \frac{u_{i,j+1} - u_{i,j} + u_{i,j-1}}{\Delta y^2} = g_{i,j} \tag{3.5}$$

Where $2 \leq i \leq m - 1$ and $2 \leq j \leq n - 1$, $\Delta x^2 = \Delta y^2 = 1$ and $\nabla^2 u = \nabla^2 Cb$, $g_{i,j} = \mathcal{F}(x, y)$.

2. Now, the matrix representation of Poisson’s equation is $[A][U] = [b]$,

where $[U] = [u_{11}, u_{21}, \dots, u_{m1}, u_{12}, u_{22}, \dots, u_{m2}, \dots, u_{mn}]^T$,

$$A = \begin{bmatrix} D & -I & 0 & 0 & 0 & \dots & 0 \\ -I & D & -I & 0 & 0 & \dots & 0 \\ 0 & -I & D & -I & 0 & \dots & 0 \\ \vdots & \ddots & \ddots & \ddots & \ddots & \ddots & \vdots \\ 0 & \dots & 0 & -I & D & -I & 0 \\ 0 & \dots & \dots & 0 & -I & D & -I \\ 0 & \dots & \dots & \dots & 0 & -I & D \end{bmatrix}_{mn \times mn}, D = \begin{bmatrix} 4 & -1 & 0 & 0 & 0 & \dots & 0 \\ -1 & 4 & -1 & 0 & 0 & \dots & 0 \\ 0 & -1 & 4 & -1 & 0 & \dots & 0 \\ \vdots & \ddots & \ddots & \ddots & \ddots & \ddots & \vdots \\ 0 & \dots & 0 & -1 & 4 & -1 & 0 \\ 0 & \dots & \dots & 0 & -1 & 4 & -1 \\ 0 & \dots & \dots & \dots & 0 & -1 & 4 \end{bmatrix}_{m \times m} \tag{3.6}$$

$$U = A^{-1}b$$

The scribbles are outside of missing colour regions. The Gaussian elimination method can be used to solve the system (3.6) with Dirichlet boundary conditions. Also, there is a vast field of available literature on numerical implementations of these equations leading to accurately efficient solutions (Recktenwald 2011), (Markle, Wilson 1988) and (Arbeláez et al. 2011).

Generalising Sapiro colourisation Algorithm

Proposition 3.1 is extended to cover different colour spaces as one of our initial objectives. This should help apply the Sapiro-like algorithm on any colour space and determine the colour space more effective for adding colour. In particular, Sapiro’s

Chapter 3: Colourising Greyscale Images Based on PDE Algorithms

algorithm, (Sapiro 2005) on RGB, CMY, and CMYK and as we mentioned before all these colour spaces have been derived from RGB colour space.

The RGB components can be obtained according to equation (3.2):

$$\begin{bmatrix} R \\ G \\ B \end{bmatrix} = \begin{bmatrix} 1.164 & 0.000 & 1.596 \\ 1.164 & 0.392 & -0.813 \\ 1.164 & 2.017 & 0.000 \end{bmatrix} \cdot \begin{bmatrix} Y \\ Cb \\ Cr \end{bmatrix} - \begin{bmatrix} 16 \\ 128 \\ 128 \end{bmatrix} \quad (3.7)$$

Differentiation of this formula yields the following relation on the Laplacian

$$\begin{bmatrix} \Delta R \\ \Delta G \\ \Delta B \end{bmatrix} = \begin{bmatrix} 1.164 & 0.000 & 1.596 \\ 1.164 & 0.392 & -0.813 \\ 1.164 & 2.017 & 0.000 \end{bmatrix} \cdot \begin{bmatrix} \Delta Y \\ \Delta Cb \\ \Delta Cr \end{bmatrix} \quad (3.8)a$$

Since, $\Delta Cb = \Delta Y$ and $\Delta Cr = \Delta Y$, then we get the following generalised proposition:

Proposition 3.2: Given a RGB colour image f , then in any sub-image of f :

$$\Delta R = K_1 \Delta G \text{ and } \Delta R = K_2 \Delta B, \quad (3.8)b$$

where K_1 and K_2 are constant values obtained from the columns of (3.8), i.e.

$$K_1 = 0.175 \text{ and } K_2 = 1.1525$$

The numerical method used to solve Equation (3.2) can be followed exactly to solve Equation (3.8)b for colourisation in the RGB model. The same steps have been followed to apply the algorithm in (Sapiro 2005) on CMY colour space. Also, this algorithm has applied to eight colour spaces (RGB, CMY, YCbCr, YUV, NTSC, XYZ, HIS, HSV) in both spatial and frequency domains. Table 3-1 shows the values of conversion parameters (i.e. K_1 and K_2) from different colour spaces to RGB space, when using G as the channel that has the most the texture information in the image.

Colour space	YCbCr	YUV	NTSC	XYZ	HSV	HIS	CMY
K_1 value	1.27402	1.57569	1.34973	1.06514	1.54346	1.57621	0.98643
K_2 value	1.77342	1.23276	0.83926	1.30553	1.65432	1.63345	0.75564

Table 3-1: Values of conversion parameters from different colour spaces to RGB space.

Figure 3-4 shows the result of applying Sapiro algorithm at RGB colour space, and comparison its performance with the YCbCr Sapiro algorithm.

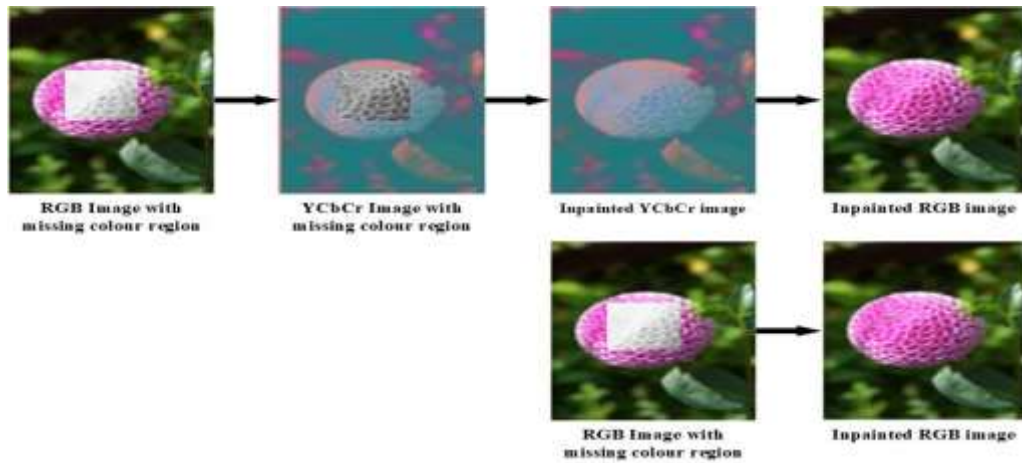


Figure 3-4: Sapiro colourisation algorithm. Row (1) Sapiro colourisation process in the YCbCr colour space, Row (2) Sapiro colourisation process in the RGB colour space.

The colourised image obtained using the Sapiro algorithm in RGB has good assessed quality (i.e. it is visually acceptable), and its result corresponds to the result of the same algorithm in YCbCr, but the quality measurement values of these images are different. The Sapiro algorithm has successfully added colour to the missing colour regions. However, this algorithm has limitations with the high texture regions, and the edges that have different colours in the large missing colour region. Figure 3-5, reveals the shortcomings of both algorithms when dealing with the reasonably large missing area or when there are many textures in the missing area.

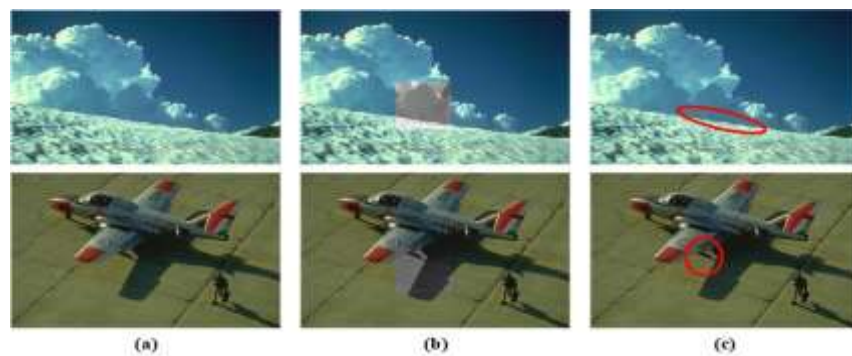


Figure 3-5: Sapiro colourisation algorithm. (a) Original image, (b) masked colour image, (c) coloured image.

The coloured image in the first row shows the bad effect of adding colour to the missing colour region that has high texture, especially in the edges, while the coloured image in the second row shows the effect of adding colour to the regions that have edges with different colours between them. This triggers our next investigations into other geometric-based minimisation problems that may result in improved colourisation.

3.4.2 Further Variation -based Formulation of Image Colourisation

This section aims to consider the potential improvement of the previous two colourisation algorithms using 2 other geometric-based functional minimisations and their Euler-Lagrange solutions. Here, assume that the user adds colour scribbles to the missing region by any image editing applications, and these greyscale images with colour scribbles are converted to YCbCr colour space. The choice of working in the YCbCr colour model is meant to simplify the discussion. The image segmentation algorithm (Arbeláez et al. 2011) allows the addition of different colours for different objects in the image at the same time.

3.4.2.1 Minimisation of Directional Derivative of Gradient in Colour Channels

We first investigate the minimisation of the direction derivatives of gradients in YCbCr coloured channels, i.e.

$$\min_{cb} \int_{\Omega} \sigma \left[\left(\frac{\nabla Y}{\|\nabla Y\|} - \frac{\nabla Cb}{\|\nabla Cb\|} \right) \cdot \nabla Cb \right] d\Omega, \quad (3.9)$$

From calculus of variations, the corresponding Euler-Lagrange equation is (for L^2 norm) is used below to prove the following new colourisation algorithm:

Proposition 3.3: Given a YCbCr colour image f , then in any sub-image of f :

$$\nabla \cdot \left(\frac{\nabla Cb}{\|\nabla Cb\|} \right) = \nabla \cdot \left(\frac{\nabla Y}{\|\nabla Y\|} \right), \quad (3.10)$$

Where $\nabla \cdot$ is the *divergence operator* given by $\nabla \cdot := \left(\frac{\partial}{\partial x} + \frac{\partial}{\partial y} \right)$, and $\nabla \cdot \left(\frac{\nabla Y}{\|\nabla Y\|} \right)$ is called the *curvature operator* defined on the luminance channel Y .

Proof: We shall deduce equation (3.10) from equation (3.9) using the Euler-Lagrange equation. Firstly, equation (3.9) can be rewritten as follows:

$$I(W) = \min_{cb} \int \int_{\Omega} \left(\left(\frac{\nabla Y}{\|\nabla Y\|} - \frac{\nabla Cb}{\|\nabla Cb\|} \right) \cdot \nabla Cb \right)^2 d\Omega, \quad (3.11)$$

where $I(W) = I(Y, Cb)$. Since $\frac{\partial I}{\partial W} = \frac{\partial W}{\partial Y} + \frac{\partial W}{\partial Cb}$, then

$$0 = \frac{\partial I}{\partial W} \cdot v = \lim_{h \rightarrow 0} \frac{I(Y + hv) - I(Y)}{h} + \lim_{h \rightarrow 0} \frac{I(Cb + hv) - I(Cb)}{h}.$$

By setting $N = \frac{\nabla Y}{\|\nabla Y\|}$, $M = \frac{\nabla Cb}{\|\nabla Cb\|}$, and $m_1 = \nabla Cb$, equation (3.11) becomes:

$$I(W) = \min_{cb} \int \int_{\Omega} ((N - M) \cdot m_1)^2 d\Omega, \quad (3.12)$$

$$\begin{aligned}
 \frac{\partial W}{\partial W} &= \lim_{h \rightarrow 0} \frac{1}{h} \int_{x_1}^{x_2} \int_{y_1}^{y_2} \left((N + hv) - M \right) \cdot m_1 - (N - M) \cdot m_1^2 dx dy \quad (3.13) \\
 &= \lim_{h \rightarrow 0} \frac{1}{h} \int_{x_1}^{x_2} \int_{y_1}^{y_2} \left((N - hv) \cdot m_1^2 - 2(N - hv)Mm_1 + (M \cdot m_1)^2 - (N - M) \cdot m_1^2 \right) dx dy \\
 &= \lim_{h \rightarrow 0} \frac{1}{h} \int_{x_1}^{x_2} \int_{y_1}^{y_2} \left(N^2 - 2N hv - h^2 v^2 \right) \cdot m_1^2 - 2NMm_1 - 2hvMm_1 + M^2 \cdot m_1^2 \\
 &\quad - (N^2 \cdot m_1^2 - 2NM + M^2 \cdot m_1^2) dx dy \\
 &= \lim_{h \rightarrow 0} \frac{1}{h} \int_{x_1}^{x_2} \int_{y_1}^{y_2} h(-2Nv - hv^2) \cdot m_1^2 - 2vMm_1 dx dy
 \end{aligned}$$

Using the Dominated Convergence theorem, it is possible to move the limit inside the integral.

$$\frac{\partial W}{\partial Y} = \int_{x_1}^{x_2} \int_{y_1}^{y_2} \lim_{h \rightarrow 0} \left(\left(-2 \frac{\nabla Y}{\|\nabla Y\|} \frac{\nabla v}{\|\nabla v\|} - h \left(\frac{\nabla v}{\|\nabla v\|} \right)^2 \right) \cdot \nabla Cb^2 - 2 \frac{\nabla v}{\|\nabla v\|} \frac{\nabla Cb}{\|\nabla Cb\|} \cdot \nabla Cb \right) dx dy$$

Where $h \rightarrow 0$ in the limitation, then

$$\frac{\partial W}{\partial Y} = \int_{x_1}^{x_2} \int_{y_1}^{y_2} -2 \frac{\nabla Y}{\|\nabla Y\|} \frac{\nabla v}{\|\nabla v\|} \cdot \nabla Cb^2 - 2 \frac{\nabla v}{\|\nabla v\|} \frac{\nabla Cb}{\|\nabla Cb\|} \cdot \nabla Cb dx dy \quad (3.13a)$$

The same steps are followed to the derivative for Cb:

$$\frac{\partial W}{\partial Cb} = \int_{x_1}^{x_2} \int_{y_1}^{y_2} 2 \frac{\nabla Y}{\|\nabla Y\|} \frac{\nabla v}{\|\nabla v\|} \cdot \nabla Cb^2 - 2 \nabla Y \cdot \frac{\nabla Y}{\|\nabla Y\|} \frac{\nabla v}{\|\nabla v\|} + 4 \frac{\nabla v}{\|\nabla v\|} \frac{\nabla Cb}{\|\nabla Cb\|} \cdot \nabla Cb dx dy \quad (3.13b)$$

Where $\frac{\partial I}{\partial W} = \frac{\partial W}{\partial Y} + \frac{\partial W}{\partial Cb}$, equations (3.13a) and (3.13b) are substituted in equation (3.13):

$$\begin{aligned}
 \frac{\partial I}{\partial W} &= \int_{x_1}^{x_2} \int_{y_1}^{y_2} -2 \frac{\nabla Y}{\|\nabla Y\|} \frac{\nabla v}{\|\nabla v\|} \cdot \nabla Cb^2 - 2 \frac{\nabla v}{\|\nabla v\|} \frac{\nabla Cb}{\|\nabla Cb\|} \cdot \nabla Cb dx dy \\
 &\quad + \int_{x_1}^{x_2} \int_{y_1}^{y_2} 2 \frac{\nabla Y}{\|\nabla Y\|} \frac{\nabla v}{\|\nabla v\|} \cdot \nabla Cb^2 - 2 \nabla Y \cdot \frac{\nabla Y}{\|\nabla Y\|} \frac{\nabla v}{\|\nabla v\|} + 4 \frac{\nabla v}{\|\nabla v\|} \frac{\nabla Cb}{\|\nabla Cb\|} \cdot \nabla Cb dx dy
 \end{aligned}$$

This long expression can be simplified as follows:

$$\frac{\partial I}{\partial W} = \int_{x_1}^{x_2} \int_{y_1}^{y_2} 2 \frac{\nabla v}{\|\nabla v\|} \frac{\nabla Cb}{\|\nabla Cb\|} \cdot \nabla Cb - 2 \nabla Y \cdot \frac{\nabla Y}{\|\nabla Y\|} \frac{\nabla v}{\|\nabla v\|} dx dy \quad (3.14)$$

Applying integration by parts twice to equation (3.14) leads to the partial differential equation,

$$\nabla \cdot \left(\frac{\nabla Cb}{\|\nabla Cb\|} \right) = \nabla \cdot \left(\frac{\nabla Y}{\|\nabla Y\|} \right).$$

i.e. equation (3.10), and the proof is complete.

Numerical Solution of Equation (3.10). Equation (3.10) is a nonlinear elliptic equation with Dirichlet boundary conditions. Therefore, equations (3.9) and (3.10) can be solved very efficiently by a number of well-developed curvature formula solvers (Osher & Sethian 1988), (Lai et al. 2009) and (Ibraheem et al. 2012). In Cartesian space, equation (3.10) can be written as

$$\nabla \cdot \left(\frac{\nabla Cb}{\|\nabla Cb\|} \right) = \mathcal{F} \quad (3.15)$$

Where,

$$\mathcal{F}(x, y) = \nabla \cdot \left(\frac{\nabla Y}{\|\nabla Y\|} \right) = \frac{Y_{xx}Y_y^2 - 2Y_xY_yY_{xy} + Y_{yy}Y_x^2}{(Y_x^2 + Y_y^2)^{\frac{3}{2}}}$$

A fixed point finite differences scheme has been used to solve equation (3.15). A discrete form of equation (3.15) is:

$$\begin{aligned} & \frac{1}{h} \Delta^x \left[\frac{1}{\sqrt{\epsilon^2 + \left(\frac{\Delta_+^x Cb_{i,j}}{h}\right)^2 + \left(\frac{\Delta_0^y Cb_{i,j}}{h}\right)^2}} \frac{\Delta_+^x Cb_{i,j}}{h} \right] + \frac{1}{h} \Delta^y \left[\frac{1}{\sqrt{\epsilon^2 + \left(\frac{\Delta_0^x Cb_{i,j}}{h}\right)^2 + \left(\frac{\Delta_+^y Cb_{i,j}}{h}\right)^2}} \frac{\Delta_+^y Cb_{i,j}}{h} \right] = g_{i,j} \\ \Rightarrow & \frac{1}{h^2} \frac{Cb_{i+1,j} - Cb_{i,j}}{\sqrt{\epsilon^2 + \left(\frac{Cb_{i+1,j} - Cb_{i,j}}{h}\right)^2 + \left(\frac{Cb_{i,j+1} - Cb_{i,j-1}}{2h}\right)^2}} - \frac{1}{h^2} \frac{Cb_{i,j} - Cb_{i-1,j}}{\sqrt{\epsilon^2 + \left(\frac{Cb_{i,j} - Cb_{i-1,j}}{h}\right)^2 + \left(\frac{Cb_{i-1,j+1} - Cb_{i-1,j-1}}{2h}\right)^2}} + \\ & \frac{1}{h^2} \frac{Cb_{i,j+1} - Cb_{i,j}}{\sqrt{\epsilon^2 + \left(\frac{Cb_{i+1,j} - Cb_{i-1,j}}{2h}\right)^2 + \left(\frac{Cb_{i,j+1} - Cb_{i,j}}{h}\right)^2}} - \frac{1}{h^2} \frac{Cb_{i,j} - Cb_{i,j-1}}{\sqrt{\epsilon^2 + \left(\frac{Cb_{i+1,j-1} - Cb_{i-1,j-1}}{2h}\right)^2 + \left(\frac{Cb_{i,j} - Cb_{i,j-1}}{h}\right)^2}} = g_{i,j} \quad (3.16) \end{aligned}$$

Where the above notations are:

$$\begin{aligned} Cb_{i,j} &= Cb(x_i, y_j), g_{i,j} = g(x_i, y_j), \Delta_{\pm}^x Cb_{i,j} = \pm(Cb_{i+1,j} - Cb_{i,j}), \Delta_{\pm}^y Cb_{i,j} \\ &= \pm(Cb_{i,j+1} - Cb_{i,j}) \end{aligned}$$

A fixed-point Gauss-Seidel iterative method for the equation (3.16), and so the following linearized equation is introduced:

$$\begin{aligned} & \frac{1}{h^2} \frac{Cb_{i+1,j}^n - Cb_{i,j}^{n+1}}{\sqrt{\epsilon^2 + \left(\frac{Cb_{i+1,j}^n - Cb_{i,j}^n}{h}\right)^2 + \left(\frac{Cb_{i,j+1}^n - Cb_{i,j-1}^n}{2h}\right)^2}} - \frac{1}{h^2} \frac{Cb_{i,j}^{n+1} - Cb_{i-1,j}^n}{\sqrt{\epsilon^2 + \left(\frac{Cb_{i,j}^n - Cb_{i-1,j}^n}{h}\right)^2 + \left(\frac{Cb_{i-1,j+1}^n - Cb_{i-1,j-1}^n}{2h}\right)^2}} \\ & + \frac{1}{h^2} \frac{Cb_{i,j+1}^n - Cb_{i,j}^{n+1}}{\sqrt{\epsilon^2 + \left(\frac{Cb_{i+1,j}^n - Cb_{i-1,j}^n}{2h}\right)^2 + \left(\frac{Cb_{i,j+1}^n - Cb_{i,j}^n}{h}\right)^2}} \\ & - \frac{1}{h^2} \frac{Cb_{i,j}^{n+1} - Cb_{i,j-1}^n}{\sqrt{\epsilon^2 + \left(\frac{Cb_{i+1,j-1}^n - Cb_{i-1,j-1}^n}{2h}\right)^2 + \left(\frac{Cb_{i,j}^n - Cb_{i,j-1}^n}{h}\right)^2}} = g_{i,j} \end{aligned}$$

And solving for $Cb_{i,j}^{n+1}$, we obtain:

$$\begin{aligned} Cb_{i,j}^{n+1} &= \left(\frac{1}{\frac{1}{h^2}(c_1 + c_2 + c_3 + c_4)} \right) \cdot \left[g_{i,j} + \frac{1}{h^2} (c_1 Cb_{i+1,j}^n + c_2 Cb_{i-1,j}^n + c_3 Cb_{i,j+1}^n \right. \\ & \left. + c_4 Cb_{i,j-1}^n) \right] \quad (3.17) \end{aligned}$$

Where the introduced notations are:

$$c_1 = \frac{1}{\sqrt{\epsilon^2 + \left(\frac{Cb_{i+1,j}^n - Cb_{i,j}^n}{h}\right)^2 + \left(\frac{Cb_{i,j+1}^n - Cb_{i,j-1}^n}{2h}\right)^2}}, c_2 = \frac{1}{\sqrt{\epsilon^2 + \left(\frac{Cb_{i,j}^n - Cb_{i-1,j}^n}{h}\right)^2 + \left(\frac{Cb_{i-1,j+1}^n - Cb_{i-1,j-1}^n}{2h}\right)^2}}$$

$$c_3 = \frac{1}{\sqrt{\epsilon^2 + \left(\frac{Cb_{i+1,j}^n - Cb_{i-1,j}^n}{2h}\right)^2 + \left(\frac{Cb_{i,j+1}^n - Cb_{i,j}^n}{h}\right)^2}}, c_4$$

$$= \frac{Cb_{i,j}^{n+1} - Cb_{i,j-1}^n}{\sqrt{\epsilon^2 + \left(\frac{Cb_{i+1,j-1}^n - Cb_{i-1,j-1}^n}{2h}\right)^2 + \left(\frac{Cb_{i,j}^n - Cb_{i,j-1}^n}{h}\right)^2}}$$

The boundary condition can be implemented in the following way:

$$Cb_{0,j}^n = Cb_{1,j}^n, Cb_{M,j}^n = Cb_{M-1,j}^n, Cb_{i,0}^n = Cb_{i,1}^n, Cb_{i,N}^n = Cb_{i,N-1}^n \text{ and } Cb_{0,0}^n = Cb_{1,1}^n, Cb_{0,N}^n = Cb_{1,N-1}^n, Cb_{M,0}^n = Cb_{M-1,1}^n, Cb_{M,N}^n = Cb_{M-1,N-1}^n.$$

Where, $1 \leq i \leq M - 1, 1 \leq j \leq N - 1$, and (M, N) is the size of the image.

The numerical solution of equation (3.17) with Dirichlet boundary conditions can be used to add colour to the missing-colour region in an image.

Equation (3.10) is once again solved using standard efficient numerical implementations (Peiyong Chen & Yuandi Wang 2008), and (Lai et al. 2009). The numerical solution of equation (3.10) that we have found represents the colour of the region of the interest in the Cb channel. The same procedure is followed to find the numerical solution of the Cr channel.

3.4.2.2 Minimisation of the Laplacian in Colour Channels

The second formula proposed is based on the Laplacian operator in coloured channels. In this case, the variational formula becomes

$$\min_{Cb} \int_{\Omega} \rho(|\Delta Y - \Delta Cb|) d\Omega, \quad (3.18)$$

The nonlinear 4th order PDE achieved by applying Euler-Lagrange equation with a Fréchet derivative of Laplacian minimisation formula (Peiyong Chen & Yuandi Wang 2008) is (for an L^2 norm):

Proposition 3.4: Given a YCbCr colour image f , then in any sub-image of f :

$$\frac{\partial^4 Cb}{\partial x^4} + \left(\frac{\partial^2 Cb}{\partial x \partial y}\right)_{yx} + \left(\frac{\partial^2 Cb}{\partial y \partial x}\right)_{xy} + \frac{\partial^4 Cb}{\partial y^4} = \frac{\partial^4 Y}{\partial x^4} + \left(\frac{\partial^2 Y}{\partial x \partial y}\right)_{yx} + \left(\frac{\partial^2 Y}{\partial y \partial x}\right)_{xy} + \frac{\partial^4 Y}{\partial y^4} \quad (3.19)$$

Proof:

Equation (3.19) is a nonlinear 4th order PDE; this equation can write as follows:

$$\frac{\partial^4 Cb}{\partial x^4} + \left(\frac{\partial^2 Cb}{\partial x \partial y}\right)_{yx} + \left(\frac{\partial^2 Cb}{\partial y \partial x}\right)_{xy} + \frac{\partial^4 Cb}{\partial y^4} = \mathcal{F} \quad (3.20)$$

Chapter 3: Colourising Greyscale Images Based on PDE Algorithms

Now, we will explain how we obtained equation (3.20) from equation (3.18) by using the Euler-Lagrange equation. Firstly, equation (3.18) can be rewritten as follows:

$$I(W) = \min_{Cb} \int_{\Omega} \|\Delta W\|^2 d\Omega, \text{ where } W = Y - Cb$$

Now, this notation is used

$$\begin{aligned} \|\Delta W\|^2 &= \Delta W \cdot \Delta W = \left(\frac{\partial^2 W}{\partial x^2} + \frac{\partial^2 W}{\partial y^2} \right) \cdot \left(\frac{\partial^2 W}{\partial x^2} + \frac{\partial^2 W}{\partial y^2} \right) \\ &= \left(\frac{\partial^2 W}{\partial x^2} \right)^2 + \left(\frac{\partial^2 W}{\partial x \partial y} \right)^2 + \left(\frac{\partial^2 W}{\partial y \partial x} \right)^2 + \left(\frac{\partial^2 W}{\partial y^2} \right)^2, \end{aligned}$$

So that, to find the corresponding Euler- Lagrange equation for the following functional

$$I(W) = \min_{Cb} \int_{x_1}^{x_2} \int_{y_1}^{y_2} \left[\left| \frac{\partial^2 W}{\partial x^2} \right|^2 + \left| \frac{\partial^2 W}{\partial x \partial y} \right|^2 + \left| \frac{\partial^2 W}{\partial y \partial x} \right|^2 + \left| \frac{\partial^2 W}{\partial y^2} \right|^2 \right] dx dy, \quad (3.21)$$

then the derivative $\frac{\partial I}{\partial W}$ of the equation (3.21) are calculated and then set equal to zero.

By using the definition of the derivative:

$$\begin{aligned} 0 &= \frac{\partial I}{\partial W} \cdot v = \lim_{h \rightarrow 0} \frac{I(W + hv) - I(W)}{h} \\ \frac{\partial I}{\partial W} \cdot v &= \lim_{h \rightarrow 0} \frac{1}{h} \int_{x_1}^{x_2} \int_{y_1}^{y_2} \left(\left(\left| \frac{\partial^2 W}{\partial x^2} + h \frac{\partial^2 v}{\partial x^2} \right|^2 + \left| \frac{\partial^2 W}{\partial x \partial y} + h \frac{\partial^2 v}{\partial x \partial y} \right|^2 + \left| \frac{\partial^2 W}{\partial y \partial x} + h \frac{\partial^2 v}{\partial y \partial x} \right|^2 \right. \right. \\ &\quad \left. \left. + \left| \frac{\partial^2 W}{\partial y^2} + h \frac{\partial^2 v}{\partial y^2} \right|^2 \right) - \left(\left| \frac{\partial^2 W}{\partial x^2} \right|^2 + \left| \frac{\partial^2 W}{\partial x \partial y} \right|^2 + \left| \frac{\partial^2 W}{\partial y \partial x} \right|^2 + \left| \frac{\partial^2 W}{\partial y^2} \right|^2 \right) \right) dx dy \quad (3.22) \end{aligned}$$

The difference between the two terms will simplify to:

$$\begin{aligned} &\left(\left(\left| \frac{\partial^2 W}{\partial x^2} + h \frac{\partial^2 v}{\partial x^2} \right|^2 + \left| \frac{\partial^2 W}{\partial x \partial y} + h \frac{\partial^2 v}{\partial x \partial y} \right|^2 + \left| \frac{\partial^2 W}{\partial y \partial x} + h \frac{\partial^2 v}{\partial y \partial x} \right|^2 + \left| \frac{\partial^2 W}{\partial y^2} + h \frac{\partial^2 v}{\partial y^2} \right|^2 \right) \right. \\ &\quad \left. - \left(\left| \frac{\partial^2 W}{\partial x^2} \right|^2 + \left| \frac{\partial^2 W}{\partial x \partial y} \right|^2 + \left| \frac{\partial^2 W}{\partial y \partial x} \right|^2 + \left| \frac{\partial^2 W}{\partial y^2} \right|^2 \right) \right) \\ &= h \left(2 \frac{\partial^2 W}{\partial x^2} \frac{\partial^2 v}{\partial x^2} + h \left(\frac{\partial^2 v}{\partial x^2} \right)^2 + 2 \frac{\partial^2 W}{\partial x \partial y} \frac{\partial^2 v}{\partial x \partial y} + h \left(\frac{\partial^2 v}{\partial x \partial y} \right)^2 + 2 \frac{\partial^2 W}{\partial y \partial x} \frac{\partial^2 v}{\partial y \partial x} + h \left(\frac{\partial^2 v}{\partial y \partial x} \right)^2 \right. \\ &\quad \left. + 2 \frac{\partial^2 W}{\partial y^2} \frac{\partial^2 v}{\partial y^2} + h \left(\frac{\partial^2 v}{\partial y^2} \right)^2 \right) \quad (3.23) \end{aligned}$$

Using the Dominated Convergence theorem, it is possible to move the limit inside the integral.

$$\begin{aligned} \frac{\partial I}{\partial W} \cdot v &= \int_{x_1}^{x_2} \int_{y_1}^{y_2} \lim_{h \rightarrow 0} \left(2 \frac{\partial^2 W}{\partial x^2} \frac{\partial^2 v}{\partial x^2} + h \left(\frac{\partial^2 v}{\partial x^2} \right)^2 + 2 \frac{\partial^2 W}{\partial x \partial y} \frac{\partial^2 v}{\partial x \partial y} + h \left(\frac{\partial^2 v}{\partial x \partial y} \right)^2 \right. \\ &\quad \left. + 2 \frac{\partial^2 W}{\partial y \partial x} \frac{\partial^2 v}{\partial y \partial x} + h \left(\frac{\partial^2 v}{\partial y \partial x} \right)^2 + 2 \frac{\partial^2 W}{\partial y^2} \frac{\partial^2 v}{\partial y^2} + h \left(\frac{\partial^2 v}{\partial y^2} \right)^2 \right) dx dy \quad (3.24) \end{aligned}$$

Where $h \rightarrow 0$ in the limitation, then

$$\begin{aligned} \frac{\partial I}{\partial W} \cdot v &= \int_{x_1}^{x_2} \int_{y_1}^{y_2} \left(2 \frac{\partial^2 W}{\partial x^2} \frac{\partial^2 v}{\partial x^2} \right. \\ &+ 2 \frac{\partial^2 W}{\partial x \partial y} \frac{\partial^2 v}{\partial x \partial y} + 2 \frac{\partial^2 W}{\partial y \partial x} \frac{\partial^2 v}{\partial y \partial x} + \left. 2 \frac{\partial^2 W}{\partial y^2} \frac{\partial^2 v}{\partial y^2} \right) dx dy \end{aligned} \quad (3.25)$$

By using integration by parts twice for the equation (3.25), the following partial differential equation is produced:

$$2 \left(\frac{\partial^2 W}{\partial x^2} \right)_{xx} + 2 \left(\frac{\partial^2 W}{\partial x \partial y} \right)_{yx} + 2 \left(\frac{\partial^2 W}{\partial y \partial x} \right)_{xy} + 2 \left(\frac{\partial^2 W}{\partial y^2} \right)_{yy} = 0 \quad (3.26)$$

where $W = Y - Cb$, then

$$\begin{aligned} \left(\frac{\partial^2 Cb}{\partial x^2} \right)_{xx} + \left(\frac{\partial^2 Cb}{\partial x \partial y} \right)_{yx} + \left(\frac{\partial^2 Cb}{\partial y \partial x} \right)_{xy} + \left(\frac{\partial^2 Cb}{\partial y^2} \right)_{yy} \\ = \left(\frac{\partial^2 Y}{\partial x^2} \right)_{xx} + \left(\frac{\partial^2 Y}{\partial x \partial y} \right)_{yx} + \left(\frac{\partial^2 Y}{\partial y \partial x} \right)_{xy} + \left(\frac{\partial^2 Y}{\partial y^2} \right)_{yy} \end{aligned} \quad (3.27)$$

Similarly, one can prove that

$$\begin{aligned} \left(\frac{\partial^2 Cr}{\partial x^2} \right)_{xx} + \left(\frac{\partial^2 Cr}{\partial x \partial y} \right)_{yx} + \left(\frac{\partial^2 Cr}{\partial y \partial x} \right)_{xy} + \left(\frac{\partial^2 Cr}{\partial y^2} \right)_{yy} \\ = \left(\frac{\partial^2 Y}{\partial x^2} \right)_{xx} + \left(\frac{\partial^2 Y}{\partial x \partial y} \right)_{yx} + \left(\frac{\partial^2 Y}{\partial y \partial x} \right)_{xy} + \left(\frac{\partial^2 Y}{\partial y^2} \right)_{yy} \end{aligned} \quad (3.28)$$

While in an L^1 norm, the Euler Lagrange equation of (3.18) by followed the same previous steps which that used to find the Euler Lagrange equation in an L^2 norm.

$$\begin{aligned} \left(\frac{Cb_{xx}}{\sqrt{|\Delta Cb|^2}} \right)_{xx} + \left(\frac{Cb_{yx}}{\sqrt{|\Delta Cb|^2}} \right)_{xy} + \left(\frac{Cb_{xy}}{\sqrt{|\Delta Cb|^2}} \right)_{yx} + \left(\frac{Cb_{yy}}{\sqrt{|\Delta Cb|^2}} \right)_{yy} \\ = \left(\frac{Y_{xx}}{\sqrt{|\Delta Y|^2}} \right)_{xx} + \left(\frac{Y_{yx}}{\sqrt{|\Delta Y|^2}} \right)_{xy} + \left(\frac{Y_{xy}}{\sqrt{|\Delta Y|^2}} \right)_{yx} + \left(\frac{Y_{yy}}{\sqrt{|\Delta Y|^2}} \right)_{yy} \end{aligned}$$

Numerical Solution of Equation (3.19).

The same procedure as described in the Poisson formula is followed. The explicit time marching scheme has been used to solve equation (3.27). We now detail the spatial discretisation,

$$\begin{aligned} [Cb_{xx}(Cb_{xx}(u_{i,j})) + Cb_{xy}(Cb_{yx}(u_{i,j})) + Cb_{yx}(Cb_{xy}(u_{i,j})) + Cb_{yy}(Cb_{yy}(u_{i,j}))] \\ = g(i,j) \end{aligned} \quad (3.29)$$

Where $Cb_{xx}(u_{i,j}) = u_{i+1,j} + u_{i-1,j} - 2u_{i,j}$, $Cb_{yy}(u_{i,j}) = u_{i,j+1} + u_{i,j-1} - 2u_{i,j}$

$Cb_{xy}(u_{i,j}) = u_{i+1,j} - u_{i,j} - u_{i+1,j-1} + u_{i,j-1}$, and $Cb_{yx}(u_{i,j}) = u_{i,j+1} - u_{i,j} - u_{i-1,j} + u_{i-1,j-1}$,

and the upwind finite difference scheme of Osher and Sethian (Osher & Sethian 1988), with Neumann boundary conditions is used. For more details about the numerical solution of the equation of (3.29) with boundary condition (3.18), see (Peiying Chen & Yuandi Wang 2008) and (Osher & Sethian 1988). The numerical solution of equations

(3.19) that adds information to the region of the interest in the Cb channel. The same procedure is followed to find the numerical solution for the Cr channel. The below Figure 3-6 shows the performance of both proposed methods when dealing with different quantity textures in the missing area.

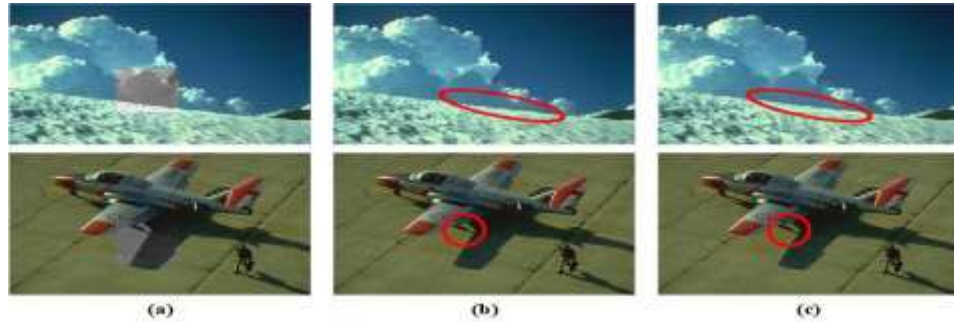


Figure 3-6: PDE colourisation algorithms. Column (a) masked colour image, column (b) and (c) colourised images using curvature and 4th order PDE methods, respectively.

3.4.2.3 Summary of the above colourisation algorithms

After the numerical solutions for Cb and Cr channels have been found, they are merged with channel Y, and leads to a YCbCr image. The conversion of YCbCr to RGB displays the colours that added to the region of interest. Also, these proposed formulas are applied on eight colours spaces which are YCbCr, YUV, NTSC, HIS, HSV, CMY, RGB, and XYZ in both spatial and frequency domains. The above algorithm is shown simplified in Figure 3-7.

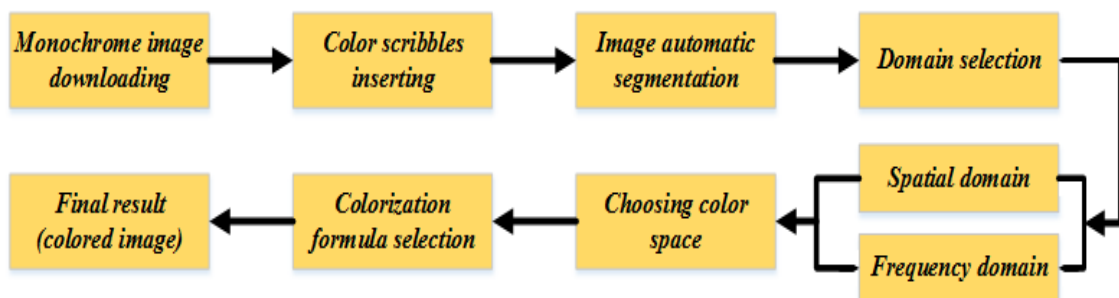


Figure 3-7: Flowchart of an algorithm for inpainting the colours

In the following section, the standard quality measures are introduced to check the quality of colourisation results, and this allows for comparison between the results of our algorithms with different existing colourisation methods.

3.5 Experimental Results

In this section, the results of the proposed algorithm are presented and compared with the results obtained from (Sapiro 2005). As mentioned in section 3.4.2, the aim was to

Chapter 3: Colourising Greyscale Images Based on PDE Algorithms

introduce two methods for adding colours into the greyscale images. The proposed approach has implemented on two domains, spatial domain and Frequency domain tested on 8 colour spaces. The colours are added to the images in two cases, the first case where the colour is partially missing from the certain region where the other regions of the image are already coloured. The second case the image is in greyscale and we try to add the colours to the different objects of the image.

In the first case, the proposed algorithms are applied to add colouration based on the colour information on the border of the un-coloured region. Figure 3-8 illustrates adding the colour to the un-coloured region which contains information about structure and texture, the numerical solution of equations 3.5, 3.17, and 3.28 above with boundary condition managed to add the colour, the results were visually acceptable, and still there is problem with edges of missing colour region. However, there is the un-noticeable difference on the edges of the recovered area, based on the PDE order (the higher, the better) as shown in Figure 3-8d (indicated by the arrows).



Figure 3-8: Colourising missing colour regions. (a) Original image with missing colour region, (b), (c), and (d) colourised image by Poisson, curvature, and 4th order PDE methods, respectively.

In the second case, the curvature approach is used for adding the colour to the whole grayscale image, but this needs to add colour hints to the image as scrabbles, but this approach produces edge issue where the colours pass over the edges of a certain object and mix with the neighbouring objects in the image, see the third image in Figure 3-9.

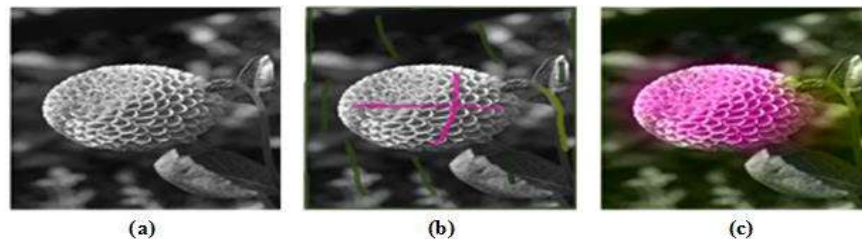


Figure 3-9: Colourising whole grayscale image. (a) Grayscale image, (b) grayscale image with added scrabbles, (c) colourised image using curvature model.

To solve this problem, the borders of objects within the image are determined by highlighting manually or using an automated object segmentation method (not

discussed in this chapter) and then adding colour scribbles (indicated by the arrows in the third image of Figure 3-9) to the image's objects to assess the colourisation algorithm. Our approach has been tested on two groups of images by using a large number of natural images. The first group of the images has not been segmented, and the second group is containing images which are already pre-segmented, where these images are obtained from the Berkeley database(Pablo Arbelaez 2007). In the next two sub-sections, the pros and cons of applying the proposed algorithm to non-segmented images and pre-segmented images respectively are discussed.

3.5.1 Using Non-Segmented Images

If the image is not segmented before colorisation, and we try to make the colouring more precise compared with to the added colour hints in Figure 3-9 above, more colour hints around the important objects are added that need to have more colour prissiness, see Figure 3-10, and if the algorithm is applied in the same way, as seen in Figure 3-9, the colours are distributed in a better way. However, this way of adding the colour hints is very time consuming and not recommended for mass image colouring.

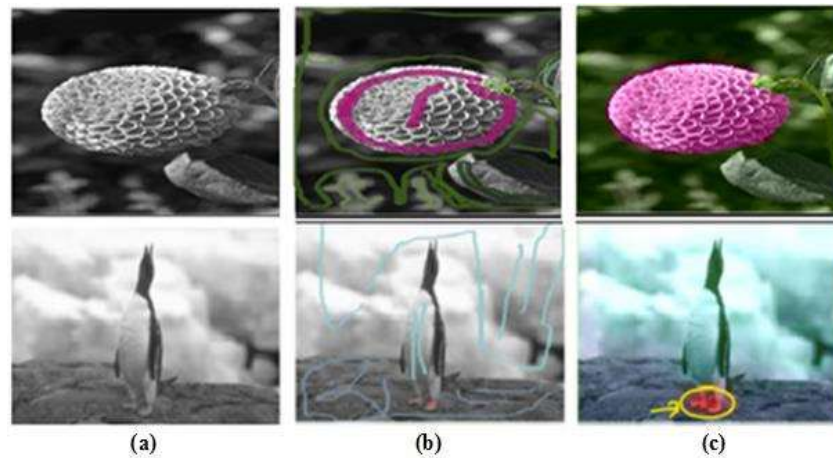


Figure 3-10: Adding colour to non-segmented images. (a) Grayscale image, (b) segmented image by colour scribbles, (c) colourised images using curvature model.

3.5.2 Using Pre-Segmented Images

To apply the image segmentation, many algorithms can be used to segment the image as seen in (Markle, Wilson 1988), and (Arbeláez et al. 2011), but this work uses pre-segmented images in(Deng Cai, Xiaofei He, Yuxiao Hu 2005). In this case, we need to label the segmented objects then apply our colourisation algorithm on each labelled object separately after adding the colour scribbles to these labelled objects, as it is shown in Figure 3-11.

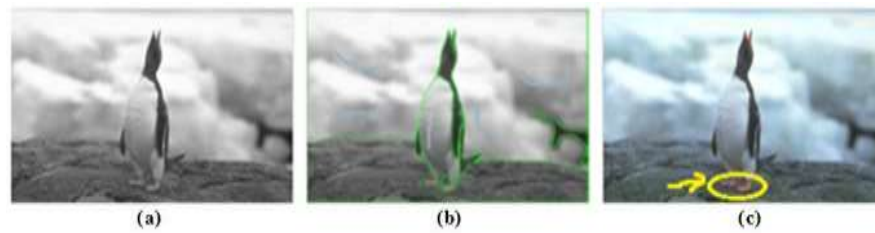


Figure 3-11: An image has segmented. (a) Grayscale image, (b) segmented image with colour scribbles, (c) colourised image using curvature method.

Therefore, Figure 3-11 is representing the result of our algorithm when applied on the segmented image; we found the result more controlling the propagation of the colours inside the border of image objects (see the difference between Figure 3-10 and 3-9). Figure 3-12 and 3-13 shows the results of our algorithm when it is applied to the same image on spatial and frequency domain (wavelet) respectively.

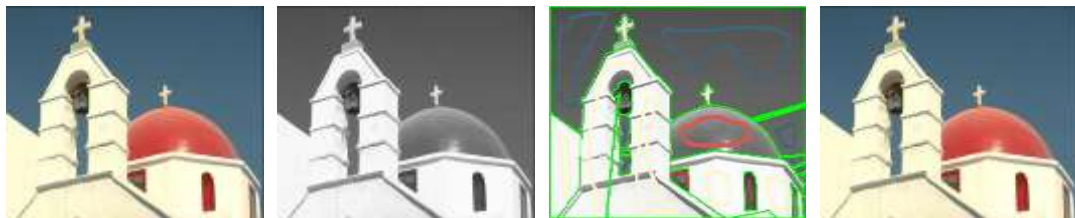


Figure 3-12: Colourising segmented image in the spatial domain. (a) Original colour image, (b) grayscale image, (c) segmented grayscale image with colour scribbles, (d) colourised image using 4th order PDE method.

Furthermore, the proposed algorithms were applied to the image which has used in Figure 3-12 on the frequency domain where the wavelet Haar filter (Chan et al. 2006) has been used to convert every channel in the grayscale image with colour scribbles added to 4 sub-bands image in the frequency domain. The proposed algorithm must run eight times for each image sub-band in the frequency domain. We noted that the colourised images in Figure 3-12 and 3-13 are visually almost identical to the original image. Also, this point is discussed in the next section. So, Figure 3-13 shows the use of the proposed algorithm in the frequency domain.

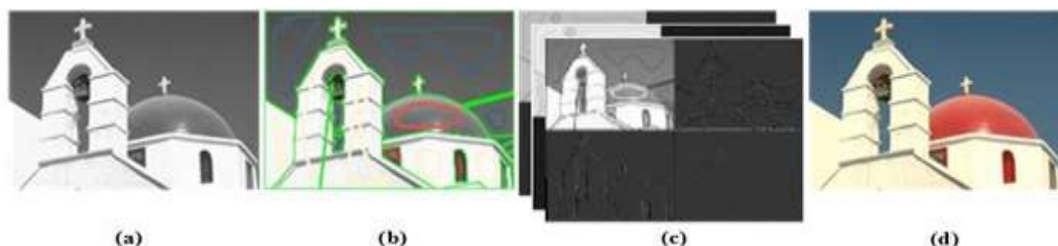


Figure 3-13: Colourising segmented image in frequency domain. (a) Grayscale image, (b) segmented grayscale image with colour scribbles, (c) grayscale image with colour scribbles to the frequency domain, (d) colourised image using 4th order PDE method.

Finally, for the sake of clarity, the proposed algorithm has been applied to several pre-segmented images to check its effectiveness.

Figure 3-14 presents some additional examples of greyscale images. The first column represents the input greyscale images and the second column shows the input images with the colour strokes that want to spread on them. The result of our algorithm is provided in the third column. Note that as in image inpainting, the original image is not available, and therefore every “reasonable” and the visually pleasant result should be considered acceptable.

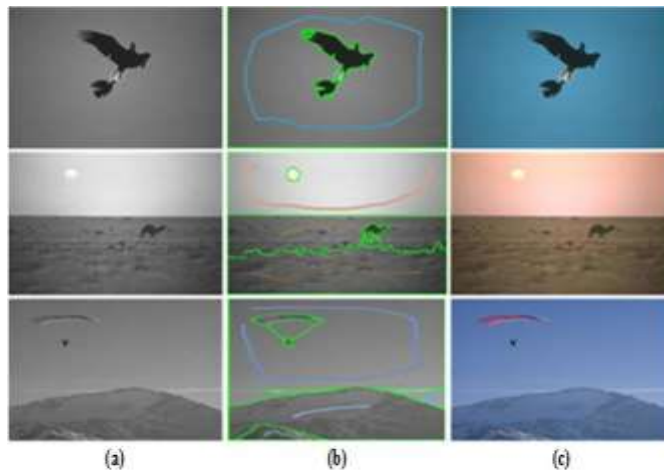


Figure 3-14: Examples of colourising grayscale images. (a) Greyscale images, (b) scribbled grayscale images, (c) colourised images by 4th order PDE method.

The next section presents the quality assessment of coloured images by using traditional statistical measurements.

3.6 Image Quality Assessments

This section describes the effectiveness of the proposed algorithms for adding colour to the greyscale image. The algorithms have been introduced in previous sections, and their results illustrated by visual examples. The quality evaluation of colourised image is carried out using standard quality measures as explained in section 2.6.1; these standard quality measures are used to check the quality our proposed algorithm and compare it with the algorithm in (Sapiro 2005). An accurate evaluation method which simultaneously assesses inpainted image qualitatively and quantitatively is not an easy task. Therefore, we depended on visual analysis to assess the qualitative tests. However, for quantitative evaluation, Peak Signal-to-Noise Ratio (PSNR), and Structural Similarity (SSIM) are computed, for more information about these measurements, (cf. Section 2.6.1). Also, there is another way to compare the colour images which is

Normalised Colour Distance (NCD). This measurement is focused on the distances between the colours in a given colour space (Russo 2014):

$$\text{NCD} = \frac{\sum_{m=1}^M \sum_{n=1}^N \sqrt{\sum_{q=1}^Q [O_q(m, n) - I(m, n)]^2}}{\sum_{m=1}^M \sum_{n=1}^N \sqrt{\sum_{q=1}^Q [O_q(m, n)]^2}} \quad (2.30)$$

The lower NCD, is the better the image quality. The NCD measurement is applied on the colourised images to evaluate the performance of colourisation methods and assess their colourised image quality results. The next subsection shows the natural images database.

3.6.1 Database Description

This subsection gives a brief description of a publicly available database; a natural image database that is used in our experiments to evaluate the suitability of the different PDE-based colourisation algorithms. Statistical measurement methods have been used to evaluate the efficacy of these PDE algorithms. The Berkeley segmentation dataset and Benchmark database in(Pablo Arbelaez 2007)which consists of 300 natural images of size 321×481, 25 for each of 12 individuals, this database is used for segmentation application in both grayscale and colour images. Figure3-15 illustrates examples of natural images from the Berkeley segmentation and Benchmark database.



Figure3-15: Example of eight out of 300 training natural images.

The purpose of using the Berkeley natural images database is that these images have different quantity of texture and structure in the image; and also, there are précised pre-segmented objects in the grayscale images of the database which helped to speed up applying PDE based colourisation methods on natural images with a reasonable accuracy. The original images of the Berkeley database were used as the reference by which to measure the quality of colourised images. The aim of these experiments is to study the effect of these methods on adding the colour to the simple structure missing colour regions in the natural images.

3.6.2 Experiment 1: Results of Berkeley Segmentation Database

We conducted experiments to measure and compare image quality in the colourised images concerning the original images in the spatial and frequency domain, using PSNR, SSIM and NCD quality measures. The test images were colourised using Poisson, curvature and 4th order PDE algorithms. The original images of the Berkeley database were used as the reference by which to measure the quality of colourised images. In this section, 80 different natural images are selected from this database which have different content images; the experiments have been applied on these images. The aim of these experiments is to study the effect of these algorithms on the colourisation of missing colour region in the natural images. In general, the missing colour region (damaged colour region) have been created in the images by removing the colour information in two channels and meanwhile left the other information (i.e. whole structure and texture) in the main channel. The next equation represents how we remove only the colours from the regions in the original images,

$$\begin{cases} f_{Damaged}(indx(K_1), indy(K_2), 1) = f_1(indx(K_1), indy(K_2)) \\ f_{Damaged}(indx(K_1), indy(K_2), 2) = f_1(indx(K_1), indy(K_2)) \\ f_{Damaged}(indx(K_1), indy(K_2), 3) = f_1(indx(K_1), indy(K_2)) \end{cases} \quad (3.31)$$

Where f is the original image, $f_{Damaged}$ is the original image with missing colour region f_1 is the channel one from the original image, and K_1 and K_2 represents the height and width of the missing colour region. Figure 3-16 represents a masked colour image in RGB space, the size of this miss colour region is 100×100 , then this mask has been applied to the database images to study the effect of colour propagation on different types of texture in the missing regions and to study the efficiency of these PDE methods. The PDE methods are applied on the masked green channel and masked blue channel separately based on the information in Red channel.

To apply this mask on other colour spaces, the original image convert to other colour spaces and then will apply the mask of missing colour region (i.e. formula 3-31), after that the PDE methods are used to recover the colour in this space then will back convert to RGB space to show the results, as see below in Figure 3-17. The PDE methods are applied on masked Cb channel and masked Cr channel separately based on the information in Y channel.



Figure 3-16: Masked colour natural image in the RGB colour space.

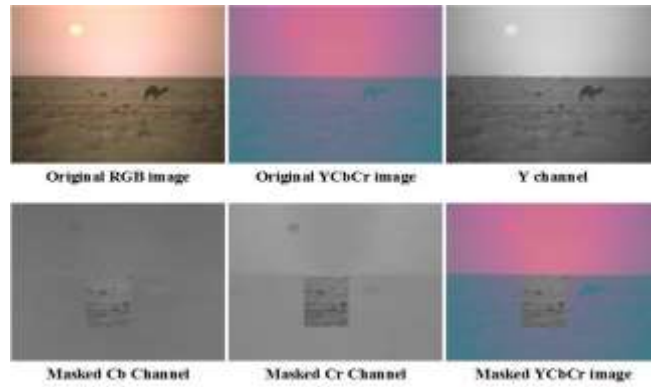


Figure 3-17: Masked colour natural image in the YCbCr colour space.

The Poisson, curvature, and 4th-order PDE algorithms have applied on 80 natural images to recover the missing colour block in eight colour spaces in both spatial and frequency domains. In these sets of experiments, the Haar wavelet transform is used to convert the image from spatial to the frequency domain (Chan et al. 2006).

Figure 3-18 shows examples of five out of 80 colourisation results of block missing colour in the natural images, where these examples selected from different colour spaces.

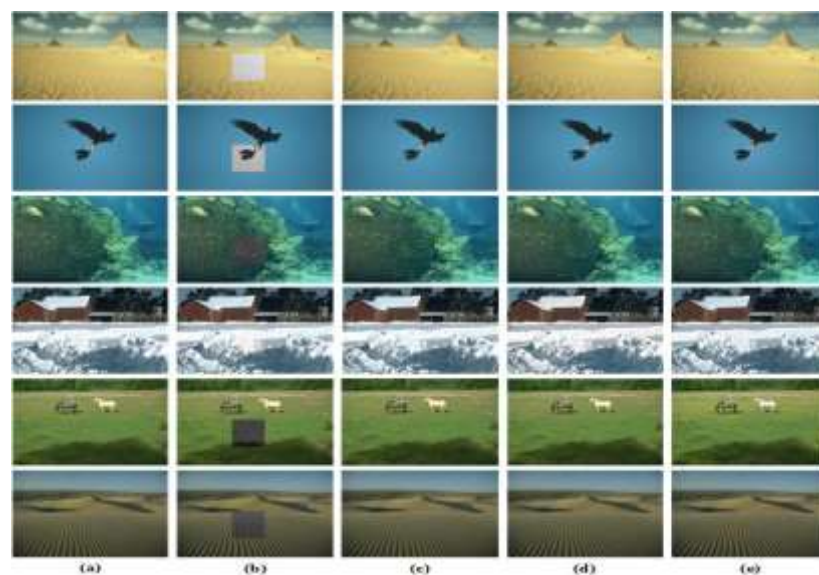


Figure 3-18: Examples of five out of 80 colourisation results of block missing colour in the natural images. (a) Original images, (b) masked colour images, (c), (d), and (e) colourised images using Poisson, curvature and 4th-order PDE colourisation algorithms, respectively.

Chapter 3: Colourising Greyscale Images Based on PDE Algorithms

As mentioned before, in Figure 3-18 these colourisation algorithms have been successfully recovered the colour in the block missing colour with smooth areas surrounding it, as seen in the first and second rows. However, these algorithms have been faced difficulties to recover block with high texture areas surrounding it (i.e. a lot of edges and corners with different colours), as seen in the 3rd, 4th and 5th rows. The results of these algorithms are as follows: the results of using 4th-order PDE algorithm are better than the results of the other two algorithms which show the effect of the order clearly. It follows by curvature and Poisson, respectively.

Now a comparison of the curvature and 4th-order PDE methods with Poisson method (Sapiro 2005) is presented. The difference in the results occurred while dealing with numerical methods. Therefore we will always end up with some errors due to truncation error and rounding off error of the mathematical model. PSNR, SSIM, and NCD have been calculated between the original image and the inpainted images in 8 different colour spaces in both Spatial and Frequency domains by Poisson, Curvature and 4th-order PDE methods. These methods applied to 80 natural images, the results are summarised below in Table 3-2 and 3-3.

Errors	Spatial Domain								
	Poisson method			Curvature method			4 th -order PDE method		
	PSNR	SSIM	NCD	PSNR	SSIM	NCD	PSNR	SSIM	NCD
RGB	20.13	0.891	0.395	26.21	0.928	0.293	29.76	0.936	0.291
CMY	17.54	0.814	0.375	19.54	0.874	0.372	30.99	0.914	0.296
YCbCr	24.82	0.906	0.299	24.91	0.813	0.395	39.88	0.964	0.128
YUV	29.5↑	0.93↑	0.20↓	41.7↑	0.96↑	0.12↓	42.5↑	0.97↑	0.11↓
HSI	26.21	0.929	0.245	28.37	0.939	0.242	31.85	0.938	0.255
HSV	26.88	0.927	0.248	29.39	0.939	0.248	29.96	0.931	0.257
NTSC	30.6↑	0.93↑	0.20↓	42.8↑	0.97↑	0.11↓	47.5↑	0.97↑	0.11↓
XYZ	27.82	0.928	0.248	30.58	0.939	0.263	30.99	0.92	0.279

Table 3-2: The average of PSNR, SSIM and NCD values from original and inpainted images in the spatial domain for 8 different colour spaces. Poisson, Curvature and 4th-order methods have been used to obtain these error values.

Errors Space Name	Frequency Domain								
	Poisson method			Curvature method			4 th -order PDE method		
	PSNR	SSIM	NCD	PSNR	SSIM	NCD	PSNR	SSIM	NCD
RGB	18.65	0.816	0.986	23.76	0.845	0.765	26.54	0.875	0.594
CMY	16.77	0.764	0.785	18.97	0.806	0.596	27.67	0.897	0.436
YCbCr	20.18	0.916	0.634	21.34	0.921	0.457	36.21	0.933	0.405
YUV	33.3↑	0.93↑	0.78↓	39.5↑	0.94↑	0.59↓	41.6↑	0.95↑	0.32↓
HSI	23.95	0.902	0.987	26.82	0.913	0.767	29.54	0.922	0.565
HSV	24.57	0.904	0.845	25.39	0.910	0.643	27.87	0.924	0.336
NTSC	29.8↑	0.94↑	0.57↓	40.6↑	0.94↑	0.35↓	44.7↑	0.95↑	0.23↓
XYZ	24.96	0.905	0.876	27.65	0.914	0.63	28.54	0.919	0.372

Table 3-3: The average of PSNR, SSIM and NCD values from original and inpainted images, in the frequency domain for 8 different colour spaces. Poisson, Curvature and 4th-order PDE methods have used to obtain these values.

3.6.3 Results Analysis

Table 3-2 and 3-3 illustrate the average values of PSNR, SSIM and NCD obtained from original and inpainted images, in both the spatial and frequency domains for 8 different colour spaces; these results have been obtained by Poisson, curvature, and 4th-order PDE methods. The values of PSNR, SSIM and NCD in spatial domain better than in the frequency domain for all colour spaces. YUV and NTSC are better than other colour spaces based on the values of PSNR, SSIM, and NCD. The components of the NTSC colour space are YIQ, ‘Y’ (the luminance component), ‘I’ (the cyan-orange component), and ‘Q’ (the green-purple component), where I and Q represent a chrominance component in the image. NTSC has a property of complete separation between the luminance and the chrominance information (Ibraheem et al. 2012) and (Yao_Wang, Jörn. Ostermann 2001). This separation explains the good performance for NTSC space in the colouring inpainting.

While in YUV colour space, YUV encoding used in some digital video based on MPEG compression. Where, the YUV model defines a colour space in terms of one luminance (Y) and two chrominance (UV) components. The luminance (Y) and two chrominance (UV) was semi-separated because the colour information (U and V) are added separately via a sub-carrier so that a black-and-white receiver would still be able to receive and display a colour picture transmission in the receiver's native black-and-white format (Ibraheem et al. 2012) and(Yao_Wang, Jörn. Ostermann 2001). NTSC and YUV better than other colour space in the colourisation process because the luminance and chrominance information are not well separated in other colour spaces.

Also, the proposed algorithm is faster when it is applied on the non-segmented image, whereas for pre-segmented image consumes relatively long time because the algorithm has to run for each object (i.e. segment) of the image. The results of a spatial domain are better than the results in Frequency domain for all PDE methods because it is clear that, these methods are worked eight times in each image which accumulates more numerical computation errors, thus will produce more error and consuming time in the Frequency domain. Therefore, the 4th-order PDE method is better than of other methods for all colour space in spatial and frequency domain based on the values of PSNR, SSIM, and NCD. “PDE property”. Finally, the results used in (Sapiro 2005) were not that promising whereas our technique achieved better results.

In the following sections, the results of our proposed algorithm with three colourisation methods by using the standard quality measures are compared for a number of examples. Subsequently, examples of important applications of semi-automatic colourisation are also illustrated.

3.6.4 Experiment 2: Examples of Semi-Automatic Image Colourisation Algorithms

Semi-automatic colourisation has several important applications such as old black and white photographic images, biomedical imaging, night vision colourisation, and astronomical image colourisation. Here, Figure 3-19 presents some sample results that obtained with the four aforementioned algorithms: isoline-based image colourisation (Popowicz & Smolka 2014), colourisation using optimisation (Levin et al. 2004), colourisation-based PDE (Sapiro 2005), and the proposed colourisation method. Although the methods differ from each other, we have to note that all the algorithms provide very realistic and high-quality colour images.

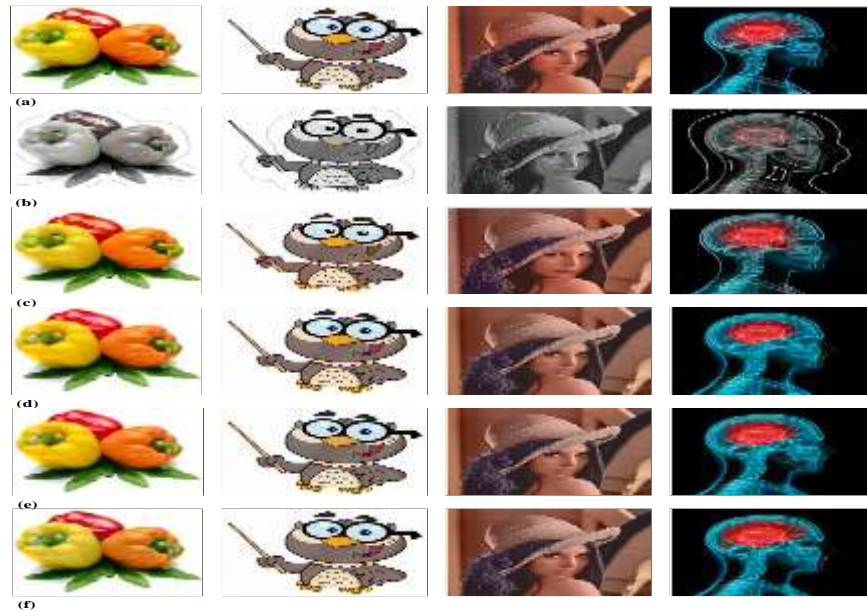


Figure 3-19: A comparison of colourisation quality achieved by different methods. Row (a) Original images, row (b) Scribbled grayscale images, rows (c) (d), (e), and (f) colourised images by Isoline algorithm (Popowicz & Smolka 2014), optimisation (Levin et al. 2004), PDE (Sapiro 2005), and the proposed colourisation methods.

In Figure 3-19, the colourised images are examined by using each quality measure which was introduced in section 2.6.1. A comparison of PDE colourisation technique with three techniques which introduced in (Levin et al. 2004), (Popowicz & Smolka 2014) and (Sapiro 2005) is presented. PSNR, SSIM, and NCD have been calculated between the original image and the inpainted images in RGB colour space in the spatial domain. These techniques applied to 40 natural images, the results are summarised below in Table 3-4.

Methods	Images in column 1			Images in column 2			Images in column 3			Images in column 4		
	PSNR	SSIM	NCD									
Method in (Popowicz & Smolka 2014)	23.77	0.886	0.146	26.06	0.922	0.119	32.14	0.946	0.372	27.96	0.898	0.135
Method in (Levin et al. 2004)	19.32	0.817	0.188	24.97	0.948	0.194	28.70	0.810	0.791	24.65	0.787	0.198
Method in (Sapiro 2005)	21.91	0.831	0.169	25.75	0.939	0.146	28.93	0.878	0.735	25.89	0.802	0.194
Our method	23.34	0.885	0.149	26.85	0.928	0.109	30.87	0.909	0.592	27.04	0.818	0.176

Table 3-4: Results of colourisation quality for all three algorithms, PSNR, SSIM, and NCD.

Moreover, Table 3-4 summarises the corresponding results of each quality measure for the results which are some of them presented in Figure 3-19; all four methods are assessed quantitatively. The results of the improved PDE technique is close enough to

the results obtained with the technique in (Popowicz & Smolka 2014), while, they are better than the results obtained by other methods (Levin et al. 2004) and (Sapiro 2005). The errors of the technique occur owing to numerical conditioning issues. Therefore we will always end up with some errors due to truncation error and rounding off errors in the implementation of the mathematical model.

3.7 Summary and Conclusion

In this chapter, a survey of grayscale image colourisation algorithms is introduced. Colourisation algorithms are divided into two groups, which are automatic and semi-automatic. The literature on these two colourisation groups' algorithms is reviewed. However, we are mainly interested in semi-automatic algorithms, as they seem to be more applicable. A PDE-based colourisation algorithm is presented, then an improved algorithm is proposed, in the outcomes of which the luminance channel represents the geometry of the whole (directional) colour image more faithfully than in the images obtained from the algorithm in (Sapiro 2005). Our colourisation algorithm has been compared with three semiautomatic colourisation algorithms which are given in (Levin et al. 2004), (Popowicz & Smolka 2014), and (Sapiro 2005). The algorithms referred to in this chapter differ, and they have one aim which is adding colour to grayscale image; however, all of them are able to provide high-quality outcomes. Finally, a methodology is provided for the assessment of colourisation results, based on several well-known statistical quality measures. The results of the improved colourisation-based PDE technique turn out to be better than those obtained using the techniques in (Levin et al. 2004), and (Sapiro 2005), while being close to those obtained using the technique in (Popowicz & Smolka 2014). The ideal colourisation results are also presented; they effectively and efficiently to meet most of the user's requirements in adding colour to the grayscale images in different applications such as biology, astronomy, medicine, and old images.

As mentioned before, a missing colour region is defined in RGB colour space, for two different cases. When the missing region has information in it, such as a "missing colour region" problem it is called colourisation problem, but when the missing region doesn't has information in it, it is an "inpainting" problem. Hence, there are several image inpainting algorithms that can be used to reconstruct missing regions, such as PDE based inpainting, exemplar-based inpainting, hybrid algorithms, and so on. The PDE inpainting algorithms are discussed in the next chapter.

Chapter 4 PDE BASED FULL INPAINTING METHODS

In Chapter 3, our investigations focused on restoring missing colour in an image region where texture information is available *via* one colour channel. The use of total variation minimisation has been shown to lead to different order Partial Differential Equation (PDE) models of colour restoration in those regions that are based on the numerical solutions of these PDEs. The aim of the investigation in this chapter is the restoration of information in a missing region where all channel information is missing.

Unsurprisingly, research over the years has shown that this full image inpainting problem can equally be solved by PDEs of different orders. Indeed, PDEs have repeatedly been shown to provide the natural model of diffusion, and the transport method was first used to describe and model the corresponding process. We shall refer to all of these methods as PDE-based Image Inpainting (PDE-BI) methods. These methods are implemented separately in all colour channels. In this chapter, the approaches taken in the last chapter are used to provide alternative efficient implementations of PDE-BI methods. The extensive comparison of the performances of higher and 2nd-order PDE-based inpainting methods is studied in terms of the qualities of inpainted images. The evaluation will not be confined to traditional statistical image quality measures but will also apply a recently developed image quality measure based on topological data analysis (TDA) scheme. Also, the efficacy of these PDE methods is checked based on the TDA scheme. The 2nd- and high-order PDE methods have been applied to reconstruct deliberately removed colour information from randomly chosen regions (to be counted as missing regions) in a large dataset of the face and natural images, in both spatial and frequency domains.

This chapter consists of seven sections, the first 4 of which give an overview of existing PDE-BI schemes with experimental work to test their performances. The proposed modification is described in the spatial domain (section 4.5) and in the frequency domain (section 4.6). The qualities of inpainted images assessed by statistical measures and the TDA approach s are presented in section 4.7. Lastly, section 4.8 presents a summary of the chapter with a list of challenges to be considered further.

4.1 General Concepts and Mathematics of PDE-BI Methods

Let $\Omega \subset \mathbb{R}^2$ denotes the entire image domain f . The basic idea then is to propagate information from the border of the missing region into it, in such a way that the border of the missing region is no longer visible to the human eye. The border of missing-region is ∂D ; Figure4-1 illustrates the inpainting based PDE steps.

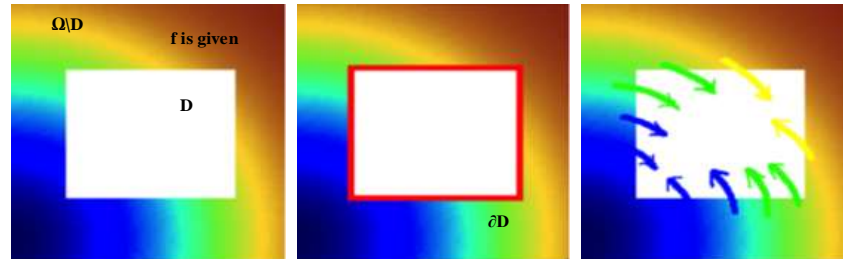


Figure4-1: Steps of inpainting based PDE method.

The missing areas represent sets of pixels, often referred to as holes, scratches, and opening objects or simply as the unknown areas. All inpainting methods, use information in the rest of the image to fill in the gaps. Mathematically, these methods have been classified as variational (Energy) methods and direct non-variation based PDE-BI methods. Variational methods compute the inpainted image as a minimiser of an objective functional. The Euler-Lagrange equation of minimisation of an objective functional produces a PDE, as described in the previous chapter. On the other hand, PDE-BI methods applied directly on images can be obtained from the use of rich and well-established mathematical approximation theory in bounded functions of 2-variables. All these methods, termed as PDE-BI methods, use diffusion to reconstruct missing regions and benefit from geometric characteristics of textured and smooth image areas.

4.1.1 Variational Methods

The variational methods can be best explained from the point of view of inverse problems. The goal is to restore/recover an original image u from the degraded image f . Inpainting-based variational methods can also be formulated within this framework. More precisely, let $\Omega \subset \mathbb{R}^2$ be an open and bounded domain, the given image f is defined over Ω , and the missing domain $D \subset \Omega$. In mathematical terms, this means to solve an inverse problem $T_u = f$, where T models the process through which the image u went before observation. For the sake of clarity, the well-known method of solving this problem and recovering digital image u is described. A general variational approach in

image inpainting is formulated as a minimisation problem defined by formula 4.1, below:

$$\min_{u \in \Omega} \|T_u - f\|_{\Omega}^2 \quad (4.1)$$

It is almost impossible to avoid the ill-posedness of the solutions of (4.1); especially when the operator T has an unbounded inverse. To overcome this issue, it is customary to use a regularisation approach that simply adds terms to represent smoothness-related properties such as total variation, (Mumford 1994). Such modifications (4.1) change the behaviour of the model to that of a regularised and well-posed model, as described here:

$$E(u) = \min_{u \in \Omega} \{ \alpha \mathcal{R}(x, u, Du, \dots, D^k u) + \lambda_0 \|T_u - f\|_{\Omega}^2 \}, \quad (4.2)$$

$$\lambda(x) = \begin{cases} \lambda_0 & \text{if } x \in \Omega \setminus D \\ 0 & \text{if } x \in D, \end{cases}$$

where $\alpha > 0$ and λ_0 are two regularisation/tuning parameters. The image of prior data term $\mathcal{R}(u)$ is known as a regularising term whereas $\|T_u - f\|_{\Omega}^2$ may be referred to as the fidelity term. The concept of the regularising term has been proposed in (Mumford 1994), and formula (4.2) plays the main role of filling the missing image domain D , e.g., by diffusion and/or transport.

Under certain regularity assumptions on a minimiser u of the functional operator E , the minimiser fulfils a so-called optimality condition on (4.2), i.e., the corresponding Euler-Lagrange equation. In other words, for a minimiser u the first variation, i.e., the Fréchet derivative of E , has to be zero. In mathematical terms, this reads

$$-\nabla \mathcal{R}(x, u, Du, \dots, D^k u) + \lambda_0 (T_u - f) = 0, \text{ in } \Omega \quad (4.3)$$

This is a partial differential equation with certain boundary conditions on $\partial\Omega$. Here $\nabla \mathcal{R}$ denotes the Fréchet derivative of \mathcal{R} . The dynamic version of (4.3) is the so-called steepest descent or gradient flow approach. More precisely, a minimiser u of (4.2) is embedded in an evolution process, denoted by $u(\cdot, t)$. At time $t = 0$, $u(\cdot, t = 0) = f$ is the original image. It is then transformed through an iterative process characterised by

$$\partial_t u = -\nabla \mathcal{R}(x, u, Du, \dots, D^k u) + \lambda_0 (T_u - f), \text{ in } \Omega, \quad \text{and} \quad \partial_n u = 0 \text{ on } \partial\Omega, \quad (4.4)$$

Given a variational formulation (4.2), the steepest-descent approach is used to numerically compute a minimiser of E , whereby (4.4) is iteratively solved until one is close enough to a minimiser of E . The model (4.4) is defined as a numerical solution of a PDE over the space of functions of bounded variation $BV(\Omega)$ which includes digital images. A numerical solution of (4.4) for noise removal or missing-region reconstruction, (see (Aubert & Kornprobst 2006)).

4.1.2 Non-Variational Methods

Alternative non-variational approaches for developing a class of PDE-BI models. Inpainting approaches in this class, are directly defined by PDE of the form:

$$\partial_t u = F(x, u, Du, \dots, D^k u),$$

where $F: \Omega \times \mathbb{R} \times \mathbb{R}^2 \times \mathbb{R}^3 \times \dots \times \mathbb{R}^k \rightarrow \mathbb{R}$ is a k^{th} -order differential operator, and Ω is an image domain. The underpinning mathematics of these approaches are based the fact that inpainting is a problem of interpolation of functions of 2 variables, defined on the domain of the input image, which can be approximated by F using Taylor polynomials of any order. In this case, the added term is an estimate of the error term of approximation.

Examples of such inpainting schemes that have been proposed in the literature include: the CDD inpainting (T. Chan and J. Shen 2001), Bertalmio (Bertalmio et al. 2000), modified Cahn-Hilliard (A. L. Bertozzi et al. 2007), and TV – H^{-1} (Burger et al. 2009). These inpainting schemes are described briefly in section 4.3.

4.1.3 Literature Overview

PDE-BI methods are well covered in the literature. The term inpainting was invented by art restoration workers, (Emile-Mâle 1976) and (Walden 1985), and first appeared in the framework of digital restoration in the work of Bertalmio et al. (Bertalmio et al. 2000), therein they designed a discrete 3rd-order nonlinear PDE intended to imitate the restoration work of museum artists, (see section 4.3.2). Filling-in of the missing region Ω is done automatically based on the information surrounding Ω via consideration of isophote lines connected to the boundaries of Ω (see Figure4-1).

The pioneering works of (Bertalmio et al. 2000), (Chan & Shen 2002), (Caselles et al. 1999), (D. Mumford 1993) and (Masnou & Morel 1998) in image restoration using PDEs and variational methods, in the last two decades, are reviewed, in order to define a starting position. Total Variation (TV) and Curvature Driven Diffusion (CDD) models have been introduced by Chan and Shen (Chan & Shen 2002), (T. Chan and J. Shen 2001) respectively. The inpainting results using the TV model generate 2nd-order nonlinear PDE which works by anisotropic diffusion inside the inpainting domain (i.e. preserving edges and diffusing homogeneous regions and small oscillations like noise). While the CDD model improves on the TV model by enabling the recovery of large areas and connecting the lines/features across large distances. The improvement is

possibly due to the use of 3rd-order nonlinear PDE at the expense of inefficiency while TV methods that use 2nd-order (linear and non-linear) PDEs can only reconstruct small regions, and struggle with edges and corners, (Schönlieb 2009). The authors in (Xu et al. 2008), proposed Quick Curvature-Driven Diffusions (QCDD) to for improved efficiency.

A variational technique for image segmentation has been proposed in (D. Mumford 1993), by removing occlusions of objects by connecting T-junctions at the occluding boundaries of objects with Euler elastic minimising curves. The minimisation of a discrete version of a constrained Euler elastic energy for all level lines was used to extend the idea of length and curvature minimisation from edges to all the level lines of the image function (Mumford 1994). This approach is contrasted invariant. The Euler elastic energy was used for inpainting later by Mumford in (Esedoglu & Shen 2002) and by Chan et al. in (T.F. Chan, S.H. Kang 2002). The model proposed in (Esedoglu & Shen 2002) is a 4th-order PDE, called the Mumford-Shah-Euler model (MESm), succeeded in recovering edges and corners and overcome the limitations intrinsic to 2nd-order PDEs. Also, 4th-order of total variation flow was suggested in (Burger et al. 2009), to remedy the shortcoming of TV inpainting which has been successful when to binary structures with large holes. On the other hand, a TV model to minimise the Laplacian norm was proposed in (Peiying Chen & Yuandi Wang 2008) as an alternative to the 4th order TV model.

The authors in (Chen & Wang 2009) have improved the Non-TV technique in (Bertalmio et al. 2000) that is based on the anisotropic diffusion principle and the connectivity principle of human visual perception; they proposed forward a novel nonlinear PDE inpainting model. The procedure allows for the transporting and diffusing of image information simultaneously. More recently, the authors in (A. L. Bertozzi et al. 2007) proposed a modified Cahn-Hilliard (mCH) equation for the inpainting of binary images. A generalisation of Cahn-Hilliard inpainting for grey value images, called $TV - H^{-1}$ inpainting, was also proposed in (Burger et al. 2009). These are the non-TV based inpainting scheme, and details are given in section 4.3.2. In the next sections, some important inpainting models of 2nd and high order PDE are described in more details.

4.2 Second-Order PDE-BI methods

Even though 2nd-order PDEs have been extensively studied theoretically, well established and not difficult to solve numerically, in inpainting they do not perform well when the size of the region of interest is substantial. The main disadvantage occurs when there are discontinuities of lines (edges) over a large distance in the image of interest and where features like corners, curvatures and edges need to be reconstructed. Next, four existing 2nd-order PDE-BI models are introduced and applied. A detailed introduction to these models is not given; for this, the interested reader needs to consult (Shen & Chan 2002), (Rudin et al. 1992), (Tsai et al. 2001), (Perona & Malik 1990), and (Haar Romeny 1994).

4.2.1 Isotropic Diffusion (Tikhonov Regularisation Technique)

The isotropic equation is simple and is the most investigated in image processing, specifically in image inpainting (Aubert & Kornprobst 2006). Initially, it was used to recover blurred images (Weickert & Stuttgart 1998), (Weickert 1996), and (Guillemot & Le Meur 2014). The heat equation is presented in two ways:

Let $f \in L^2(\Omega)$ be the given image, and $D \subset \Omega$ is a missing-information region in an image, the inpainted image u is calculated as the solution of the heat equation as below:

$$\begin{cases} \partial_t u = \Delta u, & t \geq 0, \\ u(0, x, y) = 0. \end{cases} \quad (4.5)$$

Also, the solution of equation (4.5) can be understood as the solution of the minimisation functional of squared total variation (4.6):

$$\min_{u \in L^2(\Omega)} \left\{ \int \int_D |\nabla u|^2 dx dy \quad \text{such that} \quad u = f \text{ in } \Omega \setminus D \right\} \quad (4.6)$$

The gradient descent process with the Euler-Lagrange equation has been used on minimisation functional (4.7):

$$u_t = \Delta u \quad (4.7)$$

The isotropic model for image denoising is applied by adding a fidelity term as proposed in (Weickert & Stuttgart 1998). This leads to the following formula:

$$\min_{u \in L^2(\Omega)} F(u) = \int \int_{\Omega} \left(|\nabla u|^2 + \frac{\lambda}{2} (u - f)^2 \right) dx dy \quad (4.8)$$

Applying the Euler-Lagrange equation on (4.8) leads to

$$\partial_t u = \Delta u + \lambda (u - f) \quad \dots (4.9)$$

To remove the noise from the image, the equation $u = \frac{1}{\lambda} f + \Delta u$ with Neumann boundary condition is solved by using a finite difference method, as shown in

Chapter 4: PDE Based Full Inpainting Methods

Figure4-3. For reconstructing a missing region in an image, Equation 4.7 with Neumann boundary condition is solved based the information around the missing region. The explicit finite difference method was used to find the numerical solution, as explained in section 2.5.2. The numerical solution of equation (4.7) with Neumann boundary conditions is found at each pixel in each (R, G, B) channel of the image to recover the missing regions.

The above solution of equation (4.5) mimics that of a heat equation over the image domain. The heat equation models the propagation of a temperature field over a time interval in all directions given the boundary conditions, and its solution is smooth. Equation (4.5) is meant to model a discrete process of filling missing regions, and therefore its solution may fail to reconstruct edges and corners. The Gaussian filtering and averaging of images is equivalent to diffusion of the pixel values all across the image. Figure4-3 clarifies how the image gets blurred under isotropic smoothing, because of the numerical mixing of pixels from different regions by solving model (4.9), especially in image b.

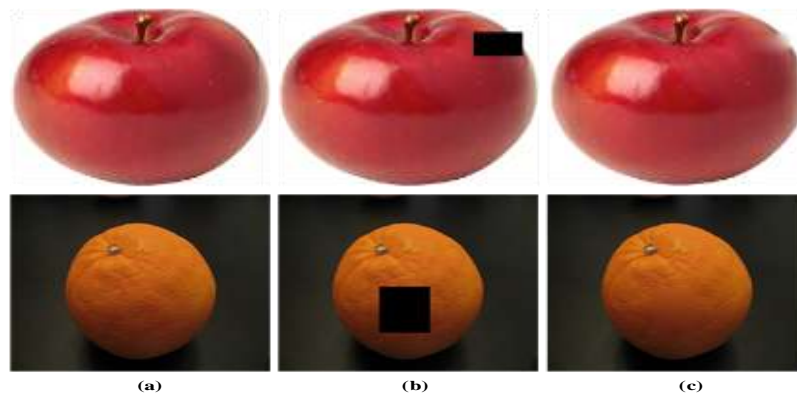


Figure4-2: Inpainting based isotropic model, (a) original image, (b) masked image, (c) inpainted image.

The results were blurry because of the edges, the averaging of pixels across edges, and letting these pixel values across edges be mainly mixed up, which is why obtained blurring, as seen in Figure4-2. The process was isotropic smoothing; it didn't matter whether or not boundaries were present. The performance of model (4.5) is done well when surrounding areas of the missing region are homogeneous; otherwise, the sharp edges are lost when the surrounding area is non-homogeneous, as seen in Figure4-2. To overcome the smoothness propagation information's, harmonic image inpainting has been proposed to solve this defect. Also, Figure4-5b clarifies the performance of heat model at the missing edges. In summary, both the connectivity principle and the

curvature preservation are not fulfilled through applying this model to recover small missing region.

4.2.2 Harmonic Extension Equation

Harmonic image inpainting represents a simple example through which to understand the image interpolation process. The inpainted image can be defined as the solution of the Laplace equation, or as the result of the minimisation of the Dirichlet energy over the inpainting domain.

Let $f \in L^2(\Omega)$ be the given image with inpainting domain $D \subset \Omega$. The authors in (Shen & Chan 2002) have used the idea of a denoising formula, where the inpainted image u can be defined as the minimiser of energy

$$\min_{u \in L^2(\Omega)} \int \int_{\Omega} (|\nabla u|^2 + \lambda |u - f|_{L^2(\Omega)}^2) dx dy = 0, \quad \text{in } D, \quad u = f \text{ on } \partial D \quad (4.10)$$

Where λ is a large constant. Minimising (4.12) over $H^1(\Omega)$, a minimiser is equivalently characterised as the solution to the corresponding Euler-Lagrange equation

$$\begin{cases} -\Delta u = 0, & \text{in } D, \\ -\Delta u = \lambda(f - u), & \text{in } \Omega \setminus D, \\ u = 0, & \text{on } \partial\Omega. \end{cases} \quad (4.11)$$

where $\lambda \geq 1$ is a tuning parameter of the technique, the second term of the functional is called the fidelity term of the inpainting technique, which forces the minimiser u to stay close to the given image f outside the inpainting domain, based on the value of λ .

The five-point finite difference method has been used to solve equation (4.11). The first step rewrites the equation (4.11) in discrete space by using a finite difference series (Euler series) as follows:

$$u_{i,j}^{n+1} = \frac{u_{i+1,j}^n - 2u_{i,j}^n + u_{i-1,j}^n}{h_1^2} + \frac{u_{i,j+1}^n - 2u_{i,j}^n + u_{i,j-1}^n}{h_2^2} + \lambda(u_{i,j}^n - f_{i,j}) \quad (4.12)$$

where $h_1 = 1, h_2 = 1$, and $\Delta t = 0.1$; equation (4.12) can be rewritten as follows:

$$u_{i,j}^{n+1} = \frac{1}{h_1^2} \left((u_{i+1,j}^n + u_{i-1,j}^n - 4u_{i,j}^n + u_{i,j+1}^n + u_{i,j-1}^n) + \lambda(u_{i,j}^n - f_{i,j}) \right) \quad (4.13)$$

Where $2 \leq i \leq M - 1$ and $2 \leq j \leq N - 1$. The equation (4.13) with Neumann boundary condition is calculated the pixel value in each channel of the image.

Figure 4-7 to 4-10, demonstrate that the harmonic model is a good candidate for inpainting smooth images. However, the harmonic equation does not deal adequately with edges and large missing regions (see in Figure 4-8, 4-9 and 4-21). The performance of the harmonic model has been a smooth reconstruction of the large

region. In general, the harmonic model outperforms the isotropic model in propagating the information in the large missing region. However, it doesn't reconstruct well the edges and corners. In summary, the curvature preservation is not fulfilled, but the harmonic model successfully recovered small missing region (the connectivity principle is fulfilled). To reconstruct the edges successfully, the total variation has been used in the proposed anisotropic model.

4.2.3 Anisotropic Diffusion (TV Regularisation Technique)

Anisotropic diffusion equation has been proposed to remove the noise from an image while preserving the edges in the image (Perona & Malik 1990). This equation is modelled on the dependence of the diffusivity constant on the size of the image gradient, to reduce the amount of diffusion that occurs near edges. Anisotropic diffusion is a nonlinear 2nd-order equation, which addresses the shortcomings that face isotropic diffusion and harmonic extension models. The model formula is introduced in two ways:

$$\begin{cases} \partial_t u = \operatorname{div} \left(\frac{\nabla u}{|\nabla u|} \right), & t \geq 0, \\ u(0, x, y) = u_0(x, y). \end{cases} \quad (4.14)$$

With initial conditions $u(t = 0)$ and $u(t = T)$. The model 4.14 with Neumann boundary conditions and initial conditions is applied to the same image in Figure4-5a Figure4-5c. Also, this equation can be obtained through minimisation of total variation as follows:

$$\min_{u \in L^1(\Omega)} \left\{ \int_D |\nabla u| \, d\Omega \text{ such that } u = f \text{ in } \Omega \setminus D \right\} \quad (4.15)$$

The Euler Lagrange equation with has been used for functional minimisation 4.15 then the gradient descent process has been used on it:

$$\partial_t u = \operatorname{div} \left(\frac{\nabla u}{|\nabla u|} \right) \quad (4.16)$$

The anisotropic model for image denoising is applied by adding a fidelity term as proposed in (Rudin et al. 1992). This leads to the following formula:

$$\min_{u \in L^1(\Omega)} F(u) = \int \int_{\Omega} \left(|\nabla u| + \frac{\lambda}{2} (u - f)^2 \right) dx dy \quad (4.17)$$

Applying the Euler-Lagrange equation on (4.17) with the gradient descent method leads to

$$\partial_t u = \operatorname{div} \left(\frac{\nabla u}{|\nabla u|} \right) + \lambda(u - f) \quad (4.18)$$

The Neumann boundary condition has been used with equation (4.18).

While, the Dirichlet boundary condition has been used with equation $u = \frac{1}{\lambda} f + \text{div} \left(\frac{\nabla u}{|\nabla u|} \right)$. The right-side term of this equation represents the curvature of the level lines of the image u . Anisotropic diffusion is going to try to average pixels values only on the right side of the object, on the right side of the edges on the correct object. Figure4-3 clarifies the application of anisotropic diffusion on the image. Image c represents the result of it; we see that this equation only mixes the pixels on the side of the boundary without going in all directions because then sharper edges are obtained, while it also removes noise inside the objects, and the image(c) of the brain is much smoother, and the boundaries are preserved very nicely.

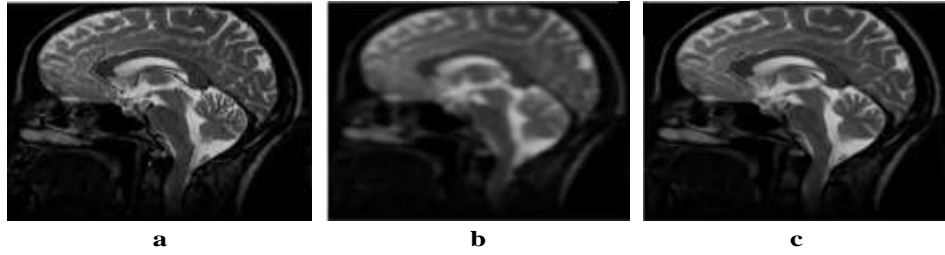


Figure4-3: Isotropic and anisotropic process: (a) original image. (b) Image by using isotropic equation. (c) Image by applying anisotropic diffusion.

For reconstructing the missing regions in an image, equation (4.14) with Neumann boundary condition is solved to reconstruct the missing region based the information around it. Equation (4.14) can be rewritten as follows:

$$u_t = \frac{\partial}{\partial x} \left(\frac{u_x}{\sqrt{u_x^2 + u_y^2}} \right) + \frac{\partial}{\partial y} \left(\frac{u_y}{\sqrt{u_x^2 + u_y^2}} \right), \quad \forall t > 0, x, y \in \Omega \quad (4.19)$$

The explicit finite difference method was used to find the numerical solution, the partial derivative in the equation (4.19) converts to the finite difference formula:

$$\begin{aligned} u_{i,j}^{n+1} &= u_{i,j}^n + \frac{k}{h} \left(\Delta^x \left[\frac{1}{\sqrt{\epsilon^2 + \left(\frac{\Delta_+^x u_{i,j}^n}{h} \right)^2 + \left(\frac{\Delta_o^y u_{i,j}^n}{h} \right)^2}} \frac{\Delta_+^x u_{i,j}^n}{h} \right] + \Delta^y \left[\frac{1}{\sqrt{\epsilon^2 + \left(\frac{\Delta_o^x u_{i,j}^n}{h} \right)^2 + \left(\frac{\Delta_+^y u_{i,j}^n}{h} \right)^2}} \frac{\Delta_+^y u_{i,j}^n}{h} \right] \right) \\ &= u_{i,j}^n + \frac{k}{h^2} \left(\left[\frac{u_{i+1,j}^n - u_{i,j}^{n+1}}{\sqrt{\epsilon^2 + \left(\frac{u_{i+1,j}^n - u_{i,j}^n}{h} \right)^2 + \left(\frac{u_{i,j+1}^n - u_{i,j-1}^n}{2h} \right)^2}} - \frac{u_{i,j}^{n+1} - u_{i-1,j}^n}{\sqrt{\epsilon^2 + \left(\frac{u_{i,j}^n - u_{i-1,j}^n}{h} \right)^2 + \left(\frac{u_{i-1,j+1}^n - u_{i-1,j-1}^n}{2h} \right)^2}} \right] \right. \\ &\quad \left. + \left[\frac{u_{i,j+1}^n - u_{i,j}^{n+1}}{\sqrt{\epsilon^2 + \left(\frac{u_{i+1,j}^n - u_{i-1,j}^n}{2h} \right)^2 + \left(\frac{u_{i,j+1}^n - u_{i,j}^n}{h} \right)^2}} - \frac{u_{i,j}^{n+1} - u_{i,j-1}^n}{\sqrt{\epsilon^2 + \left(\frac{u_{i+1,j-1}^n - u_{i-1,j-1}^n}{2h} \right)^2 + \left(\frac{u_{i,j}^n - u_{i,j-1}^n}{h} \right)^2}} \right] \right) \end{aligned}$$

We use a fixed-point Gauss-Seidel iteration method for the above equation, and solving for $u_{i,j}^{n+1}$, we obtain:

$$u_{i,j}^{n+1} = \left(\frac{1}{1 + \frac{k}{h^2}(C_1 + C_2 + C_3 + C_4)} \right) \cdot \left[u_{i,j}^n + \frac{k}{h^2}(C_1 u_{i+1,j}^n + C_2 u_{i-1,j}^n + C_3 u_{i,j+1}^n + C_4 u_{i,j-1}^n) \right] \quad (4.20)$$

$$\text{Where } C_1 = \sqrt{\epsilon^2 + \left(\frac{u_{i+1,j}^n - u_{i,j}^n}{h}\right)^2 + \left(\frac{u_{i,j+1}^n - u_{i,j-1}^n}{2h}\right)^2}, \quad C_2 = \sqrt{\epsilon^2 + \left(\frac{u_{i,j}^n - u_{i-1,j}^n}{h}\right)^2 + \left(\frac{u_{i-1,j+1}^n - u_{i-1,j-1}^n}{2h}\right)^2}$$

$$C_3 = \sqrt{\epsilon^2 + \left(\frac{u_{i+1,j}^n - u_{i-1,j}^n}{2h}\right)^2 + \left(\frac{u_{i,j+1}^n - u_{i,j-1}^n}{h}\right)^2}, \quad C_4 = \sqrt{\epsilon^2 + \left(\frac{u_{i+1,j-1}^n - u_{i-1,j-1}^n}{2h}\right)^2 + \left(\frac{u_{i,j}^n - u_{i,j-1}^n}{h}\right)^2}$$

Finally, we mention that one can perform inpainting across larger regions by considering a two-step method. The inpainting is done first and its results in the topological reconnection of shapes with edges smeared by diffusion. The second step then uses the results of the first step and continues with a much smaller value of ϵ in order to sharpen the edge after reconnection. In practice, such a two-stage process can result in inpainting of a stripe across a region that is over ten times the width of the stripe, without any a priori knowledge of the location of the stripe, as see in the Figure4-6b.

The equation (4.20) recovers the sharp geometric structures and promotes discontinuities. The shortcomings of this model are that it is unable to recover large missing regions and it also has a problem with the edges because it does not preserve their directions in the direction of the boundary of the damaged parts. Equation (4.18) has also been applied for denoising and for decomposing images into structure and texture components which that use in Chapter 6, (see Figures6.3 and 6.4 respectively).

In summary, both the connectivity principle and the curvature preservation are not fulfilled by applying this model to recover the large missing region. Nevertheless, this model successfully propagates the smooth information in the small missing region (the connectivity principle).

4.2.4 Mumford-Shah Model (MSM)

The model of MS originally designed and proposed for segmentation problem (Tsai et al. 2001) based on the idea of decomposing an image into piecewise smooth parts that are separated by an edge set Γ . Afterwards, the MSm has proposed (Esedoglu & Shen 2002) for image inpainting problems. This model is a nonlinear 2nd-order PDE, the following of the minimising energy functional:

$$E[u, \Gamma] = \min_u F(u) = \frac{\lambda}{2} \int_{\Omega \setminus D} (u - f)^2 d\vec{x} + J[u, \Gamma]. \quad (4.21)$$

with

$$J[u, \Gamma] = \frac{\gamma}{2} \int_{\Omega \setminus \Gamma} |\nabla u|^2 d\vec{x} + \beta_0 \mathcal{H}^1(\Gamma). \quad (4.22)$$

Where $\vec{x} = (x, y)$, γ and β_0 are non-negative constant, and \mathcal{H}^1 indicates to the one-dimensional Hausdorff measure, which computes the length of curves in the region and Γ indicates the collection of edges. $\mathcal{H}^1(\Gamma)$ is conveniently substituted by length (Γ), under the assumption that Γ belongs to the Lipschitz class. Formula (4.21) aims to recover a damaged region into its piecewise smooth area u in the H^1 norm and its edge set Γ in one-dimensional Hausdorff $\mathcal{H}^1(\Gamma)$. So, the authors in (Ambrosio & Tortorelli 1990) proposed the use the Ambrosio–Tortorelli approximation (i.e. convergence of Γ) (Esedoglu & Shen 2002) for finding the numerical solution of Formula (4.22) to address the problem of non-differentiability and discretisation of the unknown edge set Γ .

There a sequence of regular functionals J_σ is considered which approximates J and solves the minimisation problem for J_σ , $\sigma < 1$. Let $\mathbb{Z}_\sigma: \Omega \rightarrow [0, 1]$ which represents function of the edge set instead of Γ in (4.22); that is nearly 1 almost everywhere in Ω except on an Γ_σ around Γ , where it is close to 0. Then $\frac{1}{\sigma} |1 - \mathbb{Z}_\sigma|^p$, $p \geq 1$, is an approximation of the Dirac delta measure of Γ — $\delta\Gamma(x)$:

$$\text{Length}(\Gamma) = \int_{\Omega} \delta_\Gamma(x) d\vec{x} = \text{const.} \int_{\Omega} \frac{|1 - \mathbb{Z}_\sigma|^p}{\sigma} d\vec{x}.$$

In fact, in (Ambrosio & Tortorelli 1990) approximation, \mathbb{Z}_σ is computed for a given image u , is designed to the minimiser of

$$J_\sigma(u, \mathbb{Z}) = \frac{\gamma}{2} \int_{\Omega} \mathbb{Z}^2 |\nabla u|^2 d\vec{x} + \beta_0 \int_{\Omega} \left(\sigma |\nabla u|^2 + \frac{(1 - \mathbb{Z})^2}{4\sigma} \right) d\vec{x} \quad (4.23)$$

In summary, they propose to carry out inpainting by minimising the Γ -convergence approximation of the exact model (4.21), namely

$$J_\sigma[u, \mathbb{Z}|f, D] = \frac{\gamma}{2} \int_{\Omega} \mathbb{Z}^2 |\nabla u|^2 d\vec{x} + \beta_0 \int_{\Omega} \left(\sigma |\nabla u|^2 + \frac{(1 - \mathbb{Z})^2}{4\sigma} \right) d\vec{x} + \frac{1}{2} \int_{\Omega} \lambda (u - f)^2 d\vec{x} \quad (4.24)$$

Taking variations on u and \mathbb{Z} separately yields the Euler–Lagrange system,

$$\lambda(u - f) - \gamma \nabla \cdot (\mathbb{Z}^2 \nabla u) = 0, \quad \text{in } \Omega, \quad (4.25)$$

$$(\gamma |\nabla u|^2) \mathbb{Z} + \beta_0 \left(-2\sigma \Delta \mathbb{Z} + \frac{\mathbb{Z} - 1}{2\sigma} \right) = 0, \quad \text{in } \Omega, \quad (4.26)$$

$$\frac{\partial u}{\partial \vec{n}} = \frac{\partial \mathbb{Z}}{\partial \vec{n}} = 0, \quad \text{in } \partial\Omega, \quad (4.27)$$

where \vec{n} is the outward-pointing normal to $\partial\Omega$. For solving this nonlinear system of equations is to approximate it iteratively by sequence of linear equations as follows: $u^{(0)} = 0$ and $\mathbb{Z}^{(0)} = 0$, and solve for $k = 1, 2, \dots$

$$L_{\mathbb{Z}^{(k)}} u^{(k)} = \frac{\lambda}{\gamma} f, \quad M_{u^{(k-1)}} \mathbb{Z}^{(k)} = 1 \quad (4.28)$$

with elliptic operators

$$L_{\mathbb{Z}} = -\nabla \cdot (\mathbb{Z}^2 \nabla) + \lambda/\gamma, \quad M_u = \left(1 + \left(\frac{2\sigma\gamma}{\beta_0}\right) |\nabla u|^2\right) - 4\sigma^2 \Delta.$$

Given a pair of the current estimation u and \mathbb{Z} , both $L_{\mathbb{Z}}$ and M_u are positive definite elliptic operators. In the beginning, the solution of M_u for \mathbb{Z} is found, then using \mathbb{Z} in solving $L_{\mathbb{Z}}$ for u in equation (4.28). So the solution of equation (4.28) can be also parallelised by solving the linear equations (4.25) and (4.26) for u and \mathbb{Z} simultaneously. The numerical solution of the MSm formula (4.21) using the Ambrosio-Tortorelli approximation (4.28), for more information about numerical solution, we refer the readers to (Schonlieb 2015). Figure 4-7 to 4-10 show the inpainted image u and its edges set \mathbb{Z} in the Ambrosio-Tortorelli approximation. The previous iterate $\mathbb{Z}^{(n-1)}$ rather than the current iterate $\mathbb{Z}^{(n)}$ is used in the computation of $L_{\mathbb{Z}}$. However, this model suffers when the size of the missing region is big, or there is/are edges need to be propagated. As a 2nd-order model, it is then unable to reconstruct curved objects.

In summary, both the connectivity principle and the curvature preservation are not fulfilled by applying this model to recover the large missing region. Nevertheless, this model successfully propagates the edges and curvature in the small missing regions.

4.3 Higher-Order PDE-BI methods

As previously mentioned the 2nd-order PDEs have some limitations which led to investigating methods that higher-order PDEs ideally for better performance. Higher-order PDEs can recover/reconstruct edges, corners, and curvature as well as larger regions in comparison with 2nd-order PDEs. Next, a summary introduction to the higher-order PDEs-based inpainting methods is given. The interested reader can find more details about higher-order PDEs in (Esedoglu & Shen 2002), (Cahn & Hilliard 1958), (A. L. Bertozzi et al. 2007), (Bertalmio et al. 2000), and (Burger et al. 2009).

4.3.1 Mumford-Shah-Euler Model (MESM)

The MESm is proposed to overcome the shortcomings of the MSm by improving its embedded curve model with Euler's Elastic curve model (Esedoglu & Shen 2002). The formula of the MESm can be expressed as follow:

$$E(u, \Gamma) = \min_u F(u, \Gamma) = \frac{\lambda}{2} \int_{\Omega \setminus D} (u - f)^2 d\vec{x} + J(u, \Gamma) \quad (4.29)$$

with

$$J(u, \Gamma) = \frac{\gamma}{2} \int_{\Omega \setminus \Gamma} |\nabla u|^2 d\vec{x} + \int_{\Gamma} (\alpha + \beta k^2) ds \quad (4.30)$$

where α and β are regularisation parameters, k denotes the curvature, ds the length element. The first and second integral represents the MSm, while the second integral in (4.30) is the Euler elastic model which is based on the mechanical properties of a thin and torsion-free rod (Love 2013). For numerical purposes, the same numerical method that is used for solving MSm is followed; the authors in (Schonlieb 2015) consider an elliptic approximation De Giorgi of Euler's elastic energy in the second integral in (4.30), can be written as follows:

$$J_{\sigma}(\mathbb{Z}) = \alpha \int_{\Omega} \left(|\nabla \mathbb{Z}|^2 + \frac{W(\mathbb{Z})}{4\sigma} \right) d\vec{x} + \frac{\beta}{\sigma} \int_{\Omega} \left(2\sigma \Delta \mathbb{Z} - \frac{W'(\mathbb{Z})}{4\sigma} \right) d\vec{x}. \quad (4.31)$$

As explained before, \mathbb{Z} is an σ -approximation of the edge set Γ , and W is the symmetric double potential $W(\mathbb{Z}) = (1 - \mathbb{Z}^2)^2 = (1 - \mathbb{Z})^2(1 + \mathbb{Z})^2$.

The latter replace the regularisation energy (4.29) in the inpainting scheme, which writes as follows:

$$E_{\sigma}(u, \mathbb{Z}) = \frac{\lambda}{2} \int_{\Omega} (u - f)^2 d\vec{x} + \frac{\gamma}{2} \int_{\Omega} \mathbb{Z}^2 |\nabla u|^2 d\vec{x} + J_{\sigma}(\mathbb{Z}) \quad (4.32)$$

Taking variations on u and \mathbb{Z} separately yields the Euler–Lagrange system,

$$\lambda(u - f) - \gamma \nabla \cdot ((\mathbb{Z}^2 + h(\sigma)) \nabla u) = 0, \quad (4.33)$$

$$\gamma |\nabla u|^2 \mathbb{Z} - \alpha f - \beta_0 \left(-4\Delta f + \frac{W''(\mathbb{Z})}{2\sigma^2} f \right) = 0, \quad (4.34)$$

$$2\sigma \Delta \mathbb{Z} - \frac{W''(\mathbb{Z})}{4\sigma} = f, \quad (4.35)$$

Now the steepest-descent method is used for solving J_{σ} in \mathbb{Z} , that is,

$$\mathbb{Z}_t = -\gamma |\nabla u|^2 \mathbb{Z} + \alpha f - 4\beta_0 \Delta f + \frac{\beta_0 W''(\mathbb{Z})}{2\sigma^2} f = 0,$$

Then to discretise in time, the semi-implicit scheme is used as

$$(1 + \Delta t A_u) \mathbb{Z}^{n+1} = \mathbb{Z}^n + \Delta t g(\mathbb{Z}^n), \quad (4.36)$$

where

$$A_u = \gamma |\nabla u|^2 \mathbb{Z} - 2\alpha \sigma \Delta + 8\beta_0 \sigma \Delta^2,$$

and $g(\mathbb{Z})$ collects all the non-linear terms in \mathbb{Z} , that is

$$g(\mathbb{Z}) = -\frac{\alpha}{4\sigma}W'(\mathbb{Z}) + \frac{\beta_0}{2\sigma^2}W''(\mathbb{Z})f + \frac{\beta_0}{\sigma}\Delta W'(\mathbb{Z})$$

The numerical solution of this model recovers the missing regions in a digital image. More details about this model can be found in (Esedoglu & Shen 2002); it succeeded in recovering the lines, and corners in the small non-textured missing regions in the processed images. The MESm has been used to deal with large-scale image-inpainting problems, where this model uses the curvature to overcome the issue of large missing regions and accurately recovers the borders of missing regions. As a result, in (Esedoglu & Shen 2002), the researchers proposed the MESm to improve the shortcomings of the MSm. The minimisation of (4.29) leads to a 4th-order PDE via the Euler-Lagrange Equation. Implementations of this model are illustrated in Figure 4-8 and 4-9.

In summary, both the connectivity principle and the curvature preservation are fulfilled through applying this model to recover large missing region in the non-texture images. Nevertheless, this model failed to propagate the more edges and curvature in the large missing regions.

4.3.2 Bertalmio Approach (Transport Model)

The underlying mechanism of the previous equations was diffusion. In this section, PDE-BI methods that are solely based on transport dynamics are introduced. Bertalmio et al. in (Bertalmio et al. 2000), paved the way for modern digital image inpainting based PDE. Their discrete PDE model was motivated by the work of art conservators, borrowing heavily from the idea of manual inpainting. The changed of information's δL^n due to smoothing propagation equals zero when projected onto the propagation direction \vec{N}^n :

$$\delta L^n \cdot \vec{N}^n = 0 \tag{4.37}$$

In other words, the gradient of information is propagated to be perpendicular to the direction in which are propagating. This information needs to be perpendicular in the sense that we want to propagate information L^n such a way that it is not changed in the direction of the propagation by being moved in that direction. The equation (4.37) basically describes how the L^n propagation of information along with directions \vec{N}^n . To make the image change in time, information propagation is governed by the condition:

$$u_t^n(i, j) = \delta L^n(i, j) \cdot \vec{N}^n(i, j) \tag{4.38}$$

where $\delta L^n(i, j)$ is a measure of the change in the information $L^n(i, j)$. With this equation, the information $L^n(i, j)$ is estimated and its change along the $\vec{N}^n(i, j)$ direction is computed. When the change of the image via propagation approaches zero, the steady state has been attained (4.37). The propagation of information should be smooth to avoid big jumps inside the missing region. The Laplacian is the better operator for describing smooth information. If there is an edge, the gradient of the image is perpendicular to the edge, where $\vec{N}^n(i, j) = \nabla^\perp u^n(i, j)$. In order to implement this, we must first define what a direction \vec{N}^n for the 2D information propagation will be. One possibility is to define \vec{N}^n as the normal to the signed distance to $\partial\Omega$, i.e., at each point (i, j) in Ω the vector \vec{N}^n will be normal to the "shrank version" of $\partial\Omega$ to which (i, j) belongs, see Figure4-4.

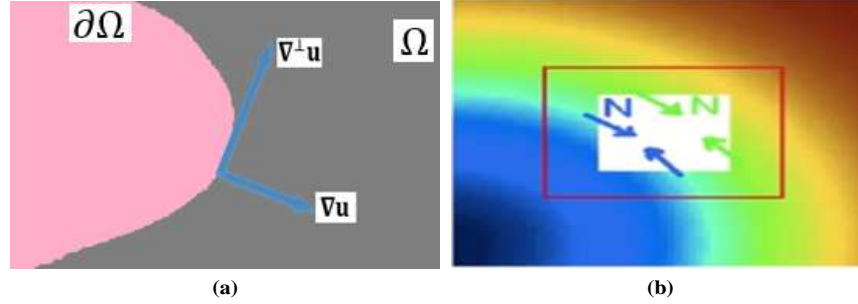


Figure4-4: Explanation of Bertalmio module. (a) Propagation direction by perpendicular normal operator to the edge, (b) Propagation direction in missing region.

This iterative process propagates linear structures (edges) of the surrounding area (i.e. isophotes) into the missing region; it is denoted by using a diffusion process given by

$$\Delta t u_t^n(i, j) = u^{n+1}(i, j) - u^n(i, j), \quad \forall (i, j) \in \Omega \quad (4.39)$$

where n is the iteration number, (i, j) are pixel co-ordinates, Δt is the rate of the change of inpainting and $u_t^n(i, j)$ is the update factor on the image $u^n(i, j)$.

$$u_t^n(i, j) = \left(\delta L^n(i, j) \cdot \frac{\vec{N}^n(i, j)}{|\vec{N}^n(i, j)|} \right) |\nabla u^n(i, j)|, \quad (4.40)$$

Where

$$\delta L^n(i, j) = (L^n(i + 1, j) - L^n(i - 1, j), L^n(i, j + 1) - L^n(i, j - 1)) \quad (4.41)$$

$$L^n(i, j) = u^n_{xx}(i, j) + u^n_{yy}(i, j), \quad (4.42)$$

$$\frac{\vec{N}^n(i, j)}{|\vec{N}^n(i, j)|} = \frac{(-u^n_y(i, j), u^n_x(i, j))}{\sqrt{(u^n_x(i, j))^2 + (u^n_y(i, j))^2}}, \quad (4.43)$$

$$\beta^n(I, j) = \delta L^n(I, j) \cdot \frac{\vec{N}^n(i, j)}{|\vec{N}^n(i, j)|}, \quad (4.44)$$

and

$$|\nabla u^n(i, j)| = \begin{cases} \sqrt{(u^n_{x_{bm}})^2 + (u^n_{x_{fM}})^2 + (u^n_{y_{bm}})^2 + (u^n_{y_{fM}})^2}, & \text{when } \beta^n > 0 \\ \sqrt{(u^n_{x_{bM}})^2 + (u^n_{x_{fm}})^2 + (u^n_{y_{bM}})^2 + (u^n_{y_{fm}})^2}, & \text{when } \beta^n < 0 \end{cases} \quad (4.45)$$

We first compute the 2D smoothness estimation L in (4.42) and the isophote direction $\vec{N} / |\vec{N}|$ in (4.43). Then in (4.44), we compute β^n , the projection of L onto the (normalised) vector \vec{N} , that is, the change of L is computed along the direction of \vec{N} . Finally, β^n is multiplied by a slope-limited version of the norm of the gradient of the image, $|\nabla u|$, in (4.45). A central differences realisation would turn the scheme unstable, and that is the reason for using slope-limiters. The sub-indexes b and f denote backward and forward differences respectively, while the subindexes m and M denote the minimum or maximum, respectively, between the derivative and zero (we have omitted the space coordinates (i, j) for simplicity), see (Osher & Sethian 1988) for details. Finally, let us note that the choice of a non-normalised field \vec{N} instead of a normalised version of it allows for a simpler and more stable numerical scheme, see (Rudin et al. 1992) and (Osher & Sethian 1988).

Note once again that when the inpainting method arrives at steady state, that is, $u_t = 0$, $\nabla^\perp u = 0$, is geometrically solved, meaning that the ‘‘smoothness’’ is constant along the isophotes. When applying equations (4.39)-(4.45) to the pixels in the border $\partial\Omega$ of the region Ω to be inpainted, known pixels from outside this region are used. That is, conceptually, equations (4.39)-(4.45) are computed in the region, although only the values inside Ω are updated (that is, (4.39) is applied only inside Ω). One of the main drawbacks of this technique is that it underperforms in the replication of large textured regions due to blurring artefacts created by the diffusion process and the lack of explicit treatment of the pixels on edges. The transport model considers one of the pioneering works within PDE-BI approaches in (Bertalmio et al. 2000) which the result of multiplying the directional propagation by the change of the rate of the smoothness operator. This model succeeded in reconstructing edges. It is a 3rd-order PDE, and it is applied as shown in Figure 4-7 to 4-10. In summary, the curvature preservation is not fulfilled in the large missing regions, but the transport model successfully recovered large missing region (the connectivity principle is fulfilled).

4.3.3 Modified Cahn-Hilliard Model (mCH)

The mCH equation is a semi-linear 4th-order PDE which is proposed for binary image inpainting (A. L. Bertozzi et al. 2007). Also, this equation uses in material sciences (Cahn & Hilliard 1958). Let $f(\vec{x})$ be a given image in domain Ω , where $\vec{x} = (x, y)$, and suppose that $D \subset \Omega$ is that the inpainting domain. The formula of this equation introduced as follows:

$$\partial_t u = \Delta \left(-\epsilon \Delta u - \frac{1}{\epsilon} F'(u) \right) + \lambda(\vec{x})(f - u), \text{ in } \Omega \quad (4.46)$$

Where $\lambda(\vec{x}) = \begin{cases} 0 & \text{if } \vec{x} \in D \\ \lambda_0 & \text{if } \vec{x} \in \Omega \setminus D \end{cases}$

Equation (4.46) is called the mCH equation, due to the added fidelity term $\lambda(\vec{x})(f - u)$, where $F(u)$ is called a double-well potential, and $F(u) = (1 - u^2)^2/4$, where ϵ is a positive parameter that is intended to go to zero. To solve equation (4.50), it is enough to solve the energy functional (4.47):

$$\int_{\Omega} \frac{\epsilon}{2} |\nabla u|^2 + \frac{1}{\epsilon} F(u) d\vec{x} + \lambda_0 \int_{\Omega \setminus D} (f - u)^2 d\vec{x} \quad (4.47)$$

where the left term represents the energy of a gradient flow using an H^{-1} the norm which will produce the mCH equation (4.47), and the second term is the fidelity term in (4.47) which can be derived from a gradient flow under an L^2 norm for the energy.

Similar to the convexity splitting for the anisotropic diffusion inpainting, the following splitting leads to the 4th-order total variation equation. The fitting term is a gradient flow in $H^{-1}(\Omega)$ and $L^2(\Omega)$ of the energy respectively. Where $H^{-1}(\Omega)$ is the dual Sobolev space of $H_0^1(\Omega)$ with corresponding norm $\|\cdot\|_{-1}$. For $f \in H^{-1}(\Omega)$, the norm is defined as follows:

$$\|f\|_{-1}^2 = \|\nabla \Delta^{-1} f\|_{-1}^2 = \int_{\Omega} (\nabla \Delta^{-1} f)^2 d\vec{x}.$$

Where Δ^{-1} denotes the inverse of Laplacian operator, such that $u = \Delta^{-1} f$ is the unique solution to

$$-\Delta u = f, \text{ in } \Omega, \text{ where } u = 0, \text{ on } \partial\Omega$$

Let

$$R_1 = \int_{\Omega} \frac{\epsilon}{2} |\nabla u|^2 + \frac{1}{\epsilon} F(u) d\vec{x} \quad \text{and} \quad R_2 = \lambda_0 \int_{\Omega \setminus D} (f - u)^2 d\vec{x} \quad (4.48)$$

A convexity splitting is applied for both R_1 and R_2 separately; R_1 is splitted as $R_1 = R_{11} - R_{12}$, where

$$R_{11} = \int_{\Omega} \frac{\epsilon}{2} |\nabla u|^2 + \frac{C_1}{2} |u|^2 d\vec{x} \quad \text{and} \quad R_{12} = \int_{\Omega} -\frac{1}{\epsilon} F(u) + \frac{C_1}{2} |u|^2 d\vec{x} \quad (4.49)$$

Likewise, $R_2 = R_{21} - R_{22}$ can be written as follows:

$$R_{21} = \int_{\Omega \setminus D} \frac{C_2}{2} |u|^2 d\vec{x} \quad \text{and} \quad R_{22} = \int_{\Omega \setminus D} -\lambda_0 (f - u)^2 + \frac{C_2}{2} |u|^2 d\vec{x} \quad (4.50)$$

Analogous to the above the resulting time stepping scheme is

$$\begin{aligned} \frac{u^{n+1} - u^n}{k} + \epsilon \nabla^4 u^{n+1} - C_1 \nabla^2 u^{n+1} + C_2 u^{n+1} \\ = \nabla^2 \left(\frac{1}{\epsilon} F'(u^n) \right) + \lambda(\vec{x})(f(\vec{x}) - u^n) - C_1 \nabla^2 u^n + C_2 u^n \end{aligned} \quad (4.51)$$

The success of this model is that it can recover large missing gaps without producing artefacts (A. L. Bertozzi et al. 2007), as seen in Figure 4-6c. The results of this model and MESm have outperformed on other inpainting models; introduced in (A. L. Bertozzi et al. 2007).

In summary, both the connectivity principle and the curvature preservation are fulfilled through applying this model to recover large missing region.

4.3.4 Fourth-Order Total Variation Model

The 4th-order version of the total variation flow model corresponds to a generalisation of the mCH equation on grey-value images (Burger et al. 2009). Higher-order PDEs treat the shortcomings of the TV flow approach. The formula of this model is as follows:

$$\partial_t u = - \Delta \left(\text{div} \left(\frac{\nabla u}{|\nabla u|} \right) \right) + \lambda(\vec{x})(f - u) \quad (4.52)$$

Similar again to the convexity splitting for anisotropic diffusion inpainting, the following splitting leads to the 4th-order total variation equation. The fitting term is a gradient flow in H^{-1} and L^2 of the energy respectively.

$$R_1 = \int_{\Omega} |\nabla u| d\vec{x} \quad \text{and} \quad R_2 = \frac{1}{2} \int_{\Omega \setminus D} \lambda_0 (f - u)^2 d\vec{x} \quad (4.53)$$

We split R_1 in $R_{11} - R_{12}$, where

$$R_{11} = \int_{\Omega} \frac{C_1}{2} |\nabla u|^2 d\vec{x} \quad \text{and} \quad R_{12} = \int_{\Omega} -|\nabla u| + \frac{C_1}{2} |\nabla u|^2 d\vec{x} \quad (4.54)$$

Likewise, $R_2 = R_{21} - R_{22}$ can be written as follows

$$R_{21} = \int_{\Omega} \frac{C_2}{2} |u|^2 d\vec{x} \quad \text{and} \quad R_{22} = \frac{1}{2} \int_{\Omega} -\lambda_0 (f - u)^2 + C_2 |u|^2 d\vec{x} \quad (4.55)$$

Analogous to the above, the resulting time stepping scheme is

$$\begin{aligned} \frac{u^{n+1} - u^n}{k} + C_1 \nabla^4 u^{n+1} + C_2 u^{n+1} \\ = C_1 \nabla^4 u^n - \nabla^2 \left(\nabla \cdot \left(\frac{\nabla u^n}{|\nabla u^n|} \right) \right) + C_2 u^n + \lambda(\vec{x})(f(\vec{x}) - u^n) \end{aligned} \quad (4.56)$$

To make the scheme unconditionally stable, the constants C_1 and C_2 have to be chosen so that R_{11}, R_{12}, R_{21} , and R_{22} are convex. The choice of C_1 depends on the regularisation of the total variation that is used. Using the square regularisation, $|\nabla u|$ is replaced by $\sqrt{|\nabla u|^2 + \delta^2}$ the conditions turn out to be $C_1 > \frac{1}{\delta}$ and $C_2 > \lambda_0$. This model with two boundary conditions gives improved results, especially on edges. It is applied to reconstruct the edges even within large holes (See Figure4-6d). In summary, both the connectivity principle and the curvature preservation are fulfilled through applying this model to recover large missing regions.

4.4 Examples of PDE-BI Methods in Spatial Domain

This section introduces examples of recovering missing regions in natural RGB colour images by using PDE-BI methods. The selected 2nd- and high-order PDE methods will be applied to recover the missing regions separately in each colour channel. To compare the performance of the 2nd- and high-order PDEs, two sets of experiments have been conducted. The first experiment was a study of the effect of the choice of order in PDE methods on the reconstruction of edges in missing regions of different sizes in the natural images. The second experiment was a study of the abilities of the 2nd- and high order PDE methods to remove texts in the natural images. Isotropic diffusion, anisotropic diffusion, 4th-order total variation and the mCH equation have been studied; these represent linear 2nd-order, nonlinear 2nd-order and nonlinear 4th-order PDEs respectively. These models are discussed in the following Figures: Figure4-5b shows the recovery of a missing region through the use of isotropic diffusion (i.e. via heat equation) where the result was not good because these results spread in four directions which causes restoration blur in the missing region.

Meanwhile, anisotropic diffusion (i.e. TV model) solved the problem which was faced as shown in Figure4-5a by propagating the restoration information in the missing region in two directions, as seen in Figure4-5c.



Chapter 4: PDE Based Full Inpainting Methods

Figure4-5: Recovering hole in an image. (a) Masked image, (b) inpainted image using isotropic method, (c) inpainted image using anisotropic method.

Although the anisotropic diffusion equation performed better than the heat equation, it failed to build the sharp edges over large missing areas in an image because it is a 2nd-order PDE, as seen in Figure4-6b.

The deficiencies of the anisotropic diffusion equation have been addressed by higher-order PDEs. Higher-order PDEs satisfy the connectivity principle because of their ability to recover large missing regions. In the same vein, they also succeeded in reconstructing edges and corners inside missing patches. There are many higher-order PDEs which may be used to solve the inpainting problem, such as 4th-order total variation and the mCH equation, as can be seen in Figure4-6c and Figure4-6d.



Figure4-6: Recovering large hole in an image. (a) Masked image, (b) inpainted image using anisotropic method, (c) inpainted image using mCH method, (d) inpainted image using 4th order TV method.

The second experiment is focused on removing texts and dates from images by using, which are harmonic, MS, transport, MES and mCH methods. Figure 4-7 to 4-10 represent examples of the removal of texts in different-sized images. The Figure 4-8 and 4-10 show the removal of texts that have small- size fonts and large size, respectively; all these models have succeeded in reconstructing the image after removing the texts. The harmonic equation is faster than MS, and transport, equations in removing the texts and repairing images. The harmonic equation has a simple computation because it is a 2nd-order PDE. On the other hand, the MS and transport models utilise huge and time-consuming computation in repairing an image.



Figure4-7: Removing text using a PDE inpainting method. (a) Masked image, (b), (c), and (d) inpainted image using Harmonic, MS and Transport models, respectively.

Figure 4-8 and 4-9 display the scratches and texts removal that has a thick size font, where the performance of the harmonic model was not good, while other models have succeeded in removing texts from the images. The results using the harmonic model were not that promising, whereas the MES and transport models achieved better results.

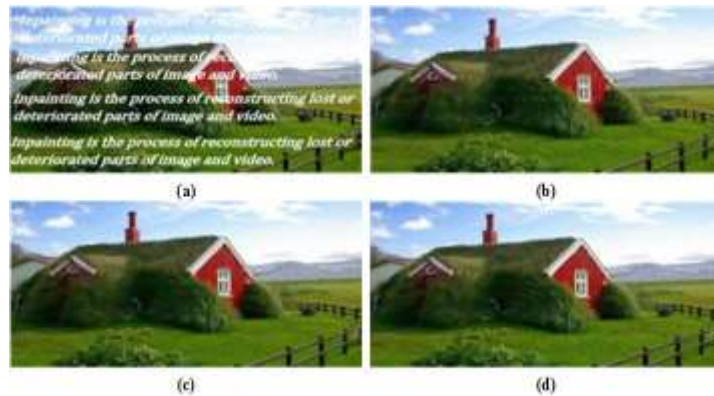


Figure4-8: Removing scratches PDEs inpainting methods. (a) Masked image, (b), (c), and (d) inpainted image using Harmonic, MES and Transport models, respectively.

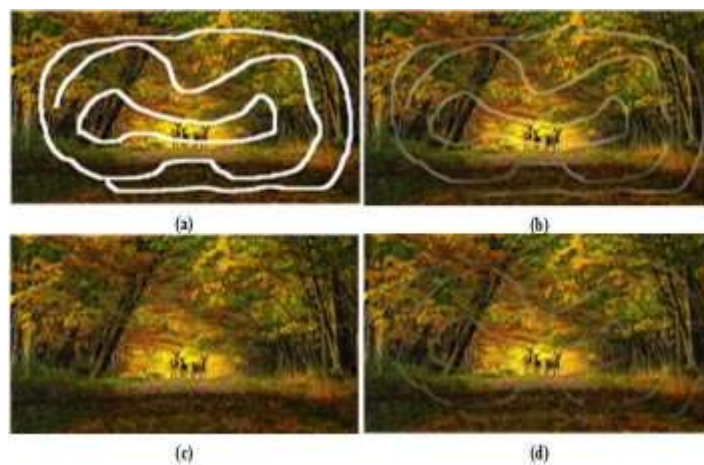


Figure4-9: Removing bold text using PDEs inpainting methods. (a) Masked image, (b), (c), and (d) inpainted image using Harmonic, MES and Transport models, respectively.

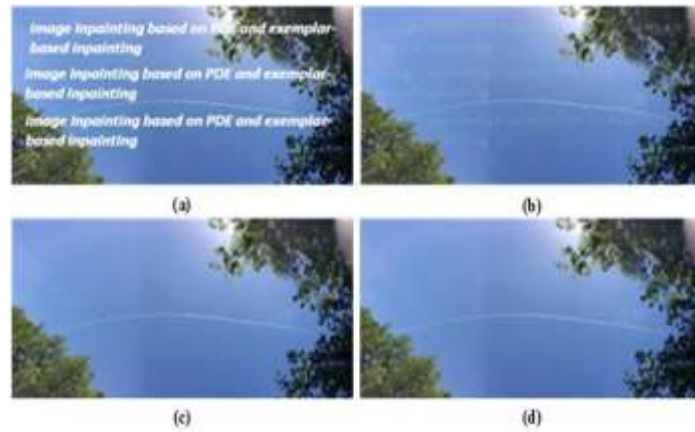


Figure4-10: Removing bold text by PDEs inpainting methods. (a) Masked image, (b), (c), and (d) inpainted image using Harmonic, MS and Transport models, respectively.

For image inpainting problems, the inpainting domain could be determined depending on the particular applications scenarios. So for text, scratch, and object removal, the inpainting domain is spatial, while the wavelet domain is used to recover the missing information which that especially lost through the image compression process (Chan et al. 2006). So, the linear and nonlinear 2nd-order PDEs techniques cannot preserve discontinuous image features such as edges that span large holes in an image and not good in the connection and holistic principle.

High-order PDE methods have been managed to address the shortcoming of the connection and holistic principle in the 2nd-order PDEs techniques, the researchers have found the higher-order PDEs able to repair this shortcoming. Where these techniques have utilised much of information from the source region that used to propagate the information in the missing region into an image. These techniques managed to fix edges problem in the damaged region, and their results were better than 2nd-order results, but these techniques still not have able to restoration large missing region in an image. To overcome this issue, the results of those 4th-order PDEs when they are used to recover the damaged regions of a structured (geometry) part in hybrid technique are analysed; see Chapter 5.

On the other hand, unlike most classical inpainting problems briefly reviewed above, the available image information is often given on complicated transform-based (spatial or frequency domain) sets instead of finite discrete ones (i.e. the given images). These complicated sets could contain 2-D sub-domains. An ideal inpainting scheme should be able to simultaneously benefit from all these different types of available information, to reconstruct the original images as faithfully as possible.

4.4.1 Second-Versus Higher-Order PDE Methods in Inpainting

In this section, the differences between the performances of 2nd- and higher-order models in inpainting are highlighted in order to analyse their impact on image quality. First of all, the order of TV inpainting methods is determined by the derivatives of the highest order in the corresponding Euler-Lagrange equation, while the order of PDE-BI methods is determined by the derivatives of the highest order in the equation formula.

C.-B. Schönlieb in (Schönlieb 2009) emphasised the difference between 2nd- and higher-order PDE-BI models in inpainting, and the author clarified their preference for using higher-order models instead of 2nd-order models in inpainting. For example, the TV model in (Chan & Shen 2002) has drawbacks when it comes to the connection of edges over large distances (i.e. Connectivity Principle) and the smooth propagation of level lines into the damaged domain (i.e. Curvature Preservation), because of the minimising process with 2nd-order derivatives in connecting level lines from the boundary of the inpainting domain via the shortest distance (linear interpolation), and this process has limitation with the length of the level lines.

The higher-order variational inpainting methods usually use two boundary conditions, whereby the second boundary condition is necessary for the well-posedness of the corresponding Euler-Lagrange equation of 4th-order. For example, the Dirichlet $u = f$ and Neumann $\nabla u = \nabla f$ conditions are defined on ∂D of given image f ; these conditions are used with the mCH inpainting model; the performance of this model supports the continuation of the image gradient into the inpainting domain. More precisely, the authors in (A. Bertozzi et al. 2007) proved the performance of mCH inpainting equation fulfils a stationary solution through recovering missing region; this means the information that wants to propagate in the inpainting domain will not only specified on the boundary of the missing region but also the gradient of the given image (i.e. on the directions of the level lines).

Also, there are drawbacks with the variational 3rd-order method to image inpainting, for example, the CDD model in (T. Chan and J. Shen 2001) successfully propagate the smooth information in missing regions (i.e. solving the problem of connecting level lines over large distances) but it failed to preserve the edges and curvature because the level lines are still interpolated linearly.

Finally, it is worth mentioning that high-order PDE-BI methods are time-consuming and not easy to compute. Also, when the missing region has a large and rich-textured

neighbourhood, PDE methods, in general, will produce blurring artefacts. In the next section, the proposed new approach is presented. The PDE-BI methods are used for the recovery of missing regions based on the concepts of the colourisation process.

4.5 Inpainting based on PDE and Colourisation Methods in Spatial Domain

The above PDE methods recover missing image regions by applying the adopted methods in each colour channel separately. A new class of PDE-BI methods is proposed, that benefits from the colourisation methods of section 3.4.2. Below, the steps of this proposed approach are presented:

1. Converting the masked image into YCbCr colour space.
2. Recovering the missing regions in the Y channel by applying PDE-BI methods,
3. Adding the colour to missing colour regions in Cb and Cr channels by using PDE colourisation methods.
4. Converting the inpainted YCbCr image back to the RGB colour space.

In particular, after converting the masked RGB image to YCbCr space, the MES and the mCH methods are applied to recover the missing regions in the Y channel, then the Poisson and 4th order PDE colourisation methods as developed in Chapter 3 are used, , to add colours to missing Cb and Cr colour channels. Finally, the inpainted images in the YCbCr space have been converted to RGB image space. The proposed scheme has been applied on a set of natural in the database images, and its results are compared with results of applying only PDE-BI methods, as shown in Figure 4-11 and Figure 4-12.

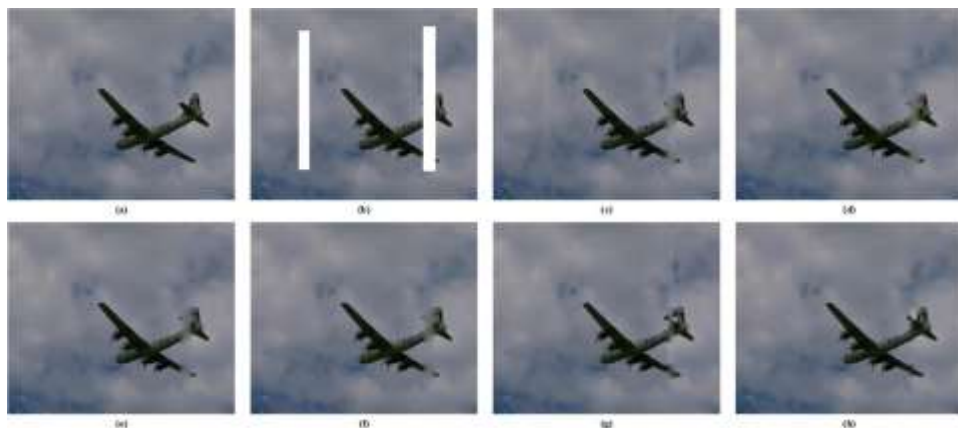


Figure 4-11: Recovering missing regions using PDE-based inpainting and colourisation methods in the spatial domain. (a) Original image, (b) masked image, (c), (e), and (g) inpainted image using harmonic, MESm, and mCH models, respectively, (d), (f), and (h) inpainted image using harmonic, MESm, and mCH models with colourisation method, respectively.

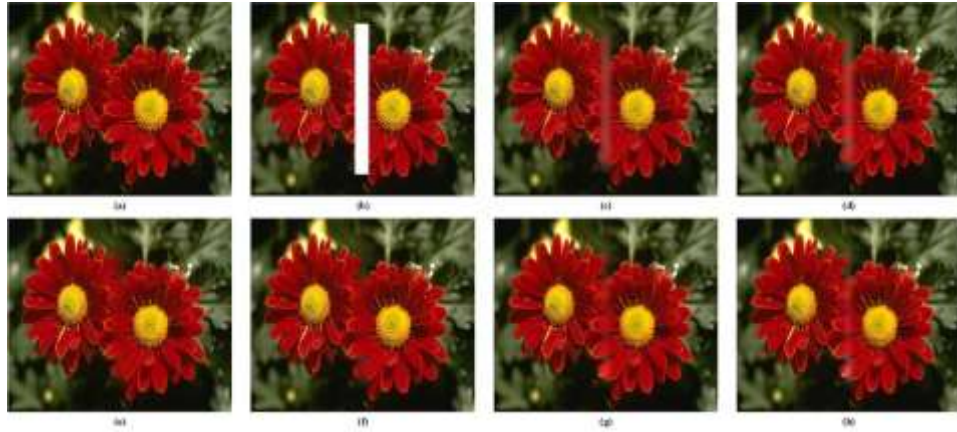


Figure 4-12: Recovering missing regions using PDE-based inpainting and colourisation methods in the spatial domain. (a) Original image, (b) masked image, (c), (e), and (g) inpainted image using harmonic, MESm, and mCH models, respectively, (d), (f), and (h) inpainted image using harmonic, MESm, and mCH models with colourisation method, respectively.

We note our combined colourisation and PDE methods slightly improve visual quality compared to only using PDE methods (Figure 4-11 & Figure 4-12). However, the proposed method has the same limitations, of the original methods, when used with large size missing regions and with the high texture surrounding areas. A more detailed study of the performance of the various methods was conducted to recover two inpainting domains on 100 natural images, the traditional statistical measurements have applied to assess the quality of inpainted regions, as can be seen in section 4.7.2.

4.6 PDE-BI Method in the Frequency Domain

In this section, the PDE-BI method is applied in a frequency domain whereby the image is first converted from the spatial domain into the frequency domain using mathematical transforms, there are many kinds of transformation, but we confine our discussion on the use of the Discrete Wavelet Transform (DWT).

In the frequency domain obtained by using wavelet transforms various image analysis problems have been solved due to their multiresolution properties and decoupling characteristics. The wavelet transform has advantages, for application to image inpainting; in this way, for instance, the size of a missing region will be reduced, which has a very favourable effect on the application of PDE methods. By comparison with other inpainting methods, we can expect a better global structure estimation of a damaged region in addition to better shape- and texture-preserving properties. The utilisation of wavelet transforms for image inpainting are proposed, owing to their advantages, as mentioned previously. The next section shows the application of PDE-based inpainting methods on the natural images in the wavelet domain.

Chapter 4: PDE Based Full Inpainting Methods

This PDE-BI method mimics the approach taken in the previous chapter, and reconstruct damaged regions of images in the wavelet domain using the following steps:

- Step 1.** The region from the original image to be inpainted is marked manually by the user.
- Step 2.** The original image with a damaged region is decomposed into the low and high-frequency components based on the Haar wavelet filter.
- Step 3.** The damaged region is repaired by using the PDE method applied to the low-frequency sub-band.
- Step 4.** The intensity values of the damaged region in high-frequency sub-bands are set to zero, this will cause some quality loss in the inpainted area, but this will not be noticeable especially if the area has relatively less edges.
- Step 5.** The inverse wavelet transform will be applied to reconstruct the inpainted image. (i.e. the inverse wavelet transform is used to convert these four sub-bands to one image which is called the inpainted image).

Initially, the PDE method is applied to recover the damaged region in each sub-band, and after studying the nature of the high-frequency coefficients (Gonzalez & Woods 2008), we found that the high three sub-bands have information in relation to the vertical, horizontal, and diagonal edges. Setting these values to zero for the inpainting area only will have a small effect on the quality after applying the wavelet inverse transform. Moreover, we could apply the PDE differently based on the edge direction in these three sub-bands, but this needs more investigation as there is some discontinuity in the edges information in these high-frequency sub-bands. So, we decided to sacrifice the quality and leave applying PDE on the high-frequency sub-bands for the future.

This method has been applied to natural images in two scenarios, referred to as the first- and 2nd-level wavelet domains. In the first scenario, the PDE has been applied to reconstruct the missing region in the low-frequency sub-band (i.e. approximation sub-band), and in the other three sub-bands, the values of missing high-frequency coefficients have been estimated. In the second scenario, the PDE has been applied to reconstruct the missing region in the low-frequency sub-band in the 2nd level wavelet domain, and the values of missing high-frequency coefficients have been estimated in six other sub-bands. Four PDE methods have been applied to reconstruct the missing region in the low-frequency sub-band see Table 4-1. The steps of this method in several

Chapter 4: PDE Based Full Inpainting Methods

instances are illustrated in Figure4-13. This Figure shows the implementation of the PDE-BI methods in the first and 2nd level wavelet domains. The harmonic model has been applied to recover the missing regions in the low-frequency sub-band domain.

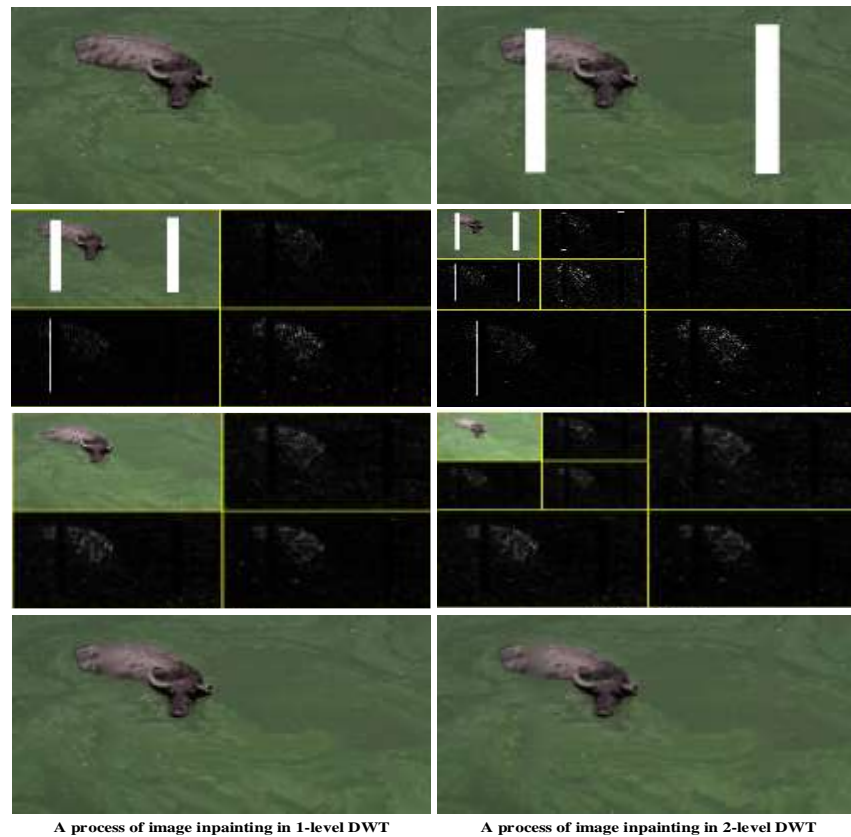


Figure4-13: Inpainting based-PDE method in 1st and 2nd level Haar wavelet domain.

The left column represents the process of the PDE method in level-1in DWT domain, while the process of the PDE method in the level-2 DWT domain is represented in the right column. There is no difference between the inpainted images visually in the last row of each column, but the inpainted image in the level-1DWT domain may be described as a little better than in the level-2 DWT domain based on values of MSE and PSNR measures. The white mask that was used in Figure4-13 will be applied to a set of natural images; then different PDE-BI methods will be used to recover the missing regions in different levels of the DWT domain. Table 4-1represents the averages of MSE and PSNR for image inpainted in different level DWTs via PDE-BI methods.

Equations	Harmonic		Transport		MESm		mCH	
	MSE	PSNR	MSE	PSNR	MSE	PSNR	MSE	PSNR
1 st	953.209	19.7273	916.273	19.6507	802.234	20.4884	766.063	20.4429
2 nd	1023.694	18.1239	975.391	18.7723	886.348	19.6722	813.759	19.8872
3 rd	1153.776	17.8537	1016.87	18.1962	964.997	19.9472	905.358	19.9723

Table 4-1: The average values of MSE and PSNR of inpainted images of PDE methods in different levels of DWT.

Chapter 4: PDE Based Full Inpainting Methods

The averages of MSE and PSNR from inpainted images in level-1 DWT are better than those resulting from other levels of DWT; the values of MSE and PSNR become gradually worse as the levels of DWT rise, which means that the efficacies of the PDE-BI methods became gradually worse in recovering the missing regions when applied to increasingly high-level DWT sub-bands. In the figures below, some of the experimental results are demonstrated for different PDE-BI methods in different inpainting domains. So, these PDE-BI methods have been applied to recover the missing regions in level-1 DWT domain.

Figure4-14 shows inpainted images by using PDE-BI methods in the Haar wavelet domain while in Figure 4-15 presents the inpainted images by applying PDE methods in the Daubechies 8 wavelet domain.

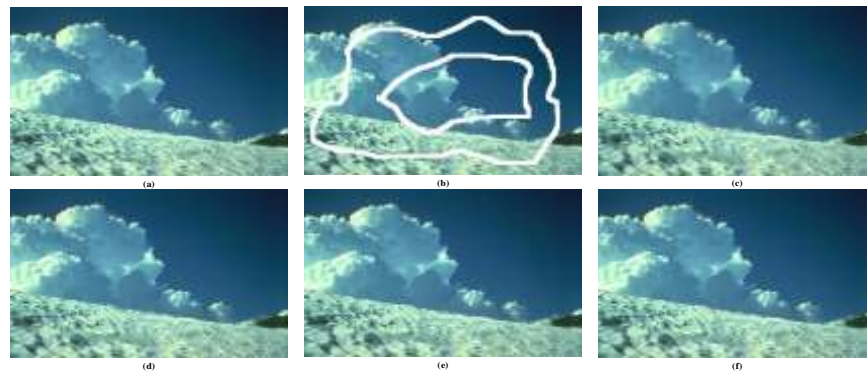


Figure4-14: Removing scratches using PDE inpainting methods in the frequency domain. (a) Original image, (b) original image with scratches, (c), (d), (e) and (f) inpainted images using Harmonic, Transport, MES and mCH models, respectively.

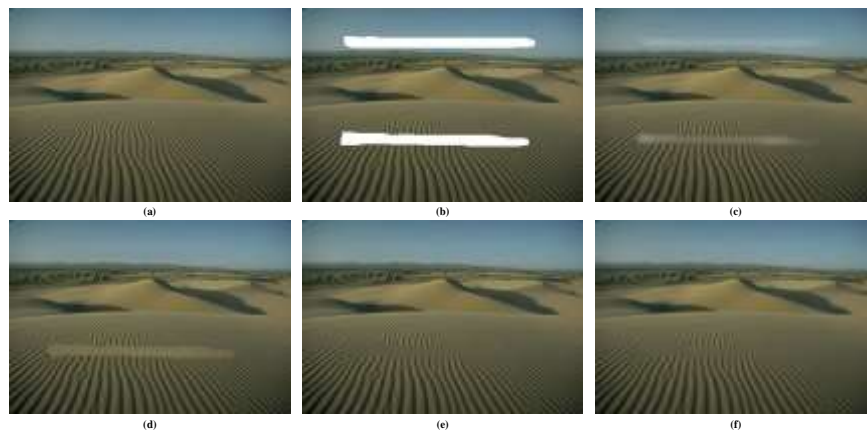


Figure4-15: Removing scratches using PDE inpainting methods in the frequency domain. (a) Original image, (b) original image with scratches, (c), (d), (e) and (f) inpainted images using Harmonic, Transport, MES and mCH models, respectively.

As shown in the above Figures, PDE-BI methods have succeeded in recovering small, smooth missing regions with non-textured areas around them, while PDE-BI methods

still have a problem in recovering missing regions with textured surrounding areas in the spatial domain, as seen in

Figure4-14 and 4-15.

In Chapter 6, the properties of wavelet transforms in image analysis are used to characterise non-textured and textured image components (i.e. low-frequency coefficients and high-frequency coefficients). Moreover, the PDE-BI methods are used to recover missing regions via the low-frequency sub-band, and another inpainting method will be used to recover the high-frequency sub-bands then the results will be combined. Comparisons will be made about the performances and efficacies of methods as well as their abilities to recover deleted areas in the spatial and frequency domains, in sections 4.7.2.1, 4.7.2.2 and 4.7.2.3.

To deeply study the efficacies of 2nd and high PDE-BI methods in the spatial and wavelet domains, we have applied them to two sets of images (natural and faces databases). Statistical measurements and the TDA approach have been used to study and compare the results of the implementations of these equations in each domain. The next section will show these databases and the results of applying these methods to them in the spatial and frequency domains.

4.7 Image Quality Assessment Post Inpainting

The aim in this section is to test the qualities of various images which have been inpainted using various PDE-BI methods. In general, high-order PDE-BI methods are expected to produce better quality images than the 2nd-order PDE-BI methods. Therefore, the efficacies of the various 2nd- and high-order PDE-BI methods as bases for inpainting in spatial and frequency domains are compared by assessing the qualities of their output images using a variety of quality measures. Next, two databases used in our experiments, the first consisting of natural images and the other of face images.

4.7.1 Databases Description

This subsection gives a brief description of two publicly available databases; a face biometric database and a natural image database that is used in our experiments to evaluate the suitability of the different PDE-BI methods. Statistical measurement methods and topological data analysis methods have been used to evaluate the efficacy of these PDE-BI methods. The first database is Berkeley segmentation dataset and Benchmark database (Pablo Arbelaez 2007) as described in Chapter 3. The inpainting-

Chapter 4: PDE Based Full Inpainting Methods

based PDE methods have been applied to 100 images of this database. These images have been selected based on the quantity of texture and structure which helps to check the efficacy of the PDE-based inpainting methods in recovering small missing regions. Figure 4-16 illustrates examples of natural images from the Berkeley segmentation and Benchmark database.



Figure 4-16: Example of eight out of 300 training natural images.

The second database is the Extended Yale B database (Lee et al., 2005) in (Deng Cai, Xiaofei He, Yuxiao Hu 2005) which is widely used to test the performance of face recognition schemes. This database consists of 2414 face images of 38 individuals each having 64 images, in frontal pose. The reason of choosing this database is the fact that the inpainting techniques can improve the performance of face recognition applications, for example, in the case of having occluded face images with missing regions, these PDE-BI methods recover the missing region and provide a better-quality image which boosts the application performance. Moreover, these techniques can be used for object removal, for example, removing glasses from face images. The size of these images is 192×168 . The images in the database are divided into five subsets. The inpainting-based PDE methods have been applied to 76 images of this database.

Figure 4-17 shows some examples of training face images taken from the Extended Yale B database.



Figure 4-17: Example of eight out of 114 training face images.

4.7.2 Statistical Measurements for Image Quality

This subsection shows the results of two groups of experiments, which have been conducted and are reported in both; spatial and frequency domain. Also, the quality assessment of the inpainted images for these experiments is checked by using statistical measurements and the TDA approach. On the other hand, the performance of each PDE-BI method used in these experiments has been studied and discussed by using the TDA approach. To keep to chronological order, the statistical measurements to check the quality of inpainted images of these two groups of experiments in the spatial and frequency domains.

4.7.2.1 Experiment 1: Results of using PDE on the natural dataset

Different experiments are conducted to measure and compare image quality in the inpainted images concerning the original images in the spatial and frequency domain, using MSE, PSNR, SSIM and entropy quality measures. The test images were inpainted using various PDE-BI methods. The original images of the Berkeley database were used as the reference by which to measure the quality of inpainted images. In this section, five experiments have been applied to 100 images of this data set. The aim of these experiments is to study the effect of the order of PDE-BI methods on the reconstruction of the edges in different sizes of missing regions in the natural images and to study the performance of these methods in reconstructing these missing regions. These experiments have used harmonic, transport, MES, and mCH methods in the spatial and frequency domains. In general, image inpainting can be described as follows: Let Ω be the image domain, let $f: \Omega \rightarrow R^+$ be the given original image, and domain $D \subset \Omega$ represents the region with missing information. We refer to domain D as the inpainting domain, and we assume it has already been identified, as illustrated in Figure4-1.

Five cases of inpainting domains (damaged regions) have been created in the images by using binary masks. The next equation represents how the scratches and texts are added to the original images,

$$f_{\text{Damaged}}(x, y) = M^{-1}(x, y) \times f(x, y) + M(x, y) \quad (4.57)$$

where f is the original image, M is the mask image and M^{-1} is the logical inverse of the mask image, where

$$M^{-1}(x, y) = 1 - M(x, y)$$

The size of the mask is the same as that of the original image. Multiply every element in the inverse mask matrix by the corresponding element in the original image matrix. The

Chapter 4: PDE Based Full Inpainting Methods

mask images have been chosen based on the width of the texts and scratches; the first two masks represent the different sizes of text. The font sizes in the texts of the mask images in C1 and C2 are 12pt, and 16pt respectively. The other mask images represent two different-sized scratches (C3, C4) and two missing blocks (C5). Figure4-18 represents these five cases of damaged regions in images which have been applied to the database images to study the efficiency of these PDE-BI methods. The first four masks will be applied to the set of natural images to study the efficacy of PDE-BI methods. On the other hand, as mentioned before, we are dealing with high textured colour natural images, and these PDE-BI methods cannot deal with the highly textured images. Therefore, the mask C5 will be used to check the ability of PDE-BI methods to recover large missing regions. These PDE-BI methods will be applied to recover the missing regions in each channel image.

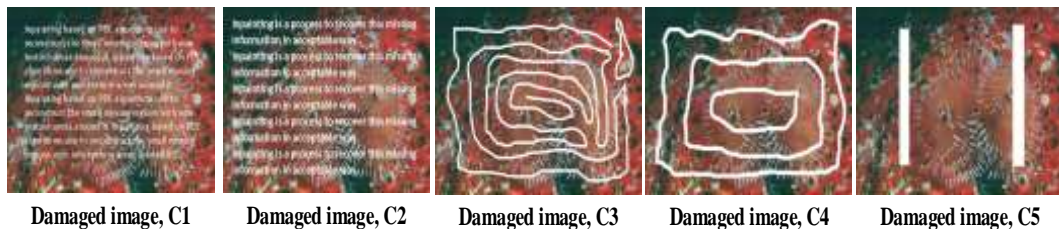


Figure4-18: The same natural image with five different inpainting domains.

Harmonic, transport, MES, and mCH methods have been used to remove the texts and scratches from the damaged natural images; these methods are applied on 100 images from the Berkeley database in spatial and frequency domain.

Figure4-19 and 4-20 show the results of removing the scratches in the natural images in the spatial domain. An accurate evaluation of PDE-BI methods which simultaneously assesses inpainted images qualitatively and quantitatively is not an easy task. The qualitative evaluation of PDE-BI methods is conducted visually for inpainted images, while the quantitative evaluation of PDE-BI methods is done by applying statistical measurements between original and inpainted images.

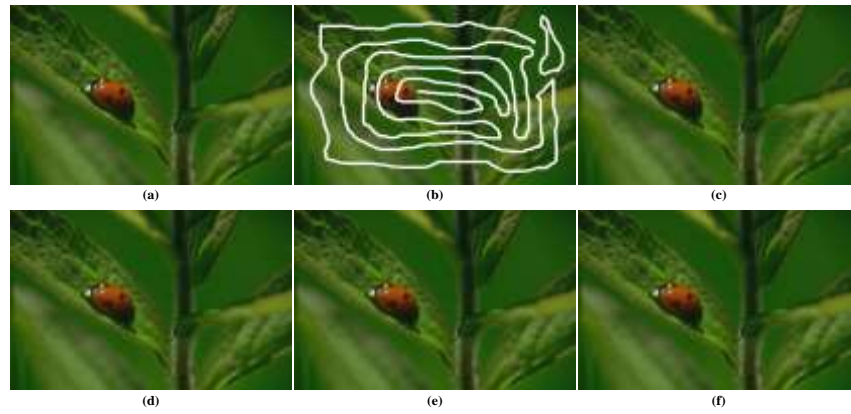


Figure4-19: Removing scratches using PDE-BI methods in the spatial domain. (a) Original image, (b) original image with scratches, (c), (d), (e), and (f) inpainted image using Harmonic, Transport, MES, and mCH models, respectively.

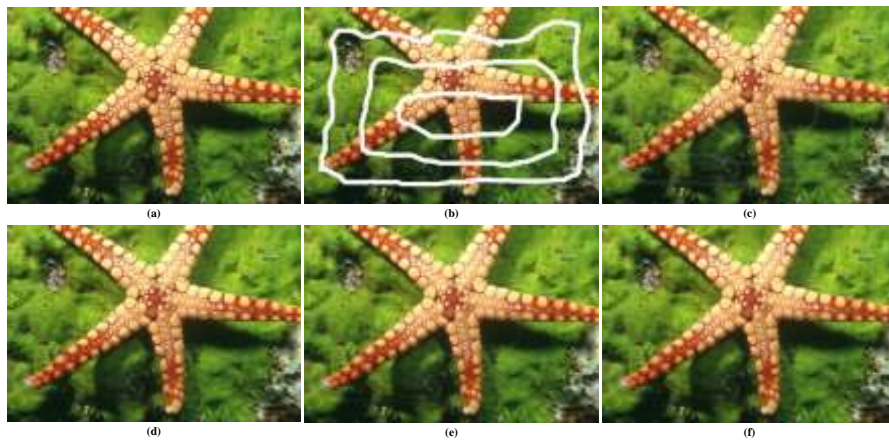


Figure4-20: Removing scratches using PDE-BI methods in the spatial domain. (a) Original image, (b) original image with scratches, (c), (d), (e), and (f) inpainted image using Harmonic, Transport, MES, and mCH models, respectively.

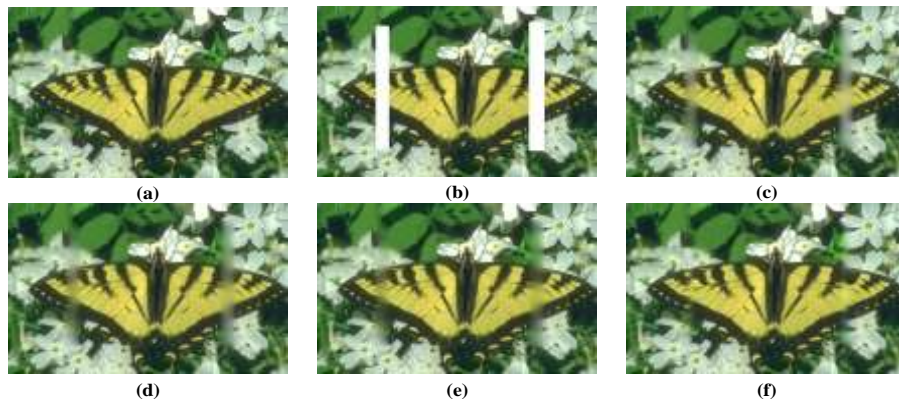


Figure4-21: Recovering missing regions using PDE-BI methods in the spatial domain. (a) Original image, (b) masked image, (c) Harmonic inpainted image at iteration 800, (d) Transport inpainted image at iteration 900, (e) MES inpainted image, (f) mCH inpainted image at iteration 550.

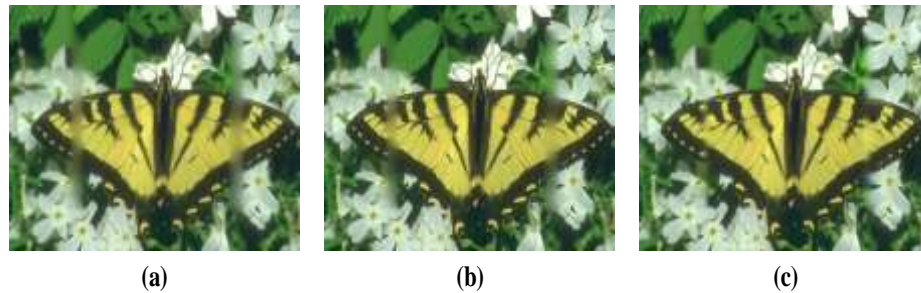


Figure4-22: Recovering missing regions using PDE-BI methods in the wavelet domain. (a) Transport inpainted image at iteration 600, (b) MES inpainted image, (c) mCH inpainted image at iteration 400.

We note that the inpainted images in Figure4-19 are visually almost identical to the original images. In Figure4-20 and 4-24, the harmonic inpainted images are visually not identical to the original images, whereas other inpainted images are visually identical to the original images. Also, the inpainted images created in the wavelet domain, as shown in Figure4-22 can be seen to be visually identical to those created in the spatial domain, shown in Figure4-21. Experimental testing shows that visually acceptable images may have different image qualities by numerical measures. The efficacy of these methods in recovering small missing regions has been studied by using the first four masks on the set of natural images. Their abilities to recover large missing regions have also studied by applying C5 on the set of images; this is the challenge for these methods.

To check further the quality of an inpainted image, statistical measurements are used, in particular, to check the efficacy of PDE-BI methods in the spatial and frequency domains. To get better-quality image inpainting, the qualities of the inpainted regions are checked by statistical measurements, so the SSIM, PSNR, MSE and entropy have been calculated only between the inpainted regions and the corresponding regions in the original images in both domains. Table 4-2 and 4-3 will summarise the comparison of the qualities of PDE-BI methods in the spatial and frequency domain respectively; the times taken to get the results using these models are also shown.

Cases	Equations	MSE	PSNR	SSIM	Entropy	Time (S)	Iteration
Case1	Harmonic	105.066	29.058	0.9230	2.6235	90	300
	Transport	99.4891	29.329	0.9324	2.6247	213	250
	MESm	48.7816	32.227	0.9376	2.6230	107	1
	mCH	76.0662	31.817	0.9168	2.6218	128	150
Case2	Harmonic	80.5039	30.263	0.9201	2.8960	135	300
	Transport	75.9052	30.568	0.9352	2.8971	159	200
	MESm	32.8185	33.929	0.9347	2.8961	112	1
	mCH	71.7534	34.892	0.9215	2.8941	131	100
Case3	Harmonic	145.232	27.613	0.9075	3.2861	143	350
	Transport	138.855	27.838	0.9201	3.2893	188	250
	MESm	102.398	27.992	0.9231	3.2835	142	1
	mCH	125.403	28.472	0.9024	3.1910	129	200
Case4	Harmonic	124.396	28.467	0.9296	1.4232	142	400
	Transport	120.454	28.618	0.9422	1.4230	210	300
	MESm	121.108	28.980	0.9430	1.4222	191	1
	mCH	112.138	29.350	0.9080	1.4212	175	250
Case5	Harmonic	906.190	19.618	0.9696	1.8905	285	800
	Transport	899.007	19.660	0.9705	1.9075	293	900
	MESm	803.808	20.493	0.9713	1.8911	179	1
	mCH	711.960	21.284	0.9942	1.8855	253	550

Table 4-2: The average values of MSE, PSNR, SSIM, and entropy are shown for image inpainting using Harmonic Transport, MES and mCH models in the spatial domain.

Cases	Equations	MSE	PSNR	SSIM	Entropy	Time (s)	Iteration
Case1	Harmonic	213.048	25.913	0.9883	2.6232	60	220
	Transport	188.726	26.371	0.9892	2.6231	165	200
	MESm	179.757	26.577	0.9897	2.6189	80	1
	mCH	158.180	28.021	0.9885	2.6170	90	100
Case2	Harmonic	175.986	26.766	0.9870	2.8888	100	250
	Transport	148.280	27.424	0.9886	2.8939	124	150
	MESm	143.517	27.577	0.9890	2.8206	85	1
	mCH	125.296	28.352	0.9894	2.7767	116	80
Case3	Harmonic	264.086	24.776	0.9843	3.2756	121	280
	Transport	277.645	24.751	0.9826	3.2868	151	200
	MESm	238.389	25.356	0.9845	3.2789	128	1
	mCH	185.293	26.998	0.9892	2.9002	91	150
Case4	Harmonic	226.494	25.868	0.9948	1.4185	117	300
	Transport	199.765	26.265	0.9952	1.4225	181	250
	MESm	195.582	26.378	0.9953	1.3903	168	1
	mCH	176.072	27.778	0.9911	1.3682	156	200
Case5	Harmonic	953.209	19.727	0.9124	1.2445	240	550
	Transport	916.273	19.650	0.9705	1.1035	237	600
	MESm	802.234	20.488	0.9712	1.0996	120	1
	mCH	766.063	20.442	0.9708	1.0923	190	400

Chapter 4: PDE Based Full Inpainting Methods

Table 4-3: The average values of MSE, PSNR, SSIM, and entropy are shown for image inpainting using harmonic transport, MES and mCH models in the frequency domain.

Table 4-2 and 4-3 show the average values of MSE, PSNR, SSIM and entropy resulting from the applications of harmonic, transport, MES and mCH equations for recovering the missing regions in the spatial and frequency domain. In both domains, the values of MSE, PSNR, SSIM and entropy obtained using the MES and mCH equations are better than those obtained using the harmonic and transport equations and the number of iterations of these equations to accomplish their tasks is less than required with other equations. On the other hand, the harmonic equation requires less time per iteration than those applied in the transport, MES and mCH methods. Also, MSm can be solved in a single step.

In the qualitative assessment, the images inpainted in the spatial and frequency domains look almost identical. On the other hand, in the quantitative assessment, the MSE, PSNR, SSIM and entropy measures resulting from these methods in the spatial domain are a little better than those obtained by using frequency-domain methods, while the number of iterations and computation time needed to recover the missing regions is less in the frequency domain than in the spatial domain. Also, the above tables show that high order PDE-BI methods are capable of effective region filling and give relatively high PSNR values with low MSE values, and the SSIM values are close to 1. Also, the MES and mCH methods got lower entropy value than harmonic and transport methods in both spatial and frequency domains.

To confirm current results regarding each PDE-BI method in both domains, Yale B database face images have been used to check the efficacy of the PDE-BI methods because face-recognition methods provide an excellent test for the qualities of inpainted images. In the next section, the results of applying PDE methods on Yale B Database images are introduced.

4.7.2.2 Experiment 2: Results of using PDE on the face dataset

The Yale B. database is famous, and this database has been used in the assessment of resolution enhancement of face images and image classification (image recognition). As the face images in this database are sensitive, even small changes are visually noticeable. Therefore, a set of experiments was conducted on the frontal face images from the Extended Yale B database, where the damaged images were generated by different mask images. Five mask images have been used to study the performance of the PDE-

Chapter 4: PDE Based Full Inpainting Methods

BI methods and the quality of the inpainting results in the spatial and frequency domains. In general, the size of the damaged region affects the performance of the PDE-BI methods in the reconstruction of an image, which means it will affect the result of inpainting images as well. Equation (4.62) has been used to restore missing regions in the original images (i.e. face images) based on the mask images. These inpainting domains (damaged regions) have been chosen based on the width of the scratches, texts and blocks. The scratch inpainting domains (damaged regions) have contained different-sized scratches, where three mask images are scratches, and one consists of text and one of the blocks. Figure4-23 represents these five cases of database face images in which damaged regions have been created to study the efficiency of these PDE-BI methods in the spatial and frequency domains.



Figure4-23: The same face image with five different inpainting domains.

These inpainting domains (damaged regions) have been applied on the 76 face database images. Harmonic, transport, MES, and mCH methods have been used to remove the scratches, text, and blocks from the damaged face images. Figure4-24 to

Figure4-28 show the results of removing the scratches, text and blocks in the natural images in the spatial domain.

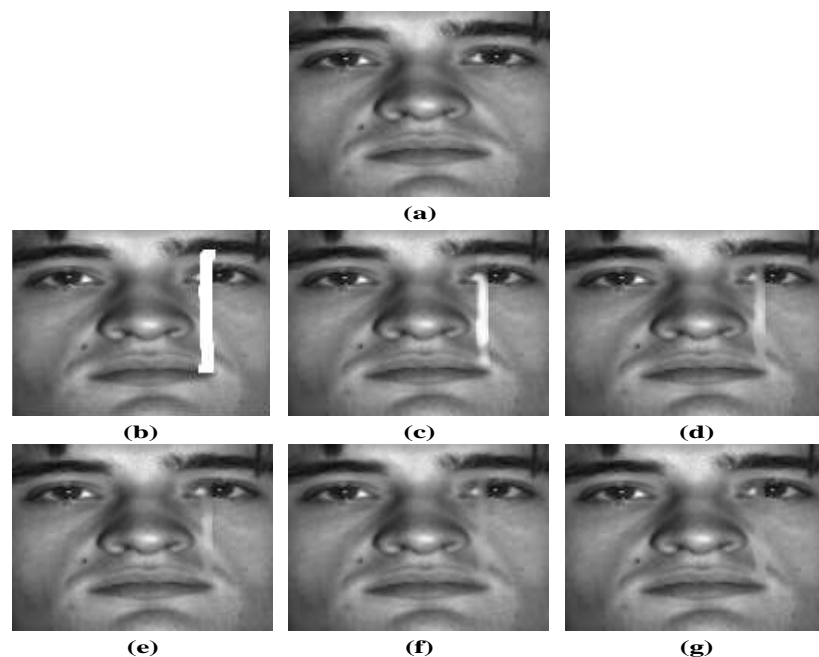


Figure4-24: Scratch removal using the harmonic model in the spatial domain. (a) Original image, (b) masked image, (c) at iteration 100, (d) at iteration 200, (e) at iteration 300, (f) at iteration 400, (g) at iteration 500.

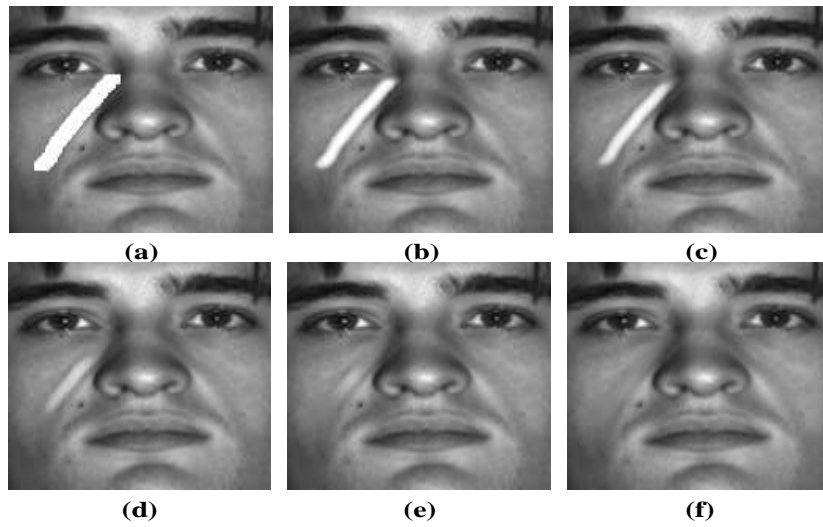


Figure4-25: Scratch removal using the mCH model in the spatial domain. (a) Masked image, (b) at iteration 50, (c) at iteration 100, (d) at iteration 200, (e) at iteration 250, (f) at iteration 300.

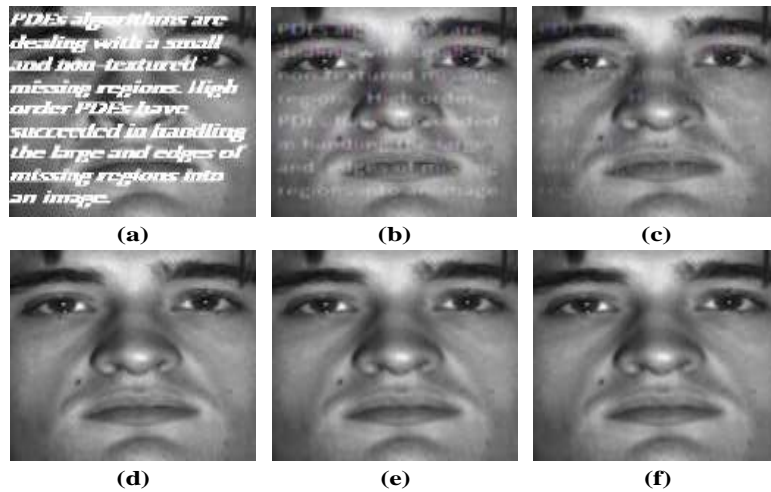


Figure4-26: Text removal using the harmonic model in the spatial domain. (a) Masked image, (b) at iteration 25, (c) at iteration 50, (d) at iteration 100, (e) at iteration 200, (f) at iteration 250.

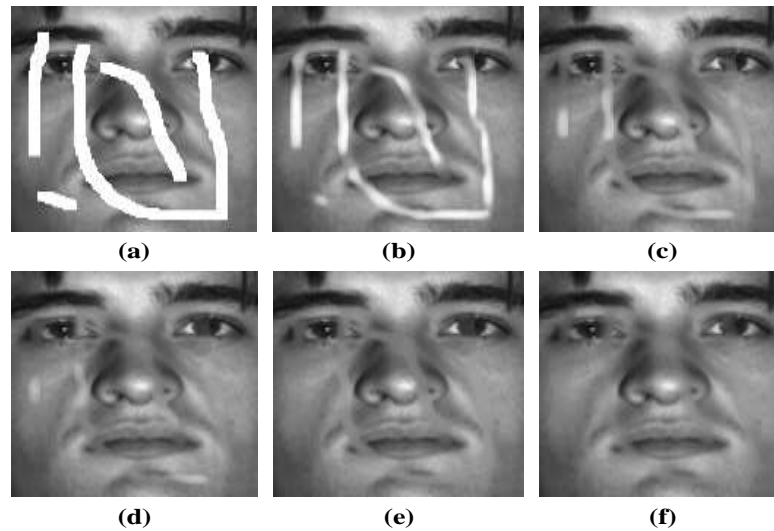


Figure4-27: Scratches removal using the transport model in the spatial domain. (a) Masked image, (b) at iteration 100, (c) at iteration 200, (d) at iteration 300, (e) at iteration 500, (f) at iteration 800.

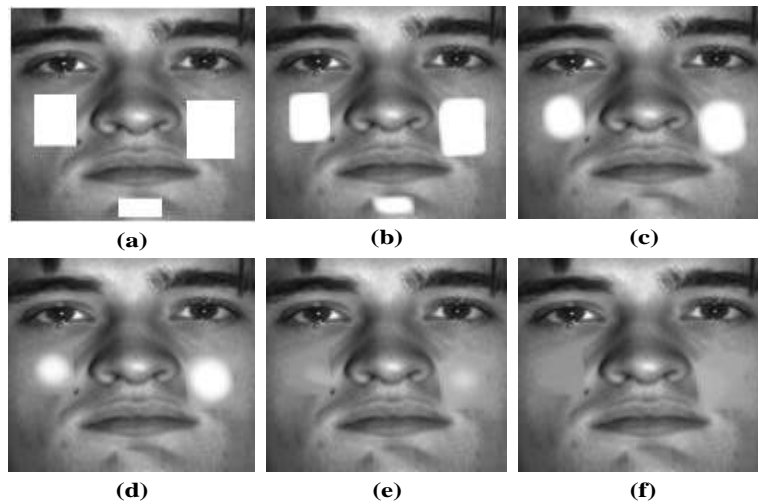


Figure4-28: Object removal using the transport model in the spatial domain. (a) Masked image, (b) at iteration 100, (c) at iteration 400, (d) at iteration 700, (e) at iteration 1300, (f) at iteration 2000.

Different scratches have been removed in Figure4-24, Figure4-25, and Figure4-27 by using harmonic, mCH and transport methods respectively at different numbers of iterations in the spatial domain. The scratches have different thicknesses. Figure4-26 illustrates the removal of text from the face image in the spatial domain by using the harmonic method at different numbers of iterations.

Figure4-28 introduces the replacement of missing regions (i.e. blocks) from the face image in the spatial domain by using the transport method at different numbers of iterations. Figure4-29 and Figure4-30 show the results of PDE-BI methods in the frequency domain.

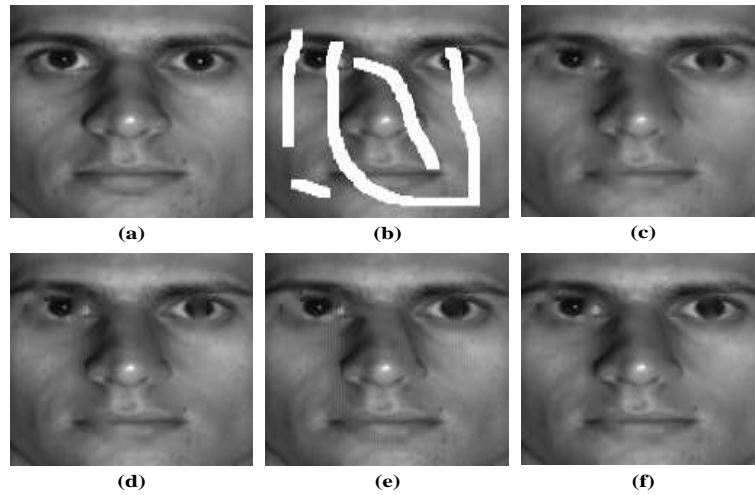


Figure4-29: Scratches removal using PDE-BI methods in the frequency domain. (a) Original image, (b) masked image, (c) Harmonic inpainted image at iteration 1100, (d) Transport inpainted image at iteration 1000, (e) MES inpainted image, (e) mCH inpainted image at iteration 400.

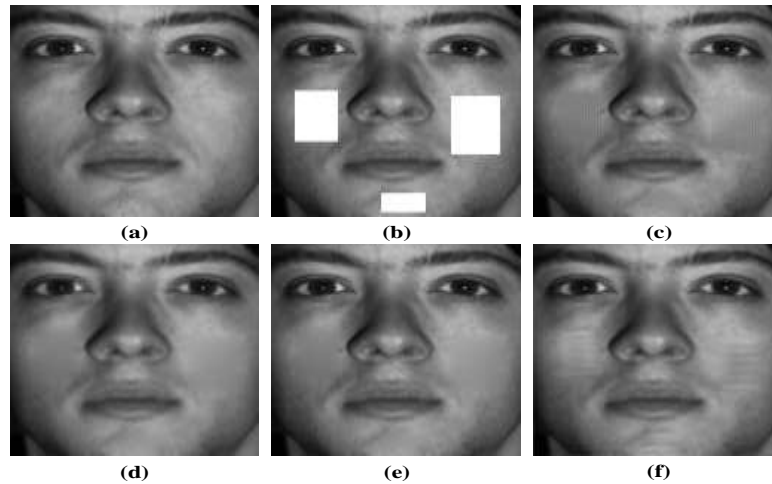


Figure4-30: Object removal using PDE-BI methods in the frequency domain. (a) Original image, (b) masked image, (c) Harmonic inpainted image at iteration 1100, (d) Transport inpainted image at iteration 1000, (e) MES inpainted image, (e) mCH inpainted image at iteration 400.

In the above Figures, experimental testing shows that visually acceptable images may have different numerically-assessed image qualities. Also, that the numbers of iterations needed to remove the scratches, text, and blocks by using the harmonic and transport method were more than were needed when using the MES and mCH methods in the spatial domain.

In the above Figures, all inpainting PDE-BI methods which were applied to recover the missing regions were faster in the frequency domain than in the spatial domain. Statistical measurements been have used to check numerically the quality of inpainted images and the efficacy of PDE-BI methods. SSIM, PSNR, MSE and entropy have been calculated only between the inpainted regions and the corresponding regions in the

Chapter 4: PDE Based Full Inpainting Methods

original images to get better measures of image inpainting quality. Table 4-4 and 4-5 will summarise the qualitative comparison of the inpainting PDE-BI methods in the spatial and frequency domain, where MSE, SSIM, PSNR and entropy have been used to measure the quality of image inpainting and the times taken to get the results using these models are shown as well.

Cases	Equations	MSE	PSNR	SSIM	Entropy	Time (s)	Iteration
Case1	Harmonic	307.125	23.843	0.9375	0.5924	60	450
	Transport	272.136	20.550	0.9375	0.5897	195	500
	MESm	52.5334	31.988	0.9426	0.5846	78	1
	mCH	134.103	25.193	0.9599	0.5838	71	250
Case2	Harmonic	162.620	23.597	0.9415	1.2619	95	500
	Transport	135.300	23.523	0.9407	1.2829	127	500
	MESm	131.798	28.291	0.9454	1.2606	88	1
	mCH	133.947	27.593	0.9589	1.2525	89	300
Case3	Harmonic	89.7650	28.770	0.9104	0.9324	104	250
	Transport	46.6170	28.673	0.9293	0.9297	165	300
	MESm	44.5452	31.922	0.9327	0.9146	108	1
	mCH	25.4027	34.458	0.9476	0.9238	97	100
Case4	Harmonic	117.959	23.889	0.9282	2.5001	102	500
	Transport	113.496	23.622	0.9325	2.5327	180	700
	MESm	103.051	28.179	0.9407	2.5004	165	1
	mCH	109.507	27.440	0.9522	2.4828	140	400
Case5	Harmonic	210.958	23.948	0.9311	1.3364	241	1700
	Transport	243.732	24.770	0.9543	1.3321	254	2000
	MESm	185.653	24.978	0.9522	1.3090	111	1
	mCH	201.333	25.129	0.9617	1.3025	210	550

Table 4-4: The average values of MSE, PSNR, SSIM, and entropy are demonstrated for image inpainting using harmonic, transport, MES and mCH models in the spatial domain.

Cases	Equations	MSE	PSNR	SSIM	Entropy	Time (s)	Iteration
Case1	Harmonic	500.004	21.673	0.9953	0.5818	45	300
	Transport	591.847	21.253	0.9951	0.5816	165	350
	MESm	155.775	22.349	0.9951	0.5802	57	1
	mCH	279.081	24.235	0.9971	0.5536	53	200
Case2	Harmonic	282.439	25.263	0.9970	0.5714	69	350
	Transport	260.869	25.236	0.9966	0.5711	88	300
	MESm	197.422	26.519	0.9974	0.5708	67	1
	mCH	229.500	26.300	0.9972	0.5699	64	200
Case3	Harmonic	170.002	21.073	0.9783	2.6289	81	150
	Transport	163.588	22.226	0.9950	2.6327	123	200
	MESm	107.365	23.292	0.9958	2.6275	78	1
	mCH	131.978	23.498	0.9852	2.6072	69	50
Case4	Harmonic	313.530	23.378	0.9809	2.4888	85	350
	Transport	308.715	23.408	0.9779	2.4932	150	400
	MESm	303.160	23.534	0.9811	2.4839	132	1
	mCH	276.612	24.846	0.9938	2.4837	111	250
Case5	Harmonic	514.422	22.236	0.9756	1.2987	214	1100
	Transport	453.196	23.613	0.9813	1.3050	217	1000
	MESm	339.910	23.771	0.9814	1.2654	82	1
	mCH	309.268	23.833	0.9749	1.2928	180	400

Table 4-5: The average values of MSE, PSNR, SSIM, and entropy are demonstrated for image inpainting using harmonic, transport, MES and mCH models in the frequency domain.

Table 4-4 and 4-5 showed the average values of MSE, PSNR, SSIM and entropy resulting from the application of the harmonic, transport, MES and mCH models for recovering the missing regions in the spatial and frequency domains respectively. In both domains, the values of MSE, PSNR, SSIM and entropy using the MES and mCH models are better than those obtained by application of the harmonic and transport models, and the number of iterations needed for this equation to accomplish its tasks is less than needed for other equations. Also, the harmonic equation consumes less time to accomplish its tasks than the transport, MES and mCH equations. In the qualitative assessment, the inpainted images in the spatial and frequency domains look almost identical. On the other hand, in the quantitative assessment, the results of MSE, PSNR, SSIM and entropy assessments show that spatial domain applications of the methods give better than frequency domain applications. Also, the above tables show that high-order PDE-BI methods are capable of effective region filling and give relatively high PSNR values with low MSE values, and the SSIM values are close to 1. Also, the MES and mCH methods got lower entropy value than harmonic and transport methods in both spatial and frequency domains.

4.7.2.3 Experiment 3: Results of using PDE and colourisation methods

The PDE with colourisation methods have been used to recover two inpainting domains on 100 natural images which shown in Figure 4-11 and Figure 4-12. The traditional statistical measurements have applied to assess the quality of inpainted regions in the spatial domain. Table 4-6 presents the statistical results of using the proposed method and traditional inpainting based PDE methods.

Cases	Equations	MSE	PSNR	SSIM	Entropy	Time (s)
Case1	Harmonic	614.707	21.8401	0.97940	0.89047	1500
	Harmonic & colourisation	456.952	23.1512	0.98149	0.89367	1900
	MESm	462.342	22.9065	0.98025	0.86222	100
	MESm & colourisation	339.608	24.2289	0.98214	0.87801	350
	mCH	526.774	22.0069	0.97874	0.86251	650
	mCH & colourisation	361.611	23.9189	0.98152	0.87516	800
Case2	Harmonic	1410.73	17.7137	0.97550	0.68849	2000
	Harmonic & colourisation	1353.16	18.4127	0.97588	0.68549	2200
	MESm	1027.05	18.1708	0.97721	0.65637	100
	MESm & colourisation	1017.18	19.5025	0.97725	0.65813	400
	mCH	1307.31	17.2358	0.97521	0.66711	750
	mCH & colourisation	1234.91	17.9722	0.97545	0.66334	1100

Table 4-6: The average values of MSE, PSNR, SSIM, and entropy are demonstrated for image inpainting using only harmonic, MES and mCH models and these models with colourisation method in the spatial domain.

In Table 4-6, the MSE, PSNR, SSIM and entropy measurements resulting from these methods are a little better than only PDE methods obtained in the spatial-domain methods because the colourisation helped to add colours to Cb and Cr channels based the information that recovered in the Y channel. Also, the PDE methods work better on the greyscale images.

4.7.2.4 Results Analysis

This section discusses the qualitatively and quantitatively evaluation of inpainted images obtained by using harmonic, transport, MES, and mCH models in both the spatial and frequency domains. In the qualitative evaluation, the inpainted images obtained by using four PDE models in Figure4-19 are visually almost identical to the original images because the scratches are small and all these PDE models successfully fulfilled the connectivity principle and the curvature preservation through recovering the missing regions in the spatial domain. Moreover, Figure4-20 and 4-21, the harmonic inpainted images are visually not identical to the original images, whereas other inpainted images are visually identical to the original images because the harmonic model is not connectivity propagate the information in the large missing region without

Chapter 4: PDE Based Full Inpainting Methods

produce artefacts and not preserve the curvatures by recovering the missing regions. On the other hand, the high order PDE models successfully in preserving the curvatures and connectivity propagate the information in the large missing region without produce any artefacts. On the other hand, the inpainted images created in the wavelet domain, shown in Figure4-22 are visually identical to those created in the spatial domain, shown in Figure4-21. Therefore, these inpainting PDE models need to assess the quality of inpainted images and the efficacy of these models quantitatively.

To sum up, the experimental testing shows that visually acceptable images may have different image qualities by statistical measurements. The inpainted images using 2nd and high order PDE methods in the spatial and frequency domains look almost identical in the first four masks on the set of natural and faces images. While their abilities of these methods to recover large missing regions have also studied by applying C5 on the set of natural and faces images; this is the challenge for these methods, the high order PDE methods have the ability to recover the large missing regions partly better than the 2nd-order PDE methods. Also, the inpainted images in both spatial and frequency domains are almost identical but at the same time, they have different statistical quality measurements.

On the other hand, in the quantitative assessment, the MSE, PSNR, SSIM and entropy measurements resulting from these methods in the spatial domain are a little better than those obtained in the frequency-domain methods because the intensity values of the damaged region in high-frequency sub-bands are estimated to zero, this will affect the quality of the inpainted area, and that will produce more error. Moreover, the number of iterations and computation time needed to recover the missing regions is less in the frequency domain than in the spatial domain, because the size of the damaged region in the frequency domain is smaller than its size in the spatial domain, as seen in Table 4-2, 4-3, Table 4-4, and 4-5.

In both domains, these tables show that high-order PDE methods (i.e. MES and mCH) are outperforming the 2nd- and 3rd-order PDE methods (i.e. Harmonic and transport), where the high order PDE methods are capable of effective region filling and give relatively high PSNR values with low MSE values, and the SSIM values are close to 1 for all the natural and faces images. The high order PDE models have been successful in preserving the curvatures and connectivity while propagating information into the missing regions and produce less error than the other equations. The reason behind this

Chapter 4: PDE Based Full Inpainting Methods

is that high order partial derivatives contain lower errors than 2nd order ones, and also because there is more information in the boundary conditions. Also, the MES and mCH methods got lower entropy value than harmonic and transport methods in both spatial and frequency domains, which means that the amount of disorder in the inpainted image obtained by using MES and mCH methods less than in the inpainted images obtained by harmonic and transport methods.

In both domains, the values of MSE, PSNR, SSIM and entropy obtained using the MES and mCH equations are better than those obtained using the harmonic and transport equations and the number of iterations of these equations to accomplish their tasks is less than required with other equations. On the other hand, the harmonic equation requires less time per iteration (because of its lower-order PDE) than those applied in the transport, MES and mCH methods. Also, the MESm can be solved in a single step because it is an elliptic equation. During the testing, it was found that while some images could look visually pleasing and similar, they have different PSNR values in both domains.

Moreover, these statistical approaches used to evaluate the outcome of inpainting based PDE methods in spatial and frequency domain such as MSE, PSNR, SSIM and entropy. During the work, we noticed the MSE is not always an ideal error estimation. An example of this is that a low error value will result in a visually pleasing result, but a large error value does not necessarily has to result in a poor visual result. This observation is shown in Figure4-31. We want to investigate if this quantitative estimation matches the quality of the images as perceived by human beings eyes. This is done by creating an experiment to analyse some of these observations; the high value of MSE in the natural images does not mean the image is not visually acceptable.

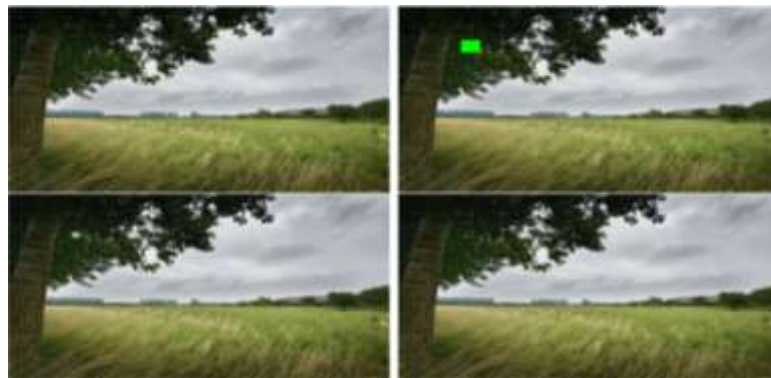


Figure4-31: Example to the MSE of image. First row: input image, masked image, second row: first result (high error) and the second result (low error).

Chapter 4: PDE Based Full Inpainting Methods

Despite its popularity in the image processing community, PSNR is not a reliable image quality measure. The PSNR depends on differences between corresponding pixels in the images under comparison and does not correlate well the visually perceived qualities of the images from which it is derived. In particular, PSNR does not take into consideration the spatial distribution of image pixel values. For instance, Figure4-32 shows two images which have the same PSNR whereas their perceived quality is very different, together with two inpainted images where one is visually more acceptable than its counterpart but with contradicting PSNR values.

In the end, the some of the quantitative evaluation measurements inversely proportional with the qualitative evaluation of the PDE inpainting results are concluded. This means the MSE and PSNR measurements do not match with visual assessment especially when the high texture images. The MSE and PSNR are not reliable quality measurements for assessing the image inpainting results.



Figure4-32: First row; an example of two images with different perceptual quality but the same PSNR (Winkler & Mohandas 2008). Second row; two inpainted images (a) visually acceptable inpainted image with PSNR = 15.3988 and (b) not the good inpainted version with PSNR= 17.0959.

In 2016, Aras et al. in (Asaad et al. 2017) proposed a method to assess the quality of degraded images using the emerging scheme of topological data analysis (TDA). They used Local Binary Pattern (LBP) as a texture feature descriptor, then they construct simplicial complexes for selected groups of uniform LBP bins and calculate persistent homology invariants (e.g. a number of CCs). Then they investigated image quality discriminating characteristics of these simplicial complexes by computing these models for a large dataset of face images. Lastly, they clarified the number of CCs not only distinguish between different levels of shadow effects but also help detect the infected

Chapter 4: PDE Based Full Inpainting Methods

regions as well. So the TDA approach deals well with texture in the images using LBP landmarks. Also, the TDA has been used to detect the tampering in the images which that been applied to detect the image shadow (Asaad et al. 2017), morphing (Asaad & Jassim 2017), and steganalysis (Asaad et al. 2018), so we will use it to detect the inpainted regions in the image.

The same topological approach is used to assess the quality of PDE-based inpainted images in spatial and frequency domain. Next, the TDA approach will use to check the quality of inpainted images based on build topological objects from images (inpainted regions).

4.7.3 TDA for Image Quality Assessment

The idea introduced in section 2.6.2 is followed, which builds a sequence of SC to assess the quality of the inpainted region. Here, the task is to assess the quality of inpainted methods, we deploy to recover the missing regions in natural and face images.

Figure4-33, below illustrates this idea by showing the simplicial complexes constructed from the positions of a single ULBP code for an original image and its inpainted version. The Rips complex graph for inpainted image and the original image are identical, except the inpainted region which we highlighted by red box. Therefore, the CCs will be calculated for inpainted regions and the same regions in the original image.

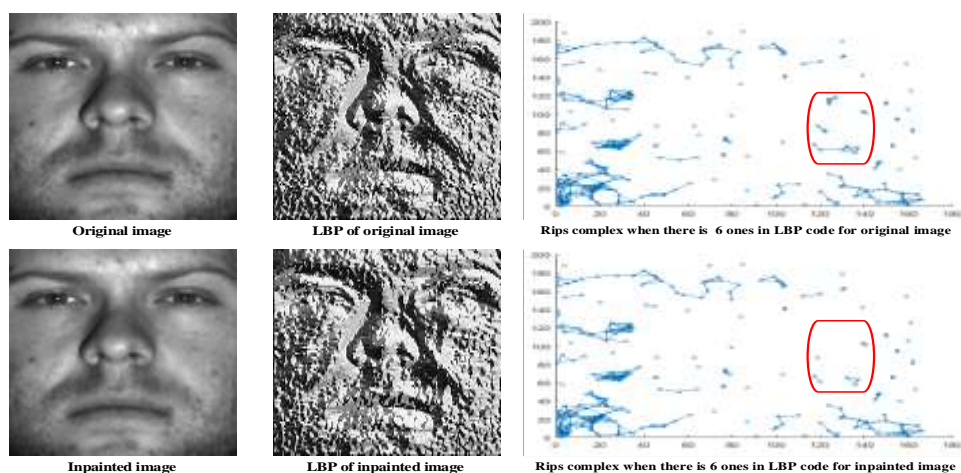


Figure4-33: LBP and simplicial complexes of the original and inpainted image at threshold $T=10$.

TDA approach is applied to study the performance of PDE-BI schemes, by quantifying the quality of the inpainted image at different iterations. As mentioned in section 2.6.2,

Chapter 4: PDE Based Full Inpainting Methods

the uniform LBP patterns determined by the number of ones in such patterns in natural images from the database of (Ojala et al. 2002). To estimate image inpainting quality, the number of CCs, at different thresholds, in the inpainted regions and the original regions are compared.

The TDA approach for evaluating the image inpainting quality is applied by counting the number of CCs in the inpainted regions, where the CCs is computed in 8 rotations in each one of these 7 geometries at different thresholdings. The TDA approach is successful in studying texture deeply in the inpainted regions. The results of the TDA approach matched the qualitative results. These results are outperformed by those obtained using statistical measurements in terms of their corresponding with their qualitative results, which means that the TDA approach gives good evaluation of image inpainting quality, as seen in the first row of Figure4-32, where the two images have the same PSNR value, but visually these images are not corresponding.

The TDA approach gives good description of these images in terms of the drawing of SC and the numbers of CCs in these images at the eight rotations in each one of the 7 geometries at different thresholds, as seen in Figure 4-34 which represents the SC shape of rotation R1 of geometry G6 at threshold T=10 (as mentioned in 2.6.2). The SC shapes of these images are clearly different and also the numbers of CCs are different. Hence, the TDA approach is successful in detecting the differences between these images where some of the statistical measurements failed. These results are also important in applications such as image forgery detection. For future work, the TDA approach can be used to detect forged images and to locate suspect regions in them.

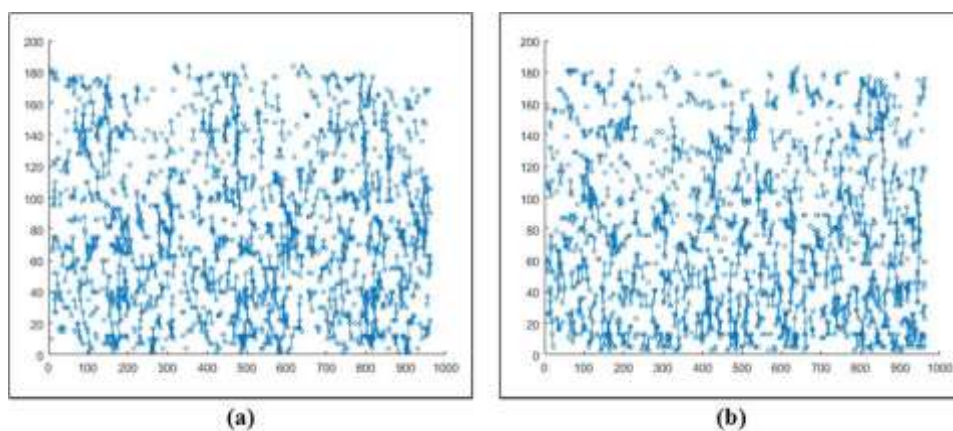


Figure 4-34: Example of drawing SC for two images that have same value of PSNR described in first row in figure 4-32. (a) SC of left image in the first row. (b) SC of right image in the first row.

Chapter 4: PDE Based Full Inpainting Methods

Figure 4-34 shows the SC of the images which have a different shapes of SC and also different numbers of CC.

The limitations of using the TDA approach are the time consumed when checking all these rotations in each of these geometries, then repeating them at different thresholds. In the future, we will try to reduce these huge computational processes.

The 7 ULBP geometries (G1, G2, ..., G7) in eight rotations (R1, R2, ..., R8) are studied at different thresholds $T=0$, $T=5$, $T=10$, and $T=15$, for the inpainted images of the two above experiments, the geometries G4 and G6 at threshold $T=10$ giving a good description of the results of PDE-BI methods at different iterations in five cases of damaged images that been studied, and below it is shown that geometries G4 and G6 are more sensitive to differences between inpainted and original regions in the natural images. Figure4-35 shows the average number of CCs of inpainted regions obtained using PDE-BI methods at different iterations for five damaged regions from natural images in both spatial and frequency domains. The Geometry 6 at threshold $T=10$ is shown below.

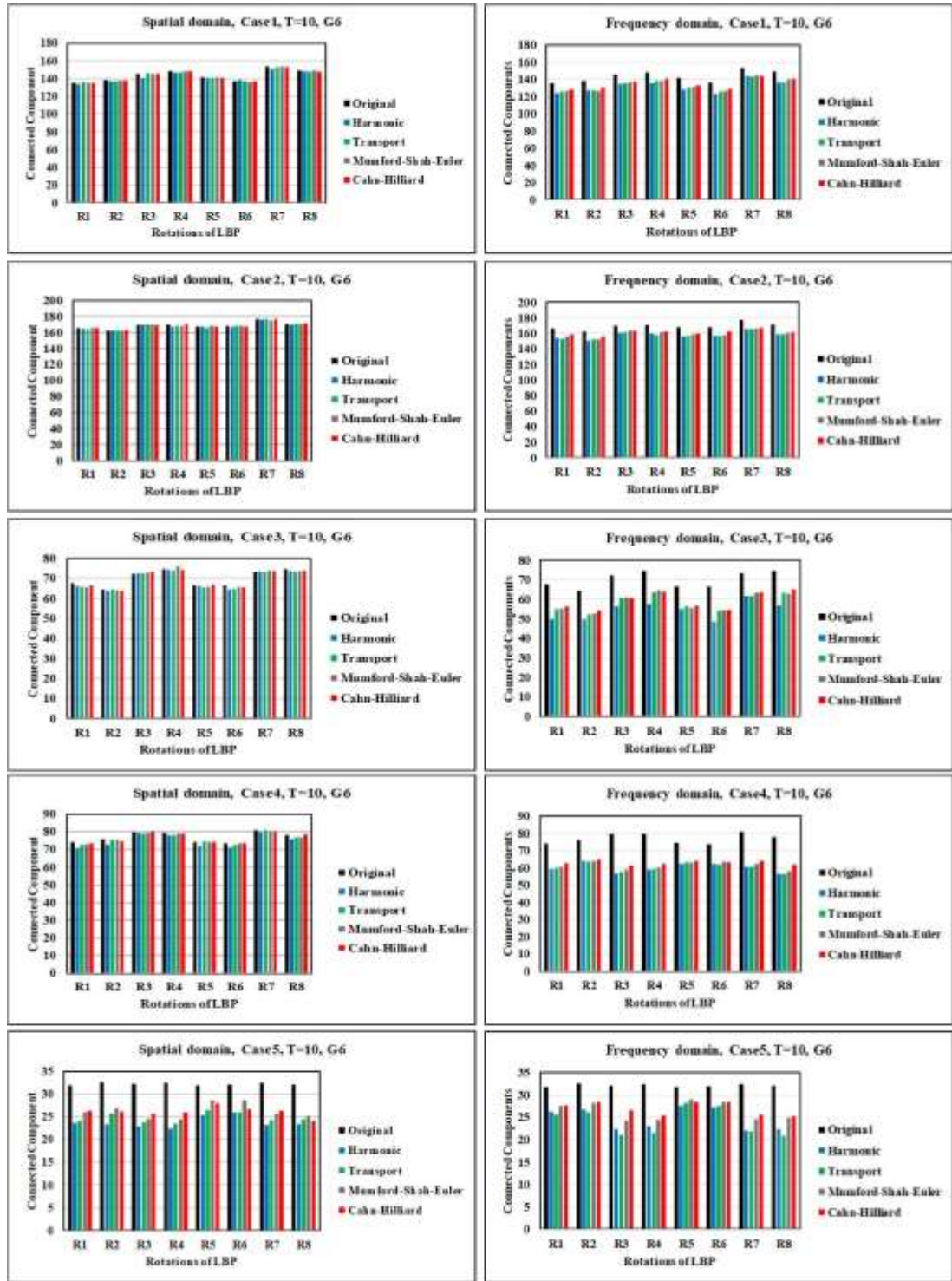


Figure4-35: Evaluation of performance of PDE-BI methods using TDA approach at 8 iterations in G6 at threshold $T=10$ for 5 inpainting cases of natural images. Left column: Average of the number of CCs in inpainted regions in the spatial domain. Right column: Average of the number of CCs in inpainted regions in the Frequency domain.

Figure4-35 clarifies the number of CCs. It has been found that in the G6 domain at threshold $T=10$, the inpainted images obtained using MES and mCH methods are closer than those obtained by the harmonic and transport methods to the original regions with respect to the the numbers of CCs in the both spatial and frequency domains.

Chapter 4: PDE Based Full Inpainting Methods

Figure4-36 shows the average number of CCs of inpainted regions which obtained using PDE-BI methods at different iterations for five damaged regions from natural images in the both spatial and frequency domains. The Geometry 3 at threshold $T=10$ describe below.

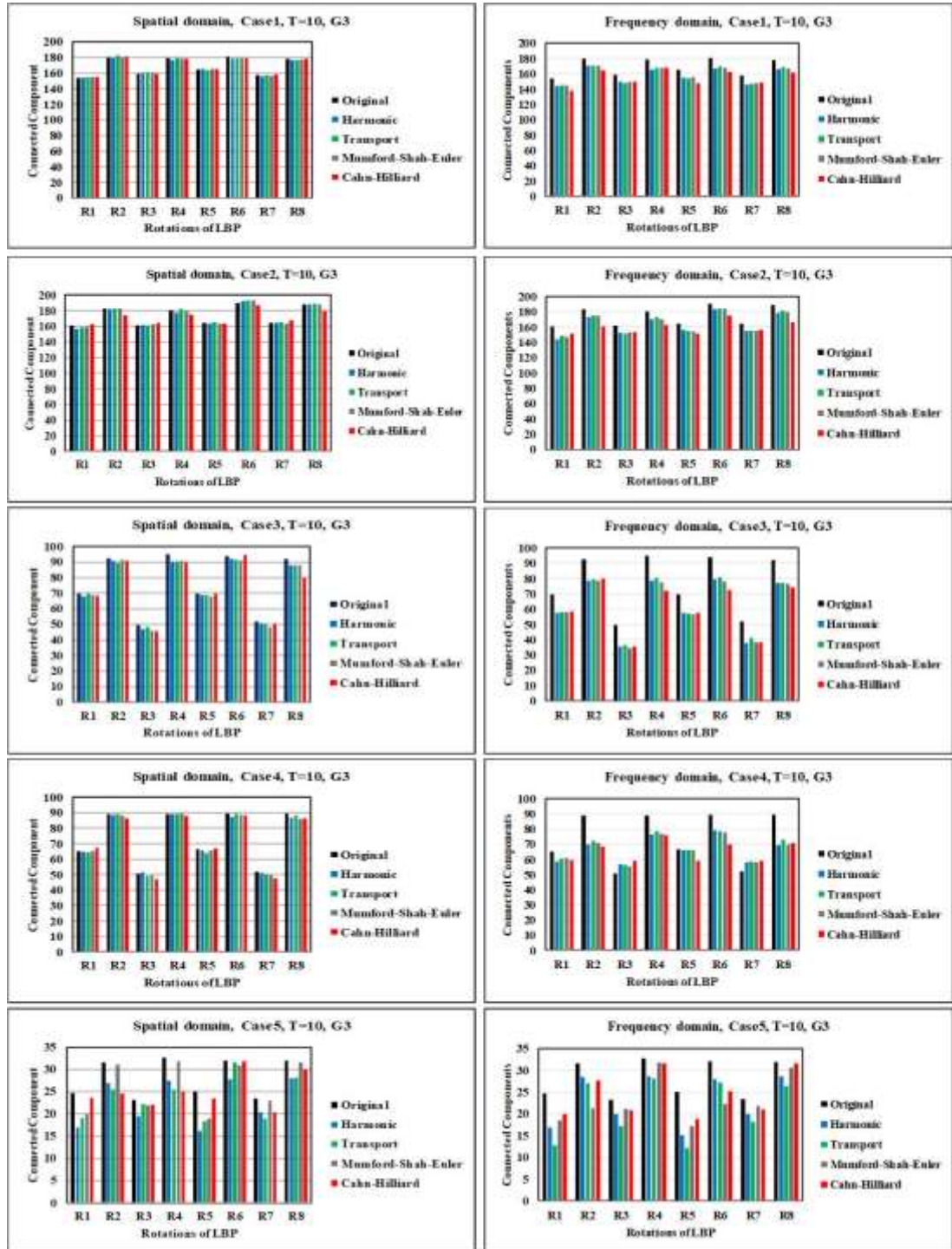


Figure4-36: Evaluation of performance of PDE-BI methods using TDA approach at 8 iterations in G3 at threshold $T=10$ for 5 inpainting cases of natural images. Left column: Average of the number of CCs in inpainted regions in the spatial domain. Right column: Average of the number of CCs in inpainted regions in the Frequency domain.

Chapter 4: PDE Based Full Inpainting Methods

The number of CCs in the other geometries at threshold $T=10$ is fickle. Moreover, the numbers of CCs in inpainted regions obtained by using harmonic and transport equations are close to those found in the original regions of natural images, which means that these geometries do not correspond well to the image quality assessments of these inpainting methods, as can be seen in Figure4-36; geometry G3 at threshold $T=10$. On the other hand, in the face images database, the number of CCs have been calculated in the inpainted images which were obtained by using four different PDE-BI methods in four inpainting domains (damage cases) in the both of spatial and frequency domains. Figure4-37 and Figure4-38 show the results of G6 and G3 in the spatial and frequency domains respectively. Also, the numbers of CCs in the inpainted areas which obtained using PDE-BI methods in the spatial domain are closer to those of the original areas in comparison with those obtained in the frequency domain.

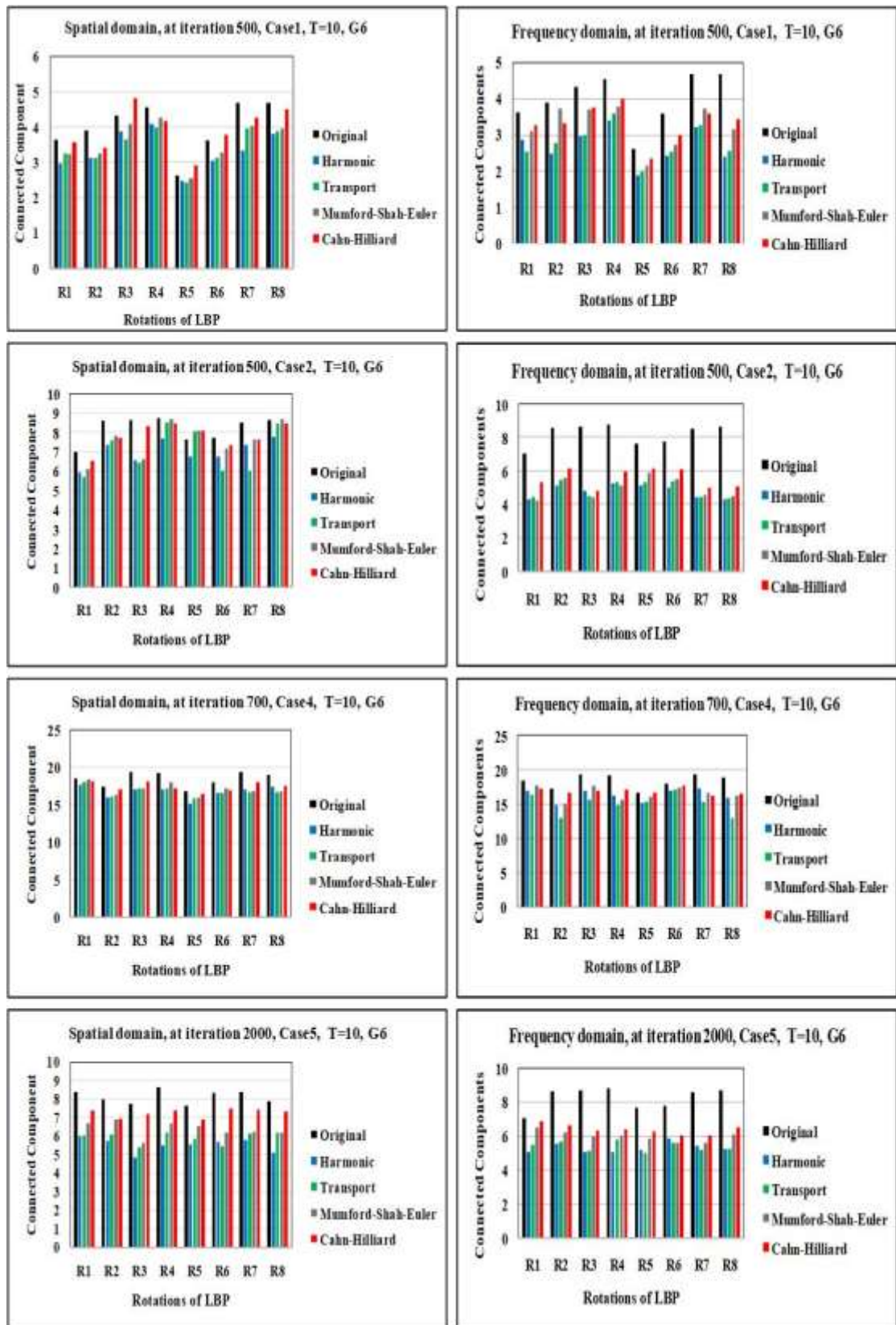


Figure4-37: Evaluation of performance of PDE-BI methods using TDA approach at 8 iterations in G6 at threshold T=10 for 5 inpainting cases of face images. Left column: Average of the number of CCs in inpainted regions in the spatial domain. Right column: Average of the number of CCs in inpainted regions in the Frequency domain.

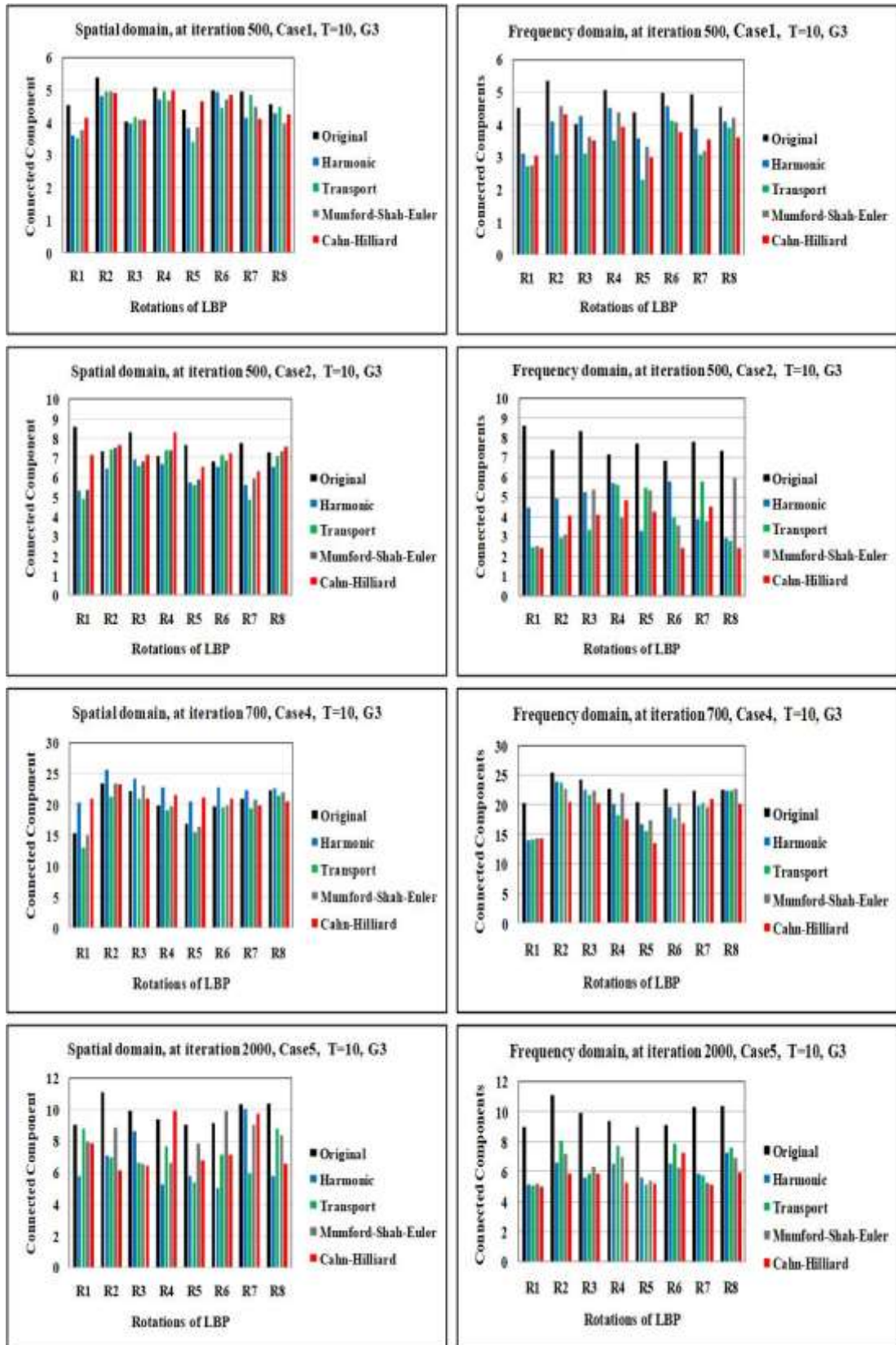


Figure4-38: Evaluation of performance of PDE-BI methods using TDA approach at 8 iterations in G3 at threshold $T=10$ for 5 inpainting cases of face images. Left column: Average of the number of CCs in inpainted regions in the spatial domain. Right column: Average of the number of CCs in inpainted regions in the Frequency domain.

Chapter 4: PDE Based Full Inpainting Methods

The results of face images are similar to the results of natural images. The numbers of CCs in the geometries G4 and G6 at threshold $T=10$ of inpainted images obtained by using MESm and mCH are closer to the numbers of CCs of the original regions than in the inpainted images obtained using harmonic and transport methods. The geometries G4 and G6 are a better descriptor to image inpainting quality, as seen in the above Figure4-35 and Figure4-37 which that show the number of CCs in the inpainted areas and corresponding original areas at threshold $T=10$, in G6.

For other geometries, the numbers of CCs are wobbling in the inpainted images, as seen in Figure4-36 and Figure4-38, which clarify the numbers of CCs in G3 at threshold $T=10$. In all these PDE-BI methods, the numbers of CCs of the inpainted areas in the spatial domain are closer to the CCs of original areas in comparison with the obtained in the frequency domain.

4.7.3.1 Results Analysis

As mentioned in section 2.6.2, the TDA is sensitive to tampering in the image (Asaad et al. 2018), (Asaad et al. 2017), and (Asaad & Jassim 2017), so any change in the image will be detected by the TDA approach, based on the number of CCs in certain regions (i.e. inpainted regions). In both spatial and frequency domains, the TDA approach has been applied to the inpainted regions and corresponding original regions in both the natural and face images in seven geometries at different thresholds; using the numbers of CCs in geometries G4 and G6 at threshold $T=10$ of inpainted images as measures of similarity to the original images, those obtained using the MES and mCH methods are closer to the original images than those obtained using harmonic and transport methods, in both spatial and frequency domains. The geometries 4 and 6 describe the edges and the end lines in the natural images (Ojala et al. 2002), while the same geometry describes the corners in the face images (Chan 2007). That means the MES and mCH methods have succeeded in reconstructing the edges and the end lines in the missing regions of the natural images and in reconstructing the corners in the missing regions of the face images (Esedoglu & Shen 2002), (A. L. Bertozzi et al. 2007).

Therefore, the best descriptor for image quality is based on the number of CCs resulting from the inpainting methods, where the best image inpainted quality is mCH then MESm then transport and the lastly harmonic equation for all rotations in the geometries G4 and G6. Moreover, the number of CCs of the inpainted areas obtained by using PDE-BI methods in the spatial domain is closer to the CCs of original areas in

comparison with the results obtained in the frequency domain because the intensity values of the damaged region in high-frequency sub-bands are estimated to zero, and this will affect the quality of the inpainted area and will produce more error, as shown in Figure4-35 and Figure4-37.

On the other hand, the number of CCs in the other geometries (i.e. G1, G2, G3, G5, and G7) at threshold $T=10$ are fickle, the numbers of CCs of inpainted regions in both natural and face images obtained by using harmonic and transport equations are close to those in the original regions of natural images. This means that these geometries at threshold $T=10$ do not correspond well to the image quality assessments of these inpainting methods in both spatial and frequency domains, as seen in Figure4-36 and Figure4-38. The results of the geometries G1, G2, G4, G5, and G7 at threshold $T=10$ will be presented in the appendix (see Appendix A).

The TDA approach has been successfully used to study and check the image inpainting qualities, because it is a very sensitive process which enables the study of inpainted regions at seven geometries, and each geometry has eight rotations which means that all the inpainted regions will be covered. Therefore, the TDA approach will be used to study the performance of PDE-BI methods in the next section.

4.7.4 TDA for PDEs Performance

This subsection shows the use of TDA to study the behaviour of PDE-BI methods and compare the results of 2nd-and high-order PDE-BI methods at different iterations. The TDA approach has been used to study the behaviour of PDE-BI methods. As mentioned before, two types of PDE-BI methods are applied which are elliptic and parabolic. The elliptic equations each have only one solution, while the parabolic equations have a finite iteration number of numerical solutions through which to recover the missing regions. For these reasons, the solutions of these equations are studied at different iterations, in order to check which one of these equations arrives at a steady state rapidly and thereby takes a low number of iterations to recover a missing region. The TDA approach has been applied to the inpainted image obtained by using these methods at different iterative solutions of the PDEs. After checking the quality of the results obtained by PDE-BI methods; the geometries G4 and G6 at threshold $T=10$ gives a good description to PDE-BI methods at different iterations in five cases of damaged images. Therefore, the TDA approach is used to study the behaviour of PDE-BI methods on four cases of damaged regions; we focus only on the study of these

Chapter 4: PDE Based Full Inpainting Methods

damaged cases on geometries G4 and G6. The number of CCs has accounted for the differences between inpainted regions and corresponding original regions at different iterations. The performances of PDEs have been checked based on the number of CCs of inpainted areas and corresponding original areas.

Figure4-39, 4-41, 4-43, and 4-45 below, show inpainting results of images at different iterations of four PDE-BI methods. Each row in these Figures represents inpainted images by using four PDEs at a specific iteration and so on for other rows.

Figure4-40, 4-42, 4-44, and 4-46 below, display the numbers of CCs in the inpainted regions and corresponding original regions at threshold $T=10$ in G6. Each Figure has four graphs which clarify the numbers of CCs for original and inpainted regions obtained by 4th PDE-BI methods at different iterations.

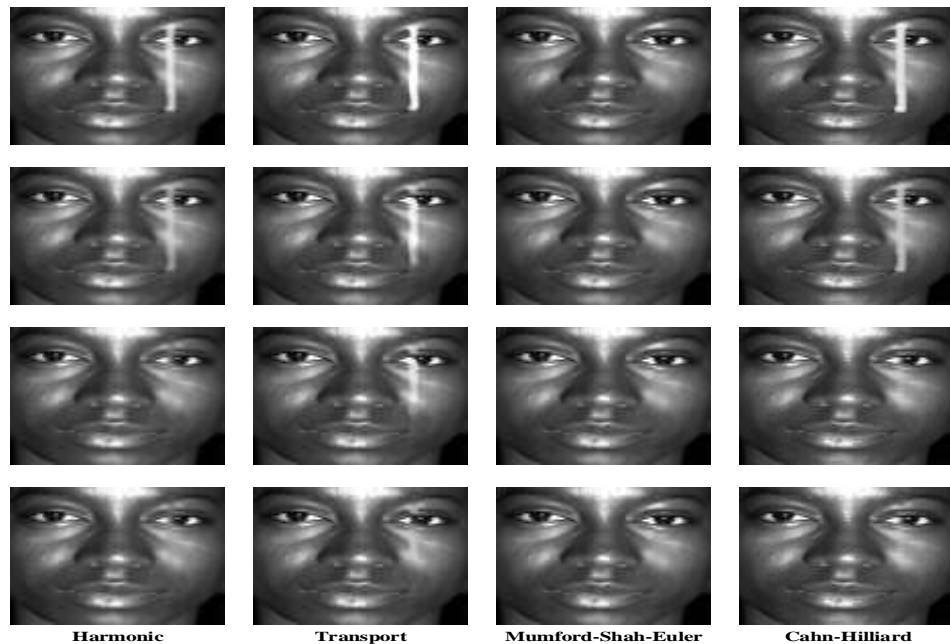


Figure4-39: Object removal using PDE-BI methods. Row 1, Row 2, Row 3, and Row 4 inpainted images using four models at 100, 200, 400, and 500 iterations, respectively.

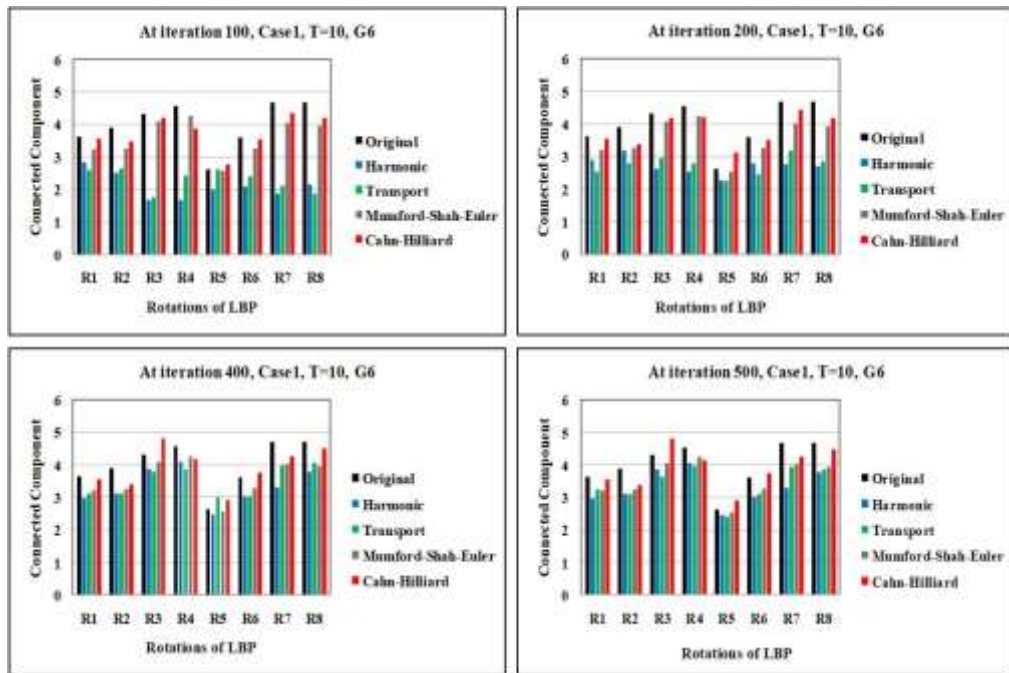


Figure 4-40: Evaluation of performance of PDE-BI methods using TDA approach at different iterations for case inpainting 1 in G6 at threshold $T=10$.

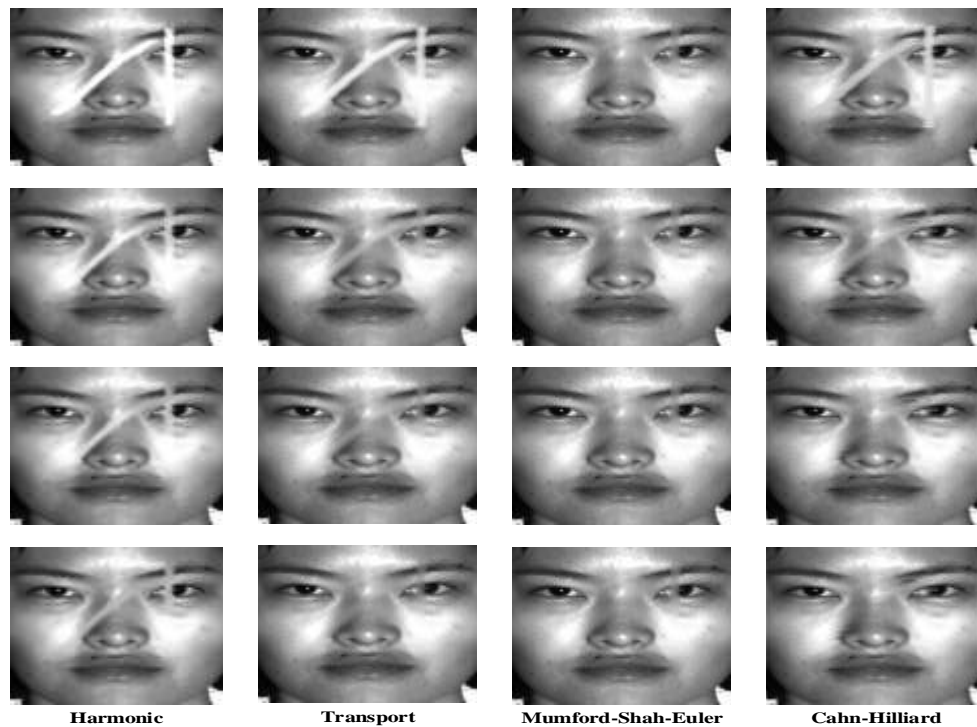


Figure 4-41: Object removal using PDE-BI methods. Row 1, Row 2, Row 3, and Row 4 inpainted images using four models at 100, 200, 400, and 500 iterations, respectively.

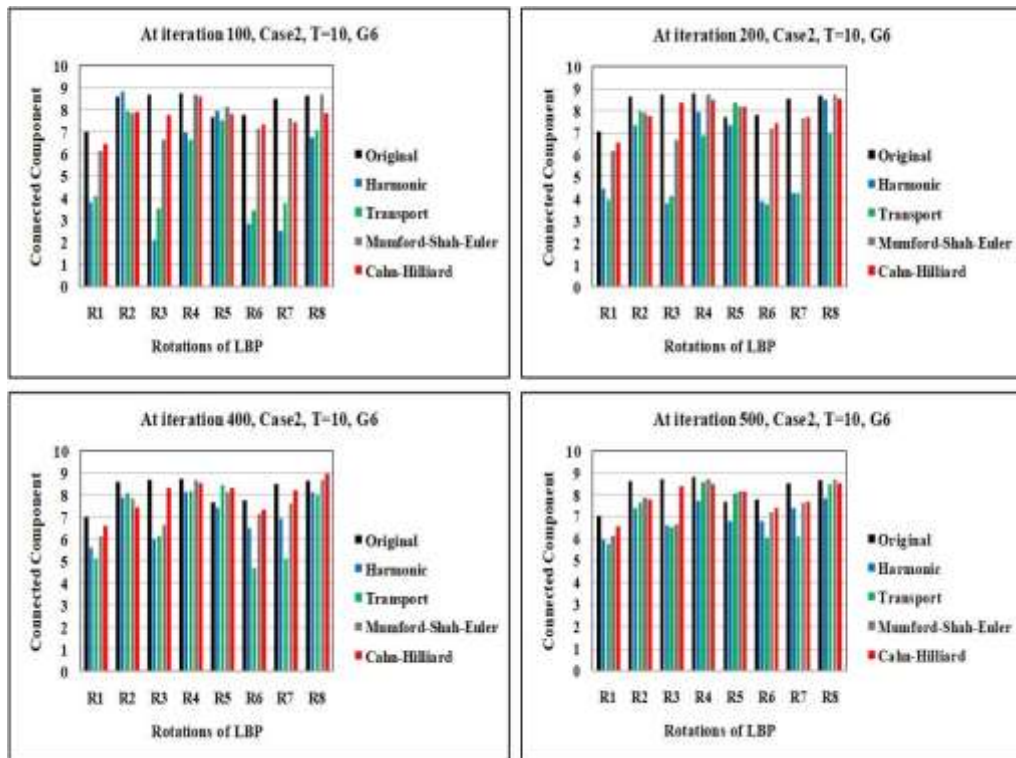


Figure4-42: Evaluation of performance of PDE-BI methods using TDA approach at different iterations for case inpainting 2 in G6 at threshold T=10.



Figure4-43: Object removal using PDE-BI methods. Row 1, Row 2, Row 3, and Row 4 inpainted images using four models at 100, 200, 400, and 700 iterations, respectively.

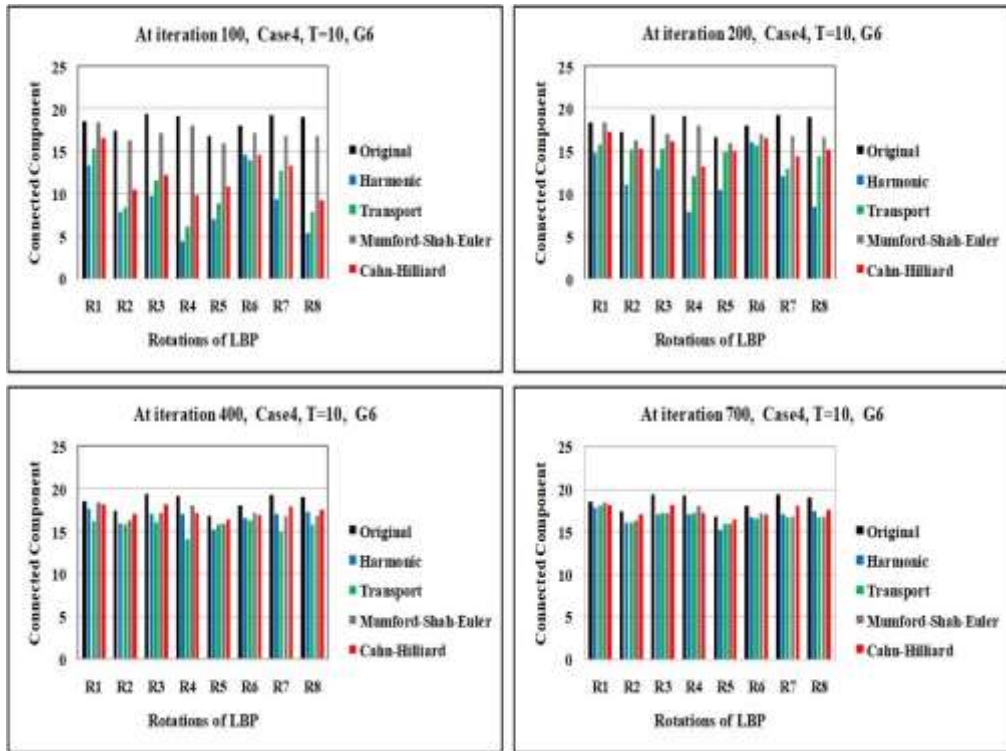


Figure4-44: Evaluation of performance of PDE-BI methods using TDA approach at different iterations for case inpainting 4 in G6 at threshold T=10.

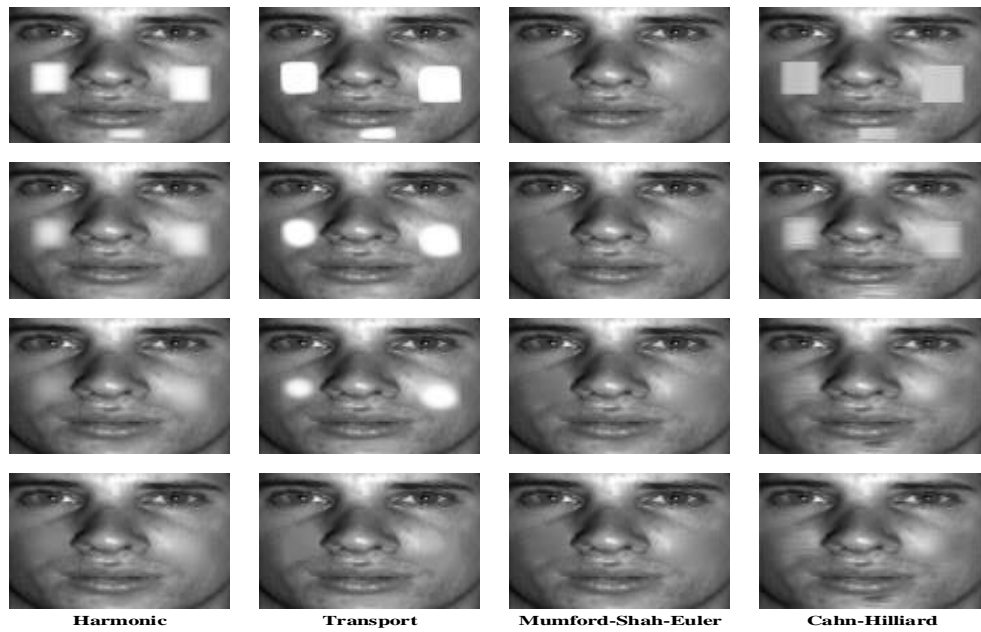


Figure4-45: Object removal using PDE-BI methods. Row 1, Row 2, Row 3, and Row 4 inpainted images using four models at 200, 500, 1700, and 2000 iterations, respectively.

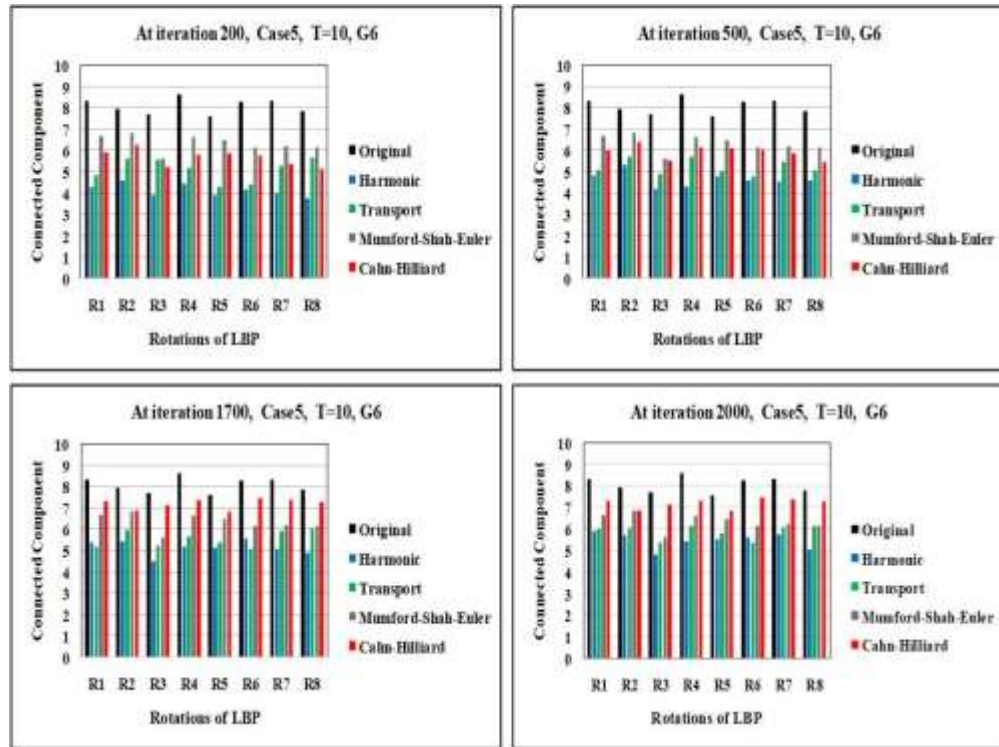


Figure4-46: Evaluation of performance of PDE-BI methods using TDA approach at different iterations for case inpainting 5 in G6 at threshold T=10.

We found the high-order PDEs takes less number of iteration than the 2nd-order to recover the missing areas in the face and natural images. Also, the transport equation consumes time more than other PDEs for reconstructing missing areas.

4.7.4.1 Results Analysis

As obtained in section 2.6.2, the best topological threshold is T=10, and the geometries G4 and G6 give the best description to the quality of inpainted images obtained by using PDE-BI methods. The TDA approach is used to study the performance of PDE-BI methods based on studying the outputs of these methods at different iterations. This study aims to evaluate the performance of PDE-BI methods by studying these progressions iteration gradually. The performances of PDE-BI methods are assessed by applying the TDA approach to the G6 at the threshold T=10; the numbers of CCs in the inpainted region obtained by those methods get closer to the number of CCs of the original regions as the number of iterations gradually increases. Moreover, the numbers of CCs of inpainted images by MES and mCH methods are closer to those in the original regions than are the corresponding numbers of CCs in the results of harmonic and transport methods. The MESm can be solved in a single step because it is an elliptic equation. The iterations of the harmonic equation arrive in the steady state faster than in the transport and mCH methods because the harmonic equation is of 2nd order.

On the other hand, in the transport and mCH methods need large numbers of iterations to arrive in a steady state. This means the high-order PDE-BI methods outperform the 2nd-order methods in recovering missing regions in an image. The efficacies of high-order PDE-BI methods for recovering missing regions are better 2nd-order equation methods, based on the numbers of CCs.

4.8 Summary and Conclusion

The aim of this chapter is the quality evaluation of the PDE based image inpainting method. Topological and statistical-measurements are proposed to evaluate the qualities of the image inpaintings in both the spatial and frequency domains. Also, the TDA is used to study the efficiency of PDE-BI methods. The MSE, PSNR, SSIM and entropy statistical measurements have been used for quality evaluation. The TDA method is used to count the numbers of CCs in the inpainted images and the corresponding original images to see in which inpainted image the number of CCs is closest to that found in the original image.

Two experiments have been conducted on natural and human face datasets obtained from the Berkeley and Yale databases respectively. Four PDE-BI methods have been applied to the two datasets in both the spatial and the frequency domains. The results of each method on both datasets are similar, as assessed by using both TDA and statistical measurements. It can be observed from the results that the image inpainting quality obtained by the mCH and MESm high-order PDEs are better than those obtained by harmonic and transport PDEs in both the spatial and frequency domains. Furthermore, the results of image inpainting quality obtained by PDE in the spatial domain are better than those obtained by PDE in the frequency domain.

The values of the MSE, PSNR, SSIM and entropy measurements applied to inpainted images obtained by the mCH and MES models are better than those obtained when harmonic and transport models. The TDA approach also has been applied to check the efficiency of PDEs by counting the number of CCs of the image inpainted at different iterations until the whole region is recovered. This shows that the efficiencies of harmonic and transport PDEs are less than those of the mCH and MES equations at different iterations.

To sum up, this chapter has experimentally demonstrated that high order PDE-BI methods outperform 2nd-order PDE-BI methods in recovering small missing regions in the natural images. However, these methods have limitations when they deal with large

Chapter 4: PDE Based Full Inpainting Methods

size missing regions and with large amounts of texture in the surrounding areas. Therefore, to address these problems, the next chapter will introduce the Topological EBI (TEBI) technique to reconstruct the texture and structure simultaneously in the missing regions in natural images.

Chapter 5 TOPOLOGICAL EXEMPLAR-BASED INPAINTING

The image inpainting schemes, developed over the last two chapters, focused on propagating colours into a missing region from its boundary using differently constructed PDEs in which the intention is to preserve the continuity of features through the missing regions in a manner compatible with the overall image content and semantics. However, the success of those schemes depends on a number of factors including the propagation of approximation errors resulting from numerical solutions which is particularly the case in a large missing area. The widely accepted observation that images contain many similar patches that are repeated in different places, motivated and led to the development of Exemplar-Based Inpainting (EBI) methods. Here, the similarity is not taken as rigid equality of intensities. The main challenge in designing EBI is the choice of patch size that can yield a realistic similarity measure that is relevant to the texture and structure of the missing region's neighbouring area. Existing EBI schemes tend to use relatively small size patches which can only model simple texture and structure similarities. In this chapter, a novel approach to extend the applicability of the EBI approach by using Topological Data Analysis (TDA) is presented. In particular, this is based on the topological parameters of simplicial complexes constructed, at different distance thresholds, as models of the shapes of the neighbourhoods of the missing regions. Texture-dependent parameters of particular interest are the number of CCs of simplicial complexes associated with uniform LBP landmarks. The patch propagation priority function is modified by using the curvature properties of isophotes and improves the matching criteria of patches by calculating the correlation coefficients from the spatial, gradient and Laplacian domains. The performance of the modified schemes is tested, in comparison to existing state-of-the-art EBI schemes, in terms of use several image quality measures, and demonstrate their superiority.

5.1 Introduction

In general, image inpainting schemes are application dependent, and accordingly filling a gap in an image is dependent very much on the significant texture, structure and

Chapter 5: Topological Exemplar-Based Inpainting

semantic information that are conveyed by the rest of the image. In the last two chapters, the performances of existing PDE based methods have been reviewed and improved, based on the restorations of small cracks or removed lines or texts, and the propagation of missing colour(s) into regions where grayscale information may or may not be present. These schemes used 2nd order (linear and non-linear) PDEs as well as higher order PDEs in order to preserve the continuation of certain texture/smooth features and recovering edges. However, the various PDE methods have limitations in restoring large missing region with rich textured resulting in the presence of blurring artefacts.

Alternative inpainting schemes have been investigated and developed that exploit the similarity between incomplete image blocks with patches elsewhere in the image in terms of intensity, texture and geometric information. Criminisi et al. in (Criminisi et al. 2004) were the first to propose the idea of using a patch based-exemplar method, where they simultaneously reconstructed the missing region's texture and structure. This task is mainly dependent on the filling order decision which must be made to make sure that linear structures will be propagated before texture filling in order to preserve the connectivity and continuity of object boundaries. This method does not seem to work well when removing a large object or when the surrounding area is rich with texture.

In this chapter, the ideas in (Anupam et al. 2010), (Hesabi & Mahdavi-Amiri 2012), and (Deng et al. 2015) are adopted and improved on by using the geometrical structure features of images. In particular, we will further improve the inpainted region when the surrounding area is rich in texture and structure. The main components of the developed scheme can be summarised as follows:

- (1) Determine the size of the patch (a window within the whole image) to be searched for based on its match/similarity other patches in terms of the texture quantity in the surrounding areas of the missing region *via* Topological Data Analysis (TDA) scheme.
- (2) Prioritise patch filling according to the curvature of isophotes.
- (3) Introduce different patch-matching criteria in two stages; firstly, calculate the Sum of Squared Distance (SSD) for Laplacian, gradient and spatial image domains and select the nearest 30 patches. Secondly, compute the Normalised cross-correlation coefficients of the 30 patches to select the nearest patch.

The rest of this chapter is organised as follows. Section 5.2 introduces the traditional exemplar-based inpainting method. Section 5.3 presents a literature review of the EBI method. Section 5.4 proposes a topological EBI method to recover the missing regions in high-resolution images and explains the TDA approach to the analysis of the surrounding areas of the missing region and illustrates new definitions of patch-filling priority and matching criteria. The results of the proposed method are explained in section 5.5. The performance testing experiments is presented in Section 5.6, while section 5.7 summarises the chapter and the main conclusions.

5.2 Existing Exemplar-Based Inpainting (EBI)

Unlike the non-exemplar-based schemes, the order of filling missing region by existing EBI methods is determined by what is known as a '**priority function**' which is used to select the next patch to be recovered. These schemes proceed by searching for the nearest patch outside the missing region to the selected according to a '**matching function**'. A major drawback of this EBI method is the bias caused by selection of few incorrect patches in the priority based filling mechanism, resulting in initial incorrect completions and spiralling errors that undermine the stability of the inpainting process.

In what follows, the input image I is assumed to be composed of two disjoint regions: the source region Φ and the target region Ω . The source region is defined to be the visible part and the target region is the missing one. Additionally, $\delta\Omega$ represents the pixel set of the target region boundary. The pioneering EBI method of (Criminisi et al. 2004), fixes the patch size to be a window of 9×9 pixels for any input image that has a missing region to be inpainted. For each block (patch), the priority function selects the next pixel position on the current $\delta\Omega$, and a template patch ψ_p centred at the selected pixel is determined. The priority computation is encouraged to reconstruct the patches which are on the continuation of strong edges and are surrounded by high-confidence pixels. The priority function is defined as the product of data and confidence terms. The data term is a function of computing the structure information (i.e. broken lines and corners which tend to connect) in the patches by using isophotes “flows” to encourage linear structures to be reconstructed first. While the confidence term is a measure function of the amount of reliable information surrounding the pixel (i.e. to reconstruct texture information).

A matching function is then used to find the closest patch (recover target patch) that has similar information based on the sum of squared distance (for example $\psi_{q'}$ or $\psi_{q''}$).

Chapter 5: Topological Exemplar-Based Inpainting

After selecting the target patch, they update the template patch by copying the information from the target patch. This process will be repeated until recovering all the missing regions, see Figure5-1.

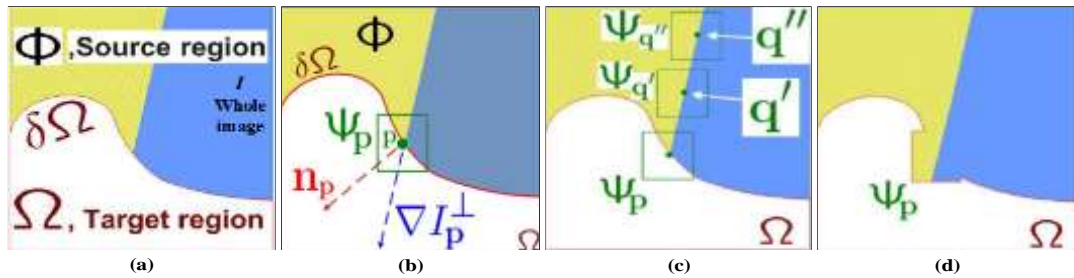


Figure5-1: The EBI procedures for recovering the missing region in the image (Criminisi et al. 2004).

This EBI Method was designed for removing large objects from digital photographs and replacing the selected object by a visually reasonable background that imitates the appearance of the source region. It proposes a unified framework, by combining the use of texture synthesis and isophote driven inpainting according to a priority mechanism. The patches in the target region are filled by selecting the highest priority patch.

Figure5-1(b) illustrates a point p with high priority lying on the contour of the target region boundary. The highest priority patch is then filled by finding the best matching patch in the known regions (rest of image) as explained in Figure5-1 (c). The pixels of the best-matching patch will be copied in the highest priority patch as described in Figure5-1 (d). This process continues until the entire gap is filled.

The patch size can be varied depending on the underlying characteristics of the image, but in this method, the patch size is fixed at 9×9 . This EBI removal technique performs well for a wide range of applications such as the restoration of small scratches and larger objects that are surrounded by simple texture and structure area. However, synthesising of regions for which similar patches are rare is a challenge, and the method doesn't handle curved structures.

5.3 Literature Review

Here, the existing attempts to improve EBI as described in (Criminisi et al. 2004) are reviewed, and the limitations and drawbacks are highlighted. The first category of those methods consists of those which are focused on improving reconstructed texture (Sharma & Mehta 2013), (Cheng et al. 2005), (Desai 2012), (Anupam et al. 2010), and (Hesabi & Mahdavi-Amiri 2012) whereas those in the second category are modifications of the work in (Criminisi et al. 2004) to restore structure into missing

regions more accurately from the surrounding areas (Sangeeth et al. 2011), (Waykule & Patil 2012), (Zongben Xu & Jian Sun 2010), (Gaikar et al. 2014), (Abdollahifard & Kalantari 2016), and (Deng et al. 2015).

Several studies attempted to adjust the EBI scheme as described in (Criminisi et al. 2004) by redefining the confidence term, the data term formula and matching criteria (Sharma & Mehta 2013), (Cheng et al. 2005), and (Sangeeth et al. 2011). Other studies focused on the efficiency of the scheme. Waykule et al. (Waykule & Patil 2012), for instance, proposed a new method for eliminating big objects from photographs/images, through redefinition of the data term on the positions of the control points of a contour going into a damaged region. The new data term formula uses a bi-dimensional Gaussian kernel filter on the positions of the control points of $\partial\Omega$, then \mathbf{n}_p is estimated as the unit vector orthogonal to the front $\partial\Omega$. The technique has been successful in reconstructing both linear structures and two-dimensional textures of small scratches and larger objects in the target region. This modified EBI scheme improves the inpainting achieved by the earlier techniques in terms of both perceptual quality and computational efficiency. Also, a Gaussian kernel filter has been used in (Sharma & Mehta 2013) to redefine the data term.

W. H. Cheng et al. in (Cheng et al. 2005) present a robust algorithm for developing a generic priority function that integrates well the overall structure and texture information into the missing region to facilitate the image reconstruction. The new priority function definition and the selection of component weighting factors are designed to reduce the difficult computations of information propagation by the EBI method. The proposed method in this paper is effective in both the visual quality improvement and user preference consideration.

K. Sangeetha et al. in (Sangeeth et al. 2011) proposed a new EBI method with an enhanced priority term that describes the filling sequence for patches in photographs/images. The proposed method is based on patch transmission by inwardly transmitting the image patches from the source area into the inside of the target area patch by patch. The exemplar-based image inpainting method with best patch match is introduced in this work, and for obtaining this best patch match an enhanced patch priority term and a suitable choice of search region are introduced. This research is not wholly limited to the reconstruction of damaged areas or the matching area complete accurately but also concerns itself with the repair the image's minute spots, scratches

Chapter 5: Topological Exemplar-Based Inpainting

and large damaged areas completely. The results of the proposed method show that it has an obvious enhancement in visual quality as compared to the conventional exemplar-based inpainting method. This work deals with the inpainting of images/photographs, and it can also be expanded for inpainting of video frames.

Also, Liang-Jian Deng et al. in (Deng et al. 2015) introduced a new priority definition to face the problem of improper selection of exemplars in the traditional EBI method. The independent strategy of priority definition has been defined based on the separation of the priority definition to first propagate structure then synthesise image textures, aiming to well recover both image properties. Also, an automatic approach has been designed to estimate steps for the new separated priority definition. This proposed method has been successfully applied to the reconstruction of the structure in missing regions. However, this method faces a problem in recovering the texture in missing regions. The idea of the estimation of the number of steps is used for recovering the structure and then the texture in the images by estimating the weight parameters of the texture and structure in our proposed method.

In a recent work, Z. Xu and S. Jian (Zongben Xu & Jian Sun 2010) proposed a gradient-based search space reduction. The spatial behaviour of selected regions to be implanted is controlled by a gradient vector. Also, they used a different distance measure for determining the patch matching.

M. Desai in (Desai 2012) presented an adapted fast and improved EBI to solve the unknown row filling difficulties. This improved method is adaptive in updating criteria in a fast and enhanced EBI method described in (Anupam et al. 2010) which presents a technique that deals with the case when two or more patches have a same mean square error, by calculating variance. A reduced search area is suggested, to decrease the computational difficulty entailed in searching the whole image. The proposed method resolves the difficulty of unknown row filling and provides better results than the original fast and enhanced exemplar-based image inpainting method. But images produced by this approach still suffer from some difficulties because it adds some unwanted incorrect information from a background in the photograph/image.

Shivani et al. in (Gaikar et al. 2014) utilised two methods to enhance the EBI method (Criminisi et al. 2004) which are: Discrete Cosine Transform (DCT) and Fast Marching Method (FMM). So, the DCT method has used with EBI to remove the unnecessary big objects from the damaged image and replace them with a visually acceptable

background by sampling & copying colour values from the source. The FMM is utilised to eliminate all scratches within the image. This scheme has several benefits including being easy to implement more efficiently.

M. Abdollah and S. Kalantari in (Abdollahifard & Kalantari 2016) introduced an efficient method harmonious with the core of the labour in (Criminisi et al. 2004). This method is presented by a gradient-based search space reduction and two changes are adopted. First, the spatial behaviours in selected regions to be implanted are controlled by a gradient vector. Secondly, the application of Euclidean distance as the only measure to compare patches (selected regions) is to be avoided. Instead of a simple gradient-based similarity measure to select the best matches (template) patch,

$$d_G(G(\psi_p), G(\psi_q)) = \{ |\psi_x(p) - \psi_x(q)| \& |\psi_y(p) - \psi_y(q)| < t \}, \quad (5.1)$$

Where $d_G(G(\psi_p), G(\psi_q))$ represents an L_2 -norm (SSD), and t is a threshold value and the partial derivatives of the image ψ in x and y directions are denoted by ψ_x and ψ_y respectively. Using the properties of gradient magnitude and making the size of patch 21×21 , the proposed method has succeeded in reducing the search space by a factor of up to 100. Therefore, similar visual results to those of the original method of (Criminisi et al. 2004) are obtained more efficiently.

The authors of (Cheng et al. 2005) presented an adapted fast and improved EBI method to solve the unknown row filling difficulties. Since EBI-method results almost always depend on the selection order, this method uses a redefined priority function to improve selection order so that the results get better.

Most of the improved methods for EBI continue to use the same 9×9 size of patch propagation, which seems to produce visual artefacts when the surrounding area of the missing region is very rich with texture and structure (Criminisi et al. 2004). Also, the priority function cannot precisely locate positions on the border of the missing region where there are strong and long edges in the surrounding area. All in all, EBI can only be applied to images which have simple texture and structure in missing regions' surrounding areas.

The work in the next section aims to overcome and consequently improve EBI regarding the size of patch propagation, to improve the priority function and matching criteria, and to reduce the artefact problem to an unnoticeable level. To accomplish this task, the emerging Topological Data Analysis scheme is applied.

5.4 Topological Exemplar-Based Inpainting Method (TEBI)

To the best of our knowledge, no method has addressed the patch size selection in Criminisi’s et al. method. We propose to adaptively select the size of the patch propagation based on quantifying the texture and structure in the surrounding areas of the missing region, using the innovative TDA based strategy. Also, a new definition of priority will be proposed to determine the priority of patch filling place based on the concepts of the curvature and the total variation of an isophote to encourage priority filling of the edges and corners in the patches. Finally, new matching criteria has been introduced to choose approximate true patches from the source region to recover the regions with high texture and structure surrounding it. Figure5-2 shows the flowchart of the proposed topological EBI method.

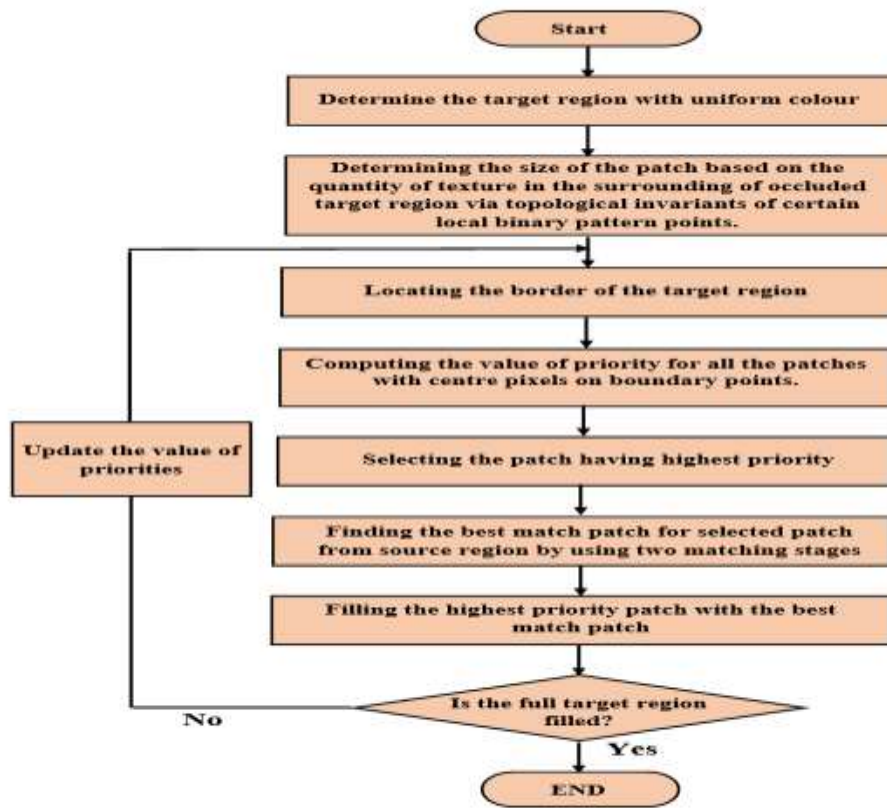


Figure5-2: Flowchart of the proposed topological EBI method.

The steps involved are determining the size of propagating patches by the TDA approach; and recovering edges and corners in the missing regions with high texture and structure areas surrounding the missing regions by using a new modified priority function and new matching criteria. These steps are illustrated in the subsections below.

5.4.1 Topological Image analysis

The TDA approach studies the correlation between structure/texture and the patch size. To quantifying the amount of local texture existing in missing region's surrounding area, the image is first transformed into the LBP domain and select landmark points of ULBP codes as the 0-simplices as the initial step in building a sequence of increasing Rips simplicial complexes from the missing region's neighbouring area. The ULBP pixels are divided into a number of geometries according to their number of 1's in their byte code, and each geometry represents a different texture type. Also, each geometry is divided into 8 different rotations depending on the initial position of the 1's run within the byte binary representation. For each geometry and each rotation, we will have an initial set of 0-simplicies that form the start of building of the sequence of simplicial complexes. At each threshold, the number of CC will automatically quantify the nature of the given geometry-related texture in the regions surrounding the missing area. The rest of this section is aimed at using these quantifications to determine the appropriate size of patch propagation of our intended TEBI scheme.

5.4.1.1 Experimental Dataset and Protocols

To test the performance of our TEBI scheme, a number of experiments is conducted by using different assembled datasets of images and adopting a number of training-testing protocols. We assembled an initial dataset of 240 randomly selected natural google images: 120 are known to be of low-texture, and 120 are known to be of rich-texture taken from (Vedaldi 2014). Figure5-3 shows a sample of these images. We recognise that image texture is not uniformly expressed in images, and any of the selected images are expected to have regions with different intensity of texture, and the given label depends on the texture in a majority of image sub-regions. Accordingly, to determine the type of texture of unknown input images, five non-overlapping blocks from each of the images are randomly selected. For our experiments, we randomly selected 5 sub-images of size 25×25 from each image in our dataset to we end up with 1200 image subsets of 240 original images where 600 of them are subsets of rich textured images, and the other 600 are subsets of low-textured ones.



Figure5-3: Samples of low texture images selected from google image.

Four different training-testing protocols are used to evaluate the performance of our developed TEBI schemes:

- S1) 17% Training - 83% testing protocol (40 images for training and 200 for testing),
- S2) 33% Training - 67% testing protocol (80 images for training and 160 for testing),
- S3) 50% Training - 50% testing protocol (120 images for training and 120 for testing),
- S4) 83% Training - 17% testing protocol (200 images for training and 40 for testing).

There are various parameters that need to be chosen that will help us determine a practical way for implementing our TEBI scheme which requires a specific way with which to classify image texture. Accordingly, our experiments are designed to determine three choices, the appropriate ULBP geometry, the best threshold to model texture, and what strategy to follow when linking the extracted topological invariant of the chosen geometry at the chosen threshold to the type of image texture. Accordingly, any input image needs to be subjected to three checks to be classified as a rich/high textured image or not. First, out of 8 uniform LBP code rotations, at least 5 rotations must vote in favor of High Texture (HT) so that an image subset will be classified as a textured subset. Second, out of 5 image subsets, at least 3 must vote in favour of high texture for the image to be cast as a rich textured image. Following the same process, an input image may be classified as a Low-Textured (LT) image. Finally, out of the 3 best ULBP geometries, at least two geometries must vote in favour of HT or LT, then the image will be casted as a HT or LT. Hence, a missing region's surrounding area will be treated as a HT or LT when the EBI method is applied.

In these experiments, the Support vector machine (SVM) method is used to obtain our optimal criteria to be used in our proposed TEBI scheme. The support vector machine (SVM) is one of the most widely used supervised classifiers which aims to find an optimal separating hyper-plane among different classes of a given n-dimensional dataset (training set). The optimal separating hyper-plane is the one that has a maximum distance to the nearest data samples (the so-called support vectors) in the training set. Such optimisation technique endeavours to maximise the margin between the hyper-plane and the support vectors, expecting a better classification accuracy.

5.4.1.2 Classification Results

As mentioned above, an increasing sequence of simplicial complexes is constructed at 6 different distance thresholds only and compute the number of CCs at each threshold. A linear SVM (i.e. classification technique) is first used to determine the best threshold that accurately discriminates images in terms of their quantified texture. The SVM classifier is used to classify the images into high and low texture based on the number of CCs in each geometry at different thresholds for the four different protocols that are used for classification. The features were fed into the classifier in two different ways in each experimental protocol: First, a feature vector of size 40×1 is created from the 8 CC numbers obtained from the five image subsets at each geometry, and the decision is based on the majority vote. Second, at the first stage, the CCs of each image subset are used as a feature vector of size 8×1 independently and decide the type of texture in image subsets using a majority vote, and at the second stage, we again make a decision among the seven-geometries-based majority vote. Each of the above four protocols will be repeated 100 times to ensure that we are covering as much as possible different selections.

Figure5-4, displays the achieved accuracy rates for the testing images showing the use of a topological feature vector of size 40×1 in an SVM classifier for 7 ULBP geometries at different thresholds in four different protocols.

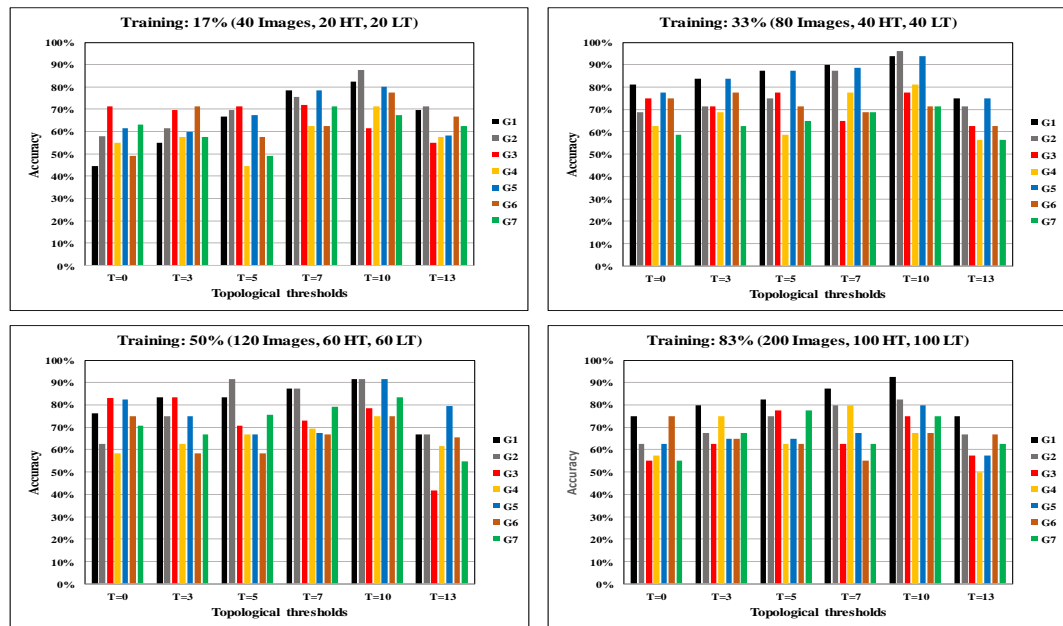


Figure5-4: Texture classification results using SVM classifier for different protocols, 7 ULBP groups at 6 topological features (thresholds).

Figure5-5 noticeably displays the use of a topological feature vector of size 8×1 in an SVM classifier for 7 ULBP geometries at different thresholds in four different protocols; where the SVM classifier will apply on each image subset and make a decision among the image subsets using a majority vote.

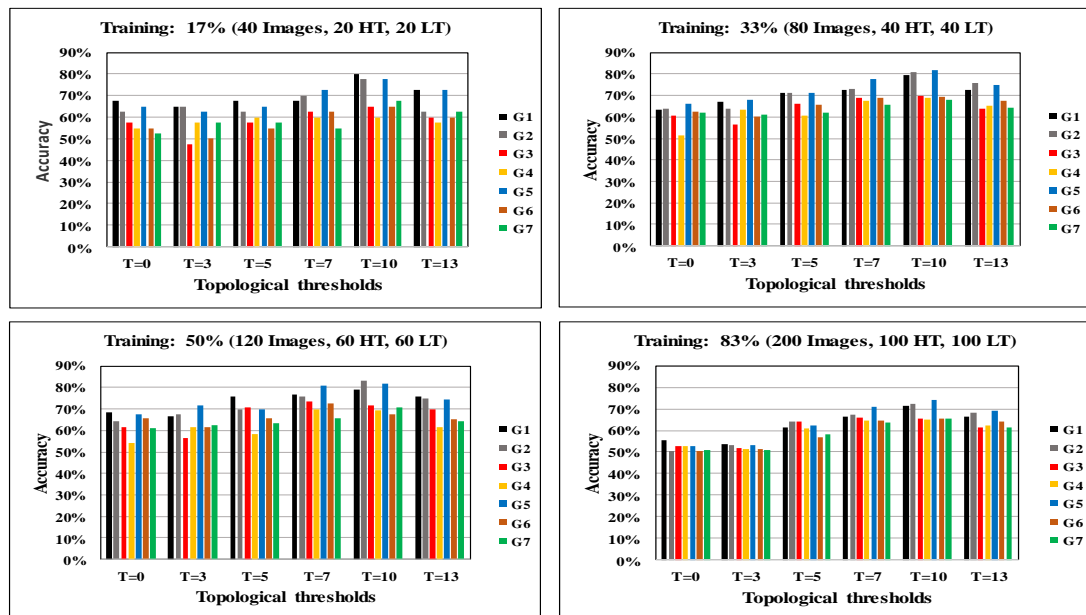


Figure5-5: Texture classification results using an SVM classifier for different protocols, 7 ULBP groups at 6 topological features (thresholds).

In these experiments, the results clearly show that topological features at threshold $T=10$ perform better in discriminating rich textured regions in comparison with other thresholds, and among 7 ULBP geometries G1, G2, and G5 are performing better at

discriminating texture features. Therefore, these three geometries are used to quantify the amount of texture in a missing region's surrounding area, and consequently, the patch size will be determined. The charts, also reveal that there is no need to have a big training set as the accuracy when the training is 17% is nearly similar to the 83%, 50%, and 33% training when using T10 that means the features (the number of CCs) that used in SVM classifier method are strong and the big training set doesn't effect on the results. Also that means the TDA approach has been successfully discriminating between the high and low texture images.

We have also seen the SVM classifier is adapted, the experimental results justify the assertion that SVM performs better in higher dimensional spaces. The input feature vector was fed to the SVM in different numbers of dimensions, the first with 8 dimensions, and the second set with 40 dimensions. We observed that SVM classifies the higher dimensional feature vector with higher accuracy, and from this comes the fact that, as the number of dimensions gets higher, the separation of different classes gets better.

5.4.1.3 Determination of Patch Size

From the above set of experiments, the topological features at threshold $T=10$ perform better discrimination of high textured regions in comparison with other thresholds, and among 7 ULBP geometries G1, G2, and G5 are performing better in discriminating texture features in each experimental protocol. However, we note that the best topological threshold is not always $T=10$; this may change according to the nature of the images as well as the landmark point distribution. Rich textured images used for training and testing have many strong edges and lines. The reason behind the good performance of ULBP geometries is that G1, G2 and G5 are edges and corners descriptors inside an LBP.

Therefore, the three best-performing geometries are used to quantify the amount of texture in the missing region's surrounding area, and consequently, the propagation patch size will be determined adaptively depending on the outcome from the 5 image subsets according to the heuristic rules:

1. If 3 image subsets voted for HT, then select a patch size of 7×7 ,
2. If 4 or 5 image subsets voted in HT, then select a patch size of 5×5 ,

3. Else if 3 image subsets voted in LT then select the patch size to be 11×11 , 13×13 or 15×15 if 4 image subsets voted LT. Otherwise, select the patch size to be 21×21 .

The next step after selecting the appropriate patch size for filling procedure is patch filling priority. In other words, where is the best place to start the information propagation into the missing region? The next section contains a discussion about the priority function which modified by adding what is known as isophote curvature to the priority function to make sure that the strong/long edges on the border of the missing region are restored sequentially.

5.4.2 Patch Filling Function

One of the challenges in filling the missing region is to decide: where should the filling procedure start? The best filling method would be the one that gives high preference to the regions that continue the structure of the image into the missing area in the beginning then propagating the texture within the missing area. Criminisi *et al.* in (Criminisi et al. 2004) proposed that one can decide the order of filling priority based on 1) how reliable is the information surrounding the pixel (known as confidence term) and 2) a function that measures the strength of the isophote that first hits the front of the border of the missing area (known as Data term). The priority function $P(p)$ is the product of two terms (Criminisi et al. 2004):

$$P(p) = C(p) \cdot D(p) \quad (5.2)$$

where $C(p)$ is the confidence term and $D(p)$ is the data term, and they are defined as follows:

$$C(p) = \frac{\sum_{q \in \psi_p \cap (\Omega - \Omega)} C(q)}{|\psi_p|} \quad (5.3)$$

$$D(p) = \frac{|\nabla I_p^\perp \cdot n_p|}{\alpha} \quad \dots (5.4)$$

Where $|\psi_p|$ is the area of ψ_p , ∇I is a gradient of the image I , α is a normalisation factor (e.g., $\alpha = 255$ for a typical grey-level image), ∇I_p^\perp is the isophote (direction and intensity) at point p , n_p is a unit vector orthogonal to the front $\partial\Omega$ in the point p and \perp denotes the orthogonal operator. The data term boosts the priority of the patch that an isophote flows into.

Chapter 5: Topological Exemplar-Based Inpainting

Different definitions of the priority function have been tested when the summation and multiplication of data and confidence terms, and different kinds of data and confidence terms also have been used. The definition of the priority function also has been tested when the subtraction of data and confidence terms; the negative sign has affected on the values of confidence and data terms. Table 5-1 shows the advantages and disadvantages of some of the priority functions $P(p)$ that were tested by using different formulas of confidence and data term.

P(p)	Advantage	Disadvantage
$C(p) \cdot D(p)$ in (Criminisi et al. 2004)	This priority function helps to recover small missing regions and to remove small objects.	Poor texture propagation in missing regions and poor geometry propagation in large missing regions
$C_1C(p) + C_2D(p)$ in (Anupam et al. 2010)	This priority function improves texture propagation in small missing regions as well as when removing larger objects.	Poor geometry propagation in missing regions. But improved results if different patch size and different weight values are used.
St1: $P(p) = D(p)$ St2: $P(p) = C(p)$ in (Deng et al. 2015)	Enhances the process of geometry propagation in the missing regions and also when removing objects.	Poor texture propagation in the missing regions as a result of using fixed patch size.
$C_1C(p) - C_2D(p)$	Helps fill the information in small missing regions and when removing small objects.	Poor texture and geometry propagation in large missing regions.

Table 5-1: Description of the priority functions tested in this study.

5.4.2.1 Innovative Adaptive Priority Function

Having implemented and observed the performance of the above-mentioned priority functions, we found that priority functions that are linearly dependent on the data and confidence terms, such as the Anupam *et al.* (Anupam et al. 2010) function, have reasonable results especially when dealing with surrounding areas of missing regions have edges and corners. Initial tests of the above schemes helped to develop a new innovative *adaptive* linear priority function by tuning the confidence and the data terms. The rest of this section is devoted to describe the tuning steps.

The first change was to add a total variation operator $|\nabla I_p|^{-\frac{1}{2}}$ to the weighted sum of the new confidence term and the data term. This TV operator is of fundamental importance because it encourages linear structures to be synthesised first, and, thereafter propagated securely into the target region. The confidence term is slightly modified, to control the smoothness of curves, using a regularization term ε as follows:

$$R_c(p) = (1 - \varepsilon) \times C(p) + \varepsilon, \quad 0 < \varepsilon < 1.$$

where ε is the regularising factor for controlling the curve smoothness of the information in $C(P)$. However, even with these two changes, we noted that in some cases the data term vanishes, producing artefacts after the filling procedure is complete. To overcome this, the data term is additionally redefined by adding the curvature of isophotes (Shen & Chan 2002), The redefined data formula after curvature isophote addition is as follows:

$$D(p) = \frac{|\nabla I_p^\perp \cdot n_p|}{\alpha} + \left| \nabla \cdot \frac{\nabla I_p}{|\nabla I_p|} \right| \quad \dots (5.5)$$

where $\frac{\nabla I_p}{|\nabla I_p|}$ is the normal direction of the isophote; $\nabla \cdot \frac{\nabla I_p}{|\nabla I_p|}$ is the curvature of the isophote. Finally, our Priority function is defined by:

$$P(p) = C_1 \times R_c(p) + C_2 \times D(p) + |\nabla I_p|^{-\frac{1}{2}} \quad \dots (5.6)$$

Where C_1 and C_2 are respectively the component weights of the confidence and the data terms and $C_1 + C_2 = 1$. Anupam *et al* in (Anupam et al. 2010) suggest the use of $C_1 = 0.7$ and $C_2 = 0.3$.

The curvature model (5.6) enhances the driving of diffusion along the isophote directions and thus allows the propagation of thicker regions in the beginning. This approach works in some scenarios. However, it will not produce a good reconstructed image in other cases when using $C_1 = 0.7$ and $C_2 = 0.3$.

Therefore, our final modification of linear priority function is based on an adaptive selection of C_1 and C_2 . Inspired by the work of Deng et al in (Deng et al. 2015), this adaptation will be based on a measure of the quantity of structure needed to propagate inside the missing region. Accordingly, the idea of the work in (Deng et al. 2015) is on separating the task of filling the template patch into two phases: the first phase is about

Chapter 5: Topological Exemplar-Based Inpainting

recovering the structure patches by propagating geometry, and the second phase is about recovering the texture.

Our adaptive estimation of C_1 and C_2 is based on computing the number of propagation steps of structure patches in the missing region; then subtracting them from all propagation steps to determine the number of propagation steps of texture patches.

Let the source region and target region are defined as $\Phi = \{\Phi_s \cup \Phi_t \setminus \Phi_s \cap \Phi_t = \emptyset\}$, and $\Omega = \{\Omega_s \cup \Omega_t \setminus \Omega_s \cap \Omega_t = \emptyset$, where Φ_s , Ω_s represent the structure in Φ and Ω , respectively, and Φ_t , Ω_t represent the textures in Φ and Ω , respectively. The structure part is computed via some edge detectors, e.g., ‘‘canny’’ or ‘‘Sobel’’ detectors. A structure patch's propagation step in the missing region may be described by the equation:

$$T_{\Omega_s} = \frac{A_{\Phi_s}}{A_{\Phi}} T_{\Omega} = 2\rho \cdot \frac{A_{E_{\Phi}} A_{\Omega}}{A_{\Phi} A_{\psi_p}}, \quad \dots (5.7)$$

where A_{Φ} and A_{Ω} represent the areas of the source Φ and target Ω regions, respectively. Also $\frac{A_{\Phi_s}}{A_{\Phi}} = \frac{A_{\Omega_s}}{A_{\Omega}}$, $A_{\Phi_s} = \rho A_{E_{\Phi}}$, and $\frac{A_{\Omega_s}}{A_{\Omega}} = \frac{T_{\Omega_s}}{T_{\Omega}}$, where E_{Φ} is the edge map of the source region Φ . $A_{E_{\Phi}}$ is computed by the quantity of nonzero elements in E_{Φ} , and ρ is set to be n , where the size of patch is $n \times n$. In addition, the total step number T_{Ω} can be estimated by the areas of patch ψ_p and the target region Ω , i.e.,

$$T_{\Omega} = A_{\Omega} / (0.5A_{\psi_p}).$$

We used equation 5.7, i.e. the ratio of the calculated number of structured patches that need to be filled in the missing region, to compute C_1 , and C_2 . As follows:

$$C_2 = \frac{T_{\Omega_s}}{T_{\Omega}}, \text{ and } C_1 = 1 - C_2.$$

We now reformulate our adaptive priority function as follows:

$$P(p) = C_1 \times R_c(p) + C_2 \times D(p) + |\nabla I_p|^{-\frac{1}{2}}$$

Where $R_c(p)$ is improved confidence term, which defined as $R_c(p) = (1 - \varepsilon) \times C(p) + \varepsilon$, $D(p)$ is improved Data term, which defined as $D(p) = \frac{|\nabla I_p^\perp \cdot n_p|}{\alpha} + \left| \nabla \cdot \frac{\nabla I_p}{|\nabla I_p|} \right|$, and C_1, C_2 are the weight components which are determined based on the quantity of structure in an image.

This adaptive priority function will be shown to improve the reconstruction of the structure of the missing region (i.e. curves, corners, and edges) in a more deterministic and trustful way that only depends on the content of the image. Having defined the patch priority function, at each step the patch of the TEBI with the highest priority (called the template) need to be filled using matching criteria that is used to search in the rest of the image. This is the aim of the next section.

5.4.3 Matching Criteria

Finding the patch that best matches the selected (template) patch, from the previous section, to reconstruct the missing region is critical. The SSD between template patch and the candidate patch outside the missing region in the spatial domain is used by (Criminisi et al. 2004), (Sharma & Mehta 2013), (Cheng et al. 2005) and (Deng et al. 2015). In (Hesabi & Mahdavi-Amiri 2012) the computed SSD between the template patch and the candidate patch outside the missing region is conducted in the spatial as well as in divergence and gradient domains. The later approach improved missing-region texture recovery. However, still in some cases, visible artefacts are produced. To avoid this in this final stage, the procedure is experimentally improved by first computing SSDs in the spatial domain then in the gradient and Laplacian domains. In other words, the SSD in the spatial, gradient and Laplacian domains is added between the template patch and candidate patches. Equation (5.8) shows the procedure to compute the SSD between a candidate and a template patch.

$$\psi_q = \arg \min_{\psi_p \in \Omega} d_s(I(\psi_p), I(\psi_q)) + d_g(G(\psi_p), G(\psi_q)) + d_L(L(\psi_p), L(\psi_q)) \dots (5.8)$$

where d_s , d_g and d_L are spatial, gradient and Laplacian distances, respectively. As can be seen in Figure 5-1, ψ_p and ψ_q are template and candidate patches respectively. Recall that this is the first stage matching criteria. The patch with the smallest Euclidean distance is not necessarily the best candidate for replacement by the template/destination patch.

Therefore, the second stage of similarity measurement is suggested as follows:

- Determine the 30 nearest patches to the template patch with the smallest SSD values.
- Measure the Normalised Correlation Coefficients (NCC) between the template and the 30 nearest candidate patches to get the patch which has the NCC value closest to 1.

The formula for NCC is given as:

$$d_{\text{NCC}}(I(\psi_p), I(\psi_q)) = \frac{(\sum(\psi_p) \cdot \psi_q)^2}{\sum(\psi_p)^2 \sum(\psi_q)^2} \quad \dots (5.9)$$

We tested the outcomes of selecting all the patches in the surrounding area of the missing region and calculated the NCC in each case, and the results with all 30 patches were similar. Therefore, to reduce the time we stick to the 30 smallest SSD patches.

As a result, texture properties will be preserved by the second matching stage. This patch-based filling criterion helps achieve speed efficiency, accuracy in the synthesis of texture and accurate propagation of linear structures. Finally, the most similar patch is copied to the destination patch and update the information of the destination patch. The process in the last two subsections will be repeated until all missing region is recovered.

5.5 Experimental Results

In this section, the results of testing the performance of our TEBI method for 100 different images are reported, in comparison to that of the Criminisi, Anupam, and Deng methods that introduced in (Criminisi et al. 2004), (Anupam et al. 2010), and (Deng et al. 2015). Table 5-2 shows the testing parameters of priority function, matching criteria and patch size used in these schemes.

P(p)	C(p)	D(p)	Matching criteria	Patch Size
$C(p) \cdot D(p)$, in (Criminisi et al. 2004)	$\frac{\sum_{q \in \psi_{p \cap (I-\Omega)}} C(q)}{ \psi_p }$	$\frac{ \nabla I_p^\perp \cdot n_p }{\alpha}$	Euclidean distance in spatial domain.	9×9
$C_1 R_c(p) + C_2 D(p)$ where $R_c(p) = (1 - \omega) \times C(p) + \omega$, in (Anupam et al. 2010)	$\frac{\sum_{q \in \psi_{p \cap (I-\Omega)}} C(q)}{ \psi_p }$ $R_c(p) = (1 - \varepsilon) \times C(p) + \varepsilon$	$\frac{ \nabla I_p^\perp \cdot n_p }{\alpha}$	Euclidean distance in spatial domain.	9×9
St1: $P(p) = D(p)$ St2: $P(p) = C(p)$ in (Deng et al. 2015)	$\frac{\sum_{q \in \psi_{p \cap (I-\Omega)}} C(q)}{ \psi_p }$	$\frac{ \nabla I_p^\perp \cdot n_p }{\alpha}$	Euclidean distance in gradient domain.	9×9
$C_1 \times R_c(p) + C_2 \times D(p) + \nabla I_p ^{-\frac{1}{2}}$, where $R_c(p) = (1 - \omega) \times C(p) + \omega$.	$\frac{\sum_{q \in \psi_{p \cap (I-\Omega)}} C(q)}{ \psi_p }$	$\frac{ \nabla I_p^\perp \cdot n_p }{\alpha} + \left \nabla \cdot \frac{\nabla I_p}{ \nabla I_p } \right $	Summation of Euclidean distance in spatial, gradient, and Laplacian domain. Then NCC	Adaptable to the quantity of texture surrounding

Chapter 5: Topological Exemplar-Based Inpainting

in our proposed method.	$R_c(p)$ $= (1 - \varepsilon) \times C(p)$ $+ \varepsilon$		to determine the best.	areas in the image
-------------------------	--	--	------------------------	--------------------

Table 5-2: comparing priority function, matching criteria and patch size in Criminisi, Anupam, Deng and TEBI.

Our test criteria is based on how visually the inpainted target region mimics the source region in appearance when we remove objects and fill the gap using the tested inpainting schemes. More precisely, the TEBI proposed method is tested on 100 natural images containing missing regions of different sizes at random locations for the same natural image. Below, in Figure5-6, 5-7, 5-8 and 5-9, the test for a selected number of images is illustrated.

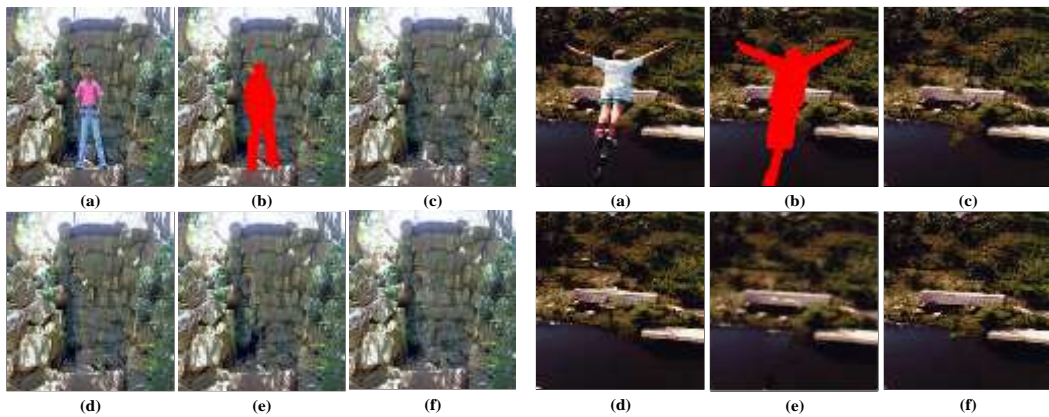


Figure5-6: Removing Objects: (a) Natural image from the internet; (b) original image with occluded areas; (c), (d), (e) and (f) Inpainted image using Criminisi, Anupam, Deng and TEBI schemes, respectively.

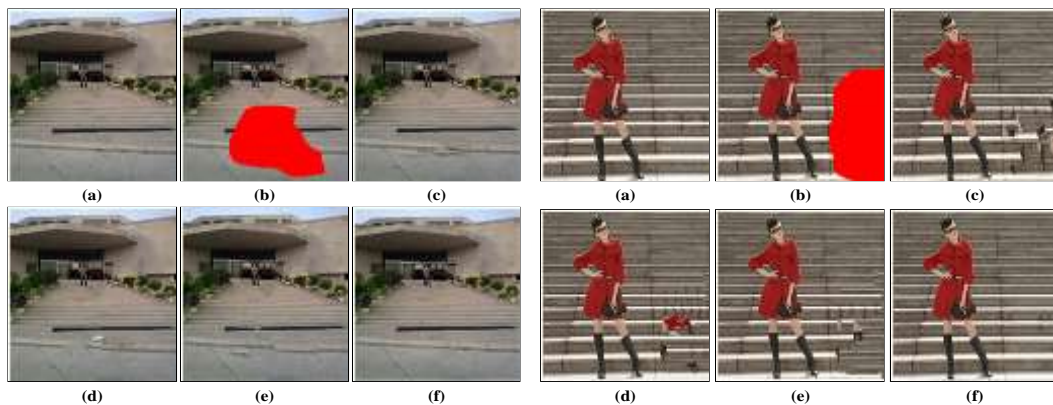


Figure5-7: Region reconstruction using EBI. The natural image from the internet (a), original image with the occluded area (b); (c), (d), (e) and (f) inpainted image using Criminisi, Anupam, Deng and TEBI schemes, respectively.

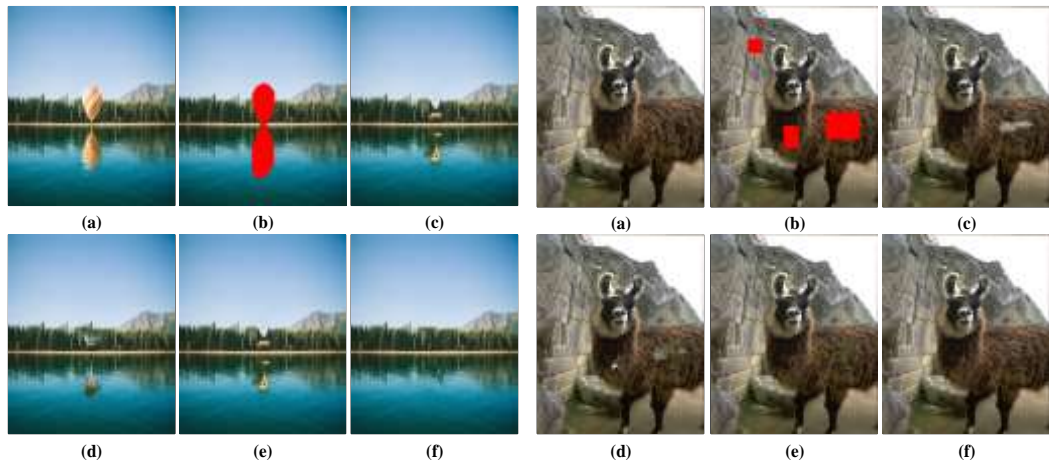


Figure5-8: Region reconstruction using EBI. The natural image from the internet (a), original image with the occluded area(s) (b); (c), (d), (e) and (f) Inpainted image using Criminisi, Anupam, Deng and TEBI schemes, respectively.

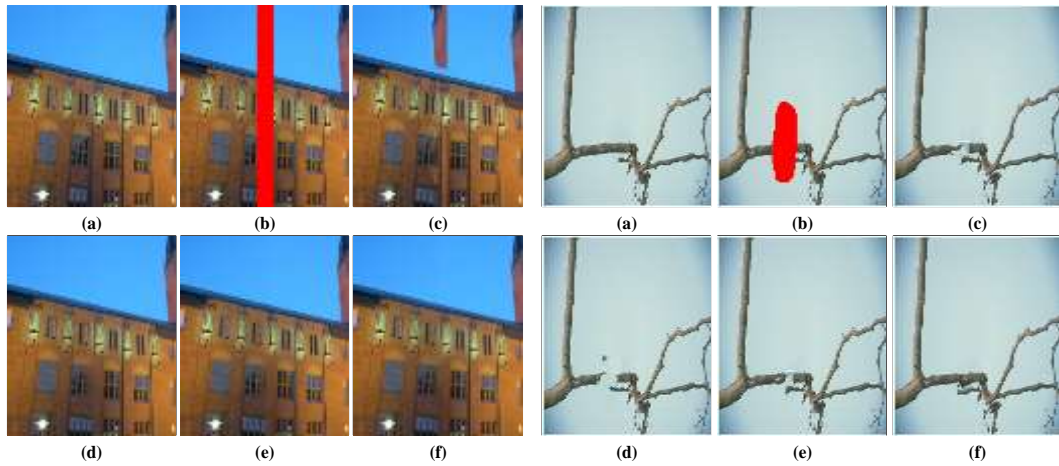


Figure5-9: Region reconstruction using EBI. The natural image from the internet (a), original image with the occluded area (b); (c), (d), (e) and (f) Inpainted image using Criminisi, Anupam, Deng and TEBI schemes, respectively.

The above figures demonstrate how our proposed method is outperforming the Criminisi, and Anupam methods while getting a result roughly similar to that obtained with the Deng method. Figure5-6 and 5-8 clearly illustrate the success of our approach in removing unwanted objects in two images, while Figure5-7 and 5-9 clearly illustrate the success of proposed method in reconstructing the missing regions in the images.

Furthermore, our approach is outperforming these state-of-the-art methods especially when the size of the missing region is big, and the surrounding area of the missing region has high texture and structure. More precisely, in Figure5-6 and 5-7 the missing region is relatively big and to reconstruct the missing information, one needs to extend the edges outside the missing region into the missing region. Figure5-7 and 5-9 illustrate the success of our method in reconstructing the edges and corners in the missing regions of the images. This shows that our method can successfully reconstruct

sharp edges sequentially even when the missing region is large, due to good patch size propagation selection using topological invariants. As a result, the priority function determined the best location in which to propagate the information in a steady manner.

The missing region reconstruction is now fully based on the information in the surrounding area. The success of any inpainting method is estimated in a precise way by the quality assessment of how well the geometric structure, photometric information and texture is propagated into the target region. Next, it is necessary to check the quality of the restored image so that one can check the suitability of the method as well as whether the produced image is visually acceptable or not. The next section will contain inpainting image quality assessment using different statistical measurements and the TDA approach.

5.6 Image Quality Assessment

The aim in this section is to test the qualities of various images which have been recovered using the proposed EBI method. The quality of its output images will be assessed by using statistical quality measurements and the TDA approach. The proposed EBI method has been applied to several natural images from the Berkeley database, as explained in section 3.6.1. The natural images in this database are classified into categories of low and high information (i.e. the quantity of texture in the images) based on TDA features that use in SVM classifier method; where the number of images in each category is 100 images. These images have been selected based on the quantity texture and structure (i.e. low and high information images) which that help to check the efficacy of EBI methods on each category of these image categories.

Thus the effectiveness of the proposed TEBI method and Criminisi, Anupam, and Deng methods will be studied by applying them to each one of these categories. Also, the output images of the proposed EBI method has been compared with the output images of Criminisi, Anupam, and Deng methods described in (Criminisi et al. 2004), (Anupam et al. 2010), and (Deng et al. 2015). Figure5-10 and 5-11 show examples of high and low information natural images from the Berkeley database, respectively.



Figure5-10: Example of eight out of 100 training low-information natural images.



Figure5-11: Example of eight out of 100 training high-information natural images.

Five experiments will be conducted to evaluate the inpainting of images from each of the two texture (high/low) categories. The aim of these experiments is to study the efficacy of proposed method on the reconstruction of the missing regions of different sizes and with high texture and structure around them in the natural images and to study the performance of the proposed method in reconstructing these missing regions.

We will be following the same steps that were presented in chapter Chapter 4 to create the inpainting mask. Five cases of inpainting masks have been used to study the efficacy of the proposed EBI method and to compare it with Criminisi, Anupam, and Deng methods. To cover all possibilities of using this TEBI method, these missing regions have been randomly selected in the mask images, and they are chosen based on different sizes of - different positions of-, and different numbers of missing regions in inpainting domains (Case1, Case2, Case3, Case4, Case5). Figure5-12 shows five cases of inpainting mask (i.e. inpainting domain) which represents five damaged regions in images that have been applied to both high and low texture database images to study the efficiency of the proposed EBI method.

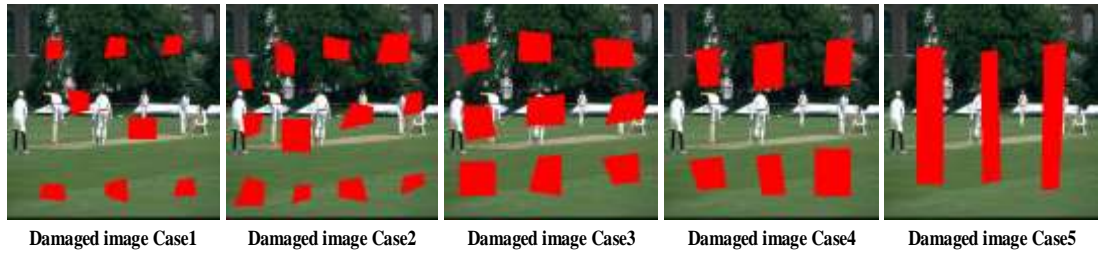


Figure5-12: The same natural image with five different inpainting domains.

To obtain evaluations of the output images of these experiments in each high and low texture category image, the statistical quality measurements and the TDA approach are used. The next two subsections will discuss and show the results of quality measures on two categories of natural database images.

5.6.1 Statistical measurements for image quality

The establishment of an accurate evaluation method which simultaneously assesses inpainted images qualitatively and quantitatively is a problem which has not been fully solved yet (Chandler 2013). Therefore, we depend on visual analysis to assess inpainted images qualitatively. However, for quantitative evaluation, the Mean Square Error (MSE), peak signal-to-noise ratio (PSNR), Structural Similarity (SSIM), Coherence structural quality measurement (CSQM), and entropy are calculated. To get better-quality image inpainting, the values of MSE, PSNR, and SSIM are only calculated between the inpainted regions and the corresponding regions in the original images; and the values of SCQM and entropy are also calculated on the inpainted regions (cf. Section 2.6.1).

Table 5-3 and 5-4 below summarise the comparison of the TEBI method with the Criminisi, Anupam, and Deng methods based on the average values of MSE, PSNR, SSIM, CSQM and entropy on the low and high information images, respectively; the times have taken to get the results using these methods are also shown.

C#	Methods	MSE	PSNR	SSIM	CSQM	Entropy	T(s)
Case1	Criminisi method	300.275	24.969	0.9755	0.47039	1.1900	55
	Anupam method	253.685	25.711	0.9761	0.47170	1.1863	67
	Deng method	348.248	24.235	0.9753	0.47152	1.1865	92
	TEBI method	252.451	25.728	0.9763	0.47361	1.1750	121
Case2	Criminisi method	283.779	25.171	0.9503	0.25397	2.0543	65
	Anupam method	279.927	25.239	0.9503	0.25477	2.0533	73
	Deng method	285.493	25.141	0.9503	0.25398	2.0545	96
	TEBI method	378.261	24.046	0.9492	0.25831	2.0336	136
Case3	Criminisi method	401.215	23.432	0.9234	0.20356	2.5216	78
	Anupam method	383.021	23.677	0.9243	0.20333	2.5145	93
	Deng method	597.413	21.549	0.9220	0.20187	2.4765	111
	TEBI method	379.917	23.668	0.9242	0.20537	2.2144	165
Case4	Criminisi method	425.420	23.288	0.9408	0.26899	1.9857	67
	Anupam method	367.423	23.562	0.9410	0.26841	1.9815	78
	Deng method	575.560	22.065	0.9397	0.26672	1.9494	93
	TEBI method	355.304	23.761	0.9414	0.27810	1.9208	133
Case5	Criminisi method	593.974	21.952	0.9178	0.22847	2.3045	88
	Anupam method	574.116	22.060	0.9182	0.22810	2.2993	95
	Deng method	809.893	20.420	0.9186	0.22469	2.2422	127
	TEBI method	573.177	22.054	0.9184	0.23808	2.2195	178

Table 5-3: Inpainted image quality assessment comparison using MSE, PSNR, SSIM, CSQM and Entropy for low information dataset images.

C#	Methods	MSE	PSNR	SSIM	CSQM	Entropy	T(S)
Case1	Criminisi method	975.919	18.883	0.9556	0.81145	1.2310	79
	Anupam method	926.117	19.089	0.9559	0.80826	1.2283	86
	Deng method	1307.57	17.705	0.9533	0.81071	1.2142	112
	TEBI method	922.282	19.408	0.9579	0.89128	1.2077	167
Case2	Criminisi method	1149.85	18.173	0.9078	0.43602	2.1312	87
	Anupam method	1025.25	18.608	0.9088	0.43608	2.1252	98
	Deng method	1404.03	17.360	0.9050	0.43624	2.0859	121
	TEBI method	1018.40	18.955	0.9189	0.45565	2.0237	183
Case3	Criminisi method	1442.66	17.155	0.8651	0.34645	2.6378	96
	Anupam method	1364.21	17.335	0.8662	0.34640	2.6296	111
	Deng method	1779.13	16.195	0.8623	0.34381	2.5674	137
	TEBI method	1359.10	17.863	0.8862	0.34913	2.4296	201
Case4	Criminisi method	1571.17	16.863	0.8938	0.45931	2.0989	83
	Anupam method	1451.14	17.075	0.8945	0.45804	2.0907	91
	Deng method	1839.31	16.103	0.8918	0.45551	2.0331	116
	TEBI method	1411.64	17.667	0.8978	0.46902	2.0189	178
Case5	Criminisi method	1995.07	15.682	0.8578	0.38833	2.4670	110
	Anupam method	1868.96	15.949	0.8586	0.38460	2.4510	132
	Deng method	2390.96	14.847	0.8564	0.38252	2.3474	165
	TEBI method	1848.71	16.378	0.8786	0.39557	2.4199	241

Table 5-4: Inpainted image quality assessment comparison using MSE, PSNR, SSIM, CSQM and Entropy for high information dataset images.

Chapter 5: Topological Exemplar-Based Inpainting

Table 5-3 and 5-4 show that the TEBI method is capable of effective region filling in low and high information natural images and gives a relatively higher PSNR value with low MSE value and that it leads to values of SSIM close to 1. The image quality measures used in Table 5-3 clearly show that TEBI is outperforming the Criminisi, Anupam, and Deng methods; however, the TEBI method takes a bit more time due to the amount of calculation entailed in the matching stage. During the testing, it was found that while some images could look visually pleasing and similar, they have different PSNR values. All the methods have succeeded in recovering the missing regions in the low information database images; the values of MSE, PSNR, SSIM from inpainted areas obtained by the TEBI method and other Criminisi, Anupam, and Deng methods are closer to each other than to the high information database images. The average values of PSNR and SSIM of inpainted areas obtained by the Anupam method are better than those obtained by the proposed method in Case2 and Case5, while the value of entropy is a measure by which the proposed method outperforms all the other methods. The TEBI method got lower entropy value than other methods. Also, the TEBI method got higher values of CSQM than other methods.

5.6.1.1 Results Analysis

To discuss the results of statistical measurements for low-information inpainted images, we found the average values of MSE, PSNR, SSIM from inpainted areas obtained by the TEBI method and other Criminisi, Anupam, and Deng methods are closer to each other in the low- information database images. The average values of PSNR and SSIM of inpainted areas obtained by the Anupam method are better than those obtained by our method in Case2 and Case5, while the value of entropy and CSQM are a measure by which TEBI outperforms all the other methods for all inpainting cases because the CSQM measure has been used to study the inpainted areas based on the coherence of inpainted areas with the remainders of the images, and entropy studies the amount of disorder in inpainted areas. So, in most situations, lower entropy is better than higher entropy.

The TEBI method got lower entropy value than those obtained other methods in both low- and high-information images. This means that the amount of disorder in the inpainted image by TEBI is less than the disorder in the inpainted images obtained by the Criminisi, Anupam, and Deng methods. While, the high values of CSQM represent better results; the TEBI method got higher values of CSQM than other methods in both

low- and high-information images; this means the inpainted regions obtained by the TEBI method are more coherent with the remainders of the images.

To sum up, the proposed TEBI method and the Criminisi, Anupam, and Deng methods succeeded in recovering the missing regions in the low-information database images. These methods have the ability to deal with simple texture and structure images (low-information images) as these methods proposed for this purpose. Moreover, we found the efficacy and the significant superiority of the TEBI in the reconstruction of the texture and structure in the missing regions in the high information images database due to good patch size propagation selection using topological invariants and the performance of matching criteria that used to give good matching patches especially for reconstructing the edges and corners in the missing regions of the image.

On the other hand, TEBI takes more time due to the amount of calculations entailed during the size patch decision and the matching stage. The TEBI and other methods need more time in reconstructing the missing regions in the high-information images than in the low-information images because the matching criteria needs more time to find the similar patch. During the testing, it was found that while some images could look visually pleasing and similar, they have different PSNR values.

As mentioned earlier, the MSE and PSNR are not reliable measures for checking the quality of image inpainting. Therefore, the TDA approach will be used, in the next section, to assess and compare the quality of inpainted images reconstructed in both the low and high information images databases.

5.6.2 Topological Data analysis for image quality

The TDA approach for the evaluation of the quality of image inpainting and the efficacy of the inpainting technique has been explained and introduced in section 2.6.2). To get inpainted-relevant image quality, this approach has been studied only the inpainted regions in the images, i.e. the number of CCs has only been calculated in the inpainted regions and the corresponding original regions. The same steps are followed in the construction of the Vietoris-Rips complex as introduced in section 2.6.2.2.

The 7 ULBP geometries have been studied at different thresholds $T=0$, $T=5$, $T=10$, $T=15$, for the inpainted images of the above experiments (i.e. five inpainting domains cases). The numbers of CCs are got in the geometries G3, G4, G5 and G6 at threshold

Chapter 5: Topological Exemplar-Based Inpainting

T=15. It needs to be said that the numbers of CCs for all methods in the other geometries at threshold T=15 are ill-conditioned.

Figure5-13 shows the average numbers of CCs of inpainted regions as obtained by the TEBI method and by the Criminisi, Anupam, and Deng methods for five damaged regions from low and high information natural images datasets in the geometry G4 at threshold T=15.

Figure5-14 shows the average numbers of CCs of inpainted regions which were obtained by the TEBI method and by the Criminisi, Anupam, and Deng methods for five damaged regions from low and high information natural images datasets in the geometry G7 at threshold T=15.

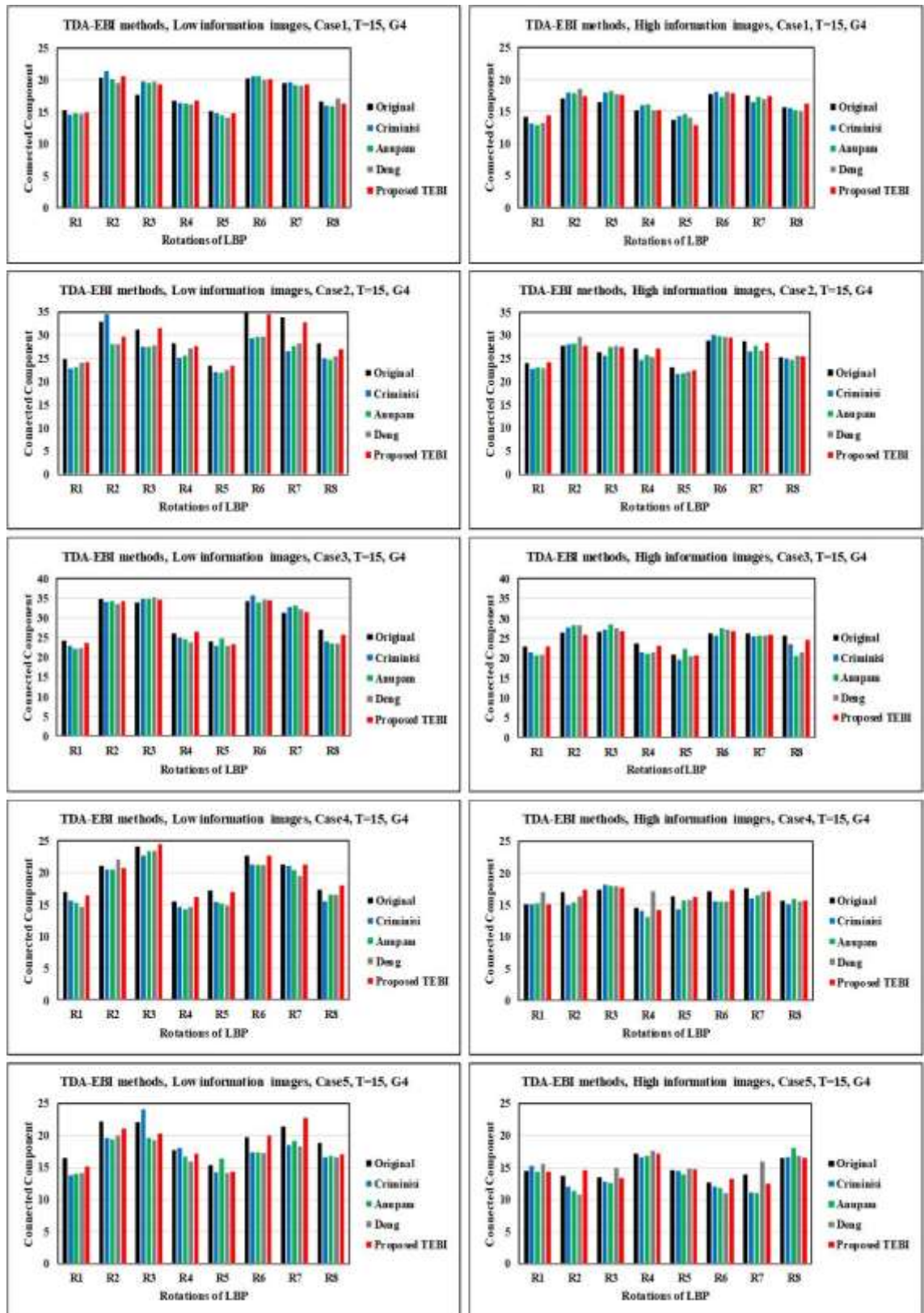


Figure5-13: Evaluation of performance of EBI techniques using TDA approach in the inpainted regions of high and low-information natural images in five inpainting domains at threshold $T=15$, in $G4$. Left column: Average of the number of CCs inpainted regions in low-information natural images. Right column: Average of the number of CCs inpainted regions in high-information natural images.

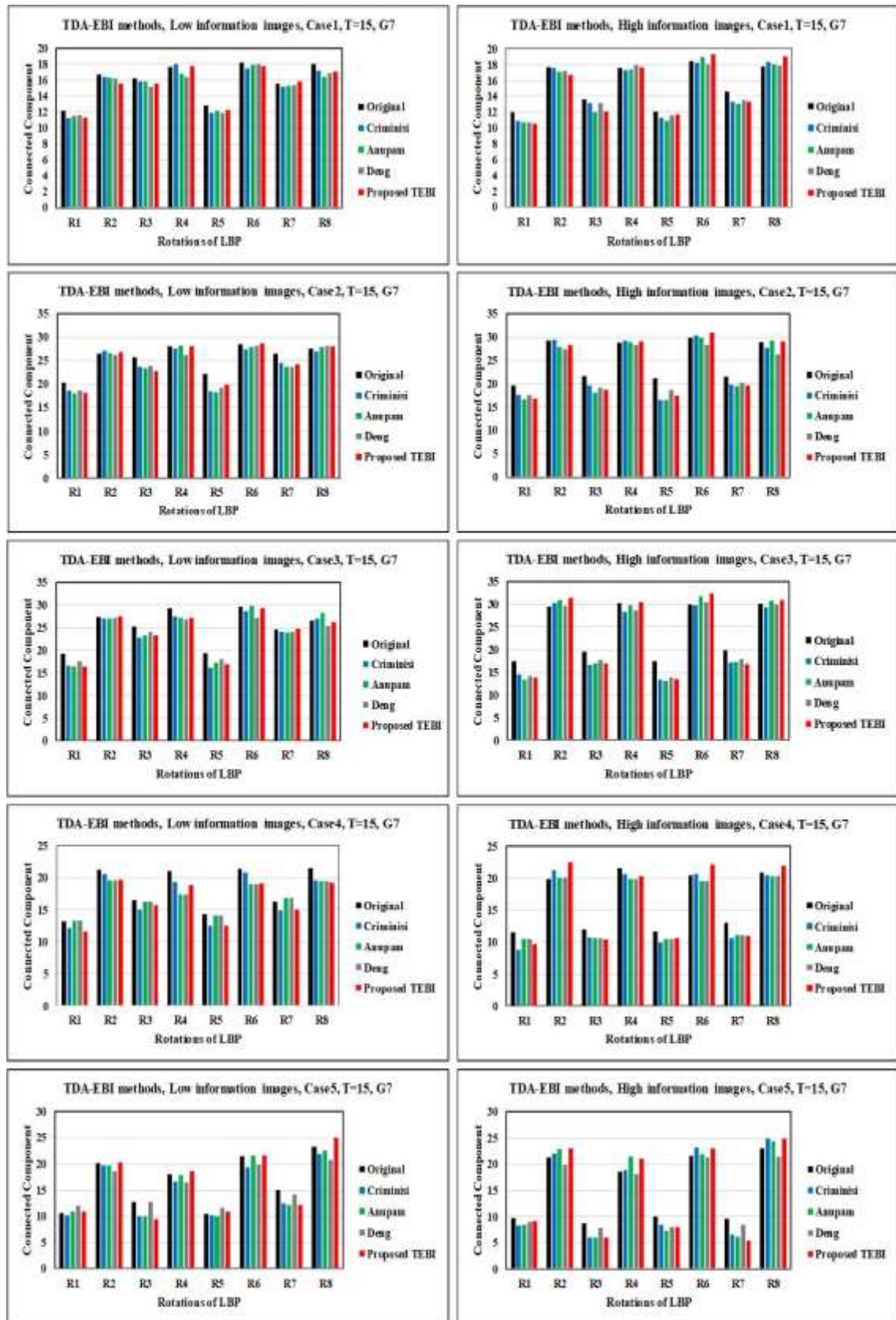


Figure 5-14: Evaluation of performance of EBI techniques using TDA approach in the inpainted regions of high and low-information natural images in five inpainting domains at threshold $T=15$, in $G7$. Left column: Average of the number of CCs inpainted regions in low-information natural images. Right column: Average of the number of CCs inpainted regions in high-information natural images.

Chapter 5: Topological Exemplar-Based Inpainting

As mentioned before, the uniform LBP pattern classifications based on the number of ones included in the pattern in the natural images database was introduced in (Ojala et al. 2002). The numbers of CCs in the inpainted areas that are recovered by the proposed method are closer to the numbers of CCs in the original areas than in the inpainted images obtained by other methods in the geometries G3, G4, G5, and G6 at threshold $T=15$ in both the low and high information natural images. Further, the numbers of CCs in the inpainted regions that are obtained by the TEBI method and by the Criminisi, Anupam, and Deng methods are wobbling in the geometries G1, G2, and G7 in both low and high-information images databases.

The rest of the numbers of CCs in other geometries G1, G2, G3, G5, and G6 at threshold $T=15$ are presented as an Appendix at the end of thesis (cf. Appendix B).

5.6.2.1 Results Analysis

The numbers of CCs in the inpainted areas that are recovered by the TEBI method are closer to the numbers of CCs in the original areas than in the inpainted images obtained by using other methods, as counted in the geometries G3, G4, G5, and G6 at threshold $T=15$ in both the low and high information natural images. This means the TEBI method has been successful in reconstructing the corners, edges and the line ends in the missing regions because of the patterns that are described in the geometries G3, G4, G5, and G6 geometries. This means the TEBI method has been successful in reconstructing the corners, edges and the line ends in the missing regions because of these geometries G3, G4, G5, and G6 geometries described the pattern of the corners, edges and the line ends in the image (Ojala et al. 2002).

The numbers of CCs in the inpainted areas in the low natural images that have been recovered by the TEBI method and other methods are closer to the numbers of CCs in the low information original areas than to the numbers of CCs in the high-information original areas. This means the TEBI and other methods have succeeded in reconstructing the missing regions in low information images because these methods already work well with simple texture and structure images (low-information images). However, the TEBI method is better than other methods in recovering the missing regions in high-information images based on the number of CCs in the inpainted regions because the proposed method is successful in reconstructing the edges and corners in the missing regions of the images due to good patch size propagation selection using topological invariants and the performance of matching criteria that have been used to

give good matching patches especially for recovering the texture in the missing regions. As a result, the priority function determined the best location in which to propagate the information in a steady manner, and the proposed method has successfully worked in recovering the missing regions in both low and high information natural images.

The numbers of CCs in the inpainted regions that are obtained by using the TEBI method and by the Criminisi, Anupam, and Deng methods are wobbling in the G1, G2, and G7 geometries in both low and high-information image databases because the inpainted regions are not totally identical to the original images owing to the inpainted region representing the approximation solution which can be close to the corresponding region of the original image but not totally identical because the missing information cannot be found in the image, although closely approximating information will be searched for in the rest of the image. Nevertheless, the TEBI method has succeeded to recover the regions in the both low- and high-information images. The TDA approach is used successfully to evaluate the qualities of inpainted images obtained by using the TEBI and other methods. The efficacy of these methods has been checked by the TDA approach as well.

5.7 Summary and Conclusion

A novel topological exemplar-based inpainting method (TEBI) has been proposed to improve the EBI method to remove and reconstruct large missing regions based on adaptive patch sizing when there is high texture in the missing region's surrounding area. An innovative adaptive priority function is introduced by adding a total variation term, uses a curvature operator to gain more insight into the structures of template patches and propagates lines and edges into the missing regions. A new criterion for matching template patches with candidate patches in the missing region's surrounding area is proposed. Experimental results illustrate the success of the TEBI method, which creates visually plausible images.

The proposed method performed well in recovering the image geometry but could not recover curved or cross-shaped structures completely. Nevertheless, the proposed method showed better visual results than other compared exemplar-based methods for the case of curved or cross-shaped structures. In particular, our method performed not so well in cases where the missing region has no similarity with other regions in the image.

Chapter 5: Topological Exemplar-Based Inpainting

The next chapter will introduce a hybrid inpainting technique based on decomposing the image into texture and structure components, after which the TEBI and PDE methods to recover the missing regions in texture and structure components, respectively.

Chapter 6 HYBRID IMAGE INPAINTING TECHNIQUE

In chapter Chapter 5, a topological data analysis approach was developed to improve the EBI technique that simultaneously reconstructs texture and structure in missing regions in an image. The resulting TEBI scheme helped determine the appropriate size of patches for propagating information into the missing regions. The success of simultaneous propagation of texture and structure, however, occurs only when there are regions similar to the missing regions in the rest of the image. In this chapter, the decoupling of the reconstructions of texture and structure information to be separately propagated into the missing region is investigated. A hybrid inpainting technique that combines a TEBI scheme to restore the missing region texture component with a high order PDE algorithm to recover the missing region structure component is developed. The results of using the hybrid inpainting technique in reconstructions of missing regions are promising, because both the TEBI and high-order PDE-based inpainting methods have been successful in recovering missing regions with high texture and structure in the surrounding areas. The hybrid scheme has been conducted in both spatial and frequency domains, and its performance has been assessed by using statistical and topological image quality measures. To clarify their superiority, the results of the proposed hybrid technique is compared to the results obtained from the techniques described in (Bertalmio et al. 2003) and (Jassim et al. 2018).

This chapter consists of five sections. Section 6.1 reviews the literature on existing hybrid-based inpainting algorithms. Sections 6.2 and 6.3 describe the design of our hybrid-based inpainting schemes in both the spatial and frequency domains, and present some experimental results of their use. Image qualities resulting from inpainting *via* the PDE algorithm are assessed by using statistical measurements and the TDA approach in both spatial and frequency domains, as discussed in section 6.4. Lastly, a summary and conclusions will be presented in section 6.5.

6.1 Hybrid inpainting techniques - A Literature Review

A hybrid inpainting scheme is meant to combine two or more inpainting approaches, each of which has own limitations but for different reasons. Ideally, a hybrid scheme should provide desirable visual results when applied to a variety of inpainting applications that cannot be achieved by its constituent schemes applied separately. In this section some papers which shed light on the studies of various hybrid inpainting techniques which include either texture Synthesis, PDE and/or exemplar-based algorithms are reviewed.

The shortcomings of existing single-approach inpainting schemes seem to be deeply rooted in the extremely difficult task of simultaneously understanding and analysing image features at different scales. By no mean is this problem confined to inpainting, and indeed many image applications that require feature detection/manipulation suffer from the difficulty of finding one image algorithm that can simultaneously manipulate/repair image features at different scales. Indeed, our inability so far to tackle the tough challenge of recovering large missing regions can be attributed in part to the difficulty of determining with certainty the scale of missing features within the region. It is worth noting that the EBI schemes that were investigated in the last chapter, including the TEBI, do recognise this issue and attempt to deal simultaneously with missing information at large scales (referred to as structural component) and small scales (referred to as textural component).

Images can be decomposed/analysed in many different ways, and multi-resolution (e.g. wavelet-based) approaches have been dominant in many applications. In relation to image inpainting, one is usually interested in decomposing an image into its structural components, representing the main large image features/objects at microscales, and a textural part, with microscales feature representations. The definition of these two components is somewhat vague as a result of the absence of agreement on scale for different applications. At a given scale, a structure may be construed as texture in another larger scale. Textural, and to a less extent structural, features are expected to appear repeatedly throughout the image perhaps with some orientational variation. Appropriate decomposition of damaged images into texture and structure components provides a useful background understanding of the challenges of image inpainting especially for large missing regions and provides the initial step of existing hybrid inpainting techniques.

Hybrid inpainting has a rich literature and remains an active area of research. Therefore, it is not an easy task if one wants to cover all aspects of these models. Most existing hybrid inpainting techniques attempt to combine inpainting schemes that are good at recovering missing information at small scales with those that are good at recovering missing information at large scales. Their success, however, strongly depends on the ability to adequately decompose/analyse images at a multi-scalar level in order to identify the types of missing information at different scales. Another factor that influences the success of hybrid schemes is their strategy for restoring the two different types of missing information.

Bertalmio et al. in (Bertalmio et al. 2003) have proposed the first known Bertalmio hybrid technique that combines the results of using texture-based synthesis and a PDE-based method. The idea of this technique is to divide the image into texture and structure components by using a total variation model (i.e. 2nd order PDE) which was applied in (Rudin et al. 1992). Restoration of each component is implemented separately. The missing regions in those components are recovered by texture based synthesis (Efros & Leung 1999) and a PDE-based method (Bertalmio et al. 2000) respectively. The transport model has been used to recover the missing region in the structure component. This scheme performs better than many other hybrid schemes proposed later when the same reconstruction algorithms is applied (e.g. either texture synthesis or PDE-based inpainting).

Many researchers in recent years have adopted the Bertalmio et al. hybrid design strategy as a benchmark. In (Jiyang Wu & Qiuqi Ruan 2008) another hybrid image inpainting model was proposed that uses a bidirectional diffusion PDE to reconstruct the missing regions in the structure components. This PDE restores information smoothly and preserves linear structures. At the same time, the missing regions in the texture components have been reconstructed by an improved EBI method which is constrained by a cross-isophote diffused data term. The inpainted regions in structure and texture components are then combined. The results of this novel hybrid model were very favourable for both the texture and structure components, and it performs better than those in (Bertalmio et al. 2003) for reconstructing small missing regions.

In an attempt to reconstruct large missing regions, the authors in (Chen 2006) proposed a method to recover the structure and texture simultaneously in the missing regions, applying a wavelet decomposition model to the texture and the structure of the image.

The wavelet transform is used to decompose the image into high frequency and low-frequency parts. Subsequently, a Compactly Supported Radial Basis Function (CSRBF) (Kojekine et al. 2003) and texture synthesis methods are used to recover the missing regions at the low and high-frequency levels, respectively. The results of this method have been compared with the results of using the transport method (Bertalmio et al. 2000) on natural images, and the outputs of this method outperform those obtained using the transport method.

The authors in (Sangeetha et al. 2011) have proposed yet another hybrid technique to recover the large missing areas based on the same idea as in (Bertalmio et al. 2003). The image is decomposed into texture and the structure components by the 3rd-optimal PDE algorithm which was proposed in (Bertalmio 2006). For recovering the missing regions in structure components. The Quick Curvature-Driven Diffusions (QCDD) model introduced in (Xu et al. 2008) has been used; the QCDD model is a 3rd-order PDE, which is an improved version of the CDD model. The authors have suggested improving the exemplar-based inpainting algorithm by using new matching criteria to measure patch similarities in order to recover the missing regions in the texture components. The inpainted image can be represented by the combination of outputs of inpainted texture and structure components. This method was very effective for reconstructing large missing regions in the texture and structure components. The results of this technique have been compared with some present methods on different natural images, which has demonstrated the eligibility of this proposed approach in providing high-quality inpainted images.

The above reviewed hybrid techniques have been shown to be capable of recovering rather small missing regions with texture and structure surrounding them, but their less than satisfactory dealing with difficult cases such as large missing regions doesn't seem to be due to an ineffective way of splitting texture and structure information but rather more to the strategy of simultaneous recovery of texture and structure information in the missing regions using the same information propagation method. Our proposed hybrid approach attempts to depart from the strategy of using the same inpainting scheme for simultaneous/separate recovery of texture and structure information, while we continue to use image decomposition methods to analyse the image into its texture and structure components. Moreover, our hybrid scheme exploits the improvements achieved in the last 3 chapters on both the EBI and PDE-based method.

6.2 Hybrid inpainting technique in the spatial domain

In this section, a new hybrid inpainting technique is proposed that is followed the above-established trend in starting with the decomposition of images into texture and structure components, to be followed by the selection of possibly different inpainting schemes for recovering these two components in the missing region. Based on our adopted TV and PDE models of the image inpainting problem, image decomposition schemes are investigated and a geometry- based structure-texture decomposition procedure is adopted. In selecting the appropriate texture and structure components for recovery, it would be natural to exploit the benefits of using the schemes developed in the earlier chapters of this thesis due their established desirable performances compared to other schemes. In chapters Chapter 3 and Chapter 4, PDE-based inpainting algorithms (using different order PDEs) are developed to recover the texture in missing regions, which succeeded in restoring the textures and structures of small missing image regions. In the last chapter, the alternative TEBI scheme was developed and tested, but its success depended on the presences of patches in the rest of the image that have similarities with the region's boundary blocks. The TEBI highlighted the importance of distinguishing between image texture and structure by dealing with them simultaneously, whereas the PDE-based schemes do not explicitly take into account this distinction in the recovery process. The TEBI performs well in recovering the geometry of a missing region but not curved or cross-shaped structures completely. These observations necessitate the need for choosing a geometry-compatible texture-structure image decomposition

The next subsection is devoted to the description of the decomposition models of interest to our hybrid inpainting. After that, subsection 6.2.2 shows the texture-structure components recovery schemes, and outlines fully the steps of our hybrid scheme.

6.2.1 Image decomposition methods

In this section, the image decomposition approach is introduced as one of the three key ingredients in the hybrid inpainting algorithm. As mentioned earlier, the preference is geometric based decomposition schemes. The main ingredient of such image decomposition schemes was originally developed in the process of image restoration and denoising using total variation minimisation (Rudin et al. 1992), (You & Kaveh 2000), and (Vese & Osher 2003). Here we note, that denoising is reliant on decomposing an image into the unknown clean image and the added noise model.

The basic idea of the decomposition model used in this chapter is: $I(x, y) = u(x, y) + v(x, y)$, where $I(x, y)$ is the input damaged image, $u(x, y)$ is the structural component, and $v(x, y)$ is the texture component. The end goal of the decomposition method is to have a very smooth image $u(x, y)$ which preserves all the dominant edges in an image but is smooth on interior regions, and an image $v(x, y)$ which contains all the texture in an image as well as the noise. These images (components) will then be fed into a PDE-based inpainting method and a TEBI method, respectively. The output of those methods can be recombined to obtain the final image.

In (Rudin et al. 1992), the problem of denoising I by taking a minimisation of this problem in the space of functions of bounded variation $BV(\mathcal{R}^2)$. The total variation $TV - L^1$ model is

$$\min_{u \in BV(\Omega)} \left\{ J_\lambda[u] = \int_{\Omega} |\nabla u| + \lambda \|v\|_{L^1}, I = u + v \right\} \quad (6.1)$$

where $\lambda > 0$ is a scaling constant. The first part represents a regularising term, to remove noise or small details with observance of important features such as sharp edges and corners. The energy (a fidelity) term is represented in the second part. The TV regularisation model is applied to decompose the image into a structure part and a texture part, where the difference between I and u represents the texture part. The minimising model is expressed formally as the Euler-Lagrange equation (6.1):

$$\begin{cases} u = I + \frac{1}{\lambda} \operatorname{div} \left(\frac{\nabla u}{|\nabla u|} \right) & \text{in } \Omega \\ \frac{\partial u}{\partial \bar{n}} = 0 & \text{on } \partial\Omega. \end{cases} \quad (6.2)$$

while the formula of the total variation that defined in $TV - L^2$ model is

$$\min_{u \in BV(\Omega)} \left\{ J_\lambda[u] = \int_{\Omega} |\nabla u|^2 + \lambda \|v\|_{L^2}, I = u + v \right\} \quad (6.3)$$

The Euler-Lagrange equation corresponding to (6.3) is:

$$\begin{cases} u = I + \frac{1}{2\lambda} \nabla^2 & \text{in } \Omega \\ \frac{\partial u}{\partial \bar{n}} = 0 & \text{on } \partial\Omega. \end{cases} \quad (6.4)$$

The finite difference method has been used to apply the model (6.2) with a simple Dirichlet boundary condition which will produce a smoothly structured image. More information about the numerical application can be found in (Vese & Osher 2003). The numerical application of the model (6.4) is similar to model (6.2).

In addition, the 4th order model has been used to decompose the image into texture and structure components. Originally, this model was proposed in (You & Kaveh 2000) again for image de-noising as well as image decomposition, and its performance was compared with that of the total variation model. This model is based on the following minimisation equation:

$$\min_{u \in BV(\Omega)} \left\{ J_\lambda[u] = \int_{\Omega} f(|\nabla^2 u|) \partial \Omega \right\} \quad (6.5)$$

where ∇^2 denotes the Laplacian operator and $f(\cdot) > 0$ and is an increasing function. The Euler-Lagrange equation derived from the model (6.5) is

$$f'(|\nabla^2 u|) \frac{\nabla^2 u}{|\nabla^2 u|} = 0 \quad (6.6)$$

The general details of the variational problem and application of the Euler-Lagrange equation on the model (6.5) can be found in (You & Kaveh 2000) and (Strobel 1989). The following gradient descent procedure has been applied to the model (6.6):

$$\frac{\partial u}{\partial t} = f'(|\nabla^2 u|) \frac{\nabla^2 u}{|\nabla^2 u|} \quad (6.7)$$

The finite difference method can be used to solve the model (6.7). This model is proposed for the removal of noise and the preservation of edges. The properties of the model (6.7) and its numerical solution have been introduced and discussed in (You & Kaveh 2000) and (Bertozzi & Bertozzi 1998).

In order to help with the determination of our preferred texture-structure decomposition scheme, the above denoising schemes are implemented. Figure6-1, below, illustrates the noise removal process from a colour image by the (6.2) model. Figure 6-2 presents the denoised images obtained from the (6.2), (6.4), and (6.7) models.

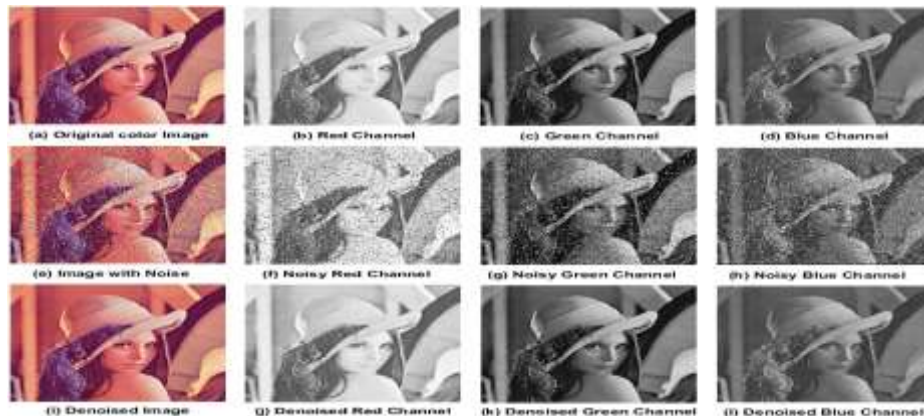


Figure6-1: Image denoising example. Row (1) original images, row (2) the noise images, row (3) denoised images by using model (6.2).

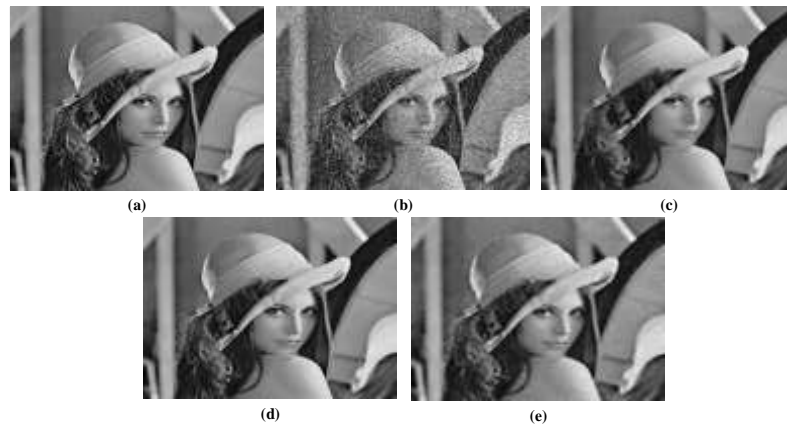


Figure 6-2: Comparison of three denoising models. (a) Original image, (b) noisy image, (c) TV-L¹ model, (d) TV-L² model, and (e) 4th-order model.

We can observe that the 4th order model has failed to completely remove the noise because piecewise planar images have less masking capability than step images. Furthermore, the edges have been preserved in the denoised image by the 4th order model while TV models tend to generate multiple false edges.

In the decomposition task, the models (6.2), (6.4) and (6.7) have been studied and used to decompose images into texture and structure components. The results of applying these models to the original image were smooth structure images, where the original image is without noise. On the other hand, the texture image is the difference between the original image and the structure image. Figure6-3 illustrates the decomposition of the previous image into texture and structure components using the (6.2) model. The decomposition of another general image into texture and structure components by the (6.2), (6.4), and (6.7) models are shown in Figure6-4.

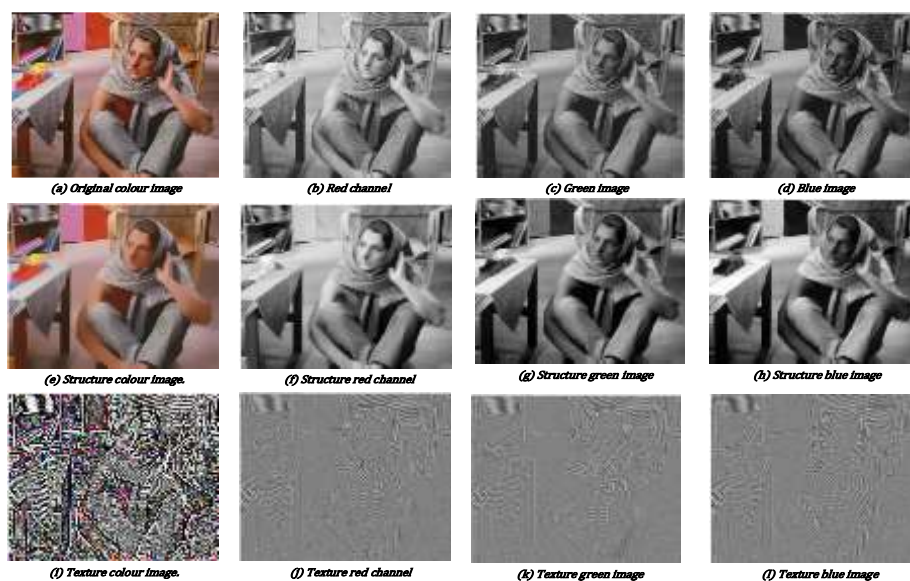


Figure6-3: Image decomposition example. Row (1) the original images, row (2) the structure component images by using model (6.2), row (3) the textured component images.

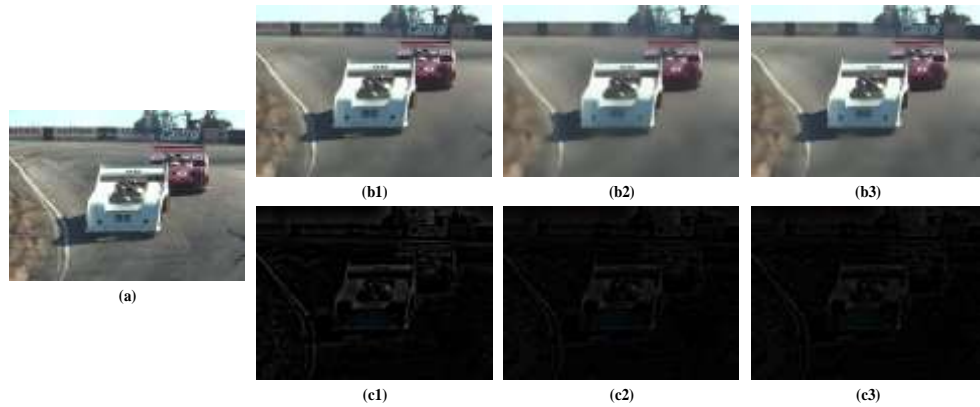


Figure6-4: Comparison of three decomposing models: (a) Original image, (b1) and (c1) structure and texture components by $TV - L^1$ model, (b2) and (c2) structure and texture components by $TV - L^2$ model, and (b3) and (c3) structure and texture components by 4th-order model.

As seen in Figure6-4, the structure component generated by $TV - L^1$ is sharper than that by $TV - L^2$ (Jiying Wu & Qiuqi Ruan 2008) and 4th order models (You & Kaveh 2000).

The structure component generated by a 4th order model (6.7) is sharper than that by $TV - L^2$ model (You & Kaveh 2000). This means that if the structure component is smoother, the texture component will be higher. Therefore, the texture and structure components of the image generated by the $TV - L^1$ model (6.2) are a better representation than those generated by other models. Therefore, the $TV - L^1$ decomposition model is used to analyse images into texture and structure components in the hybrid inpainting technique.

6.2.2 Inpainting methods for reconstructing the texture and structure images

Having decomposed an image with a missing region (s) into its texture and structure components, appropriate inpainting methods which can be used to reconstruct the missing region through these components are selected. Naturally, the results of the previous chapters in our information recovery of missing regions are exploited. In particular, the use of the TEBI and PDE-based inpainting methods to recover the missing regions in the texture and structure components, respectively, is tested.

For example, the topological exemplar-based inpainting method (TEBI described in chapter Chapter 5) is most suitable for use in reconstructing the texture components of missing regions, see (Jassim et al. 2018). This choice is also supported by efficiency consideration. In contrast, the texture synthesis method inefficiently propagates information into the missing region recursively, i.e. pixel by pixel until the entire missing region is filled. The optimal combination of these various algorithms will be

designed to form our proposed technique which will be used to reconstruct small as well as large regions. Besides improving inpainting quality, this method is computationally efficient. In the subsequent sections, the merits and shortcomings of this approach are discussed.

The proposed hybrid technique starts by decomposing the image into texture and structure components, after which the damaged regions are separately recovered by different inpainting methods. The hybrid technique has been used for the simultaneous rebuilding of the textures and structures of missing regions in an image, in the spatial domain. The ingredients that are used in this technique are the TV model, the TEBI, and the PDEs inpainting model. The idea of this approach is to first decompose the image into two components which are the texture and structure components by using the TV model then rebuilding each one of these components separately by using TEBI, and PDEs inpainting methods respectively. Finally, inpainted structure and texture components are combined.

Figure6-5, below, depicts a block diagram of our proposed hybrid inpainting algorithm. The image decomposition step is not specified in this diagram, but the proposed scheme implements the TV – L^1 decomposition model, as discussed in section 6.2.1.

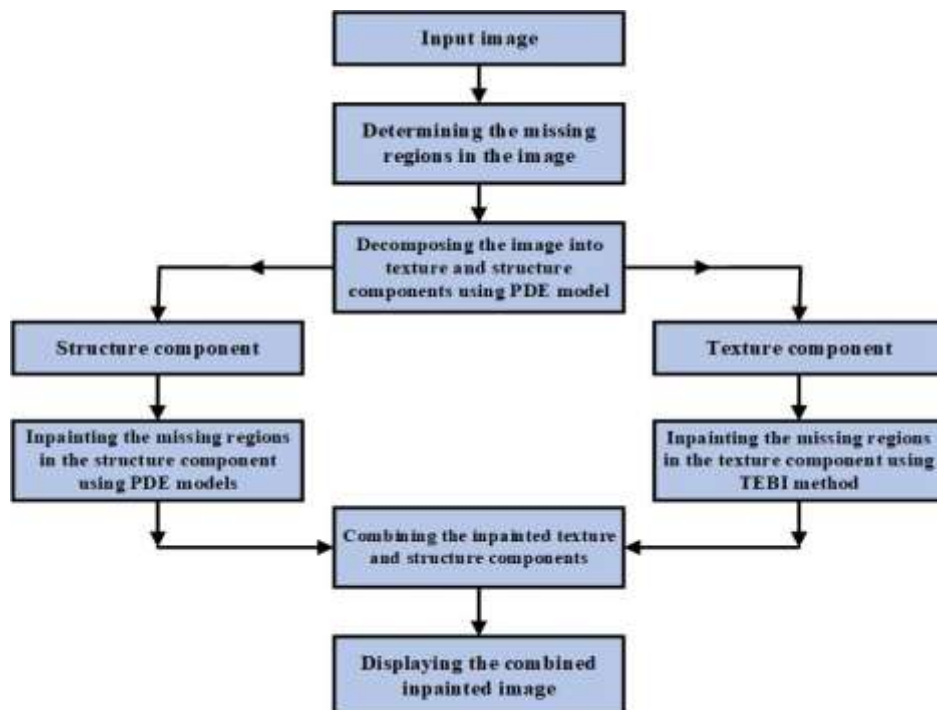


Figure6-5: Flowchart Hybrid technique in the spatial domain.

This technique works with a combination of inpainting algorithms of image structure and texture. The steps of the proposed method can be represented as follows: Firstly,

read the input image, then mark the region of interest in it. After initialisation, a marked image is decomposed into its structure and texture components. Next, inpainting of the structure and texture components of the image are carried out by the PDE-based inpainting and the TEBI methods, respectively. Two kinds of PDE-inpainting techniques (the MES, and the mCH schemes) are proposed for the reconstruction of image structures. The texture image component can be efficiently reconstructed *via* the TEBI method. The quality of the results of this hybrid technique will be compared with the results of the benchmark Bertalmio technique by using statistical measurements and the TDA approach.

Here we recall that the TEBI method has been used to rebuild missing-regions' textures by using the matching criterion described in chapter Chapter 5. In (Jassim et al. 2018), we established that this method produces very good texture synthesis results. In Figure6-6, we illustrate that the proposed TEBI approach succeeds in reconstructing the straight edges and corners, whereas a well-known inpainting algorithm, (Efros & Leung 1999), results in the appearance of highly visible artefacts. Note that this image shows the same relatively small structure repeated periodically, and therefore only the texture needs to be repaired because the TEBI method has a good priority function and a strong matching criteria that helped to success in recovering the missing regions with highly-textured surrounding areas.

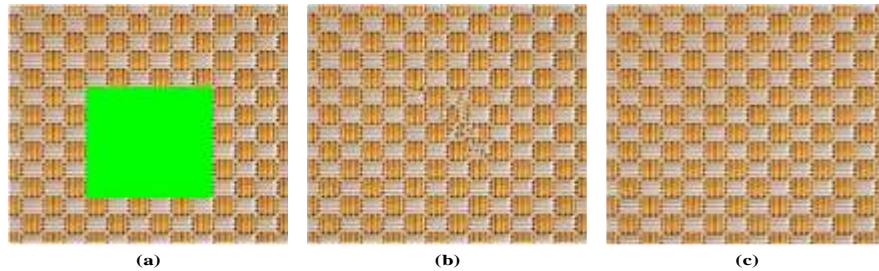


Figure6-6: Recovering missing texture region. (a) Masked image, (b) and (c) inpainted image by using the algorithm (Efros & Leung 1999) and TEBI method, respectively.

On the other hand, PDE-based inpainting methods are our obvious choice to reconstruct the missing regions in highly structure images. The key idea behind these methods is to spread the image information from outside of the missing region (i.e. boundary of the missing region) to inside it in the direction of minimal change (isophotes). The numerical solution of these algorithms creates the propagation of information in the direction of isophotes.

The work in Chapter Chapter 4, shows that high order PDE models provide the best way to treat the missing regions in structure images because these models have certain

advantages such as the ability to propagate the information into large missing regions (i.e. continuity property), and they also smoothly propagate grey-values in gradient directions. As we experimentally demonstrated in chapter 4, the performances of high order PDEs are better than that of the 2nd order PDE in recovering the missing regions in an image. Therefore, two kinds of high order PDE-inpainting methods are used to recover the missing regions in the structure image, which are MES (Esedoglu & Shen 2002) and mCH models (A. L. Bertozzi et al. 2007).

The next section introduces some examples of using the hybrid technique to recover the missing regions in the natural images in the spatial domain. Also, these results will be discussed and be compared with the results of the Bertalmio technique.

6.2.3 Experimental results in the spatial domain

The hybrid technique is applied to the rebuilding of missing structure and texture simultaneously. This approach is implemented on different size regions in several images, and MES and mCH models have been used to recover the structure missing regions as previously clarified in chapter Chapter 4. The missing texture region is recovered by the topological exemplar-based inpainting algorithm, which was previously introduced in chapter Chapter 5.

The process implemented by the hybrid technique is introduced step by step by Figure6-7. To check the efficacy of the proposed hybrid technique, some comparisons are conducted between it and the single inpainting methods and with the Bertalmio technique. Therefore, comparisons between the results of the proposed hybrid technique and the results of texture-synthesis and PDE-based inpainting methods are undertaken to demonstrate that the combining of two inpainting methods leads to better results than a single method in recovering the missing regions in natural images, as seen in the Figure6-8 and 6-9. Figure6-7 shows the recovery of the missing regions by the hybrid inpainting technique, using again the decomposition steps as in Figure6-4 to recover each component in the missing region.

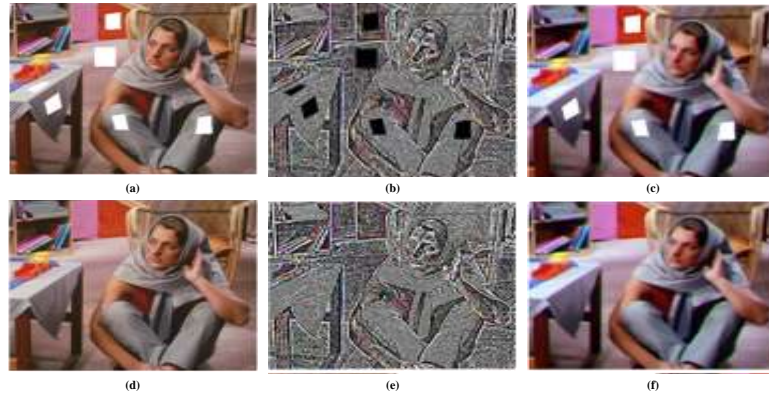


Figure6-7: Hybrid inpainting process. (a) Masked image, (b) and (c) masked texture and structure images, respectively, (e) and (f) inpainted texture and structure image, respectively, (d) combining inpainted texture and structure images,

Also, Figure6-8 illustrates the comparison between the proposed hybrid technique and three kinds of PDE-based inpainting methods used to recover the missing regions in the image; transport, MES and mCH models.

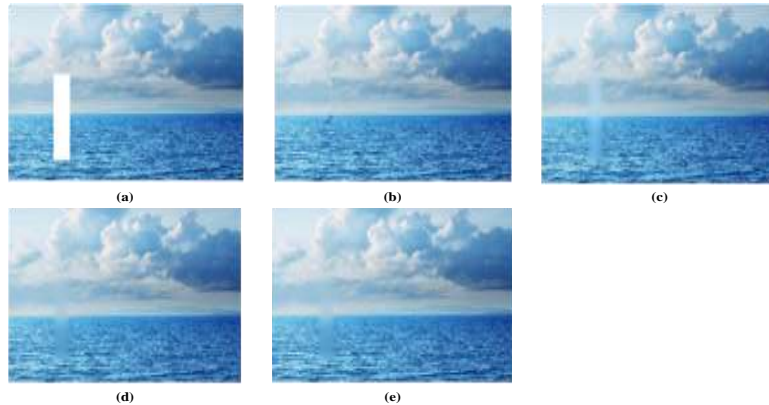


Figure6-8: Recovering the missing region using the hybrid technique. (a) Masked image, (b) (c), (d), and (e) inpainted image by our proposed hybrid approach, transport, MES and mCH PDE methods, respectively.

Figure6-9 shows examples of object removal and the results of the proposed hybrid technique with texture synthesis and transport methods.

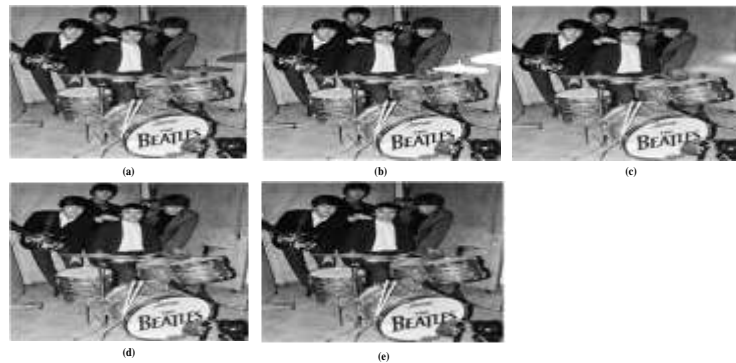


Figure6-9: Object removal by hybrid technique. (a) Original image, (b) masked image, (c), (d), and (e) inpainted image by PDE (Bertalmio et al. 2000), Texture-synthesis method (Efros & Leung 1999), and proposed hybrid technique, respectively.

Finally, Figure6-10 introduces the examples of object removal and for comparison the results of the proposed hybrid technique with the Bertalmio technique.

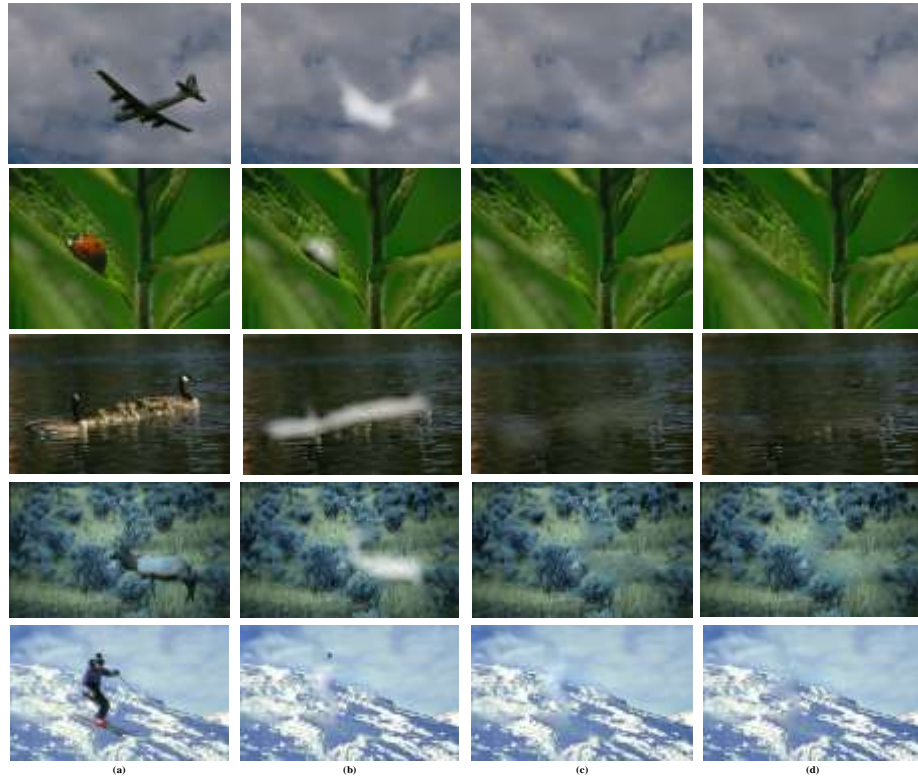


Figure6-10: Comparison of the proposed hybrid technique with the Bertalmio technique. (a) Original images, (b), (c), and (d) inpainted image by Bertalmio technique, proposed hybrid technique with MES method for structure image, and the proposed hybrid technique with mCH method for structure image, respectively.

The output of the hybrid technique, in the above examples, has outperformed the texture synthesis and PDE-inpainting methods. Visually, its results are more acceptable than those of single methods, which are texture synthesis and PDE-based inpainting methods. The TEBI method has been applied to the reconstruction of the information in the texture images; and also the propagation of information block by block. This means the propagation of information into the missing region by using the TEBI method, which is faster in this context than the texture synthesis method. The MES and mCH methods have qualitatively outperformed the transport method, as seen in Figure6-8 and 6-9.

The second comparison is made between the results of the proposed hybrid technique and the results of the original hybrid technique of Bertalmio et al. scheme. The proposed hybrid technique has been applied to recover the missing regions by using the MES method and mCH methods to recover the missing regions in the structure images.

Figure6-10, below, displays the results of the proposed hybrid technique and the original hybrid technique. Large missing regions have been recovered in different texture and structure images; the high order PDE methods have been applied to recover large missing regions in the structure images. The TEBI method has successfully reconstructed the large missing regions in the texture images. Therefore, the proposed hybrid technique when using the mCH method to recover the missing region in a structure image visually outperformed both the original hybrid technique and the proposed hybrid technique when using the MES method for the same task. Eventually, the results of the proposed hybrid technique in both cases turn out to be better than the results of the original hybrid technique. The task of assessing image inpainting quality will be studied and discussed after the discussion of the implementation of the proposed hybrid technique in the frequency domain.

As we mentioned in chapter Chapter 4, the image in the frequency domain has been analysed into non-textured and textured image components (i.e. low-frequency coefficients and high-frequency coefficients), and the size of a missing region will be reduced, which has a very favourable effect on the application of PDE algorithms. Therefore, the next section studies the hybrid technique in the frequency domain, and the application of this technique on a set of images, and the results will be compared with those obtained by applying the same technique in the spatial domain.

6.3 Hybrid inpainting technique in the frequency domain

Wavelet filter banks provide well-established tools for multi-resolution decomposition of images; the low-frequency response components capture coarser features (i.e. structure) while the higher-frequency response components capture image features at finer scales (i.e. texture). This fact motivates the development of a hybrid inpainting algorithm for digital reconstruction based on the combination of wavelet decompositions. The proposed hybrid algorithm will also use a PDE-based inpainting algorithm to recover missing coefficients in the low-frequency sub-band, and for texture recovery, TEBI methods will be used to recover missing coefficients in the high-frequency sub-band.

In the hybrid technique, the wavelet transform is used to decompose the image into low- and high-frequency sub-bands.. The steps of the technique are as follows:

1. Step 1. The region of the original image to be inpainted is marked manually by the user.

2. Step 2. The masked image is decomposed into non-texture and texture images (i.e. the low and high-frequency components) by using the Haar wavelet transform.
3. Step 3. The damaged region in the non-texture image (i.e. low-frequency sub-band) is reconstructed by using the PDE-based inpainting method.
4. Step 4. The intensity values of the damaged regions in texture images (i.e. high-frequency sub-bands) are recovered by the TEBI method.
5. Step 5. The inverse wavelet transform is used to convert these images (i.e. four sub-bands) to one image (which is called the inpainted image).

As described in the last section, the first step of the spatial domain hybrid technique decomposes the image into a non-texture image and a texture image. However, the standard wavelet image decomposition by filtering to depth 1, produces one non-texture image and three texture images. Hence, this proposed frequency-domain hybrid scheme uses PDE-based inpainting method to recover the missing region in the non-texture image and EBI method will be applied to reconstruct the missing region in each of the 3 texture images. Finally, the wavelet transform will be inverted in the usual way.

At a k -level depth wavelet decomposition there would be 1 non-texture image but $3k$ texture images at different scales. For the sake of understanding the impact of the transform depth, the wavelet-based hybrid scheme is applied to natural images in two scenarios, referred to as the 2nd and 3rd-level wavelet domains. In the first scenario, the PDE-based inpainting method has been applied to reconstruct the missing region in the non-texture image (i.e. low-frequency sub-band) in the second level of wavelet decomposition, and TEBI method has been used to recover the missing information in the six other texture images (i.e. six high-frequency sub-bands). In the second scenario, the PDE-based inpainting method has been applied to recover the missing region in the non-texture image (i.e. low-frequency sub-band) in the 3rd level wavelet domain, and TEBI method has been used to reconstruct the missing information in the nine texture images (i.e. nine high-frequency sub-bands).

Two kinds of high order PDE inpainting methods have been applied to reconstitute the missing region in the non-texture image (i.e. low-frequency (approximation) sub-band) which are MES and mCH methods. The TEBI inpainting method has been used to recover the missing regions in the LH3, HL3, and HH3 images in the 3rd level and then the same three procedures were applied to recover the missing regions in the LH1, LH2,

HL1, HL2, HH1, and HH2 images. The aim for each method in practice is to follow the same priority in choosing the block which is to be filled and the same similarity block that is determined from the rest of the image (the same steps as are used to recover the missing regions).

Therefore, if the size of the block that is used to recover the missing region in LH3, HL3, and HH3 images is 3×3 , then the size of the block that is used to recover the missing region in LH2, HL2, and HH2 images is 6×6 , while the size of the block that is used to recover the missing region in LH1, HL1, and HH1 images is 12×12 , as seen in Figure6-11.

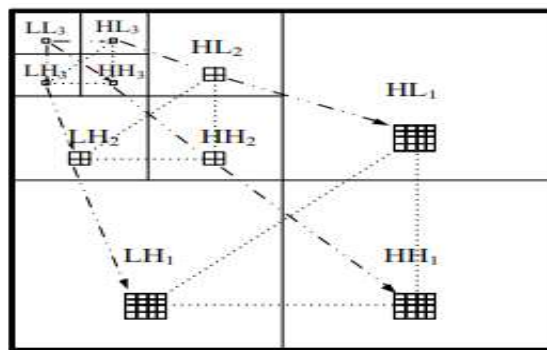


Figure6-11: The representative value of the wavelet transform for 1st, 2nd and 3rd levels.

Through the implementation of the hybrid technique in the frequency domain, we found that inverting the wavelet transform back to the spatial domain the accuracy of image reconstruction depends on the size of the image. For instance, the size of the image is 150×150 for 1st level, the size of each sub-band is 75×75 , while the size of each sub-band is 38×38 in the 2nd level. Then when using the inverse of the wavelet transform to return the image to the spatial domain, the size of the image will increase and will be 151×151 , and that will affect the accuracy of the image. Therefore, to overcome the problem, we need to use images of $2^n \times 2^n$ before to convert the image to the frequency domain.

In practice, the wavelet inverse transforms process influences the edges of objects in the image because the size of sub-bands needs to be resized as it converts from the 3rd level to the second level. Therefore, the damaged images have been cropped to be 2^n such as $2^9 = 512$, the size of the image being 512×512 , or the $2^8 = 256$, the size being 256×256 . The cropping task has been treated the effects of resizing on the edges of objects in the images, and the new size of the image means that the image doesn't need to be resized when it's converting from 3rd to second and from 2nd to the 1st

level. Figure6-12 presents the effects of resizing on the sub-bands before converting from 3rd to second and second to the first level after recovering the missing regions.

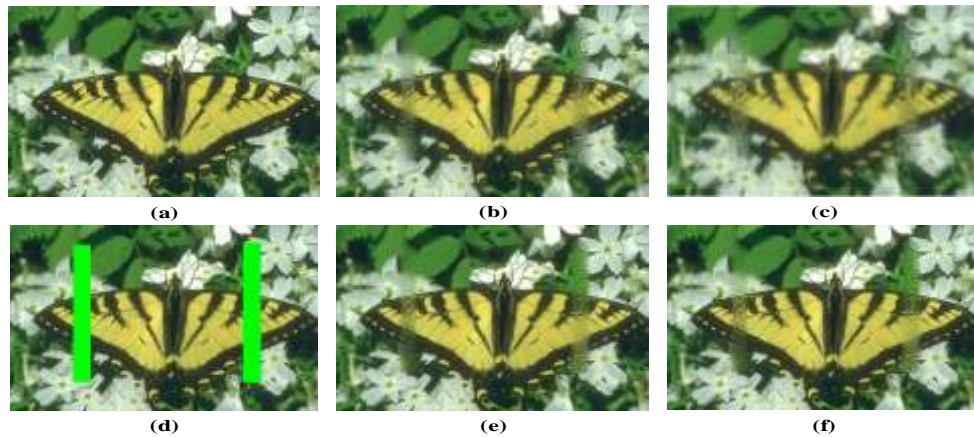


Figure6-12: Hybrid-Based Inpainting technique in the 2nd and 3rd level wavelet domains. (a) Original image. (d) masked image, (b) and (c) inpainted images in the 2nd and 3rd level wavelet domains with using resize for sub-bands, respectively, (e) and (f) inpainted images in the 2nd and 3rd level wavelet domains with using cropping the image in before reconstructing the missing regions, respectively.

The image cropping task helps to solve the effect of the resizing of the sub-bands when trying to convert the image from 3rd to 2nd level, or from 2nd to 1st level. The effect of resizing the image when converting from 3rd to the 2nd level will be more apparent than that from converting from the 2nd to the 1st level. The image cropping process has been done in two ways; either cropping whole the borders of the image even get the size $2^n \times 2^n$, or cropping the size $2^n \times 2^n$ from left to right, then using the hybrid technique to recover the missing region and after that restoring its original size then do cropping again but this time from right to left, and the same thing from up to down, or down to up. This means the missing region in each cropped piece from the image will be recovered because the hybrid technique has been applied to each cropped piece of the image. The second cropping process has been followed to recover all the missing regions in the image.

The steps of this technique in several instances are illustrated in Figure6-13 which shows the same image as recovered by the PDE algorithm described in Section 4.6. The hybrid technique is used to recover the missing regions in the 2nd and 3rd level wavelet domains. The MES method has been applied to recover the missing regions in the non-texture images (i.e. low-frequency sub-band domain). The results are better than those obtained using PDE inpainting models as shown in Figure 4-16 because the texture has been recovered by the TEBI method while the missing regions in high sub bands are

estimated zero value in Figure4-13. This is only a typical example of natural images, demonstrating that using one inpainting algorithm for both structure and texture components is less effective than our wavelet-based hybrid scheme that treats the high-frequency sub-band image differently from the structure image modelled by the low-frequency sub-band.



Figure6-13: Inpainting based-hybrid technique in 2nd and 3rd level wavelet domains. (a) Masked image, (b) and (c) inpainted images using hybrid technique in the 2nd and 3rd level wavelet domains, respectively.

To deeply study the efficacies of hybrid inpainting techniques in the spatial and frequency domains, the set of natural images is used, as described in 3.6.1. Statistical and TDA quality measures have been used to evaluate and compare the results obtained by using these techniques in each domain. The experimental results of will be presented next.

6.4 Performance of the hybrid scheme in terms of Image Quality

This section studies the quality of the inpainting of images which have been recovered using the various proposed hybrid techniques. In general, hybrid techniques are expected to produce better quality images than the single methods. Therefore, the effectiveness of the hybrid inpainting techniques are compared in both the spatial and frequency domains, by measuring the quality of their output images using a variety of quality measures. Statistical measurements and the TDA approach are used to check and estimate the quality of the image inpainting. The results of the proposed hybrid technique are also compared to the results of the Bertalmio technique, in both the spatial and frequency domains. The next subsection will show the evolution of image quality according to statistical measurements on natural images databases.

6.4.1 Statistical image quality measures

The experiments on the natural images have been conducted, and the results in both the spatial and frequency domains are reported. The MSE, PSNR, and SSIM have been used to quantify the qualities of inpainted images in both the spatial and frequency domains. The results of two kinds of hybrid techniques have been checked and

compared with the results of the Bertalmio and TEBI techniques described in (Bertalmio et al. 2003) and (Jassim et al. 2018), respectively. This subsection clarifies and presents these groups of experiments and their results in both the frequency and spatial domains.

The experiments have been conducted to measure and compare image quality in the inpainted images with respect to the original images in the spatial and frequency domains, using MSE, PSNR, SSIM and entropy quality measures. The test images were inpainted using three kinds of hybrid techniques and TEBI method. The original images of the Berkeley database were used as the reference by which to measure the quality of inpainted images; this database has been introduced in chapter Chapter 4. In this section, five experiments have been applied to 80 images of this data set. The aim of these experiments is to study the effect of combining two methods on the reconstruction of the missing regions of different sizes and with high texture and structure around them in the natural images and to study the performance of the proposed techniques in reconstructing these missing regions. The steps as presented in chapter Chapter 4 are followed to create the inpainting mask. Five cases of inpainting masks have been used to study the efficacy of the hybrid technique and to compare it with the Bertalmio and TEBI techniques, respectively. The mask images have been chosen based on the size of the missing regions and quantity of texture in the surrounding areas of the missing regions; the first three masks (Case1, Case2, Case3) represent the different sizes of missing regions at different positions in the images. The other mask images represent two missing blocks at different positions in the images (Case4, Case5). These images have been selected based on the complex texture and structure which that help to check the efficacy of hybrid inpainting methods in recovering separately texture and structure in small missing regions.

Figure 6-14 shows five cases of inpainting mask (i.e. inpainting domain) which represents five damaged regions in images which have been applied on 80 images from the Berkeley database in spatial and frequency domain to study the efficiency of these hybrid techniques.

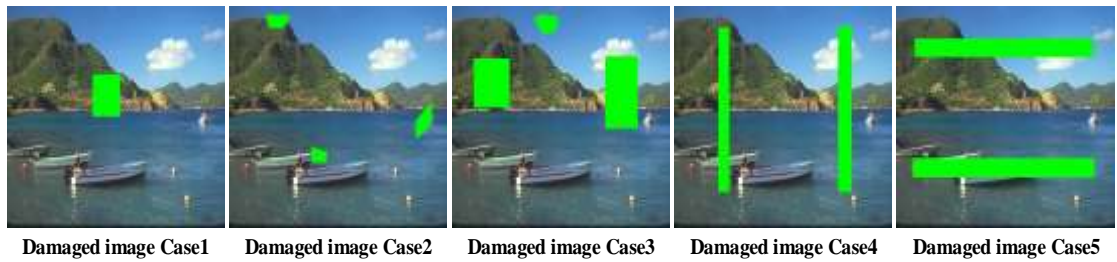


Figure 6-14: The same natural image with five different inpainting domains.

The proposed hybrid techniques are used to reconstruct missing regions in natural images; the MES method is applied to reconstruct missing areas in the structure image as part of the method referred to hybrid 1, while the hybrid scheme that uses mCH method for recovering the missing structure regions is called hybrid 2. The objective of the two inpainting domains (i.e. Case1, and Case2) is to evaluate the performance of the hybrid techniques by reconstructing the texture in small missing regions. The objective of the other inpainting domains (i.e. Case3, Case4 and Case5) is to check the ability of the hybrid technique to recover the large missing regions with texture in the surrounding areas of them. The performance of the hybrid scheme is assessed both qualitatively and quantitatively. The qualitative assessment subjectively reviews the inpainted images visual quality, but as before the quantitative evaluation is based on statistical and TDA measures. Figure 6-15 and 6-16 show the results of recovering the damaged regions for some typical natural images in the spatial domain. The achieved image quality, presented here is typical of most tested images.

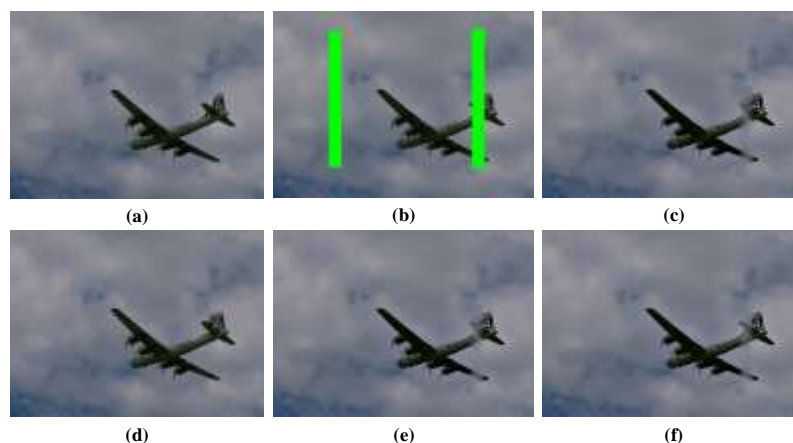


Figure6-15: Recovering missing regions in the spatial domain. (a) Original image, (b) masked image, (c, d, e, f) inpainted images using Bertalmio, TEBI, Proposed Hybrid 1 and Proposed Hybrid 2 methods, respectively.

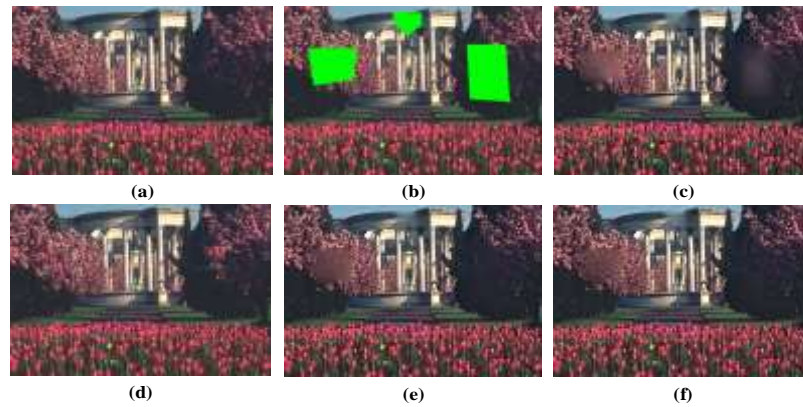


Figure6-16: Recovering missing regions in the spatial domain. (a) Original image, (b) masked image, (c, d, e, f) inpainted images using Bertalmio, TEBI, proposed Hybrid 1 and proposed Hybrid 2 methods, respectively.

Figure6-17 and 6-18 illustrate the results of reconstructing the damaged regions in natural images in the frequency domain.

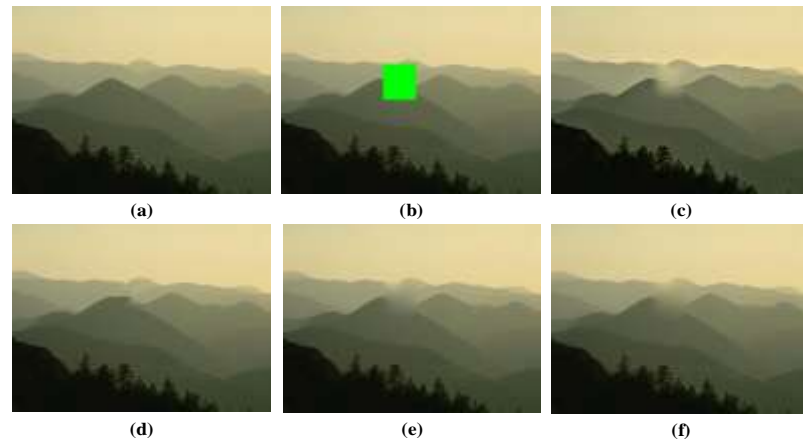


Figure6-17: Recovering missing regions in the frequency domain. (a) Original image, (b) masked image, (c, d, e, f) inpainted images using Bertalmio, TEBI, Proposed Hybrid 1 and Proposed Hybrid 2 methods, respectively.

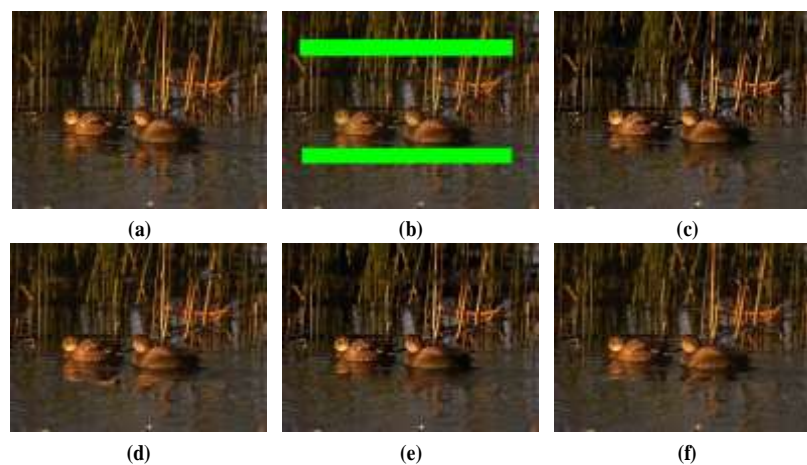


Figure6-18: Recovering missing regions in the frequency domain. (a) Original image, (b) masked image, (c, d, e, f) inpainted images using Bertalmio, TEBI, Proposed Hybrid 1 and Proposed Hybrid 2 methods, respectively.

Chapter 6: Novel Hybrid Image Inpainting Technique

To get a comprehensive quantitative inpainted image quality, the qualities of inpainted images by various schemes are checked. The SSIM, PSNR and MSE have been calculated only between the inpainted regions and the corresponding regions in the original images in both domains (cf. Section 2.6.1). Table 6-1 and 6-2 summarize the comparison of the qualities of inpainting hybrid techniques in the spatial and frequency domain respectively; the times taken to get the results using these techniques are also shown.

C#	Equations	MSE	PSNR	SSIM	Entropy	T(s)
Case1	Bertalmio method	1499.223	18.66756	0.986235	0.395273	506
	TEBI method	793.3923	21.15446	0.986612	0.394516	90
	Proposed Hybrid 1	1244.128	18.70744	0.986409	0.388296	130
	Proposed Hybrid 2	1113.426	19.92023	0.986666	0.380634	150
Case2	Bertalmio method	311.1367	24.81957	0.993912	0.346964	450
	TEBI method	193.6683	27.19607	0.995629	0.349171	78
	Proposed Hybrid 1	290.4463	25.24197	0.993989	0.336341	120
	Proposed Hybrid 2	248.5659	26.32689	0.995164	0.320051	134
Case3	Bertalmio method	974.6182	20.18458	0.954591	1.271754	680
	TEBI method	652.3106	22.02176	0.955993	1.266625	110
	Proposed Hybrid 1	829.3944	19.73906	0.954471	1.240264	145
	Proposed Hybrid 2	753.6958	20.81098	0.955591	1.238316	167
Case4	Bertalmio method	678.9732	21.01168	0.965138	1.139665	986
	TEBI method	401.5857	24.10073	0.965989	1.138165	187
	Proposed Hybrid 1	492.4136	22.71132	0.968253	1.122888	265
	Proposed Hybrid 2	476.2108	22.85803	0.968555	1.120781	289
Case5	Bertalmio method	856.9898	19.57195	0.928726	1.957309	957
	TEBI method	453.1367	23.33227	0.930119	1.947071	194
	Proposed Hybrid 1	566.7113	21.86056	0.937431	1.915651	259
	Proposed Hybrid 2	529.5586	22.12666	0.937918	1.928869	249

Table 6-1: The average values of MSE, PSNR and SSIM are shown for image inpainting using Bertalmio, TEBI techniques and our proposed hybrid techniques in the spatial domain.

C#	Equations	MSE	PSNR	SSIM	Entropy	T(s)
Case1	Bertalmio method	1066.283	20.56447	0.988515	0.395273	232
	TEBI method	894.4014	20.83924	0.987874	0.379203	65
	Proposed Hybrid 1	961.7229	20.43006	0.986235	0.378938	92
	Proposed Hybrid 2	920.8161	20.60669	0.988744	0.385993	114
Case2	Bertalmio method	343.5751	24.78881	0.994658	0.350051	253
	TEBI method	307.3867	24.85707	0.993911	0.345554	51
	Proposed Hybrid 1	316.5131	24.94827	0.994838	0.290051	89
	Proposed Hybrid 2	312.1997	25.25388	0.994994	0.345115	97
Case3	Bertalmio method	1209.187	20.20774	0.963136	1.271754	356
	TEBI method	831.9352	20.71266	0.962888	1.249958	93
	Proposed Hybrid 1	1122.919	20.37882	0.961024	1.221049	111
	Proposed Hybrid 2	924.6182	20.43458	0.954591	1.220746	129
Case4	Bertalmio method	657.7232	21.08668	0.965188	1.139665	487
	TEBI method	493.9757	22.76874	0.975935	1.119615	110
	Proposed Hybrid 1	568.8276	22.20677	0.975448	1.113111	148
	Proposed Hybrid 2	526.6572	22.55822	0.976358	1.113351	152
Case5	Bertalmio method	838.2398	19.67195	0.928726	1.957309	466
	TEBI method	566.0581	21.85964	0.949031	1.920873	123
	Proposed Hybrid 1	698.0841	21.17582	0.947483	1.908716	156
	Proposed Hybrid 2	656.9365	21.46956	0.949809	1.906103	161

Table 6-2: The average values of MSE, PSNR and SSIM are shown for image inpainting using Bertalmio, TEBI techniques and our proposed hybrid techniques in the frequency domain.

6.4.1.1 Results analysis

In this section, the performance of hybrid techniques is analysed based on statistical results for inpainted regions in the natural images. The results of these techniques have been evaluated qualitatively and quantitatively. The qualitative evaluation shows a good reconstruction of the texture in Figure6-15 and 6-16. When the PDE-inpainting methods is used to recover the missing regions in the structure component, a problem with edges of the missing regions is detected where the colours will be overlapping on the edges of objects, and this will produce a blur on the edges of objects in the image. The inpainted images created by using the proposed hybrid techniques in Figure6-17 are visually closer to the original images than the inpainted images created by the TEBI technique. On the other hand, the inpainted images obtained by using the proposed technique could not outperform those inpainted by TEBI. Also, we found inpainted images created in the wavelet domain in, shown in Figure6-17 and 6-18 to be visually identical to those created in the spatial domain.

Lastly, the hybrid technique performs well when there are regions similar to the missing region because of the TBEI process, for more information about TBEI method, we refer the reader to chapter Chapter 5. In addition, the hybrid technique performs well when the missing region is small and has a complex texture around it along with structure.

The performance of the hybrid technique in recovering large missing regions are illustrated in Figure6-10. Experimental testing shows that visually acceptable images may have different image qualities by numerical measures. The efficacy of these techniques in recovering small missing regions has been studied by using the first two masks on the set of natural images. Their abilities to recover large missing regions with high texture and structure have also studied by applying Case3, Case4, and Case5 on the set of images; this is the challenge for these techniques because of the performance of PDE-inpainting methods in recovering the missing structure regions.

In summary, the proposed hybrid techniques and the Bertalmio and TEBI techniques have successfully recovered the small missing regions in the natural images, while these techniques have reconstructed the large missing regions with some limitations about the size of the missing region and the quantity of the texture in the surrounding of missing regions. Also, when missing regions contain objects which don't have similarity in the rest of the image, this will have an effect on the reconstructing process. During the testing, it was found that while some images could look visually pleasing and similar, they have different PSNR values in both domains. The hybrid 2 technique outperforms the hybrid 1 technique. However, both proposed hybrid techniques have succeeded in removing texts, scratches and large spurious objects in images in both domains.

Moreover, in both domains the values of MSE, and PSNR obtained using the proposed hybrid techniques are better than those obtained using Bertalmio technique in four cases. While the TEBI technique performs better than hybrid 1 in case3 in the spatial domain and case1 in the frequency domain. In addition, the results obtained using the TEBI technique are better than those of proposed hybrid techniques.

On the other hand, the values of SSIM obtained using proposed techniques are better than those obtained using other techniques in 3 cases in the spatial domain and 4 cases in the frequency domain, while the TEBI technique performs better than other techniques in case2 and case3 in the spatial domain and case3 in the frequency domain. In most inpainting cases, the proposed hybrid technique outperformed other techniques in recovering the geometry of the image. In addition, the values of entropy obtained using proposed techniques are better than those obtained using other techniques in all cases in both domains. That means the hybrid techniques are capable of effective region filling and give relatively high PSNR values with low MSE values, and SSIM values are

close to 1 with the entropy value is less in the most of all inpainting cases, as shown in Table 6-1 and 6-2.

On the other hand, the proposed hybrid techniques require less time to reconstruct the missing regions in natural images than the Bertalmio technique because of their TEBI technique that use blocks to recover the missing regions in texture images. Whereas, the TEBI technique takes less time to reconstruct the missing regions in natural images than the proposed hybrid techniques. Also, the MSE, PSNR, SSIM and entropy measures resulting from these algorithms in the spatial domain are a little better than those obtained by using frequency-domain algorithms, while the computation time needed to recover the missing regions is less in the frequency domain than in the spatial domain, because the size of the damaged region in the frequency domain is smaller than its size in the spatial domain, and also it does not use any decomposition method to analyse the image, but it instead uses the wavelet transform to analyse the image into high and low-frequencies components. However, the proposed techniques take more time due to the amount of calculation in the spatial and frequency domain.

Other quality measurement which is TDA approach will be used to compare the proposed hybrid technique with Bertalmio and TEBI techniques in the next section.

6.4.2 Topological Data Analysis for image quality

As explained in Section 2.6.2, the TDA approach has been proposed to evaluate the quality of image inpainting. Therefore, the TDA approach has been applied to study the results of hybrid techniques, and it is also applied on natural image datasets. To get better results of image inpainting quality, this approach has been applied to study only the inpainted regions in the images, this means, the number of CCs has only been calculated in the inpainted regions and the corresponding original regions, where the number of CCs in the other parts of the inpainted image and the original image are the same. The same steps are followed in the construct of the Vietoris-Rips complex which was introduced in Section 2.6.2.2.

We have studied 7 ULBP geometries at different thresholds $T=0$, $T=5$, $T=10$, $T=15$, for the inpainted images of the above experiments. We found the geometries G2, G4, and G6 at threshold $T=10$ giving a good description to proposed hybrid techniques in all five cases of damaged images because the c give the best descriptors of the texture in the images.

Chapter 6: Novel Hybrid Image Inpainting Technique

Figure6-19 shows the average number of CCs of inpainted regions as obtained from the proposed hybrid techniques and Bertalmio and TEBI techniques for five damaged regions from the natural image dataset in the both spatial and frequency domains. The Geometry G6 at threshold T=10 is shown below.

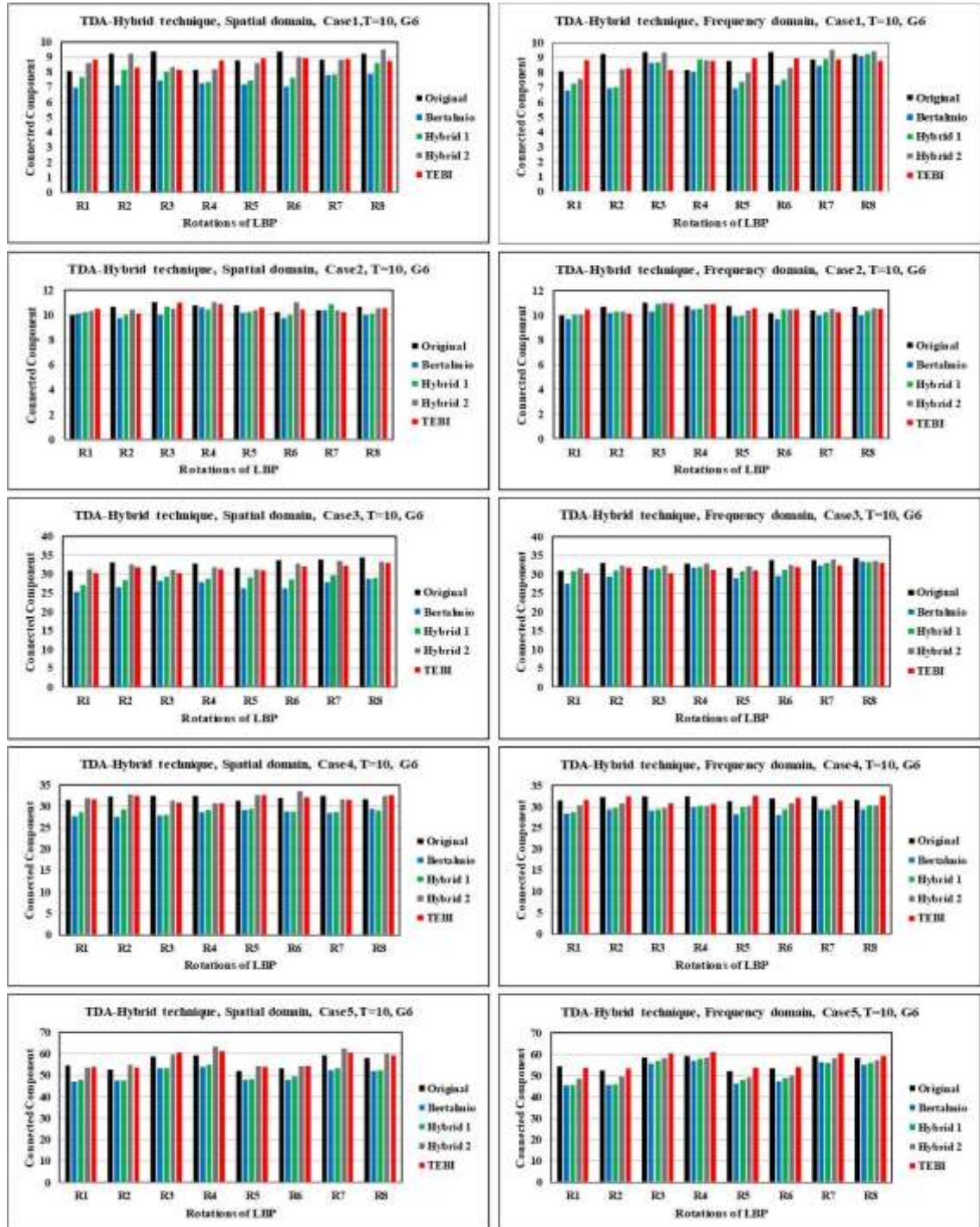


Figure6-19: Evaluation of performance of hybrid techniques using TDA approach at 8 iterations in G6 at threshold T=10 for 5 inpainting cases of natural images. Left column: Average of the number of CCs inpainted regions in the spatial domain. Right column: Average of the number of CCs inpainted regions in the Frequency domain.

Chapter 6: Novel Hybrid Image Inpainting Technique

The numbers of CCs in the other geometries at threshold $T=10$ are not robustly determined, we sometimes found the numbers of CCs in inpainted regions created by using Bertalmio technique and hybrid 1 to be close to those seen original regions of natural images. So that means these geometries at threshold $T=10$ do not describe well of the image quality assessment of these inpainting algorithms, as seen in the below Figure6-20 which illustrate the number of CCs in the geometry G5 at threshold $T=10$.

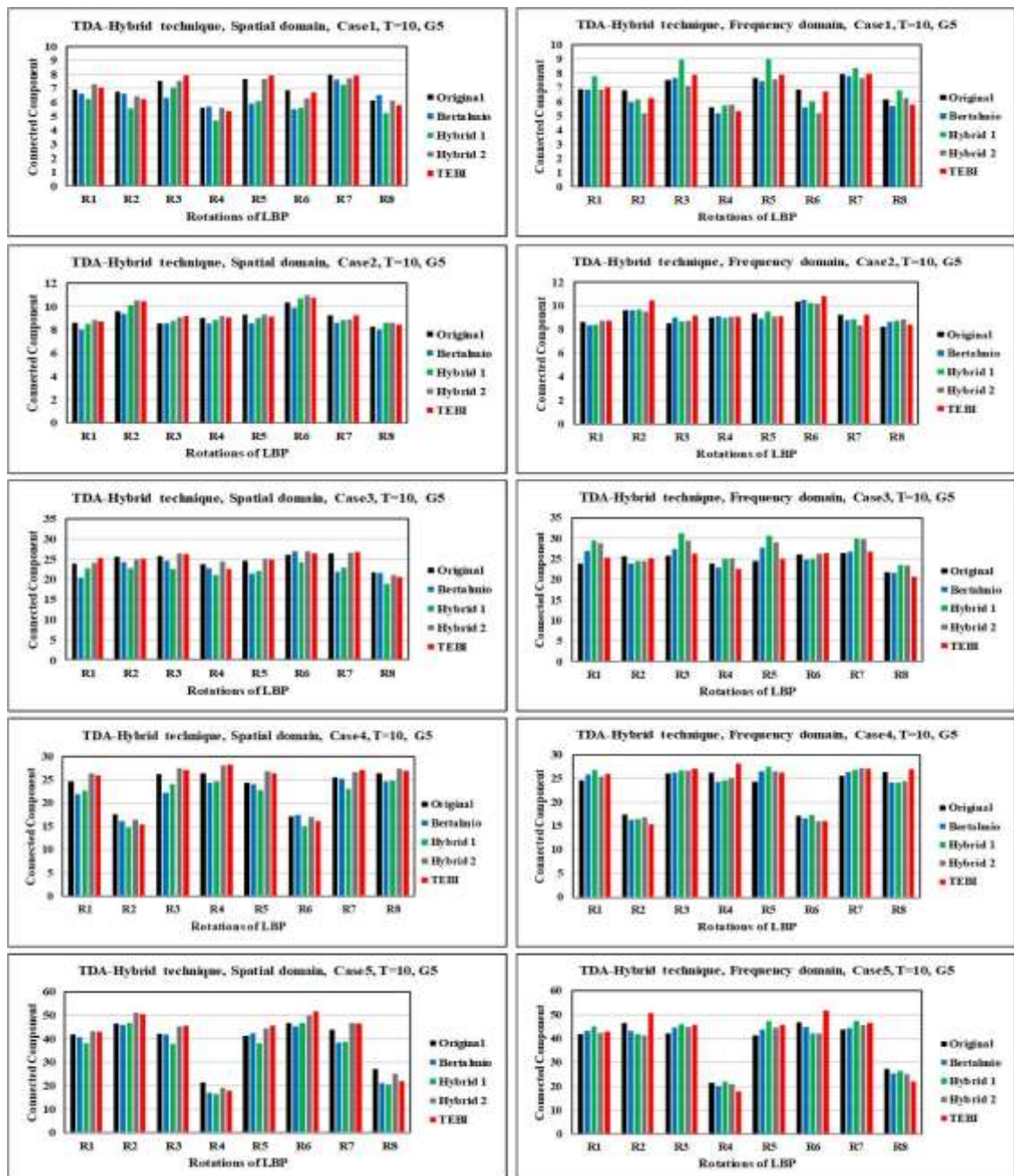


Figure6-20: Evaluation of performance of hybrid techniques using TDA approach at 8 iterations in G5 at threshold $T=10$ for 5 inpainting cases of natural images Left column: Average of the number of CCs inpainted regions in the spatial domain. Right column: Average of the number of CCs inpainted regions in the Frequency domain.

6.4.2.1 Results analysis

The TDA approach has been used to assess the results of the five inpainting domains in both spatial and frequency domains obtained by using the proposed hybrid techniques and TEBI. The TDA approach has been applied to the inpainted regions and corresponding original regions in the natural in seven geometries at different thresholds. In both spatial and frequency domains, the number of CCs in the inpainted areas that recovered by the proposed hybrid techniques close to the number of CCs in the original areas than Bertalmio method in the geometries G2, G4, and G6 at threshold $T=10$ in the natural images. The geometries G2, G4 and G6 describe the corners, edges and the end lines in the natural images (Ojala et al. 2002). This means the proposed methods have been succeeded to reconstruct each of the corners, edges and the line ends in the missing regions because of the patterns that described in the geometries G2, G4, and G6 at threshold $T=10$.

However, the numbers of CCs of inpainted regions which obtained by using TEBI technique is closer to those occurring in the corresponding original regions than those obtained using the hybrid 1, hybrid 2 techniques and the Bertalmio technique, in the both of spatial and frequency domains. Also, the numbers of CCs of the inpainted areas obtained by using hybrid techniques in the spatial domain are little closer to the numbers of CCs of original areas in comparison with frequency domain, as described in Figure6-19.

For other geometries, the number of CCs is wobbling in the inpainted regions, as seen in Figure6-20, which shows the numbers of CCs in geometry G5. In all these types of hybrid techniques, the numbers of CCs of the inpainted areas in the spatial domain are closer to those observed in the original areas than in the frequency domain. Therefore, the best descriptor for image quality based on the number of CCs of the results obtained by using these methods, where the best image inpainted quality is TEBI method then hybrid 2 then hybrid 1 and the lastly Bertalmio method for all rotations in the geometries G2, G4 and G6. The results of geometries G1, G2, G3, G4, and G7 at threshold $T=10$ which are given in Appendix C.

Finally, the TDA approach has been successful for to the study and checking of the qualities of image inpainting because this it involves a very sensitive process which enables the study of the inpainted region at seven geometries and each geometry has eight rotations which means that it will cover all the inpainted regions.

6.5 Summary and Conclusion

This chapter introduced the improvement of the Bertalmio technique by using three different methods which permit the reconstruction of textures and structures in the missing regions simultaneously. Furthermore, two kinds of hybrid techniques are proposed. Each one of them uses a combination of image decomposition with PDE-based inpainting and TEBI methods. Three kinds of decomposition methods have been studied to decompose the image into texture and structure components; the total variations in L^1 , L^2 and 4th order PDEs. The texture component obtained by using total variation in L^1 is sharper than the one obtained by using the other two methods. On the other hand, the TEBI method has been used to recover the missing region in the texture component. The results of this method show that it outperforms the texture-synthesis method described in (Efros & Leung 1999) in addition to consuming less computational time.

The last step is the high order PDE-based inpainting which has been successfully used to recover the missing regions in the structure component. All in all, the proposed hybrid technique has been applied to recover texture and structure information in the missing regions in both the spatial and frequency domains. Furthermore, the proposed hybrid technique has been used to recover the information in the frequency domain by using the wavelet transform as a decomposition method to analyse the image into high and low-frequency sub-bands (i.e. structure and texture components). The TEBI and PDE methods have been applied to recover the missing regions in the low and high-frequency sub-bands in the 2nd and 3rd level.

The hybrid technique is used in two ways: 1) recovering missing regions and 2) removing unwanted objects r , as in Figure 6-7, 6-8 and 6-10. The hybrid image inpainting technique provides better visual quality results compared to other single methods, as shown in Figure 6-7 and 6-9. These techniques have been tested experimentally by applying them to five different inpainting domains (i.e. damaged regions) by using natural image datasets in both spatial and frequency domains. The quality of inpainted images has been evaluated by statistical measurements. The experimental results of the proposed hybrid techniques have been compared with the results obtained using the Bertalmio and TEBI techniques. The results of the proposed hybrid technique outperform the results obtained by using Bertalmio technique. However, the results obtained by using TEBI technique are more efficient than those obtained by using the proposed hybrid technique. The TDA approach has been proposed

to study the quality of image inpainting, and it is more successful in this application than statistical measurements. The overall execution time of the proposed technique is about 3–5 minutes without any improvements in its speed. Most of the computing time is consumed by the execution of the PDE method which includes a high number of iterations used to recover the missing region. As explained before, the hybrid technique is a combination of three main components, each of them includes several methods. Furthermore, finding the best combination among the available methods is still an open task. In the future, many experiments should be conducted in order to accomplish this.

To conclude, the hybrid and TEBI techniques have successfully reconstructed the texture and structure simultaneously in the missing regions in the natural images. Nevertheless, these techniques still have drawbacks in reconstructing large missing regions in the natural images. Therefore, to address this issue, the next chapter introduces a novel additional step to our inpainting technique to be based on the interesting concept of seam carving.

Chapter 7 INPAINTING LARGE MISSING REGIONS BASED ON SEAM CARVING

In the last 5 chapters of this thesis, are reviewed, modified, developed and conducted extensive comparative testing of the performances of a variety of partial/total inpainting approaches to restore missing image data. The common strategy in all schemes is that of information propagation from the missing region's neighbouring areas, pixel by pixel, to fill in the missing texture and structure information. The main existing and developed schemes are modelled on numerical solutions of different order partial differential equations based inpainting (PDE-BI), a variety of exemplar-based inpainting (EBI), and also hybrids of these models. Overall, the various tests show very promising results and lead to achieving the desired effects in most cases especially when dealing with relatively small missing regions. This chapter investigates the challenge of inpainting relatively large missing image areas and develops an innovative approach that exploits the benefits of the recently developed Seam Carving concept to reduce the investigated challenge to that of inpainting “relatively small” missing areas problem. We shall demonstrate empirically the success of this innovative reductionist approach.

The rest of this chapter is organised as follows: The challenge and review existing approaches are introduced to the inpainting of large missing regions in section 7.1. The concept of the seam-carving operator is presented and explained in section 7.2. The reductionist seam-carving technique is introduced in section 7.3. The effect of different levels of seam carving on the inpainting challenge will be analysed in section 7.4, while in section 7.5 the inpainted image qualities are evaluated for various levels of seam carving. Finally, the conclusions and future directions are presented in section 7.6.

7.1 Inpainting relatively large missing regions - Introduction

The literature review that was conducted on image inpainting and the research work carried out in this thesis have shown that there are various viable single-approach based and hybrid models to solve this problem and that each has its own complexity, advantages and limitations as well as requirements. The common strategy in all schemes is the iterative propagation of information into the missing region either using numerical

solution of PDE's with certain boundary conditions or using exemplar blocks in the rest of the image (or even from other images) that have "similarities" with border blocks. Naturally, both approaches are subject to error propagation which can have adverse effects on the quality of inpainted images which become more apparent with the large missing regions. This is more obvious in the case of PDE-BI, but provides partial explanation of how this limitation also affects the EBI based inpainting schemes that was designed for the task of recovering large missing regions, (e.g. see Criminisi et al (Criminisi et al. 2004)). It is worth noting that the larger the ratio of missing region size to the overall image size the less chances are there to find good exemplar patches. The various attempts that we made to improve the performance of developed schemes have led to noticeable improvements but with very limited success in inpainting large missing regions. These schemes include the TEBI, the higher order PDEs and hybrid schemes, which were successful in reducing the effect of error propagation and in recovering edges and corners but could not recover large missing regions especially when the surrounding areas have a rich texture.

The image inpainting problem remains an active area of research and remains challenging in recovering large missing regions. There are several image inpainting approaches for recovering large missing regions which have been improved in recent years; they are roughly classified into two main types: non-Exemplar Based Inpainting (nEBI) and EBI methods.

The first type, nEBI methods uses Partial Differential Equations (PDE) to propagate the information from the surrounding (or neighbouring areas of the missing region) to the missing region. The PDE based inpainting methods have been used to recover small missing regions such as cracks, dates, texts, advertising signs, or to remove small unwanted areas, as in (Bertalmio et al. 2000), (Chan & Shen 2002), (T. Chan and J. Shen 2001), (Wei Guo & Li-Hong Qiao 2007), (Bertalmio 2006), and (Esedoglu & Shen 2002). These methods have limitations in reconstructing large missing regions with high texture in the surrounding areas (i.e. the size of missing regions more than 25%).

Secondly, the EBI method proposes the idea of using a patch-based-exemplar method, with which textures and structures are simultaneously reconstructed in the missing region. This task depends mainly on the choice of filling order; an optimal choice will ensure that linear structures will be propagated before texture filling so that the connectivity and continuity of object boundaries will be preserved, for which some

improvements have been proposed, as introduced in (Sharma & Mehta 2013), (Cheng et al. 2005), (Desai 2012), (Anupam et al. 2010), (Hesabi & Mahdavi-Amiri 2012), (Sangeeth et al. 2011), (Waykule & Patil 2012), (Zongben Xu & Jian Sun 2010), (Abdollahifard & Kalantari 2016), (Deng et al. 2015), and (Jassim et al. 2018). These methods have limitations with reconstructing large missing regions with high texture surrounding areas.

The size of the missing region affects the performances of inpainting methods, and both the nEBI and EBI methods do not perform a well in recovering large missing regions. Therefore, in this chapter, a novel inpainting technique for recovering large missing regions is introduced.

In the literature of inpainting techniques for large missing regions, there are few publications that report significant success in recovering large missing regions but are targeting narrow types of applications that use range images. Pixels in any segmented region have similar range, and depth discontinuities coincide with intensity edges. Torres et al. in (Torres-Méndez & Dudek 2008) have introduced a technique to recover large missing regions for 3D indoor environments map colour images captured with range sensors. Their approximate MAP-MRF estimation at a pixel involves sampling a histogram of its neighbours, learning the intensity, range statistics via belief propagation (BP) and edge-detection to improve estimation at discontinuities. The edges have been built by using a process similar to that used in the inpainting method described in (Criminisi et al. 2004). The similarity measure which applies a Gaussian kernel to each neighbourhood has been used.

The authors in (Bhavsar & Rajagopalan 2010) proposed a method which uses the image segmentation cue to recover large missing regions in range images. They used the improved mean-shift segmentation (Christoudias et al. 2002) which is more robust than edge detection in delineating regions. The framework of this method involved local cost computation based on plane-fitting and local medians over segments, and effectively used the properties of the mean-shift algorithm to guide the inpainting. The simple strategy involves plane-fitting and local medians over segments to compute local energies for labelling unknown pixels. This method achieved high-quality inpainting with very low errors in spite of significant missing data in observations (of the order of 60% to 90%).

Since many of the schemes investigated/developed in this thesis work well with small missing regions, perhaps with some conditions, a plausible approach would be to try to reduce/transfer the problem to one involving a relatively small missing region. Conventional resizing the image cannot work due to the fact that such a transformation doesn't change the ratio of the size of the missing region to the image size. Despite the fact that image compression reduces the image storage size, it is not clear how compression could help in this effort because the reduction is achieved by efficient data coding and decompressing restores the image size. In this respect, it is worth noting that the standard wavelet transformation of an image has the effect of reducing the inpainting of any missing region into a number of inpainting procedures of significantly smaller sizes. Unfortunately, such a transform is not shift invariant, may result in considerable loss of information and consequently may have a significant adverse impact on the quality of inpainting large missing regions. This can be clearly demonstrated by the following example, where a large region of a natural scene image was removed and recovered by the wavelet-based hybrid1 scheme presented in Section 6.3.

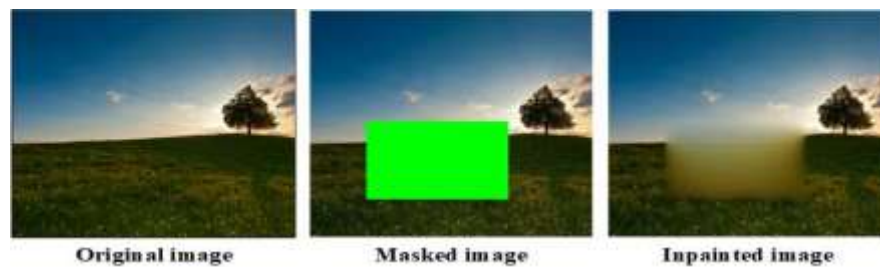


Figure 7-1: Failure of wavelet-based Hybrid inpainting for large missing region.

We note that both conventional image size reduction and wavelet transform has the effect of uniform down-sampling, and interpolation, which leads to loss of significant as well as insignificant information throughout the image. This observation shows that for the intended reductionist strategy to succeed, we need a non-uniform image down-sampling that removes pixels without losing important image content. Fortunately, the known concept of seam-carving, introduced by Avidan and Shamir in (Avidan & Shamir 2007), provide us with an appropriate content-aware approach to image resizing that can be used for both image size reduction and expansion. In this chapter, this concept is exploited to develop a novel inpainting technique designed especially for the reconstruction of relatively large missing regions without artefacts. Next, the use of the seam-carving is described and discussed for image resizing tasks.

7.2 Seam carving – Introduction and Implementation

The seam carving method, (Avidan & Shamir 2007), is used for resizing the image without affecting its contents. The basic idea of seam carving is to remove redundant connected image paths, called seams, without having a noticeable visual effect. A seam is an optimal 8-connected path of pixels in an image from left to right and/or from top to bottom of the image, where an image energy function defines the optimality of the seam. Roughly speaking, the seam carving procedure will preserve pixels that have high energies in comparison with their surrounding pixels. Mathematically speaking, the energy of a pixel with respect to the x and y axes may be computed through the magnitudes of the derivatives with respect to x and y determined by the pixel's neighbourhood, which is known as gradient operator. Different energy functions have been proposed in (Rubinstein et al. 2008), (Ye & Shi 2017), (Zhu et al. 2016), (Itti et al. 1998), and (Harris & Stephens 1988).

Throughout this thesis we adopt the following mathematical equation for the energy function; let f be an $n \times m$ image:

$$e(f) = \left| \frac{\partial f}{\partial x} \right| + \left| \frac{\partial f}{\partial y} \right| \quad (7.1)$$

This energy function is used to determine the locations of candidate seams in the image to be removed and can be implemented in different ways. The Prewitt and Sobel filters are commonly used to compute the discrete differentiation operators, in the x and y directions by convolution weighted 3×3 kernels with the input image. The Prewitt filters are defined

$$f_x = \begin{bmatrix} 1 & 0 & -1 \\ 1 & 0 & -1 \\ 1 & 0 & -1 \end{bmatrix}, \quad f_y = \begin{bmatrix} 1 & 1 & 1 \\ 0 & 0 & 0 \\ -1 & -1 & -1 \end{bmatrix}$$

While the Sobel filters are

$$f_x = \begin{bmatrix} 1 & 0 & -1 \\ 2 & 0 & -2 \\ 1 & 0 & -1 \end{bmatrix}, \quad f_y = \begin{bmatrix} 1 & 2 & 1 \\ 0 & 0 & 0 \\ -1 & -2 & -1 \end{bmatrix}$$

Where f_x and f_y represent the first derivative filters for the x and y directions respectively. **Figure7-2** shows the applications of the energy function on a natural image.

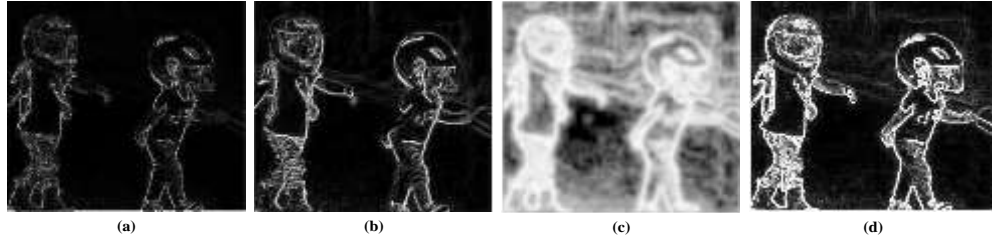


Figure7-2: Different energy functions for the natural image. (a) and (b) Energy image by a gradient operator using Prewitt and Sobel filters, respectively. (c) Energy image by the entropy of the gradient operator. (d) Energy image by the histogram of the gradient.

In the above Figure, the energy function calculated by using the gradient Sobel filter produces images with higher intensity values along edges within the image than that calculated using the gradient Prewitt filter. The output image obtained by using the entropy energy function is smoother and has higher intensity values along edges. The result of using the histogram energy function is higher intensity values along edges. More information about edge-detection filters can be found in (Gonzalez & Woods 2008).

It is worth noting that the type of energy function used to remove seams from a missing region is based on calculating an energy function from f , once by gradient and then by entropy operators, then adding both of them together as clarified in

Figure7-4 b.

The size of the image is retargeted to a smaller size by repeatedly carving out seams in both directions; a vertical seam S^x is defined as follows:

$$S^x = \{S_i^x\}_{i=1}^n = \{(x(i), i)\}_{i=1}^n \quad (7.2)$$

Such that $\forall i, |x(i) - x(i - 1)| \leq 1$, and x is a mapping defined as $x: [1, \dots, n] \rightarrow [1, \dots, m]$. A vertical seam represents an 8-connected path of pixels in the image which goes from top to bottom and contains only one pixel in each row of the image, see

Figure7-4 c.

Similarly, a horizontal seam S^y is defined as follows:

$$S^y = \{S_j^y\}_{j=1}^m = \{(j, y(j))\}_{j=1}^m \quad (7.3)$$

Such that $\forall j, |y(j) - y(j - 1)| \leq 1$, y is a mapping defined as $y: [1, \dots, m] \rightarrow [1, \dots, n]$. A horizontal seam represents an 8-connected path of pixels in the image which goes from left to right and contains only one pixel in each column of the image, see

Figure7-4 d.

The pixels of the path of seam S , for instance, a vertical seam $\{S_i\}$ will be

$$u_S = \{u(S_i)\}_{i=1}^n = \{u(x(i), i)\}_{i=1}^n$$

Observe that, after the removal of row or column from an image, the missing seam will be compensated for by shifting all the pixels of the image left or up. The energy of a seam is defined as follows:

$$E(S) = E(u_S) = \sum_{i=1}^n e(u(S_i)). \tag{7.4}$$

The optimal seam (path) S^* , which minimises the total seam energy of each pixel in the path is defined by the next formula:

$$S^* = \min_S E(S) = \min_S \sum_{i=1}^n e(u(S_i)). \tag{7.5}$$

The general aim of using the seam-carving operator on an image is to resize the whole image for extension or shrinking. Figure7-3 shows the flowchart of the general seam carving approach for reducing/enlarging the size of the image.

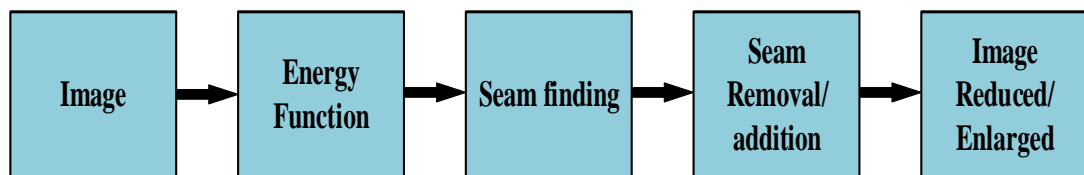


Figure7-3: The flowchart of the seam carving approach for image reduction/enlargement.

The process of applying the seam-carving approach is illustrated in Figure7-5, which shows the application of seam-carving to reduce the size of image vertically and horizontally by removing 20 seams vertically and horizontally from the image.

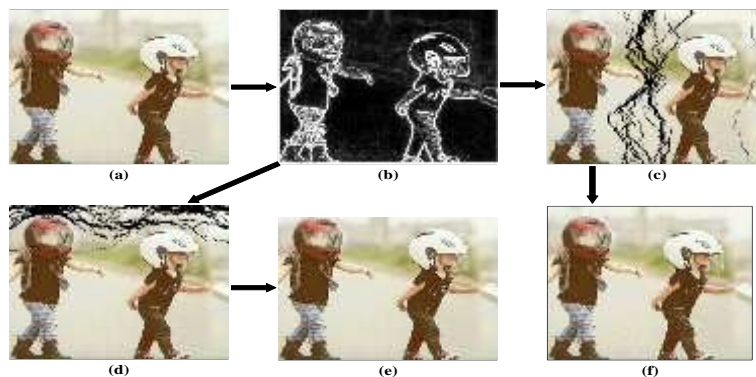


Figure7-4: Seam carving process. (a) Original image, (b) energy image, (c) and (d) determining 20 vertical and 20 horizontal seams, respectively, (e) and (f) removing 20 horizontal and 20 vertical seams in image, respectively.

As mentioned previously, the seam-carving approach targets the seams that have low energy values. Therefore, to applying seam carving to solve an image inpainting problem, the seam-carving approach is used to reduce the size of an occluded region to enhance the inpainting technique when it is applied to that region.

Figure7-5 shows the application of seam-carving to an occluded region in an image.

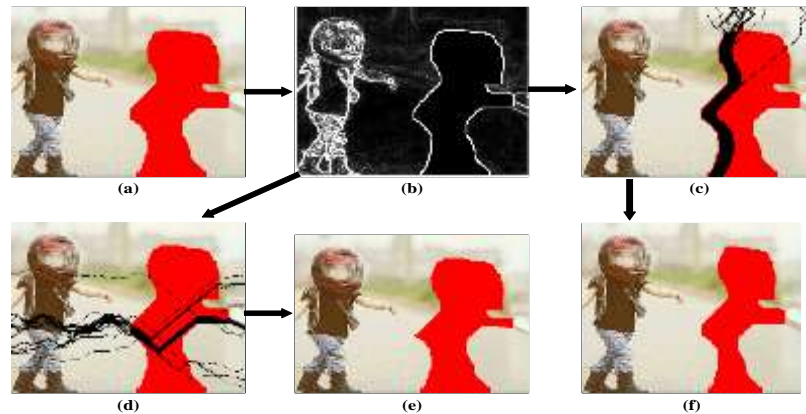


Figure7-5: Seam carving process. (a) Masked image, (b) energy image, (c) and (d) determining 20 vertical and 20 horizontal seams, respectively, (e) and (f) removing 20 horizontal and 20 vertical seams in image, respectively.

As explained before, the seam is chosen based on the energy intensity values of its pixels. The vertical and horizontal seams have been determined in different places on the pixel energy intensity values in

Figure7-4 and 7-5. To reduce/enlarge the region of interest in the image, we set to zero the values in the region which needs to be recovered which means that the region of interest will have low energy values; this will help to determine the seams in the region of interest, as seen in

Figure7-4 and 7-5. Different energy functions have been tested on the images; all these energy functions have helped to determine the seams in the occluded regions.

Many inpainting methods have limitations with large missing regions. Based on our observations from the literature, the largest missing region that can be recovered using the TEBI method is of an area corresponding to 20% of the total area of the original image. Therefore, we are proposing to reduce the size of the missing region using the seam carving method, after which the TEBI method is applied to reconstruct the reduced size missing region. To recover the original size of the image, the old seams will be added back; this will leave missing thin lines that can be recovered using PDE-BI method. The method of our technique will be explained in the next section.

7.3 Seam-carved approach to inpainting

The aim of proposing this technique is to reconstruct a large missing region by using seam carving, TEBI, and PDE methods. The steps of the proposed technique are represented as follows:

1. Read the input image with a marked region to be removed.
2. The seam-carving approach is applied to shrink the missing region.
3. The TEBI method is used to recover the shrunk missing region in the image (Jassim et al. 2018).
4. Add back the old seams to recover the original size of the image. However, the original information of the added seams is missing.
5. The MES method is applied to reconstruct the missing paths (seams).

Whether the shrinking of the missing region occurs vertically or horizontally is based on the nature of the shape of the missing region in an image. The steps of the proposed technique are illustrated in Figure7-6.

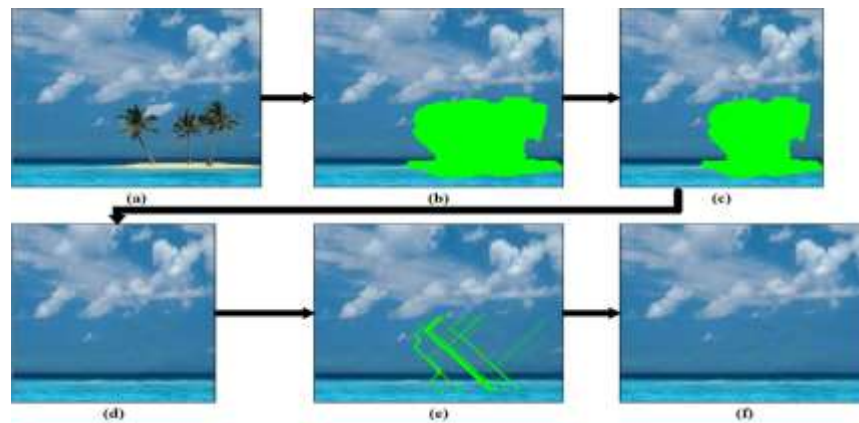


Figure7-6: Inpainting-based seam-carving approach. (a) Original image. (b) Image with occlusion, (c) Shrunk occlusion by removing 30 seams. (d) TEBI Inpainted of (c). (e) Re-inserting seams. (f) PDE-BI Inpainting of seams.

In the next section, the proposed technique is described to be used for large object removal and for recovering large missing regions in natural images.

7.4 Experimental results

In this section, the proposed technique is tested on a variety of natural images, selected from the Berkeley Segmentation Dataset and Benchmarks 500 (BSDS500), see Section 3.6.1, and compared the experimental results of the proposed technique with those of the classical EBI method (Criminisi et al. 2004) and TEBI method (Jassim et al. 2018) (i.e. which has been implemented without the use of seam-carving). The seam-carving

inpainting is used to remove large unwanted objects, and to reconstruct missing regions of various large sizes. These experiments are meant to check the effectiveness of seam-carving inpainting and establish the success of the reductionist strategy based on the direction and the number of removed seams.

Figure7-7 displays some selected sample of images resulting from the implementation of our technique besides the EBI and TEBI methods for large objects removal. This figure provides a means of visual comparison of the performances of these three methods and demonstrates the superiority of the seam-carving inpainting approach.

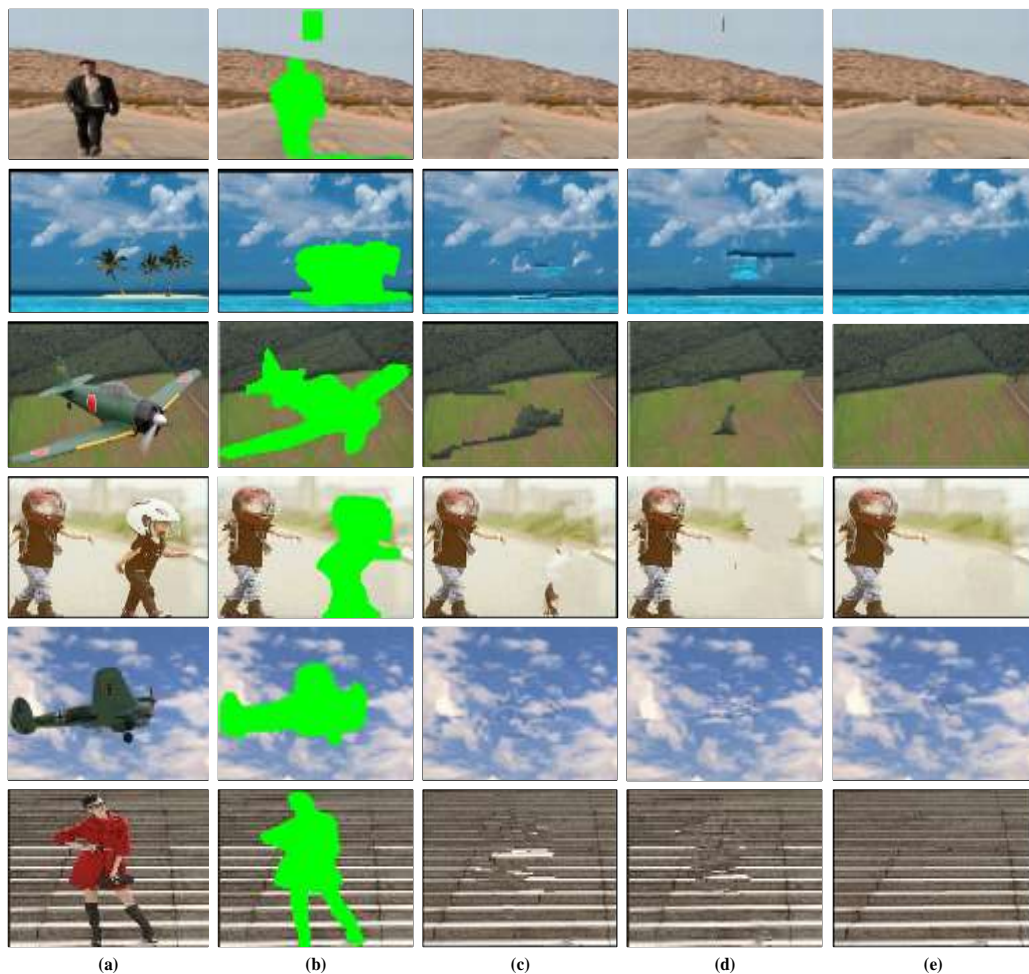


Figure7-7: Large object removal examples. (a) Original images, (b) masked images, (c), (d), and (e) inpainted images using EBI, TEBI, and proposed inpainting methods, respectively.

The above results show that the proposed technique outperforms EBI and TEBI methods. However, the number of seams to be removed is limited as it is directly related to the performance of the MESm. In the case of using a large number of seams, MESm produces artefacts when the seams are condensed next to each other. We found by experiments that the number of seams to be removed is better limited to between 20% and 30% of the size of the missing region.

Chapter 7: Inpainting Large Missing Regions Based on Seam Carving Method

The direction of seams can be determined based on the shape of a damaged region and the geometry of the surrounding areas of a missing region. That will help, after recovering the missing region, reinsert the seams without effect on the inpainted regions, as seen in Table 7-1, which presents the ratios of missing region sizes to the whole image size before and after using seam carving approach for each image illustrated in Figure7-7.

Figure7-7: row number - Seam Direction	Size % of the occluded region before reduction	Size % of the occluded region after reduction
Row 1- Horizontal	21.9097%	17.5681%
Row 2-Vertical	22.7639%	18.2821%
Row 3-Vertical &Horizontal	31.1759%	21.6329%
Row 4-Vertical	25.9162%	19.6148%
Row 5- Horizontal	23.8266%	19.3262%
Row 6-Vertical	30.2734%	20.2324%

Table 7-1: Ratios of missing regions size to whole images in figure 7-7 before and after seam-carving.

Table 7-1 is shown the direction and the quantity of removed seams that applied in the first step from the proposed technique process. The proposed seam-carving technique is also used to recover large missing regions in the natural image. Figure7-8 shows some results giving comparisons of the uses of the EBI and TEBI methods for recovering large missing regions. The visual comparison of their performances again demonstrates the superiority of the seam-carving schemes and the success of our reductionist strategy.

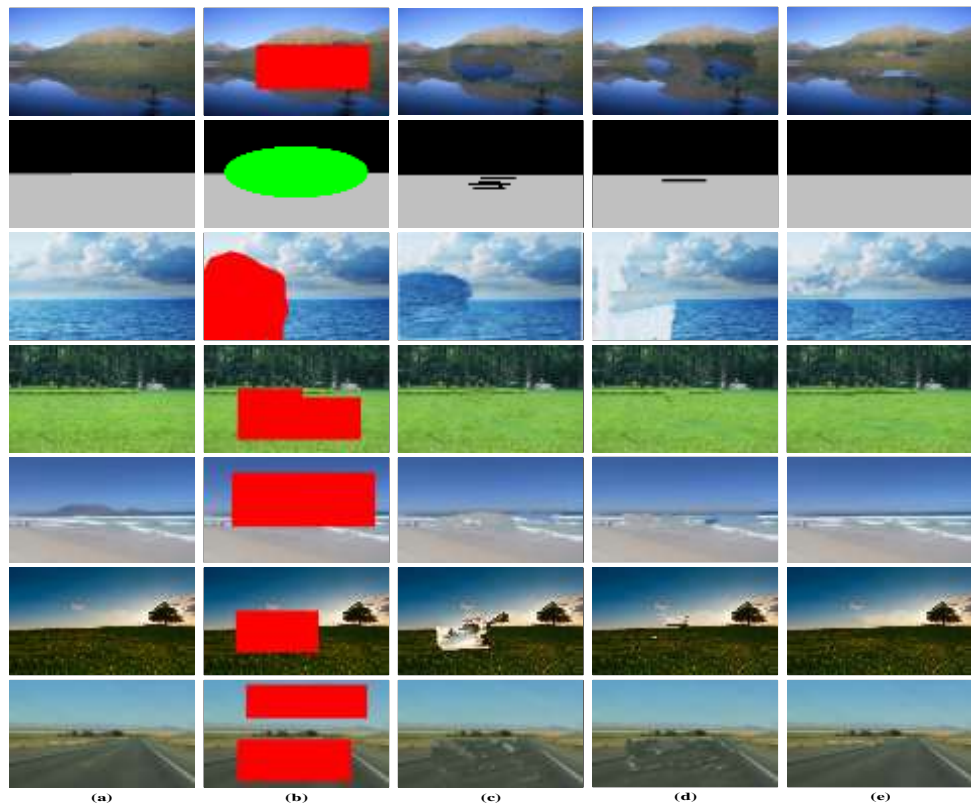


Figure7-8: Recovering large missing regions examples. (a) Original images, (b) masked images, (c), (d), and (e) inpainted images using EBI, TEBI, and proposed inpainting methods, respectively.

Similarly, the direction of seams can be determined based the shape of the damaged region and the geometry of its surrounding areas, as seen in the table below, which presents the ratios of missing regions sizes to the whole image size before and after using the seam carving approach for each natural image described in Figure7-8.

Figure 7-8: row number - Seam Direction	Size % of the occluded region before reduction	Size % of the occluded region after reduction
Row 1-Vertical	23.9573%	19.2061%
Row 2-Vertical	21.8241%	17.5991%
Row 3-Vertical	28.7831%	21.3971%
Row 4-Vertical	23.2162%	18.6818%
Row 5-Vertical	30.4921%	21.9861%
Row 6-Vertical	20.8918%	17.1562%
Row 7- Horizontal	29.8565%	23.6753%

Table 7-2: The size of the missing regions to the whole images in figure 7-8 before and after reduction using the seam-carving method.

From the various experiments, we observed that there is a clear logical link between the geometry directions of the surrounding areas of the missing region and the direction of the removed seams. More precisely, the direction of seams can be determined based on

the structure directions of the surrounding areas of missing regions. This helps the patch selection to be propagated better. As an example, the size of the missing region in row 2, 4 and 6 in Figure7-7 is reduced vertically by removing the vertical seams. We can also see in row 1, 5 and 7 in Figure7-7 and 7-8, respectively, that the size of the missing region has been reduced horizontally. Also, we reduced the size of the missing regions in both directions as seen in row 3 Figure7-7. On the other hand, We found by experiments that the number of seams to be removed is better to be limited between 20% and 30% of the size of the missing region, that allows to PDE-BI methods to get better results, where the number of removed seams affects on the performance of PDE-BI methods.

The subjective examination of the output from various experiments demonstrate beyond any doubts that the proposed technique outperforms the original EBI and TEBI methods, especially when the size of the missing region is relatively large, and the surrounding area of the missing region has high texture and structure. This can easily be seen in Figure7-7 and 7-8. More precisely, as shown in the third, fifth, and sixth rows images in Figure7-7 and the first, third, and sixth rows images in Figure7-8, the proposed method successfully reconstructed the missing regions in column (d), but there is a need to continue the edges from the outside of the missing region to the inside. Consequently, the proposed technique can successfully reconstruct sharp edges sequentially even when the missing region is relatively large, due to the use of the seam carving approach which enhances good patch-size propagation selection using topological invariants. As a result, the priority function determines the best location in which to propagate the information steadily. The missing region can then be reconstructed fully based on the information in the surrounding area.

The next section will be focusing on quantitative evaluation of inpainting schemes, by assessing image quality for a sufficient number of different natural images in terms of different objective measurements.

7.5 Image Quality Assessment

It is widely accepted that image quality assessment is not an easy task and has not been fully solved yet (Chandler 2013). Notwithsatnding this difficulty, the qualities of image inpaintings produced by using the seam carving scheme have been assessed qualitatively and quantitatively. We rely on subjective visual analysis to assess inpainted images qualitatively. However, for quantitative evaluation, the common

statistical quality measures and the TDA approach have been used to evaluate the inpainted images and the corresponding inpainting techniques. The results of the proposed technique are compared to the results of the EBI and TEBI methods. To deeply study the efficacies of the proposed inpainting technique, we have applied it to the set of images (natural databases) described in section 3.6.1. The next two sections show the assessment of image inpainting by using statistical measurements and the TDA approach respectively.

7.5.1 Statistical measurements for image quality

A set of experiments has been conducted, and the results on the natural images are reported. The inpainted images have been evaluated in two cases when a reference image (i.e. original image) is available, and when it is not. The efficacy of the proposed inpainting technique is studied by measuring the quality of its output images using a variety of statistical quality measures. The performance testing experiments are conducted for two different inpainting tasks: removing large objects and restoring large missing regions.

The original images of the Berkeley database were used as the references in order to measure the quality of inpainted images. For each of the two inpainting tasks, five experiments will be conducted on 50 images of this data set. These selected images have complex texture and structure, which help to check the efficacy of novel inpainting method in recovering texture and structure in large missing region.

The aim of these experiments is to study the effect of combining two inpainting methods on regions of different sizes and with high texture and structure around them. The steps presented in Section 4.7.2.1 are followed to create the inpainting masks. Five cases of inpainting masks have been used to study the efficacy of the proposed technique and to compare it with the EBI and TEBI methods. The mask images belong to 5 different cases (Case1, Case2, Case3, Case4, Case5) representing different sizes and a different number of missing regions in different positions within the images. Figure7-9 illustrate these five cases of inpainting mask (i.e. inpainting domain) representing five damaged/removed regions applied to the database images.



Figure7-9: The same natural image with five different inpainting domains.

Chapter 7: Inpainting Large Missing Regions Based on Seam Carving Method

Recall that the first step of using the proposed technique is the application of the seam carving approach to reduce the sizes of the damaged regions. Table 7-3, below, presents the sizes of missing regions in relation to the size of the whole image before and after applying the seam-carving approach to the damaged images cases that were shown in Figure 7-9. We note that the larger the original size of the occlusion the bigger the reduction in its size by seam-carving.

Figure 7-9: Damaged image Cases	Size % of the occluded region before reduction	Size % of the occluded region after reduction
Case1-Vertical	23.9668%	19.8533%
Case2-Vertical	25.9988%	19.8493%
Case3- Horizontal	32.2152%	21.2498%
Case4-Horizontal	34.5963%	23.8531%
Case5-Vertical	35.4977%	25.8226%

Table 7-3: The size of the missing regions to the whole images in figure 7-9 before and after reduced using the seam-carving approach.

Figure 7-10 displays some selected images that show the implementation of the proposed technique and the EBI and TEBI methods to recover the large missing regions in different inpainting domains.

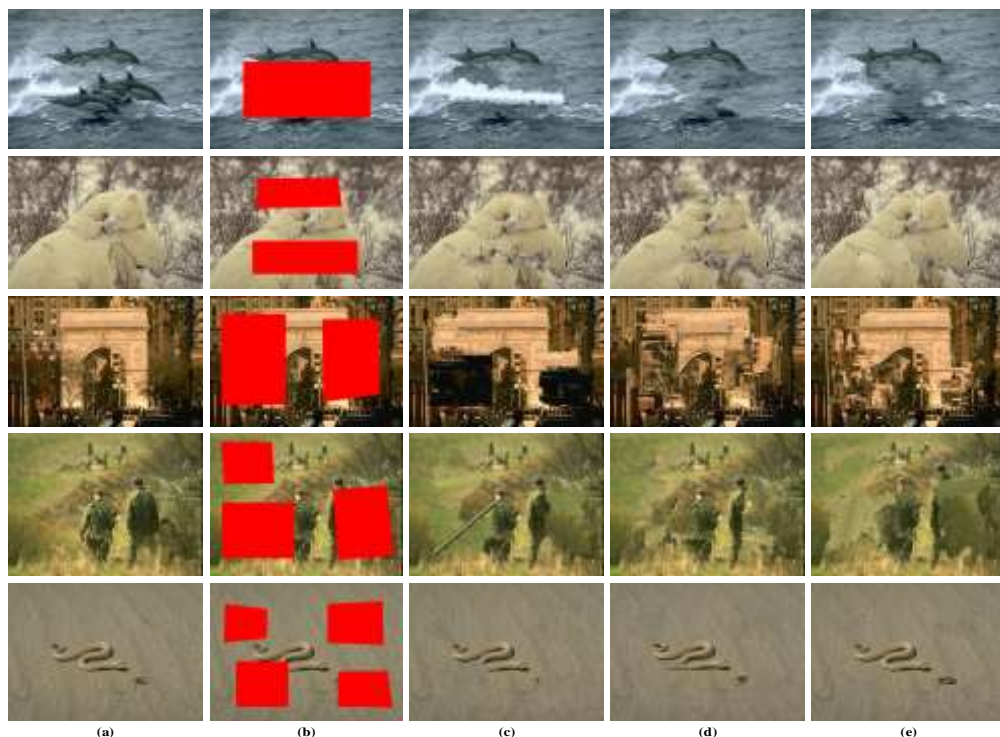


Figure 7-10: Recovering large missing regions examples. (a) Original image, (b) masked image, (c), (d), and (e) inpainted image using the EBI, TEBI and proposed inpainting methods, respectively.

7.5.1.1 Quality measures for removing large regions

In the first case experiments, the proposed technique has been used to remove large objects in the natural images; its outputs have been visually compared with those obtained by using the EBI and TEBI methods, as illustrated in Figure7-7. Through the analysis of image inpainting results, we found that two main aspects need to be considered in image quality assessment. First, the completion is blindly performed without any cue from the original content of the image, that is, the restored regions depend only on the rest of the image. Therefore, the newly generated pixels should be consistent with those in the rest of the image. This refers to the coherence of inpainted regions and enables the detection of undesired visual artefacts. Second, the human gaze is more attracted by structures or contours than other parts; hence more impose should be associated with these salient features. As a result, the MSSIM (Shi et al. 2009), entropy (E) (Gabarda & Cristóbal 2007) and Coherence structure quality measurement (CSQM) (A. DANG Thanh Trung, B. Azeddine BEGHADADI 2013) have been used to check quantitatively the qualities of inpainted images. For more details information about these measurements see Section2.6.1.

Table 7-4 presents the comparison of the statistical quality measurements values resulting from inpainting using the EBI, TEBI and proposed methods; the times taken to get the results using these techniques are also shown.

Figure 7-7: row number	Methods used	Entropy	MSSIM	CSQM	T(S)
Results of Row 1	EBI Method	4.5917	0.7347	0.0280	89
	TEBI Method	4.5827	0.7538	0.0289	117
	Proposed Method	4.5615	0.7970	0.0320	234
Results of Row 2	EBI Method	3.3167	0.8919	0.0231	84
	TEBI Method	3.4780	0.8835	0.0243	121
	Proposed Method	3.1094	0.8974	0.0271	231
Results of Row 3	EBI Method	5.2871	0.7834	0.0231	132
	TEBI Method	4.8853	0.8440	0.0236	167
	Proposed Method	4.5833	0.9045	0.0257	292
Results of Row 4	EBI Method	3.5814	0.8115	0.0234	137
	TEBI Method	3.5750	0.8426	0.0243	181
	Proposed Method	3.3842	0.8798	0.0266	265
Results of Row 5	EBI Method	4.6786	0.7613	0.0511	129
	TEBI Method	4.6783	0.7635	0.0514	141
	Proposed Method	4.6781	0.7887	0.0519	386
Results of Row 6	EBI Method	4.5643	0.8059	0.0232	137
	TEBI Method	4.4483	0.8494	0.0272	178
	Proposed Method	4.2549	0.8963	0.0283	297

Table 7-4: Inpainted image quality assessment comparison using E, MSSIM, and CSQM.

Chapter 7: Inpainting Large Missing Regions Based on Seam Carving Method

In Table 7-4, the statistical quality results following removal of large objects demonstrated that our proposed technique is capable of effective region filling and gives high CSQM values with low Entropy values, and the MSSIM values are close to 1.

7.5.1.2 Quality measures for reconstructing large missing regions

This section continues the analysis of the statistical quality measures, but here we consider images with large missing regions in natural images. The proposed technique is applied to restore missing regions in a sample of 40 images from the Berkeley database. The outputs have been visually compared with the results of EBI and TEBI methods, as seen in Figure 7-10. The quality of inpainted regions has been studied when the reference images (i.e. original images) are available. The table below shows calculated averages of MSE, PSNR, SSIM and EI of our seam-carving inpainting in comparison with the averages obtained by using the EBI and TEBI methods.

C#	Methods used	MSE	PSNR	SSIM	CSQM	Entropy	T(s)
Case1	EBI Method	2680.99	14.650	0.801	0.137	2.848	63
	TEBI Method	2971.46	14.823	0.838	0.147	2.722	120
	Proposed Method	2071.12	15.692	0.833	0.151	2.629	181
Case2	EBI Method	1804.44	16.417	0.842	0.146	2.671	72
	TEBI Method	1501.45	17.486	0.886	0.147	2.691	131
	Proposed Method	1189.15	18.182	0.883	0.161	2.629	197
Case3	EBI Method	2654.84	15.220	0.763	0.085	3.933	96
	TEBI Method	2144.90	15.639	0.712	0.091	4.140	176
	Proposed Method	1695.06	16.678	0.757	0.096	3.833	227
Case4	EBI Method	2409.83	15.617	0.756	0.001	3.940	103
	TEBI Method	1915.83	16.658	0.798	0.093	3.764	184
	Proposed Method	1519.99	17.183	0.792	0.097	3.713	243
Case5	EBI Method	1676.91	16.827	0.799	0.114	3.354	110
	TEBI Method	1294.35	18.160	0.864	0.115	3.332	196
	Proposed Method	934.440	19.460	0.866	0.118	3.312	283

Table 7-5: Inpainted image quality assessment comparison using MSE, PSNR, SSIM, CSQM and Entropy.

Table 7-5 clearly shows that the proposed technique again outperforms the EBI and TEBI methods when using them to recover the large missing regions.

7.5.1.3 Results analysis

This section introduces the analysis of the statistical results of the proposed technique for large object removal and recovering large missing regions. Firstly, for large object removal, Table 7-4 shows that our proposed technique is capable of effective removal of large object by region filling and gives high CSQM values with low Entropy values, and

MSSIM values close to 1. The entropy represents the amount of disorder in the inpainted image. Therefore, generally speaking, lower entropy values are better than higher entropy (Gabarda & Cristóbal 2007). The proposed technique obtained lower entropy value than the EBI and TEBI methods. The MSSIM measure is used to study the coherence extent of the inpainted region in comparison with the rest of the image. In addition, CSQM characterises the visual coherence of the inpainted regions and the visual saliency characterising the visual importance of the inpainted region. High values of MSSIM and CSQM represent better results (A. DANG Thanh Trung, B. Azeddine BEGHADADI 2013). The seam-carving scheme obtained higher values of MSSIM and CSQM than the EBI and TEBI methods, and hence the inpainted regions obtained by using our technique are more coherent with the rest of their images.

For recovering large missing regions, the image quality measures used in Table 7-5 clearly show that the proposed technique again outperforms the EBI and TEBI methods. The proposed technique is clearly capable of effective region filling giving high PSNR values and the SSIM values are close to 1. Moreover, the high CSQM values confirm the success of the proposed technique. However, it takes a bit more time due to the amount of calculation entailed during the matching stage. During the testing, it was found that while some images could look visually pleasing and alike, although they have different PSNR values.

The performance of the proposed technique has dramatically improved the reconstruction of edges and corners in large missing regions. The reduced size of the missing regions introduces massive assistance and allows good patch propagation selection. We directed the seam carving approach to reduce the size of the missing region vertically if we want to reconstruct it horizontally and that helps the patch selection to propagate better as seen in Figure7-8 and 7-10. On the other hand, the seam carving approach has been applied to reduce the size of the missing regions horizontally, when we want to reconstruct the missing regions vertically. As mentioned earlier, the MSE and PSNR are not reliable measures to check the quality of image inpainting. Therefore, in the following section, the TDA approach will be used to assess the efficacy of the proposed technique and its output results (i.e. inpainted images).

A warning. The proposed technique directly restores a clear image from a corrupted input image without any assumptions about the corrupted regions as seen in Figure7-7 and 7-8. However, it does not work well when important structures or details are damaged because its work depends on the information in the rest of image. These

structures or details are usually unique to each image. The first four rows in Figure 7-10 show some examples of undesired failure. This warning is a declaration that the results of restoring large regions that do not have high similarity with the rest of the image are less than acceptable. This may be due to difficulty in finding matching patches within the image, and such cases our technique is not guaranteed to recover some missing regions. Remedying this shortcoming will be a challenge to be dealt with in the future. Possible solutions could be developed by dictionary of images when searching for matching patches rather than searching the image itself. The use of deep learning may provide another solution, but this is outside the realm of this thesis.

7.5.2 Topological Data analysis for image quality

The TDA approach, as a measure of image quality was introduced in (Asaad et al. 2017), and has been used to evaluate the quality of image inpainting and study the efficacy of the various developed inpainting techniques. The TDA quality measure is defined in terms of the number of CCs, but its computation was confined to the inpainted regions in natural images, because the numbers of CCs in the remaining parts of the inpainted image and the original image are the same. The same steps are followed in the construction of the Vietoris-Rips complex which was introduced in 2.6.2.

Recall that there are 7 ULBP geometries each coming in 8 rotations. In our experiments, the number of CCs is counted at different thresholds $T=0$, $T=5$, $T=10$, and $T=15$, for the inpainted images of the above experiments (i.e. five inpainting-domain cases). The volume of the resulting data from the experiments is far too large to be included in the thesis, but the results for $T=10$ are selected as a good representation of the patterns of TDA values for the entire set of experiment. Figure 7-11 and 7-12 show the average number of CCs of inpainted regions as obtained by using the proposed technique and the EBI and TEBI methods for five damaged regions from the natural image dataset in the geometries G5 and G1 at threshold $T=10$, respectively. The rest of the results of geometries G2, G3, G4, G6, and G7 at threshold $T=10$ are presented as an Appendix at the end of thesis (cf. Appendix D).

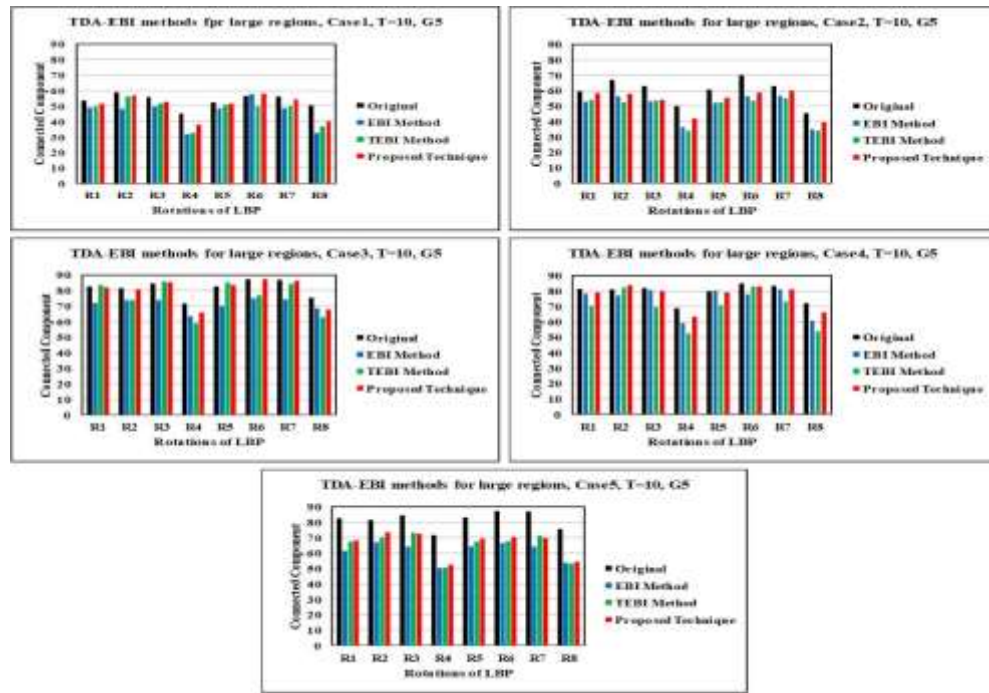


Figure7-11: Evaluation of performance of the proposed inpainting technique using TDA approach at 8 iterations in G5 at threshold T=10 for 5 inpainting cases of natural images.

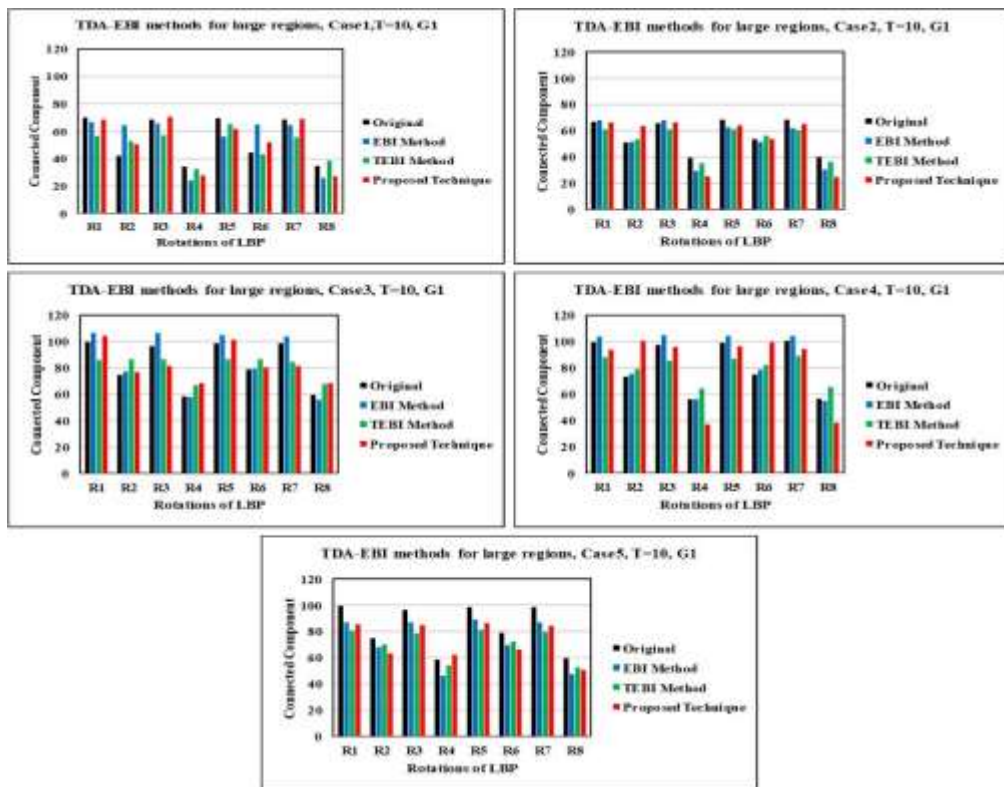


Figure7-12: Evaluation of performance of the proposed inpainting technique using the TDA approach at 8 iterations in G1 at threshold T=10 for 5 inpainting cases of natural images

Examining these charts we can easily ascertain that the numbers of CCs in the inpainted areas as recovered by the proposed method are closer to the numbers of CCs in the

original areas than those observed in the output images from other methods in Geometry G5 but to less extent in G1. We observed the same pattern of results for the geometries G4, and G6 at threshold $T=10$ in the natural images. The geometries G4, G5 and G6 describe the corners, edges and the end lines in the natural images (Ojala et al. 2002). This means the proposed technique has been successful in reconstructing corners, edges and the line ends in the missing regions because of the patterns that are described in the geometries G4, G5, and G6 at threshold $T=10$. However, the numbers of CCs of inpainted regions obtained by using the TEBI technique are closer to the numbers of CCs of corresponding original regions than those ensuing from the EBI method.

Unfortunately, the number of CCs in the inpainted regions for the geometries G1, G2, G3 and G7 do not follow a clear pattern, however, although the results of using method described in (Bertalmio et al. 2000) are not visually acceptable, sometimes the numbers of CCs of inpainted regions by using method described in (Bertalmio et al. 2000) are close to those observed in the original regions of natural images, which means that these geometries at threshold $T=10$ do not act as reliable measures of the image qualities resulting from these inpainting techniques, as seen in Figure7-12, where this Figure clarifies the number of CCs in geomatry G1 at threshold $T=10$.

In conclusion, the TDA approach has been successfully used to study and check the qualities of image inpainting because this approach is a very sensitive process which allows the inpainted region to be studied via at seven geometries, and each geometry has eight rotations which means it will cover all the inpainted regions.

7.6 Summary and Conclusion

We have proposed a novel technique to reconstruct large missing regions in natural images using seam carving. This technique is based on a reductionist strategy which can be used to recover large missing regions with high texture contents around them. It could be used to remove large objects in natural images. Since most of the existing methods cannot recover large missing regions, the size of the missing region is reduced by using the seam carving approach. The developed approach acts in a hybrid manner, in that the TEBI method is used to recover the missing region after which the PDE method is used to recover the seam lines after adding them back to the inpainted image. This technique has been tested on many natural images with visually acceptable results. The proposed technique has succeeded in reconstructing the corners, edges, and line ends in the missing regions. Our results exhibit high-quality inpainting with very low

Chapter 7: Inpainting Large Missing Regions Based on Seam Carving Method

errors. The qualities of the inpainted images that were obtained by using the proposed technique have been checked by statistical measurements and the TDA approach. Furthermore, the proposed technique shows better performance than the EBI and TEBI methods without the resizing approach, as in (Criminisi et al. 2004).

Chapter 8 CONCLUSIONS AND FUTURE RESEARCH

Over the last few years, there has been a growing interest in the process of Image inpainting (image editing) for a variety of purposes and outcomes including the recovery of lost image data such as colour in different types of regions, or the removal of undesired image objects. It has several applications such as automatic scratch removal in old images and films, the removal of dates, text, subtitles, or publicity from an image/film, adding colour to grayscale images after object removal. In addition, the emergence of tougher new challenges in this research field in parallel with rapid advances in, and convergence of, a variety of computational mathematics areas provided me with a strong motivation to embark on a PhD program of research in this field exploring its link with my background in numerical solutions of PDEs. Moreover, the existence of so many inpainting research publications made me realise that for my project to make useful contribution in the field I must keep awareness of other related advances in the mathematics of image processing/analysis field *in order to inject and integrate* relevant new emerging concepts and/or procedures into my work. In what follows, the main conclusions from this research work are presented, and then we briefly report few items of future work including a description of on-going pilot study extension of this research.

8.1 Work summary

The investigations conducted and frequently refined over the duration of the research programme, and reported in several chapters of this thesis, focused on reviewing, modifying, and developing a variety of novel partial/total inpainting approaches to restore missing image data/colour. Our work was of general nature targeting different types of images including natural images as well as other types that are subject to variations in the level and distribution of texture and structure.

The extensive literature review, conducted continuously throughout the project-life, revealed a variety of general and special purpose inpainting schemes naturally reflecting the historical changes in the focus of relevant research as well as the emergence of new

well-intentioned as well as the malicious application of image restoration/reconstruction. Accordingly, our initial work focused on establishing an in-depth understanding of the working, and properties, of existing inpainting techniques. We found that a well-performing PDE-based colourisation scheme was developed under unnecessarily restricted to certain 3-colour channels system that overlooked the well-established linear relationship to the other widely used 3-colour schemes. We also found that the less than adequate visual quality of that scheme was possibly due to restricting the geometric propagation criteria to a simple TV-model and low order PDE. The relaxation of these restrictions raised a new challenge on how to quantitatively compare the performances of our schemes with those of existing schemes. Due to the general objectives of inpainting, performances need to be evaluated in terms of the connection of edges over large distances (i.e. the Connectivity Principle) and depend on how smooth level lines are propagated into the damaged areas (i.e. Curvature Preservation).

Testing the adequacy of such measures must be done through reconstructing small removed regions surrounded by limited when texture areas for a sufficiently large image dataset of different types (e.g. natural and face images). The current success of research conducted in the department on developing *topological data analysis* tools for detecting image tampering, revealed the relevance of using TDA approach as an image quality measure.

Moreover, the study of the non-PDE inpainting approach, i.e. the EBI schemes, revealed that their success was limited to inpainting regions that are surrounded by highly textured areas. Again, the ability of TDA parameters to establish such properties highlighted the relevance of TDA to reducing the limitations of this inpainting approach.

At that stage it was clear than neither of the two approaches, even with our improvements, could persistently produce visually acceptable images by reconstructing large missing regions, especially when these regions are surrounded by highly textured areas. Hence, the next obvious move was to develop hybrid combination inpainting schemes. However, the success of hybrid approaches has been found to be less than remarkable. Hence the alternative, was to attempt to develop a mechanism to reduce the problem of inpainting of large regions into a problem of inpainting relatively smaller sub-regions. Again, we found several benefits from incorporating the recently developed *seam-carving* content-aware image resizing procedure which helped by

providing us with an innovative reductionist strategy to deal with inpainting of large missing regions.

The work done, and the achievements of this thesis can be summarised as follows:

1. We extended the partial (YCbCr) colourisation technique proposed by Sapiro in (Sapiro 2005) for application in other colour spaces. This was based on the linear/affine relations between the colour spaces then these relations were used in order to apply this technique on seven other colour spaces. To overcome the overlapped colours on the edges (artefacts), the Sapiro technique by minimising total variation of (YCbCr) colour channels of two other geometric functionals is improved: (1) the directional derivatives of the gradients, and (2) the Laplacian. The performance of these proposed new schemes is tested on a known database of natural images in different colour spaces both in the spatial and frequency domains. Traditional statistical image quality measures have been used to demonstrate that the PDE algorithm cannot only compete with other algorithms but also creates acceptable visual inpainting in comparison with three colourisation algorithms which are given in (Levin et al. 2004), (Popowicz & Smolka 2014), and (Sapiro 2005). Furthermore, we successfully added colours to entire grayscale images by using the PDE method in different colour spaces in both the spatial and frequency domains.
2. The success of the above PDE based partial inpainting algorithms was then used for total inpainting, when all colour channels are missing. We modified existing PDE total schemes, which apply the same PDE to restore each of the channels, by recovering the (grayscale channel) and then following the above Sapiro-like schemes to recover the rest of the channels. We compared the effects of using 2nd and high order PDE methods. Two experiments have been conducted on natural and human face images sampled from the Berkeley and Yale databases respectively. Four PDE algorithms have been applied to the two datasets in both the spatial and the frequency domains. To quantitatively assess the performances of the various schemes with respect to the quality of the inpainted regions, we introduced the TDA quality measure to the traditionally used statistical image quality measures. While the qualitative subjective image quality assessment results were not reflective of the statistical quantitative measures, the quantitative TDA approach measures were reflective of the visual quality. The

results demonstrated that the image inpainting qualities obtained by using the high-order PDEs are better than those obtained by using 2nd and 3rd order PDEs in both spatial and frequency domains. Furthermore, the results of image inpainting quality obtained by using PDE algorithms in the spatial domain are better than those obtained by using the same algorithms in the frequency domain. Our modified total PDE-based algorithms were shown to be more efficient than existing ones.

3. A novel topological exemplar-based inpainting method (TEBI) has been proposed to remove large objects and reconstruct large missing regions when there is high texture in the missing region's surrounding area. The TEBI method has been introduced to improve the EBI method by selecting adaptively the size of the patch propagation based on the quantity of texture and structure in the surrounding areas of the missing region. Also, a new definition of priority has been proposed to determine the prioritisation of patch filling places based on the concepts of the curvature and the total variation of an isophote to encourage priority filling of the edges and corners in the patches. Finally, a new matching criteria has been introduced to choose approximate true patches from the source region to recover the regions surrounded with high texture and structure.

Experimental results illustrated the success of the TEBI method, and image quality measures confirmed the suitability of the TEBI method. The proposed method performed well in recovering the image geometries but could not recover curved or cross-shaped structures completely. Nevertheless, the proposed method showed better visual results than other exemplar-based methods in such cases. In particular, the proposed method performed not so well in cases where the missing region has no similarity to other regions in the image.

4. To allow the reconstruction of missing regions with high texture in the surrounding areas using PDE methods, we introduced the improvement of the technique described in (Bertalmio et al. 2003) by using a hybrid of a PDE and TEBI methods to reconstruct the textures and structures in the missing regions simultaneously. The scenario of this technique starts by decomposing the image into texture and structure components using the PDE method, after which the damaged regions are separately reconstructed by TEBI and PDE methods respectively. Different PDE methods have been used for decomposing the image and for reconstructing the missing regions in the structure component.

Furthermore, the proposed hybrid technique has been used to recover the information in the frequency domain by using the wavelet transform as a decomposition method to analyse the image into high and low-frequency sub-bands (i.e. structure and texture components). The TEBI and PDE methods have been applied to recover the missing regions in the low and high-frequency sub-bands in the 2nd and 3rd level.

The proposed technique has been tested experimentally on natural image datasets in both spatial and frequency domains. The hybrid technique is used in two applications which are: 1) recovering missing regions and 2) unwanted object removal. The experimental results of the proposed hybrid techniques have been compared with the results obtained from the techniques described in (Bertalmio et al. 2003) and (Jassim et al. 2018). The results of the proposed hybrid technique outperform those obtained in (Bertalmio et al. 2003). However, the results obtained in (Jassim et al. 2018) are more efficient than our hybrid technique. The quality of inpainting images has been evaluated by traditional statistical measurements and by the TDA approach. Meanwhile, the proposed method has failed to recover large missing regions with high texture and structure in the surrounding areas.

5. Since most of the existing methods cannot recover large missing regions, we designed a reductionist strategy to reduce the problem to inpainting a relatively smaller regions. We developed a novel technique to reconstruct general large missing regions in the natural images using the seam carving content-aware resizing procedure. This technique can be used to recover large missing regions with high texture contents around them. Also, the proposed technique could be used to remove large objects in natural images. The size of the missing region is reduced by using the seam carving approach. Next, the TEBI method is used to recover the missing region. Then the PDE method is used to recover the seam lines after adding them back to the inpainted image. This technique has been tested on many natural images with visually acceptable results. The proposed technique has succeeded in reconstructing the corners, edges, and line ends in the missing regions. Our results exhibit high-quality inpainting with very low errors. The qualities of the inpainted images that were obtained by using the proposed technique have been checked by traditional statistical measurements and the TDA approach. Furthermore, the proposed technique shows better

performance than the EBI and TEBI methods without the resizing approach, as in (Criminisi et al. 2004).

To sum up, the answers to the research questions that arose in section 1.3 have now been given in chapters 3, 4, 5, 6 and 7.

8.2 Ongoing and Future Research Directions

The work reported in this thesis not only demonstrated the viability of the adaptive PDE technique along with other inpainting techniques to overcome the problem of large missing regions in the natural images. However, several potential research directions have been identified for further exploration. Future work for this research includes immediate work to address the identified limitations of our current work, follow-up investigations, and new approaches and methods for inpainting. The immediate future work includes the following:

1. As explained before, the hybrid technique is a combination of three main components, each of which includes several methods. Furthermore, finding the best combination among the available methods is still an open task. In the future, many experiments should be conducted to accomplish this. On the other hand, the step of segmentation of textured images will further improve the results on images with large variability in texture types might not be correctly handled by the TEBI step without segmentation. Different parameter selections at the image decomposition stage might also be needed for images containing textures at many different scales. This opens the door for future investigations in PDE-based inpainting and TEBI combined with using decomposition method to split the image into more than two parts (e.g., texture and structure in a series of images at different scales).
2. Expand the research on the TDA issues. Besides ULBP landmark points, that we used to quantify TDA measures, one can also use operators like local derivative pattern (Baochang Zhang et al. 2010), to build simplicial complexes and consequently extract topological features, and then use the TDA approach to study the quality of the inpainted image and also to study the efficacy of inpainting techniques.

3. The work of TEBI method can also be extended to check the suitability of the TEBI method (Jassim et al. 2018) when the size of the missing region is more than 25% of that of the whole image. Computational complexity needs to be further reduced while retaining the quality of inpainting based on testing other definitions for priority function and patch matching.
4. In relation to the seam-carving procedure, other definitions of energy functions that avoid content changing, can be explored for dealing with even larger missing areas.
5. Automatic detection of inpainting based forgery images is a very challenging project that we have some evidences that it could benefit from using TDA. In collaboration with Buckingham colleagues, we recently conducted pilot study to test an innovative TDA-bases scheme to detect inpainting-tampered images (using the EBI method). The limited experimental results were promising when applied to natural and eyeglasses images. Collaborative research will be continued to refine the first version schemes and to extend this work in detecting the suspicious (inpainted) regions in the forged images, by studying the coherence between the blocks in the inpainted images and the original images (Yang et al. 2017), (Jian Li et al. 2015), and (Chang et al. 2013).
6. Finally, we shall also investigate recent attempts to use Convolutional Neural Network (CNN) deep learning inpainting algorithms to explore their performances in comparisons to the traditional schemes discussed in this thesis. In this respect and in order to mimic some kind of efficient machine learning, we also plan to modify the EBI scheme by not relaxing the search for exemplar patches within the image itself and instead using dictionaries of images patches constructed randomly from a large dataset of images (Laube et al. 2018), (Varga & Szirányi 2017) and (Dong et al. 2015).

References

- A. DANG Thanh Trung, B. Azeddine BEGHDAI, C.C.L., 2013. PERCEPTUAL QUALITY ASSESSMENT FOR COLOR IMAGE INPAINTING. *IEEE*, pp.398–402. Available at: <http://f4k.dieei.unict.it/proceedings/ICIP2013/pdfs/0000398.pdf> [Accessed August 8, 2018].
- Abdollahifard, M.J. & Kalantari, S., 2016. Gradient - Based Search Space Reduction for Fast Exemplar - Based Image Inpainting. *International Conference on New Research Achievements in Electrical and Computer Engineering*. Available at: https://www.researchgate.net/profile/Sadegh_Kalantari/publication/306017532_Gradient-Based_Search_Space_Reduction_for_Fast_Exemplar-Based_Image_Inpainting/links/57ad67ff08ae0932c974ff42/Gradient-Based-Search-Space-Reduction-for-Fast-Exemplar-Based-Image-I [Accessed February 16, 2018].
- Adcock, A., Rubin, D. & Carlsson, G., 2014. Classification of hepatic lesions using the matching metric. *Computer Vision and Image Understanding*, 121, pp.36–42. Available at: <https://www.sciencedirect.com/science/article/pii/S1077314213002221> [Accessed July 31, 2018].
- Ahonen, T., Hadid, A. & Pietikainen, M., 2006. Face Description with Local Binary Patterns: Application to Face Recognition. *IEEE Transactions on Pattern Analysis and Machine Intelligence*, 28(12), pp.2037–2041. Available at: <http://ieeexplore.ieee.org/document/1717463/> [Accessed February 16, 2018].
- Ambrosio, L. & Tortorelli, V.M., 1990. Approximation of functional depending on jumps by elliptic functional via t-convergence. *Communications on Pure and Applied Mathematics*, 43(8), pp.999–1036. Available at: <http://doi.wiley.com/10.1002/cpa.3160430805> [Accessed April 29, 2018].
- Anupam, Goyal, P. & Diwakar, S., 2010. Fast and Enhanced Algorithm for Exemplar Based Image Inpainting. In *2010 Fourth Pacific-Rim Symposium on Image and Video Technology*. IEEE, pp. 325–330. Available at: <http://ieeexplore.ieee.org/document/5673977/> [Accessed February 16, 2018].
- Arbeláez, P. et al., 2011. Contour Detection and Hierarchical Image Segmentation. *IEEE Transactions on Pattern Analysis and Machine Intelligence*, 33(5), pp.898–916. Available at: <http://ieeexplore.ieee.org/document/5557884/> [Accessed February 9, 2018].
- Asaad, A. & Jassim, S., 2017. Topological Data Analysis for Image Tampering Detection. In Springer, Cham, pp. 136–146. Available at: http://link.springer.com/10.1007/978-3-319-64185-0_11 [Accessed February 16, 2018].
- Asaad, A.T., Jassim, S.A. & Rashid, R.D., 2018. Topological data analysis as image steganalysis technique. In S. S. Agaian & S. A. Jassim, eds. *Mobile Multimedia/Image Processing, Security, and Applications 2018*. SPIE, p. 17. Available at: <https://www.spiedigitallibrary.org/conference-proceedings-of-spie/10668/2309767/Topological-data-analysis-as-image-steganalysis-technique/10.1117/12.2309767.full> [Accessed July 31, 2018].
- Asaad, A.T., Rashid, R.D. & Jassim, S.A., 2017. Topological image texture analysis for quality assessment. In S. S. Agaian & S. A. Jassim, eds. *International Society for Optics and Photonics*, p. 102210I. Available at:

Reference

- <http://proceedings.spiedigitallibrary.org/proceeding.aspx?doi=10.1117/12.2268471> [Accessed July 31, 2018].
- Aubert, G. & Kornprobst, P., 2006. *Mathematical problems in image processing: partial differential equations and the calculus of variations*, Springer. Available at: <https://books.google.co.uk/books?hl=en&lr=&id=MACXNook-VIC&oi=fnd&pg=PR10&dq=Gilles+Aubert+Pierre+Kornprobst+Mathematical+Problems+in+Image+Processing&ots=dq1TOnUG4S&sig=JQLdW2Bx0lIPiJb1OFDt4kSmiZI#v=onepage&q=Gilles+Aubert+Pierre+Kornprobst+Mathematical+Problems+in+Image+Processing&f=false> [Accessed April 18, 2018].
- Avidan, S. & Shamir, A., 2007. Seam carving for content-aware image resizing. In *ACM SIGGRAPH 2007 papers on - SIGGRAPH '07*. New York, New York, USA: ACM Press, p. 10. Available at: <http://portal.acm.org/citation.cfm?doid=1275808.1276390> [Accessed March 22, 2018].
- Babacan, S.D., Molina, R. & Katsaggelos, A.K., 2008. Total variation super resolution using a variational approach. In *2008 15th IEEE International Conference on Image Processing*. IEEE, pp. 641–644. Available at: <http://ieeexplore.ieee.org/document/4711836/> [Accessed November 8, 2018].
- Ballester, C. et al., 2001. Filling-in by joint interpolation of vector fields and gray levels. *IEEE Transactions on Image Processing*, 10(8), pp.1200–1211. Available at: <http://ieeexplore.ieee.org/document/935036/> [Accessed February 9, 2018].
- Baochang Zhang et al., 2010. Local Derivative Pattern Versus Local Binary Pattern: Face Recognition With High-Order Local Pattern Descriptor. *IEEE Transactions on Image Processing*, 19(2), pp.533–544. Available at: <http://ieeexplore.ieee.org/document/5308376/> [Accessed October 16, 2018].
- Bendich, P. et al., 2016. Persistent Homology Analysis of Brain Artery Trees. *The annals of applied statistics*, 10(1), pp.198–218. Available at: <http://www.ncbi.nlm.nih.gov/pubmed/27642379> [Accessed July 31, 2018].
- Bertalmio, M. et al., 2000. Image inpainting. In *Proceedings of the 27th annual conference on Computer graphics and interactive techniques - SIGGRAPH '00*. New York, New York, USA: ACM Press, pp. 417–424. Available at: <http://portal.acm.org/citation.cfm?doid=344779.344972> [Accessed February 9, 2018].
- Bertalmio, M. et al., 2003. Simultaneous structure and texture image inpainting. *IEEE Transactions on Image Processing*, 12(8), pp.882–889. Available at: <http://ieeexplore.ieee.org/document/1217265/> [Accessed February 16, 2018].
- Bertalmio, M., 2006. Strong-continuation, contrast-invariant inpainting with a third-order optimal PDE. *IEEE Transactions on Image Processing*, 15(7), pp.1934–1938. Available at: <http://ieeexplore.ieee.org/document/1643700/> [Accessed January 2, 2019].
- Bertozi, A., Esedolu, S. & Gillette, A., 2007. Analysis of a Two-Scale Cahn–Hilliard Model for Binary Image Inpainting. *Multiscale Modeling & Simulation*, 6(3), pp.913–936. Available at: <http://epubs.siam.org/doi/10.1137/060660631> [Accessed March 30, 2018].
- Bertozi, A.L. & Bertozi, A.L., 1998. The Mathematics of Moving Contact Lines in Thin Liquid Films. Available at: <http://citeseerx.ist.psu.edu/viewdoc/summary?doi=10.1.1.130.4774> [Accessed July 16, 2018].
- Bertozi, A.L., Esedoglu, S. & Gillette, A., 2007. Inpainting of Binary Images Using the Cahn–Hilliard Equation. *IEEE Transactions on Image Processing*, 16(1), pp.285–291. Available at: <http://ieeexplore.ieee.org/document/4032803/> [Accessed April 27, 2018].

Reference

- Bertsekas, D.P., 2014. *Constrained optimization and Lagrange multiplier methods*,
- Bhavsar, A. V & Rajagopalan, A.N., 2010. Inpainting Large Missing Regions in Range Images. In *2010 20th International Conference on Pattern Recognition*. IEEE, pp. 3464–3467. Available at: <http://ieeexplore.ieee.org/document/5597544/> [Accessed July 30, 2018].
- Black, M.J. et al., 1998. Robust anisotropic diffusion. *IEEE Transactions on Image Processing*, 7(3), pp.421–432. Available at: <http://ieeexplore.ieee.org/document/661192/> [Accessed February 10, 2018].
- Burger, M., He, L. & Schönlieb, C.-B., 2009. Cahn–Hilliard Inpainting and a Generalization for Grayvalue Images. *SIAM Journal on Imaging Sciences*, 2(4), pp.1129–1167. Available at: <http://epubs.siam.org/doi/10.1137/080728548> [Accessed March 30, 2018].
- Cahn, J.W. & Hilliard, J.E., 1958. Free Energy of a Nonuniform System. I. Interfacial Free Energy. *The Journal of Chemical Physics*, 28(2), pp.258–267. Available at: <http://aip.scitation.org/doi/10.1063/1.1744102> [Accessed April 18, 2018].
- Carlsson, G., 2009. TOPOLOGY AND DATA. *BULLETIN (New Series) OF THE AMERICAN MATHEMATICAL SOCIETY*, 46(209), pp.255–308. Available at: <http://www.ams.org/journals/bull/2009-46-02/S0273-0979-09-01249-X/S0273-0979-09-01249-X.pdf> [Accessed February 16, 2018].
- Caselles, V., Morel, J.-M. & Sbert, C., 1999. *An Axiomatic Approach to Image Interpolation*, Available at: <http://citeseerx.ist.psu.edu/viewdoc/download?doi=10.1.1.7.5959&rep=rep1&type=pdf> [Accessed September 16, 2018].
- Chambolle, A. & Pock, T., 2010. A first-order primal-dual algorithm for convex problems with applications to imaging. Available at: <https://hal.archives-ouvertes.fr/hal-00490826> [Accessed July 9, 2018].
- Chan, C.-H., 2007. Multi-scale Local Binary Pattern Histograms for Face Recognition Performance evaluation in biometrics View project 3D-aided face analysis View project. Available at: <https://www.researchgate.net/publication/224936218> [Accessed September 4, 2018].
- Chan, T.F. & Shen, J., 2002. Mathematical Models for Local Nontexture Inpaintings. *SIAM Journal on Applied Mathematics*, 62, pp.1019–1043. Available at: <http://www.jstor.org/stable/3061798> [Accessed March 4, 2018].
- Chan, T.F. & Shen, J., 2001. Nontexture Inpainting by Curvature-Driven Diffusions. *Journal of Visual Communication and Image Representation*, 12(4), pp.436–449. Available at: <https://www.sciencedirect.com/science/article/pii/S1047320301904870> [Accessed February 16, 2018].
- Chan, T.F. & Shen, J. (Jackie), 2005. Variational image inpainting. *Communications on Pure and Applied Mathematics*, 58(5), pp.579–619. Available at: <http://doi.wiley.com/10.1002/cpa.20075> [Accessed May 11, 2018].
- Chan, T.F., Shen, J. & Zhou, H.-M., 2006. Total variation wavelet inpainting. *Journal of Mathematical imaging and Vision*, 25.1, pp.107–125. Available at: http://people.math.gatech.edu/~hmzhou/publications/ChShZh06_1.pdf [Accessed February 9, 2018].
- Chandler, D.M., 2013. Seven Challenges in Image Quality Assessment: Past, Present, and Future Research. *ISRN Signal Processing*, pp.1–53. Available at: <http://www.hindawi.com/journals/isrn/2013/905685/>.

Reference

- Chang, I.-C., Yu, J.C. & Chang, C.-C., 2013. A forgery detection algorithm for exemplar-based inpainting images using multi-region relation. *Image and Vision Computing*, 31(1), pp.57–71. Available at: <http://linkinghub.elsevier.com/retrieve/pii/S0262885612001722> [Accessed April 4, 2018].
- Charpiat, G. et al., 2010. *Machine Learning Methods for Automatic Image Colorization*, Available at: <http://www.cs.huji.ac.il/> [Accessed November 14, 2018].
- Chen, H., 2006. *Image Reconstruction Based on Combination of Wavelet Decomposition, Inpainting and Texture Synthesis*, Available at: <https://otik.uk.zcu.cz/bitstream/11025/866/1/Chen.pdf> [Accessed October 23, 2018].
- Chen, P. & Wang, Y., 2009. A New Fourth-order Equation Model for Image Inpainting. In *2009 Sixth International Conference on Fuzzy Systems and Knowledge Discovery*. IEEE, pp. 320–324. Available at: <http://ieeexplore.ieee.org/document/5360606/> [Accessed November 22, 2018].
- Cheng, W.-H. et al., 2005. Robust Algorithm for Exemplar-based Image Inpainting. *Processing of International Conference on Computer Graphics*, pp.64–69. Available at: http://cmlab.csie.org/new_cml_website/media/publications/Cheng-2005-RAE.pdf [Accessed February 16, 2018].
- Cheng, Z., Yang, Q. & Sheng, B., 2015. Deep Colorization. *The IEEE International Conference on Computer Vision (ICCV)*, pp.415–423. Available at: http://openaccess.thecvf.com/content_iccv_2015/papers/Cheng_Deep_Colorization_ICC_V_2015_paper.pdf [Accessed March 6, 2018].
- Christoudias, C.M., Georgescu, B. & Meer, P., 2002. Synergism in low level vision. In *Object recognition supported by user interaction for service robots*. IEEE Comput. Soc, pp. 150–155. Available at: <http://ieeexplore.ieee.org/document/1047421/> [Accessed July 30, 2018].
- Cocquerez, J.P., Chanas, L. & Blanc-Talon, J., 2003. Simultaneous Inpainting and Motion Estimation of Highly Degraded Video-Sequences. In Springer, Berlin, Heidelberg, pp. 685–692. Available at: http://link.springer.com/10.1007/3-540-45103-X_91 [Accessed May 11, 2018].
- Criminisi, A., Perez, P. & Toyama, K., 2004. Region Filling and Object Removal by Exemplar-Based Image Inpainting. *IEEE Transactions on Image Processing*, 13(9), pp.1200–1212. Available at: <http://ieeexplore.ieee.org/document/1323101/> [Accessed February 16, 2018].
- D. Mumford, T.S.M.N., 1993. Filtering, Segmentation, and Depth.
- Daubechies, I., 1990. The wavelet transform, time-frequency localization and signal analysis. *IEEE Transactions on Information Theory*, 36(5), pp.961–1005. Available at: <http://ieeexplore.ieee.org/document/57199/> [Accessed June 24, 2018].
- Deng Cai, Xiaofei He, Yuxiao Hu, J.H. and T.H., 2005. Codes and Datasets for Feature Learning. Available at: <http://www.cad.zju.edu.cn/home/dengcai/Data/data.html> [Accessed May 22, 2018].
- Deng, L.-J., Huang, T.-Z. & Zhao, X.-L., 2015. Exemplar-Based Image Inpainting Using a Modified Priority Definition J. Malo, ed. *PLOS ONE*, 10(10), p.e0141199. Available at: <http://dx.plos.org/10.1371/journal.pone.0141199> [Accessed February 16, 2018].
- Desai, M., 2012. Modified Fast and Enhanced Exemplar based Inpainting Algorithm for Solving Unknown Row Filling Problem. *International Journal of Computer Applications*, 56(9),

Reference

- pp.975–8887. Available at:
<http://citeseerx.ist.psu.edu/viewdoc/download?doi=10.1.1.244.7695&rep=rep1&type=pdf> [Accessed February 16, 2018].
- Dijkstra, E.W., 1959. A note on two problems in connexion with graphs. *Numerische Mathematik*, 1(1), pp.269–271. Available at:
<http://link.springer.com/10.1007/BF01386390> [Accessed February 9, 2018].
- Ding, X. et al., 2012. Colorization Using Quaternion Algebra with Automatic Scribble Generation. In *Proceedings of the 18th international conference on Advances in Multimedia Modeling*. Springer-Verlag, pp. 103–114. Available at:
http://link.springer.com/10.1007/978-3-642-27355-1_12 [Accessed January 18, 2018].
- Dong, C. et al., 2015. *Image Super-Resolution Using Deep Convolutional Networks*, Available at:
<http://mmlab.ie.cuhk.edu.hk/> [Accessed August 20, 2018].
- Edelsbrunner, H., 2012. PERSISTENT HOMOLOGY: THEORY AND PRACTICE. *Ernest Orlando Lawrence Berkeley National Laboratory, Berkeley, CA, LBNL-6037E*.
- Efros, A.A. & Leung, T.K., 1999. Texture synthesis by non-parametric sampling. In *Proceedings of the Seventh IEEE International Conference on Computer Vision*. IEEE, pp. 1033–1038 vol.2. Available at: <http://ieeexplore.ieee.org/document/790383/> [Accessed February 16, 2018].
- Ekeland, I. (Ivar) & Temam, R., 1976. *Convex analysis and variational problems*, North-Holland Pub. Co.
- Emile-Mâle, G., 1976. The restorer's handbook of easel painting. *Van Nostrand Reinhold*.
- Esedoglu, S. & Shen, J., 2002. DIGITAL INPAINTING BASED ON THE MUMFORD-SHAH-EULER IMAGE MODEL. *European Journal of Applied Mathematics*, 4, pp.353–370. Available at:
<https://conservancy.umn.edu/bitstream/handle/11299/3690/1812.pdf?sequence=1&isAllowed=y> [Accessed March 30, 2018].
- Felzenszwalb, P.F. & Huttenlocher, D.P., 2004. Efficient Graph-Based Image Segmentation. *International Journal of Computer Vision*, 59(2), pp.167–181. Available at:
[http://fcv2011.ulsan.ac.kr/files/announcement/413/IJCV\(2004\) Efficient Graph-Based Image Segmentation.pdf](http://fcv2011.ulsan.ac.kr/files/announcement/413/IJCV(2004) Efficient Graph-Based Image Segmentation.pdf) [Accessed February 9, 2018].
- Le Floch, H. & Labit, C., 1996. Irregular image sub-sampling and reconstruction by adaptive sampling. In *Proceedings of 3rd IEEE International Conference on Image Processing*. IEEE, pp. 379–382. Available at: <http://ieeexplore.ieee.org/document/560510/> [Accessed September 30, 2018].
- Gabarda, S. & Cristóbal, G., 2007. Blind image quality assessment through anisotropy. *Journal of the Optical Society of America A*, 24(12), p.B42. Available at:
<https://www.osapublishing.org/abstract.cfm?URI=josaa-24-12-B42> [Accessed August 8, 2018].
- Gaikar, S. et al., 2014. Image inpainting using Exemplar based, DCT and FMM Algorithm. *International Conference of Advance Research and Innovation*, ISBN, pp.978–993. Available at: <http://www.ijari.org/CurrentIssue/ICARI2014/ICARI-CS-14-02-109.pdf> [Accessed February 16, 2018].
- Ghrist, R., 2008. Barcodes: The persistent topology of data. In *Bulletin of the American Mathematical Society*. pp. 61–75.
- Giansiracusa, N., Giansiracusa, R. & Moon, C., 2017. Persistent homology machine learning for fingerprint classification. Available at: <http://arxiv.org/abs/1711.09158> [Accessed July 31,

Reference

2018].

- Gonzalez, R.C. & Woods, R.E. (Richard E., 2008. *Digital image processing*, Prentice Hall. Available at: <https://books.google.co.uk/books?id=8uGONjRGEzoC&q=digital+image+processing+gonzalez+5th+edition+pdf&dq=digital+image+processing+gonzalez+5th+edition+pdf&hl=en&sa=X&ved=0ahUKEwiNzri90s7cAhUkzLUKHUiQDiEQ6AEIKTAA> [Accessed August 2, 2018].
- Guillemot, C. & Le Meur, O., 2014. Image Inpainting : Overview and recent advances. *IEEE Signal Processing Magazine*.
- Haar Romeny, B.M., 1994. *Geometry-Driven Diffusion in Computer Vision*, Springer Netherlands.
- Hadamard, J., 2003. *Lectures on Cauchy's problem in linear partial differential equations*, Dover Publications. Available at: https://books.google.co.uk/books?hl=en&lr=&id=9RNeBAAAQBAJ&oi=fnd&pg=PA3&dq=J.+Hadamard.+Lectures+on+Cauchy's+Problem+in+Linear+Partial+Differential+Equations.+Dover,+1953.&ots=Eq9kCbl6eN&sig=BL1hs_ba-2wb2Yy2Yek4BoMoRWA#v=onepage&q&f=false [Accessed April 18, 2018].
- Harris, C. & Stephens, M., 1988. A COMBINED CORNER AND EDGE DETECTOR. In *Alvey vision conference*, 15(50), pp.10–5244. Available at: <http://citeseerx.ist.psu.edu/viewdoc/download?doi=10.1.1.434.4816&rep=rep1&type=pdf> [Accessed March 30, 2018].
- Hesabi, S. & Mahdavi-Amiri, N., 2012. A modified patch propagation-based image inpainting using patch sparsity. In *The 16th CSI International Symposium on Artificial Intelligence and Signal Processing (AISP 2012)*. IEEE, pp. 043–048. Available at: <http://ieeexplore.ieee.org/document/6313715/> [Accessed February 16, 2018].
- Do Hyun Chung & Sapiro, G., 2000. On the level lines and geometry of vector-valued images. *IEEE Signal Processing Letters*, 7(9), pp.241–243. Available at: <http://ieeexplore.ieee.org/document/863143/> [Accessed February 20, 2018].
- Ibraheem, N.A. et al., 2012. ARPN Journal of Science and Technology:: Understanding Color Models: A Review. , 2(3). Available at: <http://www.ejournalofscience.org> [Accessed March 5, 2018].
- Igehy, H. & Pereira, L., 1997. Image replacement through texture synthesis. In *Proceedings of International Conference on Image Processing*. IEEE Comput. Soc, pp. 186–189. Available at: <http://ieeexplore.ieee.org/document/632049/> [Accessed September 30, 2018].
- Itti, L., Koch, C. & Niebur, E., 1998. A model of saliency-based visual attention for rapid scene analysis. *IEEE Transactions on Pattern Analysis and Machine Intelligence*, 20(11), pp.1254–1259. Available at: <http://ieeexplore.ieee.org/document/730558/> [Accessed March 30, 2018].
- Jacob, V.G. & Gupta, S., 2009. Colorization of grayscale images and videos using a semiautomatic approach. In *2009 16th IEEE International Conference on Image Processing (ICIP)*. IEEE, pp. 1653–1656. Available at: <http://ieeexplore.ieee.org/document/5413392/> [Accessed January 18, 2018].
- Jacobson, A. & Sorkine-Hornung, O., 2012. A Cotangent Laplacian for Images as Surfaces. *Technical report / Department of Computer Science, ETH, Zurich*, 757. Available at: <https://www.research-collection.ethz.ch/handle/20.500.11850/69353> [Accessed February 20, 2018].
- Jassim, S.A. et al., 2018. Topological data analysis to improve exemplar-based inpainting. In S. S.

Reference

- Agaian & S. A. Jassim, eds. *Mobile Multimedia/Image Processing, Security, and Applications 2018*. SPIE, p. 4. Available at: <https://www.spiedigitallibrary.org/conference-proceedings-of-spie/10668/2309931/Topological-data-analysis-to-improve-exemplar-based-inpainting/10.1117/12.2309931.full> [Accessed July 16, 2018].
- Jian Li et al., 2015. Segmentation-Based Image Copy-Move Forgery Detection Scheme. *IEEE Transactions on Information Forensics and Security*, 10(3), pp.507–518. Available at: <http://ieeexplore.ieee.org/document/6987281/> [Accessed September 24, 2018].
- Jiying Wu & Qiuqi Ruan, 2008. A novel hybrid image inpainting model. In *2008 International Conference on Audio, Language and Image Processing*. IEEE, pp. 138–142. Available at: <http://ieeexplore.ieee.org/document/4589952/> [Accessed February 9, 2018].
- Jung, K.-H., Chang, J.-H. & Lee, C., 1994. Error concealment technique using projection data for block-based image coding. In A. K. Katsaggelos, ed. *International Society for Optics and Photonics*, pp. 1466–1476. Available at: <http://proceedings.spiedigitallibrary.org/proceeding.aspx?articleid=976447> [Accessed September 30, 2018].
- Kelley, C.T., 1999. *Iterative methods for optimization*, SIAM. Available at: https://books.google.co.uk/books?id=C2ePOnDKZKUC&printsec=frontcover&dq=The+method+of+steepest+descent&hl=en&sa=X&ved=0ahUKEwj2Zq_9JHcAhUCbhQKHUXBOEQ6wEINTAC#v=onepage&q=The+method+of+steepest+descent&f=false [Accessed July 9, 2018].
- Kim, T. & Cai, L., 2015. Context-driven hybrid image inpainting. *IET Image Processing*, 9(10), pp.866–873. Available at: <http://digital-library.theiet.org/content/journals/10.1049/iet-ipr.2015.0184> [Accessed September 30, 2018].
- Kojekine, N., Hagiwara, I. & Savchenko, V., 2003. Software tools using CSRBFs for processing scattered data. *Computers & Graphics*, 27(2), pp.311–319. Available at: <https://www.sciencedirect.com/science/article/pii/S009784930200287X> [Accessed October 23, 2018].
- Kokaram, A.C. et al., 1995a. Detection of missing data in image sequences. *IEEE Transactions on Image Processing*, 4(11), pp.1496–1508. Available at: <http://ieeexplore.ieee.org/document/469931/> [Accessed November 8, 2018].
- Kokaram, A.C. et al., 1995b. Interpolation of missing data in image sequences. *IEEE Transactions on Image Processing*, 4(11), pp.1509–1519. Available at: <http://ieeexplore.ieee.org/document/469932/> [Accessed November 8, 2018].
- Konushin, V. & Vezhnevets, V., 2006. Interactive Image Colorization and Recoloring based on Coupled Map Lattices. In *Graphicon'2006 conference proceedings, Novosibirsk Akademgorodok, Russia,,* pp.231–234. Available at: <https://pdfs.semanticscholar.org/74a6/3fca4a70f3c48fa73ef80ed52c4715b7a6c5.pdf> [Accessed February 9, 2018].
- Lagodzinski, P. & Smolka, B., 2014. Application of the Extended Distance Transformation in digital image colorization. *Multimedia Tools and Applications*, 69(1), pp.111–137. Available at: <http://link.springer.com/10.1007/s11042-012-1246-2> [Accessed February 9, 2018].
- Lai, M.-J., Lucier, B. & Wang, J., 2009. The Convergence of a Central - Difference Discretization of Rudin - Osher - Fatemi Model for Image Denoising. *International Conference on Scale Space and Variational Methods in Computer Vision. Springer, Berlin, Heidelberg*, pp.514–526. Available at:

Reference

- https://www.researchgate.net/profile/Bradley_Lucier/publication/221089472_The_Convergence_of_a_Central-Difference_Discretization_of_Rudin-Osher-Fatemi_Model_for_Image_Denoising/links/00463529ce1d90c549000000.pdf [Accessed February 9, 2018].
- Lamar-León, J., García-Reyes, E.B. & Gonzalez-Diaz, R., 2012. Human Gait Identification Using Persistent Homology. In Springer, Berlin, Heidelberg, pp. 244–251. Available at: http://link.springer.com/10.1007/978-3-642-33275-3_30 [Accessed July 31, 2018].
- Laube, P. et al., 2018. *IMAGE INPAINTING FOR HIGH-RESOLUTION TEXTURES USING CNN TEXTURE SYNTHESIS*, Available at: <https://arxiv.org/pdf/1712.03111.pdf> [Accessed August 20, 2018].
- Levin, A., Lischinski, D. & Weiss, Y., 2004. Colorization using Optimization. *ACM Transactions on Graphics (ToG)*, 23, no. 3, pp.689–694. Available at: <http://webee.technion.ac.il/people/anat.levin/papers/colorization-siggraph04.pdf> [Accessed February 9, 2018].
- Lezoray, O., Ta, V.T. & Elmoataz, A., 2008. Nonlocal graph regularization for image colorization. In *2008 19th International Conference on Pattern Recognition*. IEEE, pp. 1–4. Available at: <http://ieeexplore.ieee.org/document/4761617/> [Accessed February 9, 2018].
- Liang, Z. et al., 2015. An efficient forgery detection algorithm for object removal by exemplar-based image inpainting. *Journal of Visual Communication and Image Representation*, 30(C), pp.75–85. Available at: <https://linkinghub.elsevier.com/retrieve/pii/S1047320315000541> [Accessed September 24, 2018].
- Liu, K., Tan, J. & Su, B., 2014. An Adaptive Image Denoising Model Based on Tikhonov and TV Regularizations. *Advances in Multimedia*, 2014, pp.1–10. Available at: <http://www.hindawi.com/journals/am/2014/934834/> [Accessed October 1, 2018].
- Love, A.E.H. (Augustus E.H., 2013. *A treatise on the mathematical theory of elasticity*, Cambridge University Press. Available at: https://books.google.co.uk/books?hl=en&lr=&id=JFTbrz0Fs5UC&oi=fnd&pg=PA1&dq=A.+E.+H.+Love.+A+Treatise+on+the+Mathematical+Theory+of+Elasticity.+Dover,+New+York,+4th+ed.,+1927&ots=MWRdI5Kpba&sig=2_xYURHiPQkN0oyiiPVL9RMuxDU#v=onepage&q&f=false [Accessed April 18, 2018].
- Luan, Q. et al., 2007. Natural image colorization. *Proceedings of the 18th Eurographics conference on Rendering Techniques*, pp.309–320. Available at: <https://dl.acm.org/citation.cfm?id=2383887> [Accessed February 9, 2018].
- Lum, P.Y. et al., 2013. Extracting insights from the shape of complex data using topology. *Scientific Reports*, 3(1), p.1236.
- Malgouyres, F. & Guichard, F., 2001. Edge Direction Preserving Image Zooming: A Mathematical and Numerical Analysis. *SIAM Journal on Numerical Analysis*, 39(1), pp.1–37. Available at: <http://epubs.siam.org/doi/10.1137/S0036142999362286> [Accessed May 11, 2018].
- Markle, Wilson, and B.H., 1988. Coloring a black and white signal using motion detection. *U.S. Patent, Washington,* 4,755,870. Available at: <https://patents.google.com/patent/US4755870A/en> [Accessed February 9, 2018].
- Masnou, S. & Morel, J.-M., 1998. Level lines based disocclusion. In *Proceedings 1998 International Conference on Image Processing. ICIP98 (Cat. No.98CB36269)*. IEEE Comput. Soc, pp. 259–263. Available at: <http://ieeexplore.ieee.org/document/999016/> [Accessed

Reference

- September 16, 2018].
- Muhammad, G., Hussain, M. & Bebis, G., 2012. Passive copy move image forgery detection using undecimated dyadic wavelet transform. *Digital Investigation*, 9(1), pp.49–57. Available at: <https://www.sciencedirect.com/science/article/pii/S1742287612000242> [Accessed September 24, 2018].
- Mumford, D., 1994. Elastica and Computer Vision. In *Algebraic Geometry and its Applications*. New York, NY: Springer New York, pp. 491–506. Available at: http://link.springer.com/10.1007/978-1-4612-2628-4_31 [Accessed September 16, 2018].
- Neuraltek, 2004. TimeBrush Studios - Colorization, Revival, and Restoration of Black & White Television Shows, Motion Pictures, and Documentary Programs [Programmes]. *Australia*. Available at: <http://www.timebrush.com/blackmagic> [Accessed February 20, 2018].
- Nileshbhai Patel, H., 2016. A Survey on Different techniques for Image Inpainting. *International Research Journal of Engineering and Technology*. Available at: www.irjet.net [Accessed January 28, 2019].
- Nitzberg, M., Mumford, D. & Shiota, T., 1993. *Filtering, Segmentation and Depth*, Berlin, Heidelberg: Springer Berlin Heidelberg. Available at: <http://link.springer.com/10.1007/3-540-56484-5> [Accessed May 11, 2018].
- Ojala, T., Pietika, M. & Ma, T., 2002. *Multiresolution Gray-Scale and Rotation Invariant Texture Classification with Local Binary Patterns*, Available at: http://www.ee.oulu.fi/mvg/files/pdf/pdf_94.pdf [Accessed September 4, 2018].
- Ojala, T., Pietikäinen, M. & Harwood, D., 1996. A comparative study of texture measures with classification based on featured distributions. *Pattern Recognition*, 29(1), pp.51–59. Available at: <https://www.sciencedirect.com/science/article/pii/0031320395000674> [Accessed February 16, 2018].
- Oman, M.E., 1995. *Iterative methods for total variation based image reconstruction*, Available at: <https://scholarworks.montana.edu/xmlui/bitstream/handle/1/7605/31762102581772.pdf?sequence=1> [Accessed October 1, 2018].
- Osher, S. & Sethian, J.A., 1988. Fronts Propagating with Curvature Dependent Speed: Algorithms Based on Hamilton-Jacobi Formulations. *Journal of Computational Physics*, 79, pp.12–49. Available at: <https://math.berkeley.edu/~sethian/Papers/sethian.osher.88.pdf> [Accessed May 2, 2018].
- Pablo Arbelaez, C.F. and D.M., 2007. The Berkeley Segmentation Dataset and Benchmark. *The website of the Berkeley database is*. Available at: <https://www2.eecs.berkeley.edu/Research/Projects/CS/vision/bsds/> [Accessed February 9, 2018].
- Pedersen, M. & Marius, 2012. Image quality metrics for the evaluation of printing workflows. Available at: <https://www.duo.uio.no/handle/10852/9035> [Accessed August 15, 2018].
- Peiyong Chen & Yuandi Wang, 2008. Fourth-order partial differential equations for image inpainting. In *2008 International Conference on Audio, Language and Image Processing*. IEEE, pp. 1713–1717. Available at: <http://ieeexplore.ieee.org/document/4590002/> [Accessed February 16, 2018].
- Perona, P. & Malik, J., 1990. Scale-space and edge detection using anisotropic diffusion. *IEEE Transactions on Pattern Analysis and Machine Intelligence*, 12(7), pp.629–639. Available

Reference

- at: <http://ieeexplore.ieee.org/document/56205/> [Accessed April 18, 2018].
- Popowicz, A. & Smolka, B., 2017. Fast image colourisation using the isolines concept. *Multimed Tools Appl*, 76, pp.15987–16009. Available at: <https://link.springer.com/content/pdf/10.1007%2Fs11042-016-3892-2.pdf> [Accessed February 9, 2018].
- Popowicz, A. & Smolka, B., 2014. Isoline Based Image Colorization. *International Conference on Computer Modelling and Simulation 2014 UKSim-AMSS 16th*, pp.280–285. Available at: https://www.researchgate.net/profile/A_Popowicz/publication/271521019_Isoline_Base_d_Image_Colorization/links/554f2fdd08ae93634ec7341d/Isoline-Based-Image-Colorization.pdf [Accessed February 9, 2018].
- Popowicz, A. & Smolka, B., 2015. Overview of Grayscale Image Colorization Techniques. In *Color Image and Video Enhancement*. Cham: Springer International Publishing, pp. 345–370. Available at: http://link.springer.com/10.1007/978-3-319-09363-5_12 [Accessed February 9, 2018].
- Qu, Y. et al., 2006. Manga colorization. In *ACM SIGGRAPH 2006 Papers on - SIGGRAPH '06*. New York, New York, USA: ACM Press, p. 1214. Available at: <http://portal.acm.org/citation.cfm?doid=1179352.1142017> [Accessed February 9, 2018].
- Rane, S.D., Sapiro, G. & Bertalmio, M., 2003. Structure and texture filling-in of missing image blocks in wireless transmission and compression applications. *IEEE Transactions on Image Processing*, 12(3), pp.296–303. Available at: <http://ieeexplore.ieee.org/document/1197835/> [Accessed February 9, 2018].
- Recktenwald, G.W., 2011. *Finite-Difference Approximations to the Heat Equation*, Available at: <http://web.cecs.pdx.edu/~gerry/class/ME448/codes/FDheat.pdf> [Accessed August 6, 2018].
- Reinhard, E. et al., 2001. Color transfer between images. *IEEE Computer Graphics and Applications*, 21(4), pp.34–41. Available at: <http://ieeexplore.ieee.org/document/946629/> [Accessed February 9, 2018].
- Rubinstein, M., Shamir, A. & Avidan, S., 2008. Improved Seam Carving for Video Retargeting. *ACM Trans. Graph. Article*, 27(16). Available at: <http://www.merl.com> [Accessed March 22, 2018].
- Ruderman, D.L., Cronin, T.W. & Chiao, C.-C., 1998. Statistics of cone responses to natural images: implications for visual coding. *OSA A* 15, 8, p.2036–2045. Available at: http://www.theswartzfoundation.org/papers/salk/Ruderman_Cronin_Chiao_JOptSocAm_A_1998.pdf [Accessed February 9, 2018].
- Rudin, L.I., Osher, S. & Fatemi, E., 1992. Nonlinear total variation based noise removal algorithms. *Physica D: Nonlinear Phenomena*, 60(1–4), pp.259–268. Available at: <https://www.sciencedirect.com/science/article/pii/016727899290242F> [Accessed February 9, 2018].
- Russo, F., 2014. Performance Evaluation of Noise Reduction Filters for Color Images through Normalized Color Difference (NCD) Decomposition. *ISRN Machine Vision*, 2014, pp.1–11. Available at: <https://www.hindawi.com/archive/2014/579658/> [Accessed January 18, 2018].
- Saha, S. & Vemuri, R., 2000. An analysis on the effect of image activity on lossy coding performance. In *2000 IEEE International Symposium on Circuits and Systems. Emerging Technologies for the 21st Century. Proceedings (IEEE Cat No.00CH36353)*. Presses Polytech. Univ. Romandes, pp. 295–298. Available at:

Reference

- <http://ieeexplore.ieee.org/document/856055/> [Accessed August 17, 2018].
- Sangeeth, K., Sengottuvelan, P. & Balamurugan, E., 2011. A Novel Exemplar based Image Inpainting Algorithm for Natural Scene Image Completion with Improved Patch Prioritizing. *International Journal of Computer Applications*, 36(4), pp.0975-8887. Available at: https://www.researchgate.net/profile/Sangeetha_K2/publication/258045401_A_Novel_Exemplar_based_Image_Inpainting_Algorithm_for_Natural_Scene_Image_Completion_with_Improved_Patch_Prioritizing/links/0deec526b84aec072e000000/A-Novel-Exemplar-based-Image-Inpai [Accessed February 16, 2018].
- Sangeetha, K., Sengottuvelan, P. & Balamurugan, E., 2011. Combined Structure and Texture Image Inpainting Algorithm for Natural Scene Image Completion. *Journal of Information Engineering and Applications*, 1(1). Available at: www.iiste.org [Accessed July 12, 2018].
- Sapiro, G., 2005. Inpainting the colors. In *IEEE International Conference on Image Processing 2005*. IEEE, p. II-698. Available at: <http://ieeexplore.ieee.org/document/1530151/> [Accessed January 18, 2018].
- Sc, C.-B., And, O. & Bertozzi, A., 2011. UNCONDITIONALLY STABLE SCHEMES FOR HIGHER ORDER INPAINTING *. , 9(2), pp.413–457. Available at: https://www.intlpress.com/site/pub/files/_fulltext/journals/cms/2011/0009/0002/CMS-2011-0009-0002-a004.pdf [Accessed March 30, 2018].
- Schonlieb, C.-B., 2015. *Partial Differential Equation Methods for Image Inpainting*, Cambridge: Cambridge University Press. Available at: <http://ebooks.cambridge.org/ref/id/CBO9780511734304> [Accessed July 9, 2018].
- Schönlieb, C.-B. et al., 2010. Image Inpainting Using a Fourth-Order Total Variation Flow. *SAMPTA'09*, p.Special session on sampling and (in)painting. Available at: <https://hal.archives-ouvertes.fr/hal-00452296/> [Accessed February 16, 2018].
- Schönlieb, C.-B., 2009. Modern PDE Techniques for Image Inpainting. Available at: http://www.damtp.cam.ac.uk/user/cbs31/Publications_files/thesis.pdf [Accessed July 9, 2018].
- Shah, A.A., Gandhi, M. & Shah, K.M., 2013. Medical Image Colorization using Optimization Technique. *International Journal of Scientific and Research Publications*, 3(1), pp.2250–3153. Available at: www.ijsrp.org [Accessed January 18, 2018].
- Sharma, N. & Mehta, N., 2013. Region Filling and Object Removal by Exempeler Based Image Inpainting. *International Journal of Inventive Engineering and Sciences*, (13), pp.2319–9598. Available at: <http://citeseerx.ist.psu.edu/viewdoc/download?doi=10.1.1.684.5847&rep=rep1&type=pdf> [Accessed March 4, 2018].
- Shen, J. & Chan, T.F., 2002. Mathematical Models for Local Nontexture Inpaintings. *SIAM Journal on Applied Mathematics*, 62(3), pp.1019–1043. Available at: <http://epubs.siam.org/doi/10.1137/S0036139900368844> [Accessed February 16, 2018].
- Shi, Y. et al., 2009. Structure and Hue Similarity for Color Image Quality Assessment. In *2009 International Conference on Electronic Computer Technology*. IEEE, pp. 329–333. Available at: <http://ieeexplore.ieee.org/document/4795977/> [Accessed August 14, 2018].
- Smith, G.D. (Gordon D., 1985. *Numerical solution of partial differential equations: finite difference methods*, Clendon Press. Available at: <https://global.oup.com/academic/product/numerical-solution-of-partial-differential-equations-9780198596509?cc=gb&lang=en> [Accessed July 9, 2018].

Reference

- Strobel, H., 1989. Strang, G., Introduction to Applied Mathematics. Wellesley, Mass. Wellesley-Cambridge Press 1986. IX, 758 pp. ISBN 0-9614088-0-4. *ZAMM - Journal of Applied Mathematics and Mechanics / Zeitschrift für Angewandte Mathematik und Mechanik*, 69(9), pp.311–312. Available at: <http://doi.wiley.com/10.1002/zamm.19890690917> [Accessed July 16, 2018].
- Sukho Lee et al., 2013. Colorization-Based Compression Using Optimization. *IEEE Transactions on Image Processing*, 22(7), pp.2627–2636. Available at: <http://ieeexplore.ieee.org/document/6482621/> [Accessed February 10, 2018].
- Suthar, R. et al., 2014. *A Survey on Various Image Inpainting Techniques to Restore Image*, Available at: www.ijera.com [Accessed January 28, 2019].
- T. Chan and J. Shen, 2001. Non-Texture Inpainting by Curvature-Driven Diffusions (CCD). *Journal of Visual Communication and Image Representation*, 12(4), pp.436–449. Available at: <https://conservancy.umn.edu/bitstream/handle/11299/3528/1743.pdf?sequence=1> [Accessed March 4, 2018].
- T.F. Chan, S.H. Kang, and J.S., 2002. Euler's elastica and curvature-based inpainting. *SIAM J. Appl. Math.*, 63, pp.564–592.
- Takamichi Miyata et al., 2009. Novel inverse colorization for image compression. In *2009 Picture Coding Symposium*. IEEE, pp. 1–4. Available at: <http://ieeexplore.ieee.org/document/5167413/> [Accessed February 10, 2018].
- Tang, K.-T., 2007. Calculus of Variation. In *Mathematical Methods for Engineers and Scientists 3*. Berlin, Heidelberg: Springer Berlin Heidelberg, pp. 367–429. Available at: http://link.springer.com/10.1007/978-3-540-44697-2_7 [Accessed April 8, 2018].
- Tavakoli, A., Mousavi, P. & Zarmehi, F., 2018. Modified algorithms for image inpainting in Fourier transform domain. *Computational and Applied Mathematics*, 37(4), pp.5239–5252. Available at: <http://link.springer.com/10.1007/s40314-018-0632-4> [Accessed November 20, 2018].
- Telea, A., 2018. University of Groningen An Image Inpainting Technique Based on the Fast Marching Method An Image Inpainting Technique Based on the Fast Marching Method. Available at: <https://core.ac.uk/download/pdf/148284148.pdf> [Accessed July 12, 2018].
- Tikhonov, A.N., 2014. *Nonlinear Ill-posed Problems.*, Springer Verlag.
- Torres-Méndez, L.A. & Dudek, G., 2008. Inter-Image Statistics for 3D Environment Modeling. *International Journal of Computer Vision*, 79(2), pp.137–158. Available at: <http://link.springer.com/10.1007/s11263-007-0108-2> [Accessed July 30, 2018].
- Tsai, A., Yezzi, A. & Willsky, A.S., 2001. Curve Evolution Implementation of the Mumford–Shah Functional for Image Segmentation, Denoising, Interpolation, and Magnification. *IEEE TRANSACTIONS ON IMAGE PROCESSING*, 10(8), pp.1169–1186. Available at: <https://pdfs.semanticscholar.org/035c/3e0009b5623505af55bc68129e1343b31f9b.pdf> [Accessed April 18, 2018].
- Vadhel, B. & Limbasiya, B., 2016. Survey on Different Techniques for Image Inpainting. *International Research Journal of Engineering and Technology*. Available at: www.irjet.net [Accessed January 28, 2019].
- Varga, D. & Szirányi, T., 2017. Convolutional Neural Networks for automatic image colorization. , pp.1–15. Available at: http://eprints.sztaki.hu/9292/1/Varga_1_3306455_ny.pdf [Accessed February 9, 2018].

Reference

- Vedaldi, M.C. and S.M. and I.K. and S.M. and and A., 2014. Describable Textures Dataset. Available at: <https://www.robots.ox.ac.uk/~vgg/data/dtd/index.html> [Accessed February 16, 2018].
- Veeravasaru, V.S.R. & Sivaswamy, J., 2012. Fast and fully automated video colorization. In *2012 International Conference on Signal Processing and Communications (SPCOM)*. IEEE, pp. 1–5. Available at: <http://ieeexplore.ieee.org/document/6290028/> [Accessed February 9, 2018].
- Vese, L.A. & Osher, S.J., 2003. Modeling Textures with Total Variation Minimization and Oscillating Patterns in Image Processing. *Journal of Scientific Computing*, 19(1/3), pp.553–572. Available at: <http://link.springer.com/10.1023/A:1025384832106> [Accessed February 16, 2018].
- W. Rudin, 1976. PRINCIPLES OF MATHEMATICAL ANALYSIS. , Third edit. Available at: https://merounak.files.wordpress.com/2016/02/walter_rudin_principles_of_mathematical_analysisbookfi.pdf [Accessed July 9, 2018].
- Walden, S., 1985. The ravished image.
- Wang, Z. et al., 2004. Image Quality Assessment: From Error Visibility to Structural Similarity. *IEEE Transactions on Image Processing*, 13(4), pp.600–612. Available at: <http://ieeexplore.ieee.org/document/1284395/> [Accessed February 10, 2018].
- Wang, Z. & Bovik, A.C., 2006. Modern Image Quality Assessment. *Synthesis Lectures on Image, Video, and Multimedia Processing*, 2(1), pp.1–156. Available at: <http://www.morganclaypool.com/doi/abs/10.2200/S00010ED1V01Y200508IVM003> [Accessed August 15, 2018].
- Waykule, M. & Patil, M., 2012. Region Filling and Object Removal by Exemplar- Based Image Inpainting. *International Journal of Scientific & Engineering Research*, 3(1), pp.2229–5518. Available at: <http://www.ijser.org> [Accessed February 16, 2018].
- Wei Guo & Li-Hong Qiao, 2007. Inpainting based on total variation. In *2007 International Conference on Wavelet Analysis and Pattern Recognition*. IEEE, pp. 939–943. Available at: <http://ieeexplore.ieee.org/document/4420804/> [Accessed February 16, 2018].
- Wei, L.-Y. & Levoy, M., 2000. Fast Texture Synthesis using Tree-structured Vector Quantization. In *Proceedings of the 27th annual conference on Computer graphics and interactive techniques,, ACM Press*, pp.479–488. Available at: <http://graphics.stanford.edu/projects/texture/> [Accessed July 12, 2018].
- Weickert, J., 1996. *THEORETICAL FOUNDATIONS OF ANISOTROPIC DIFFUSION IN IMAGE PROCESSING*, Available at: <https://pdfs.semanticscholar.org/60b1/f3d452696feafd0fe54621ff015e688adcd2.pdf> [Accessed September 4, 2018].
- Weickert, J. & Stüttgart, B.G.T., 1998. *Anisotropic Diffusion in Image Processing*, Available at: http://www.lpi.tel.uva.es/muitic/pim/docus/anisotropic_diffusion.pdf [Accessed September 4, 2018].
- Winkler, S. & Mohandas, P., 2008. The Evolution of Video Quality Measurement: From PSNR to Hybrid Metrics. *IEEE Transactions on Broadcasting*, 54(3), pp.660–668. Available at: <http://ieeexplore.ieee.org/document/4550731/> [Accessed May 22, 2018].
- Xiang, Y., Zou, B. & Li, H., 2009. Selective color transfer with multi-source images. *Pattern Recognition Letters*, 30(7), pp.682–689. Available at: <https://www.sciencedirect.com/science/article/pii/S0167865509000191> [Accessed

Reference

February 9, 2018].

- Xu, Z., Lian, X. & Feng, L., 2008. Image Inpainting Algorithm Based on Partial Differential Equation. In *2008 ISECS International Colloquium on Computing, Communication, Control, and Management*. IEEE, pp. 120–124. Available at: <http://ieeexplore.ieee.org/document/4609482/> [Accessed February 16, 2018].
- Yang, G. et al., 2017. A robust forgery detection algorithm for object removal by exemplar-based image inpainting. Available at: <https://www.researchgate.net/publication/317300165> [Accessed September 24, 2018].
- Yao_Wang, Jörn. Ostermann, Y.-Q.Z., 2001. Video Processing and Communications (Prentice-Hall Signal Processing Series). , pp.1–32.
- Yao Wang & Qin-Fan Zhu, 1998. Error control and concealment for video communication: a review. *Proceedings of the IEEE*, 86(5), pp.974–997. Available at: <http://ieeexplore.ieee.org/document/664283/> [Accessed May 11, 2018].
- Yatziv, L. & Sapiro, G., 2006. Fast image and video colorization using chrominance blending Chrominance Blending. *IEEE transactions on image processing*, 15, no. 5, pp.1120–1129. Available at: <http://www.ima.umn.edu> [Accessed February 9, 2018].
- Ye, J. & Shi, Y.-Q., 2017. A Hybrid Feature Model for Seam Carving Detection. In *International Workshop on Digital Watermarking*. Springer, Cham, pp. 77–89. Available at: http://link.springer.com/10.1007/978-3-319-64185-0_7 [Accessed March 22, 2018].
- You, Y.-L. & Kaveh, M., 2000. Fourth-order partial differential equations for noise removal. *IEEE Transactions on Image Processing*, 9(10), pp.1723–1730. Available at: <http://ieeexplore.ieee.org/document/869184/> [Accessed July 12, 2018].
- Zhang, R., Isola, P. & Efros, A.A., 2016. Colorful Image Colorization. In Springer, Cham, pp. 649–666. Available at: http://link.springer.com/10.1007/978-3-319-46487-9_40 [Accessed October 16, 2018].
- Zhang, Z. et al., 2009. A Colorization Method Based on Fuzzy Clustering and Distance Transformation. In *2009 2nd International Congress on Image and Signal Processing*. IEEE, pp. 1–5. Available at: <http://ieeexplore.ieee.org/document/5304487/> [Accessed February 9, 2018].
- Zhao, Y. et al., 2007. Colorizing Biomedical Images Based on Color Transfer. In *2007 IEEE/ICME International Conference on Complex Medical Engineering*. IEEE, pp. 820–823. Available at: <http://ieeexplore.ieee.org/document/4381855/> [Accessed February 9, 2018].
- Zhen, Z., Yan, G. & Lizhuang, M., 2012. An automatic image and video colorization algorithm based on pattern continuity. In *2012 International Conference on Audio, Language and Image Processing*. IEEE, pp. 531–536. Available at: <http://ieeexplore.ieee.org/document/6376674/> [Accessed November 14, 2018].
- Zhu, J.-Y. et al., 2016. Generative Visual Manipulation on the Natural Image Manifold. In *European Conference on Computer Vision*, Springer, Cham, pp.597–613. Available at: <https://arxiv.org/pdf/1609.03552.pdf> [Accessed March 22, 2018].
- Zongben Xu & Jian Sun, 2010. Image Inpainting by Patch Propagation Using Patch Sparsity. *IEEE Transactions on Image Processing*, 19(5), pp.1153–1165. Available at: <http://ieeexplore.ieee.org/document/5404308/> [Accessed February 16, 2018].
- A. DANG Thanh Trung, B. Azeddine BEGHADADI, C.C.L., 2013. PERCEPTUAL QUALITY ASSESSMENT FOR COLOR IMAGE INPAINTING. *IEEE*, pp.398–402. Available at: <http://f4k.dieei.unict.it/proceedings/ICIP2013/pdfs/0000398.pdf> [Accessed August 8,

Reference

2018].

- Abdollahifard, M.J. & Kalantari, S., 2016. Gradient - Based Search Space Reduction for Fast Exemplar - Based Image Inpainting. *International Conference on New Research Achievements in Electrical and Computer Engineering*. Available at: https://www.researchgate.net/profile/Sadegh_Kalantari/publication/306017532_Gradient-Based_Search_Space_Reduction_for_Fast_Exemplar-Based_Image_Inpainting/links/57ad67ff08ae0932c974ff42/Gradient-Based-Search-Space-Reduction-for-Fast-Exemplar-Based-Image-I [Accessed February 16, 2018].
- Adcock, A., Rubin, D. & Carlsson, G., 2014. Classification of hepatic lesions using the matching metric. *Computer Vision and Image Understanding*, 121, pp.36–42. Available at: <https://www.sciencedirect.com/science/article/pii/S1077314213002221> [Accessed July 31, 2018].
- Ahonen, T., Hadid, A. & Pietikainen, M., 2006. Face Description with Local Binary Patterns: Application to Face Recognition. *IEEE Transactions on Pattern Analysis and Machine Intelligence*, 28(12), pp.2037–2041. Available at: <http://ieeexplore.ieee.org/document/1717463/> [Accessed February 16, 2018].
- Ambrosio, L. & Tortorelli, V.M., 1990. Approximation of functional depending on jumps by elliptic functional via t-convergence. *Communications on Pure and Applied Mathematics*, 43(8), pp.999–1036. Available at: <http://doi.wiley.com/10.1002/cpa.3160430805> [Accessed April 29, 2018].
- Anupam, Goyal, P. & Diwakar, S., 2010. Fast and Enhanced Algorithm for Exemplar Based Image Inpainting. In *2010 Fourth Pacific-Rim Symposium on Image and Video Technology*. IEEE, pp. 325–330. Available at: <http://ieeexplore.ieee.org/document/5673977/> [Accessed February 16, 2018].
- Arbeláez, P. et al., 2011. Contour Detection and Hierarchical Image Segmentation. *IEEE Transactions on Pattern Analysis and Machine Intelligence*, 33(5), pp.898–916. Available at: <http://ieeexplore.ieee.org/document/5557884/> [Accessed February 9, 2018].
- Asaad, A. & Jassim, S., 2017. Topological Data Analysis for Image Tampering Detection. In Springer, Cham, pp. 136–146. Available at: http://link.springer.com/10.1007/978-3-319-64185-0_11 [Accessed February 16, 2018].
- Asaad, A.T., Jassim, S.A. & Rashid, R.D., 2018. Topological data analysis as image steganalysis technique. In S. S. Agaian & S. A. Jassim, eds. *Mobile Multimedia/Image Processing, Security, and Applications 2018*. SPIE, p. 17. Available at: <https://www.spiedigitallibrary.org/conference-proceedings-of-spie/10668/2309767/Topological-data-analysis-as-image-steganalysis-technique/10.1117/12.2309767.full> [Accessed July 31, 2018].
- Asaad, A.T., Rashid, R.D. & Jassim, S.A., 2017. Topological image texture analysis for quality assessment. In S. S. Agaian & S. A. Jassim, eds. *International Society for Optics and Photonics*, p. 102210I. Available at: <http://proceedings.spiedigitallibrary.org/proceeding.aspx?doi=10.1117/12.2268471> [Accessed July 31, 2018].
- Aubert, G. & Kornprobst, P., 2006. *Mathematical problems in image processing: partial differential equations and the calculus of variations*, Springer. Available at: <https://books.google.co.uk/books?hl=en&lr=&id=MACXNookK-VIC&oi=fnd&pg=PR10&dq=Gilles+Aubert+Pierre+Kornprobst+Mathematical+Problems+in+Image+Processing&ots=dq1TOnUG4S&sig=JQLdW2Bx0lIPjB1OFDt4kSmiZl#v=onepage&q=Gilles+Aubert+Pierre+Kornprobst+Mathematical+Problems+in+Image+Processing&f=false>

Reference

- [Accessed April 18, 2018].
- Avidan, S. & Shamir, A., 2007. Seam carving for content-aware image resizing. In *ACM SIGGRAPH 2007 papers on - SIGGRAPH '07*. New York, New York, USA: ACM Press, p. 10. Available at: <http://portal.acm.org/citation.cfm?doid=1275808.1276390> [Accessed March 22, 2018].
- Babacan, S.D., Molina, R. & Katsaggelos, A.K., 2008. Total variation super resolution using a variational approach. In *2008 15th IEEE International Conference on Image Processing*. IEEE, pp. 641–644. Available at: <http://ieeexplore.ieee.org/document/4711836/> [Accessed November 8, 2018].
- Ballester, C. et al., 2001. Filling-in by joint interpolation of vector fields and gray levels. *IEEE Transactions on Image Processing*, 10(8), pp.1200–1211. Available at: <http://ieeexplore.ieee.org/document/935036/> [Accessed February 9, 2018].
- Baochang Zhang et al., 2010. Local Derivative Pattern Versus Local Binary Pattern: Face Recognition With High-Order Local Pattern Descriptor. *IEEE Transactions on Image Processing*, 19(2), pp.533–544. Available at: <http://ieeexplore.ieee.org/document/5308376/> [Accessed October 16, 2018].
- Bendich, P. et al., 2016. Persistent Homology Analysis of Brain Artery Trees. *The annals of applied statistics*, 10(1), pp.198–218. Available at: <http://www.ncbi.nlm.nih.gov/pubmed/27642379> [Accessed July 31, 2018].
- Bertalmio, M. et al., 2000. Image inpainting. In *Proceedings of the 27th annual conference on Computer graphics and interactive techniques - SIGGRAPH '00*. New York, New York, USA: ACM Press, pp. 417–424. Available at: <http://portal.acm.org/citation.cfm?doid=344779.344972> [Accessed February 9, 2018].
- Bertalmio, M. et al., 2003. Simultaneous structure and texture image inpainting. *IEEE Transactions on Image Processing*, 12(8), pp.882–889. Available at: <http://ieeexplore.ieee.org/document/1217265/> [Accessed February 16, 2018].
- Bertalmio, M., 2006. Strong-continuation, contrast-invariant inpainting with a third-order optimal PDE. *IEEE Transactions on Image Processing*, 15(7), pp.1934–1938. Available at: <http://ieeexplore.ieee.org/document/1643700/> [Accessed January 2, 2019].
- Bertozzi, A., Esedolu, S. & Gillette, A., 2007. Analysis of a Two-Scale Cahn–Hilliard Model for Binary Image Inpainting. *Multiscale Modeling & Simulation*, 6(3), pp.913–936. Available at: <http://epubs.siam.org/doi/10.1137/060660631> [Accessed March 30, 2018].
- Bertozzi, A.L. & Bertozzi, A.L., 1998. The Mathematics of Moving Contact Lines in Thin Liquid Films. Available at: <http://citeseerx.ist.psu.edu/viewdoc/summary?doi=10.1.1.130.4774> [Accessed July 16, 2018].
- Bertozzi, A.L., Esedoglu, S. & Gillette, A., 2007. Inpainting of Binary Images Using the Cahn–Hilliard Equation. *IEEE Transactions on Image Processing*, 16(1), pp.285–291. Available at: <http://ieeexplore.ieee.org/document/4032803/> [Accessed April 27, 2018].
- Bertsekas, D.P., 2014. *Constrained optimization and Lagrange multiplier methods*,
- Bhavsar, A. V & Rajagopalan, A.N., 2010. Inpainting Large Missing Regions in Range Images. In *2010 20th International Conference on Pattern Recognition*. IEEE, pp. 3464–3467. Available at: <http://ieeexplore.ieee.org/document/5597544/> [Accessed July 30, 2018].
- Black, M.J. et al., 1998. Robust anisotropic diffusion. *IEEE Transactions on Image Processing*, 7(3), pp.421–432. Available at: <http://ieeexplore.ieee.org/document/661192/> [Accessed February 10, 2018].

Reference

- Burger, M., He, L. & Schönlieb, C.-B., 2009. Cahn–Hilliard Inpainting and a Generalization for Grayvalue Images. *SIAM Journal on Imaging Sciences*, 2(4), pp.1129–1167. Available at: <http://epubs.siam.org/doi/10.1137/080728548> [Accessed March 30, 2018].
- Cahn, J.W. & Hilliard, J.E., 1958. Free Energy of a Nonuniform System. I. Interfacial Free Energy. *The Journal of Chemical Physics*, 28(2), pp.258–267. Available at: <http://aip.scitation.org/doi/10.1063/1.1744102> [Accessed April 18, 2018].
- Carlsson, G., 2009. TOPOLOGY AND DATA. *BULLETIN (New Series) OF THE AMERICAN MATHEMATICAL SOCIETY*, 46(209), pp.255–308. Available at: <http://www.ams.org/journals/bull/2009-46-02/S0273-0979-09-01249-X/S0273-0979-09-01249-X.pdf> [Accessed February 16, 2018].
- Caselles, V., Morel, J.-M. & Sbert, C., 1999. *An Axiomatic Approach to Image Interpolation*, Available at: <http://citeseerx.ist.psu.edu/viewdoc/download?doi=10.1.1.7.5959&rep=rep1&type=pdf> [Accessed September 16, 2018].
- Chambolle, A. & Pock, T., 2010. A first-order primal-dual algorithm for convex problems with applications to imaging. Available at: <https://hal.archives-ouvertes.fr/hal-00490826> [Accessed July 9, 2018].
- Chan, C.-H., 2007. Multi-scale Local Binary Pattern Histograms for Face Recognition Performance evaluation in biometrics View project 3D-aided face analysis View project. Available at: <https://www.researchgate.net/publication/224936218> [Accessed September 4, 2018].
- Chan, T.F. & Shen, J., 2002. Mathematical Models for Local Nontexture Inpaintings. *SIAM Journal on Applied Mathematics*, 62, pp.1019–1043. Available at: <http://www.jstor.org/stable/3061798> [Accessed March 4, 2018].
- Chan, T.F. & Shen, J., 2001. Nontexture Inpainting by Curvature-Driven Diffusions. *Journal of Visual Communication and Image Representation*, 12(4), pp.436–449. Available at: <https://www.sciencedirect.com/science/article/pii/S1047320301904870> [Accessed February 16, 2018].
- Chan, T.F. & Shen, J. (Jackie), 2005. Variational image inpainting. *Communications on Pure and Applied Mathematics*, 58(5), pp.579–619. Available at: <http://doi.wiley.com/10.1002/cpa.20075> [Accessed May 11, 2018].
- Chan, T.F., Shen, J. & Zhou, H.-M., 2006. Total variation wavelet inpainting. *Journal of Mathematical imaging and Vision*, 25.1, pp.107–125. Available at: http://people.math.gatech.edu/~hmzhou/publications/ChShZh06_1.pdf [Accessed February 9, 2018].
- Chandler, D.M., 2013. Seven Challenges in Image Quality Assessment: Past, Present, and Future Research. *ISRN Signal Processing*, pp.1–53. Available at: <http://www.hindawi.com/journals/isrn/2013/905685/>.
- Chang, I.-C., Yu, J.C. & Chang, C.-C., 2013. A forgery detection algorithm for exemplar-based inpainting images using multi-region relation. *Image and Vision Computing*, 31(1), pp.57–71. Available at: <http://linkinghub.elsevier.com/retrieve/pii/S0262885612001722> [Accessed April 4, 2018].
- Charpiat, G. et al., 2010. *Machine Learning Methods for Automatic Image Colorization*, Available at: <http://www.cs.huji.ac.il/> [Accessed November 14, 2018].
- Chen, H., 2006. *Image Reconstruction Based on Combination of Wavelet Decomposition*,

Reference

- Inpainting and Texture Synthesis*, Available at: <https://otik.uk.zcu.cz/bitstream/11025/866/1/Chen.pdf> [Accessed October 23, 2018].
- Chen, P. & Wang, Y., 2009. A New Fourth-order Equation Model for Image Inpainting. In *2009 Sixth International Conference on Fuzzy Systems and Knowledge Discovery*. IEEE, pp. 320–324. Available at: <http://ieeexplore.ieee.org/document/5360606/> [Accessed November 22, 2018].
- Cheng, W.-H. et al., 2005. Robust Algorithm for Exemplar-based Image Inpainting. *Processing of International Conference on Computer Graphics*, pp.64–69. Available at: http://cmlab.csie.org/new_cml_website/media/publications/Cheng-2005-RAE.pdf [Accessed February 16, 2018].
- Cheng, Z., Yang, Q. & Sheng, B., 2015. Deep Colorization. *The IEEE International Conference on Computer Vision (ICCV)*, pp.415–423. Available at: http://openaccess.thecvf.com/content_iccv_2015/papers/Cheng_Deep_Colorization_ICCV_2015_paper.pdf [Accessed March 6, 2018].
- Christoudias, C.M., Georgescu, B. & Meer, P., 2002. Synergism in low level vision. In *Object recognition supported by user interaction for service robots*. IEEE Comput. Soc, pp. 150–155. Available at: <http://ieeexplore.ieee.org/document/1047421/> [Accessed July 30, 2018].
- Cocquerez, J.P., Chanas, L. & Blanc-Talon, J., 2003. Simultaneous Inpainting and Motion Estimation of Highly Degraded Video-Sequences. In Springer, Berlin, Heidelberg, pp. 685–692. Available at: http://link.springer.com/10.1007/3-540-45103-X_91 [Accessed May 11, 2018].
- Criminisi, A., Perez, P. & Toyama, K., 2004. Region Filling and Object Removal by Exemplar-Based Image Inpainting. *IEEE Transactions on Image Processing*, 13(9), pp.1200–1212. Available at: <http://ieeexplore.ieee.org/document/1323101/> [Accessed February 16, 2018].
- D. Mumford, T.S.M.N., 1993. Filtering, Segmentation, and Depth.
- Daubechies, I., 1990. The wavelet transform, time-frequency localization and signal analysis. *IEEE Transactions on Information Theory*, 36(5), pp.961–1005. Available at: <http://ieeexplore.ieee.org/document/57199/> [Accessed June 24, 2018].
- Deng Cai, Xiaofei He, Yuxiao Hu, J.H. and T.H., 2005. Codes and Datasets for Feature Learning. Available at: <http://www.cad.zju.edu.cn/home/dengcai/Data/data.html> [Accessed May 22, 2018].
- Deng, L.-J., Huang, T.-Z. & Zhao, X.-L., 2015. Exemplar-Based Image Inpainting Using a Modified Priority Definition J. Malo, ed. *PLOS ONE*, 10(10), p.e0141199. Available at: <http://dx.plos.org/10.1371/journal.pone.0141199> [Accessed February 16, 2018].
- Desai, M., 2012. Modified Fast and Enhanced Exemplar based Inpainting Algorithm for Solving Unknown Row Filling Problem. *International Journal of Computer Applications*, 56(9), pp.975–8887. Available at: <http://citeseerx.ist.psu.edu/viewdoc/download?doi=10.1.1.244.7695&rep=rep1&type=pdf> [Accessed February 16, 2018].
- Dijkstra, E.W., 1959. A note on two problems in connexion with graphs. *Numerische Mathematik*, 1(1), pp.269–271. Available at: <http://link.springer.com/10.1007/BF01386390> [Accessed February 9, 2018].
- Ding, X. et al., 2012. Colorization Using Quaternion Algebra with Automatic Scribble

Reference

- Generation. In *Proceedings of the 18th international conference on Advances in Multimedia Modeling*. Springer-Verlag, pp. 103–114. Available at: http://link.springer.com/10.1007/978-3-642-27355-1_12 [Accessed January 18, 2018].
- Dong, C. et al., 2015. *Image Super-Resolution Using Deep Convolutional Networks*, Available at: <http://mmlab.ie.cuhk.edu.hk/> [Accessed August 20, 2018].
- Edelsbrunner, H., 2012. PERSISTENT HOMOLOGY: THEORY AND PRACTICE. *Ernest Orlando Lawrence Berkeley National Laboratory, Berkeley, CA*, LBNL-6037E.
- Efros, A.A. & Leung, T.K., 1999. Texture synthesis by non-parametric sampling. In *Proceedings of the Seventh IEEE International Conference on Computer Vision*. IEEE, pp. 1033–1038 vol.2. Available at: <http://ieeexplore.ieee.org/document/790383/> [Accessed February 16, 2018].
- Ekeland, I. (Ivar) & Temam, R., 1976. *Convex analysis and variational problems*, North-Holland Pub. Co.
- Emile-Mâle, G., 1976. The restorer's handbook of easel painting. *Van Nostrand Reinhold*.
- Esedoglu, S. & Shen, J., 2002. DIGITAL INPAINTING BASED ON THE MUMFORD-SHAH-EULER IMAGE MODEL. *European Journal of Applied Mathematics*, 4, pp.353–370. Available at: <https://conservancy.umn.edu/bitstream/handle/11299/3690/1812.pdf?sequence=1&isAllowed=y> [Accessed March 30, 2018].
- Felzenszwalb, P.F. & Huttenlocher, D.P., 2004. Efficient Graph-Based Image Segmentation. *International Journal of Computer Vision*, 59(2), pp.167–181. Available at: [http://fvc2011.ulsan.ac.kr/files/announcement/413/IJCV\(2004\) Efficient Graph-Based Image Segmentation.pdf](http://fvc2011.ulsan.ac.kr/files/announcement/413/IJCV(2004) Efficient Graph-Based Image Segmentation.pdf) [Accessed February 9, 2018].
- Le Floch, H. & Labit, C., 1996. Irregular image sub-sampling and reconstruction by adaptive sampling. In *Proceedings of 3rd IEEE International Conference on Image Processing*. IEEE, pp. 379–382. Available at: <http://ieeexplore.ieee.org/document/560510/> [Accessed September 30, 2018].
- Gabarda, S. & Cristóbal, G., 2007. Blind image quality assessment through anisotropy. *Journal of the Optical Society of America A*, 24(12), p.B42. Available at: <https://www.osapublishing.org/abstract.cfm?URI=josaa-24-12-B42> [Accessed August 8, 2018].
- Gaika, S. et al., 2014. Image Inpainting using Exemplar based, DCT and FMM Algorithm. *International Conference of Advance Research and Innovation*, ISBN, pp.978–993. Available at: <http://www.ijari.org/CurrentIssue/ICARI2014/ICARI-CS-14-02-109.pdf> [Accessed February 16, 2018].
- Ghrist, R., 2008. Barcodes: The persistent topology of data. In *Bulletin of the American Mathematical Society*. pp. 61–75.
- Giansiracusa, N., Giansiracusa, R. & Moon, C., 2017. Persistent homology machine learning for fingerprint classification. Available at: <http://arxiv.org/abs/1711.09158> [Accessed July 31, 2018].
- Gonzalez, R.C. & Woods, R.E. (Richard E., 2008. *Digital image processing*, Prentice Hall. Available at: <https://books.google.co.uk/books?id=8uGONjRGEzoC&q=digital+image+processing+gonzalez+5th+edition+pdf&dq=digital+image+processing+gonzalez+5th+edition+pdf&hl=en&sa=X&ved=0ahUKEwiNzri90s7cAhUkzIUKHUiQDiEQ6AEIKTAA> [Accessed August 2, 2018].
- Guillemot, C. & Le Meur, O., 2014. Image Inpainting : Overview and recent advances. *IEEE*

Reference

Signal Processing Magazine.

- Haar Romeny, B.M., 1994. *Geometry-Driven Diffusion in Computer Vision*, Springer Netherlands.
- Hadamard, J., 2003. *Lectures on Cauchy's problem in linear partial differential equations*, Dover Publications. Available at: https://books.google.co.uk/books?hl=en&lr=&id=9RNeBAAAQBAJ&oi=fnd&pg=PA3&dq=J.+Hadamard.+Lectures+on+Cauchy's+Problem+in+Linear+Partial+Differential+Equations.+Dover,+1953.&ots=Eq9kCbl6eN&sig=BL1hs_ba-2wb2Yy2Yek4BoMoRWA#v=onepage&q&f=false [Accessed April 18, 2018].
- Harris, C. & Stephens, M., 1988. A COMBINED CORNER AND EDGE DETECTOR. *In Alvey vision conference*, 15(50), pp.10–5244. Available at: <http://citeseerx.ist.psu.edu/viewdoc/download?doi=10.1.1.434.4816&rep=rep1&type=pdf> [Accessed March 30, 2018].
- Hesabi, S. & Mahdavi-Amiri, N., 2012. A modified patch propagation-based image inpainting using patch sparsity. *In The 16th CSI International Symposium on Artificial Intelligence and Signal Processing (AISP 2012)*. IEEE, pp. 043–048. Available at: <http://ieeexplore.ieee.org/document/6313715/> [Accessed February 16, 2018].
- Do Hyun Chung & Sapiro, G., 2000. On the level lines and geometry of vector-valued images. *IEEE Signal Processing Letters*, 7(9), pp.241–243. Available at: <http://ieeexplore.ieee.org/document/863143/> [Accessed February 20, 2018].
- Ibraheem, N.A. et al., 2012. ARPN Journal of Science and Technology:: Understanding Color Models: A Review. , 2(3). Available at: <http://www.ejournalofscience.org> [Accessed March 5, 2018].
- Igehy, H. & Pereira, L., 1997. Image replacement through texture synthesis. *In Proceedings of International Conference on Image Processing*. IEEE Comput. Soc, pp. 186–189. Available at: <http://ieeexplore.ieee.org/document/632049/> [Accessed September 30, 2018].
- Itti, L., Koch, C. & Niebur, E., 1998. A model of saliency-based visual attention for rapid scene analysis. *IEEE Transactions on Pattern Analysis and Machine Intelligence*, 20(11), pp.1254–1259. Available at: <http://ieeexplore.ieee.org/document/730558/> [Accessed March 30, 2018].
- Jacob, V.G. & Gupta, S., 2009. Colorization of grayscale images and videos using a semiautomatic approach. *In 2009 16th IEEE International Conference on Image Processing (ICIP)*. IEEE, pp. 1653–1656. Available at: <http://ieeexplore.ieee.org/document/5413392/> [Accessed January 18, 2018].
- Jacobson, A. & Sorkine-Hornung, O., 2012. A Cotangent Laplacian for Images as Surfaces. *Technical report / Department of Computer Science, ETH, Zurich*, 757. Available at: <https://www.research-collection.ethz.ch/handle/20.500.11850/69353> [Accessed February 20, 2018].
- Jassim, S.A. et al., 2018. Topological data analysis to improve exemplar-based inpainting. *In S. S. Agaian & S. A. Jassim, eds. Mobile Multimedia/Image Processing, Security, and Applications 2018*. SPIE, p. 4. Available at: <https://www.spiedigitallibrary.org/conference-proceedings-of-spie/10668/2309931/Topological-data-analysis-to-improve-exemplar-based-inpainting/10.1117/12.2309931.full> [Accessed July 16, 2018].
- Jian Li et al., 2015. Segmentation-Based Image Copy-Move Forgery Detection Scheme. *IEEE Transactions on Information Forensics and Security*, 10(3), pp.507–518. Available at: <http://ieeexplore.ieee.org/document/6987281/> [Accessed September 24, 2018].

Reference

- Jiying Wu & Qiuqi Ruan, 2008. A novel hybrid image inpainting model. In *2008 International Conference on Audio, Language and Image Processing*. IEEE, pp. 138–142. Available at: <http://ieeexplore.ieee.org/document/4589952/> [Accessed February 9, 2018].
- Jung, K.-H., Chang, J.-H. & Lee, C., 1994. Error concealment technique using projection data for block-based image coding. In A. K. Katsaggelos, ed. *International Society for Optics and Photonics*, pp. 1466–1476. Available at: <http://proceedings.spiedigitallibrary.org/proceeding.aspx?articleid=976447> [Accessed September 30, 2018].
- Kelley, C.T., 1999. *Iterative methods for optimization*, SIAM. Available at: https://books.google.co.uk/books?id=C2ePOnDKZKUC&printsec=frontcover&dq=The+method+of+steepest+descent&hl=en&sa=X&ved=0ahUKEwjd2Zq_9JHcAhUCbhQKHUXBOEQ6wEINTAC#v=onepage&q=The+method+of+steepest+descent&f=false [Accessed July 9, 2018].
- Kim, T. & Cai, L., 2015. Context-driven hybrid image inpainting. *IET Image Processing*, 9(10), pp.866–873. Available at: <http://digital-library.theiet.org/content/journals/10.1049/iet-ipr.2015.0184> [Accessed September 30, 2018].
- Kojekine, N., Hagiwara, I. & Savchenko, V., 2003. Software tools using CSRBFs for processing scattered data. *Computers & Graphics*, 27(2), pp.311–319. Available at: <https://www.sciencedirect.com/science/article/pii/S009784930200287X> [Accessed October 23, 2018].
- Kokaram, A.C. et al., 1995a. Detection of missing data in image sequences. *IEEE Transactions on Image Processing*, 4(11), pp.1496–1508. Available at: <http://ieeexplore.ieee.org/document/469931/> [Accessed November 8, 2018].
- Kokaram, A.C. et al., 1995b. Interpolation of missing data in image sequences. *IEEE Transactions on Image Processing*, 4(11), pp.1509–1519. Available at: <http://ieeexplore.ieee.org/document/469932/> [Accessed November 8, 2018].
- Konushin, V. & Vezhnevets, V., 2006. Interactive Image Colorization and Recoloring based on Coupled Map Lattices. In *Graphicon'2006 conference proceedings, Novosibirsk Akademgorodok, Russia,* pp.231–234. Available at: <https://pdfs.semanticscholar.org/74a6/3fca4a70f3c48fa73ef80ed52c4715b7a6c5.pdf> [Accessed February 9, 2018].
- Lagodzinski, P. & Smolka, B., 2014. Application of the Extended Distance Transformation in digital image colorization. *Multimedia Tools and Applications*, 69(1), pp.111–137. Available at: <http://link.springer.com/10.1007/s11042-012-1246-2> [Accessed February 9, 2018].
- Lai, M.-J., Lucier, B. & Wang, J., 2009. The Convergence of a Central - Difference Discretization of Rudin - Osher - Fatemi Model for Image Denoising. *International Conference on Scale Space and Variational Methods in Computer Vision*. Springer, Berlin, Heidelberg, pp.514–526. Available at: https://www.researchgate.net/profile/Bradley_Lucier/publication/221089472_The_Convergence_of_a_Central-Difference_Discretization_of_Rudin-Osher-Fatemi_Model_for_Image_Denoising/links/00463529ce1d90c549000000.pdf [Accessed February 9, 2018].
- Lamar-León, J., García-Reyes, E.B. & Gonzalez-Diaz, R., 2012. Human Gait Identification Using Persistent Homology. In Springer, Berlin, Heidelberg, pp. 244–251. Available at: http://link.springer.com/10.1007/978-3-642-33275-3_30 [Accessed July 31, 2018].

Reference

- Laube, P. et al., 2018. *IMAGE INPAINTING FOR HIGH-RESOLUTION TEXTURES USING CNN TEXTURE SYNTHESIS*, Available at: <https://arxiv.org/pdf/1712.03111.pdf> [Accessed August 20, 2018].
- Levin, A., Lischinski, D. & Weiss, Y., 2004. Colorization using Optimization. *ACM Transactions on Graphics (TOG)*, 23, no. 3, pp.689–694. Available at: <http://webee.technion.ac.il/people/anat.levin/papers/colorization-siggraph04.pdf> [Accessed February 9, 2018].
- Lezoray, O., Ta, V.T. & Elmoataz, A., 2008. Nonlocal graph regularization for image colorization. In *2008 19th International Conference on Pattern Recognition*. IEEE, pp. 1–4. Available at: <http://ieeexplore.ieee.org/document/4761617/> [Accessed February 9, 2018].
- Liang, Z. et al., 2015. An efficient forgery detection algorithm for object removal by exemplar-based image inpainting. *Journal of Visual Communication and Image Representation*, 30(C), pp.75–85. Available at: <https://linkinghub.elsevier.com/retrieve/pii/S1047320315000541> [Accessed September 24, 2018].
- Liu, K., Tan, J. & Su, B., 2014. An Adaptive Image Denoising Model Based on Tikhonov and TV Regularizations. *Advances in Multimedia*, 2014, pp.1–10. Available at: <http://www.hindawi.com/journals/am/2014/934834/> [Accessed October 1, 2018].
- Love, A.E.H. (Augustus E.H., 2013. *A treatise on the mathematical theory of elasticity*, Cambridge University Press. Available at: https://books.google.co.uk/books?hl=en&lr=&id=JFTbrz0Fs5UC&oi=fnd&pg=PA1&dq=A.+E.+H.+Love.+A+Treatise+on+the+Mathematical+Theory+of+Elasticity.+Dover,+New+York,+4th+ed.,+1927&ots=MWRDI5Kpba&sig=2_xYURHiPQkN0oyiiPVL9RMuxDU#v=onepage&q&f=false [Accessed April 18, 2018].
- Luan, Q. et al., 2007. Natural image colorization. *Proceedings of the 18th Eurographics conference on Rendering Techniques*, pp.309–320. Available at: <https://dl.acm.org/citation.cfm?id=2383887> [Accessed February 9, 2018].
- Lum, P.Y. et al., 2013. Extracting insights from the shape of complex data using topology. *Scientific Reports*, 3(1), p.1236.
- Malgouyres, F. & Guichard, F., 2001. Edge Direction Preserving Image Zooming: A Mathematical and Numerical Analysis. *SIAM Journal on Numerical Analysis*, 39(1), pp.1–37. Available at: <http://epubs.siam.org/doi/10.1137/S0036142999362286> [Accessed May 11, 2018].
- Markle, Wilson, and B.H., 1988. Coloring a black and white signal using motion detection. *U.S. Patent, Washington*,, 4,755,870. Available at: <https://patents.google.com/patent/US4755870A/en> [Accessed February 9, 2018].
- Masnou, S. & Morel, J.-M., 1998. Level lines based disocclusion. In *Proceedings 1998 International Conference on Image Processing. ICIP98 (Cat. No.98CB36269)*. IEEE Comput. Soc, pp. 259–263. Available at: <http://ieeexplore.ieee.org/document/999016/> [Accessed September 16, 2018].
- Muhammad, G., Hussain, M. & Bebis, G., 2012. Passive copy move image forgery detection using undecimated dyadic wavelet transform. *Digital Investigation*, 9(1), pp.49–57. Available at: <https://www.sciencedirect.com/science/article/pii/S1742287612000242> [Accessed September 24, 2018].
- Mumford, D., 1994. *Elastica and Computer Vision*. In *Algebraic Geometry and its Applications*. New York, NY: Springer New York, pp. 491–506. Available at:

Reference

- http://link.springer.com/10.1007/978-1-4612-2628-4_31 [Accessed September 16, 2018].
- Neuraltek, 2004. TimeBrush Studios - Colorization, Revival, and Restoration of Black & White Television Shows, Motion Pictures, and Documentary Programs [Programmes]. *Australia*. Available at: <http://www.timebrush.com/blackmagic> [Accessed February 20, 2018].
- Nileshbhai Patel, H., 2016. A Survey on Different techniques for Image Inpainting. *International Research Journal of Engineering and Technology*. Available at: www.irjet.net [Accessed January 28, 2019].
- Nitzberg, M., Mumford, D. & Shiota, T., 1993. *Filtering, Segmentation and Depth*, Berlin, Heidelberg: Springer Berlin Heidelberg. Available at: <http://link.springer.com/10.1007/3-540-56484-5> [Accessed May 11, 2018].
- Ojala, T., Pietika, M. & Ma, T., 2002. *Multiresolution Gray-Scale and Rotation Invariant Texture Classification with Local Binary Patterns*, Available at: http://www.ee.oulu.fi/mvg/files/pdf/pdf_94.pdf [Accessed September 4, 2018].
- Ojala, T., Pietikäinen, M. & Harwood, D., 1996. A comparative study of texture measures with classification based on featured distributions. *Pattern Recognition*, 29(1), pp.51–59. Available at: <https://www.sciencedirect.com/science/article/pii/0031320395000674> [Accessed February 16, 2018].
- Oman, M.E., 1995. *Iterative methods for total variation based image reconstruction*, Available at: <https://scholarworks.montana.edu/xmlui/bitstream/handle/1/7605/31762102581772.pdf?sequence=1> [Accessed October 1, 2018].
- Osher, S. & Sethian, J.A., 1988. Fronts Propagating with Curvature Dependent Speed: Algorithms Based on Hamilton-Jacobi Formulations. *Journal of Computational Physics*, 79, pp.12–49. Available at: <https://math.berkeley.edu/~sethian/Papers/sethian.osher.88.pdf> [Accessed May 2, 2018].
- Pablo Arbelaez, C.F. and D.M., 2007. The Berkeley Segmentation Dataset and Benchmark. *The website of the Berkeley database is*. Available at: <https://www2.eecs.berkeley.edu/Research/Projects/CS/vision/bsds/> [Accessed February 9, 2018].
- Pedersen, M. & Marius, 2012. Image quality metrics for the evaluation of printing workflows. Available at: <https://www.duo.uio.no/handle/10852/9035> [Accessed August 15, 2018].
- Peiying Chen & Yuandi Wang, 2008. Fourth-order partial differential equations for image inpainting. In *2008 International Conference on Audio, Language and Image Processing*. IEEE, pp. 1713–1717. Available at: <http://ieeexplore.ieee.org/document/4590002/> [Accessed February 16, 2018].
- Perona, P. & Malik, J., 1990. Scale-space and edge detection using anisotropic diffusion. *IEEE Transactions on Pattern Analysis and Machine Intelligence*, 12(7), pp.629–639. Available at: <http://ieeexplore.ieee.org/document/56205/> [Accessed April 18, 2018].
- Popowicz, A. & Smolka, B., 2017. Fast image colourisation using the isolines concept. *Multimed Tools Appl*, 76, pp.15987–16009. Available at: <https://link.springer.com/content/pdf/10.1007%2Fs11042-016-3892-2.pdf> [Accessed February 9, 2018].
- Popowicz, A. & Smolka, B., 2014. Isoline Based Image Colorization. *International Conference on Computer Modelling and Simulation 2014 UKSim-AMSS 16th*, pp.280–285. Available at:

Reference

- https://www.researchgate.net/profile/A_Popowicz/publication/271521019_Isoline_Base_d_Image_Colorization/links/554f2fdd08ae93634ec7341d/Isoline-Based-Image-Colorization.pdf [Accessed February 9, 2018].
- Popowicz, A. & Smolka, B., 2015. Overview of Grayscale Image Colorization Techniques. In *Color Image and Video Enhancement*. Cham: Springer International Publishing, pp. 345–370. Available at: http://link.springer.com/10.1007/978-3-319-09363-5_12 [Accessed February 9, 2018].
- Qu, Y. et al., 2006. Manga colorization. In *ACM SIGGRAPH 2006 Papers on - SIGGRAPH '06*. New York, New York, USA: ACM Press, p. 1214. Available at: <http://portal.acm.org/citation.cfm?doid=1179352.1142017> [Accessed February 9, 2018].
- Rane, S.D., Sapiro, G. & Bertalmio, M., 2003. Structure and texture filling-in of missing image blocks in wireless transmission and compression applications. *IEEE Transactions on Image Processing*, 12(3), pp.296–303. Available at: <http://ieeexplore.ieee.org/document/1197835/> [Accessed February 9, 2018].
- Recktenwald, G.W., 2011. *Finite-Difference Approximations to the Heat Equation*, Available at: <http://web.cecs.pdx.edu/~gerry/class/ME448/codes/FDheat.pdf> [Accessed August 6, 2018].
- Reinhard, E. et al., 2001. Color transfer between images. *IEEE Computer Graphics and Applications*, 21(4), pp.34–41. Available at: <http://ieeexplore.ieee.org/document/946629/> [Accessed February 9, 2018].
- Rubinstein, M., Shamir, A. & Avidan, S., 2008. Improved Seam Carving for Video Retargeting. *ACM Trans. Graph. Article*, 27(16). Available at: <http://www.merl.com> [Accessed March 22, 2018].
- Ruderman, D.L., Cronin, T.W. & Chiao, C.-C., 1998. Statistics of cone responses to natural images: implications for visual coding. *OSA A* 15, 8, p.2036–2045. Available at: http://www.theswartzfoundation.org/papers/salk/Ruderman_Cronin_Chiao_JOptSocAm_A_1998.pdf [Accessed February 9, 2018].
- Rudin, L.I., Osher, S. & Fatemi, E., 1992. Nonlinear total variation based noise removal algorithms. *Physica D: Nonlinear Phenomena*, 60(1–4), pp.259–268. Available at: <https://www.sciencedirect.com/science/article/pii/016727899290242F> [Accessed February 9, 2018].
- Russo, F., 2014. Performance Evaluation of Noise Reduction Filters for Color Images through Normalized Color Difference (NCD) Decomposition. *ISRN Machine Vision*, 2014, pp.1–11. Available at: <https://www.hindawi.com/archive/2014/579658/> [Accessed January 18, 2018].
- Saha, S. & Vemuri, R., 2000. An analysis on the effect of image activity on lossy coding performance. In *2000 IEEE International Symposium on Circuits and Systems. Emerging Technologies for the 21st Century. Proceedings (IEEE Cat No.00CH36353)*. Presses Polytech. Univ. Romandes, pp. 295–298. Available at: <http://ieeexplore.ieee.org/document/856055/> [Accessed August 17, 2018].
- Sangeeth, K., Sengottuvelan, P. & Balamurugan, E., 2011. A Novel Exemplar based Image Inpainting Algorithm for Natural Scene Image Completion with Improved Patch Prioritizing. *International Journal of Computer Applications*, 36(4), pp.0975-8887. Available at: https://www.researchgate.net/profile/Sangeetha_K2/publication/258045401_A_Novel_Exemplar_based_Image_Inpainting_Algorithm_for_Natural_Scene_Image_Completion_w

Reference

- ith_Improved_Patch_Prioritizing/links/0deec526b84aec072e000000/A-Novel-Exemplar-based-Image-Inpai [Accessed February 16, 2018].
- Sangeetha, K., Sengottuvelan, P. & Balamurugan, E., 2011. Combined Structure and Texture Image Inpainting Algorithm for Natural Scene Image Completion. *Journal of Information Engineering and Applications*, 1(1). Available at: www.iiste.org [Accessed July 12, 2018].
- Sapiro, G., 2005. Inpainting the colors. In *IEEE International Conference on Image Processing 2005*. IEEE, p. II-698. Available at: <http://ieeexplore.ieee.org/document/1530151/> [Accessed January 18, 2018].
- Sc, C.-B., And, O. & Bertozzi, A., 2011. UNCONDITIONALLY STABLE SCHEMES FOR HIGHER ORDER INPAINTING *. , 9(2), pp.413–457. Available at: https://www.intlpress.com/site/pub/files/_fulltext/journals/cms/2011/0009/0002/CMS-2011-0009-0002-a004.pdf [Accessed March 30, 2018].
- Schonlieb, C.-B., 2015. *Partial Differential Equation Methods for Image Inpainting*, Cambridge: Cambridge University Press. Available at: <http://ebooks.cambridge.org/ref/id/CBO9780511734304> [Accessed July 9, 2018].
- Schönlieb, C.-B. et al., 2010. Image Inpainting Using a Fourth-Order Total Variation Flow. *SAMPTA'09*, p.Special session on sampling and (in)painting. Available at: <https://hal.archives-ouvertes.fr/hal-00452296/> [Accessed February 16, 2018].
- Schönlieb, C.-B., 2009. Modern PDE Techniques for Image Inpainting. Available at: http://www.damtp.cam.ac.uk/user/cbs31/Publications_files/thesis.pdf [Accessed July 9, 2018].
- Shah, A.A., Gandhi, M. & Shah, K.M., 2013. Medical Image Colorization using Optimization Technique. *International Journal of Scientific and Research Publications*, 3(1), pp.2250–3153. Available at: www.ijsrp.org [Accessed January 18, 2018].
- Sharma, N. & Mehta, N., 2013. Region Filling and Object Removal by Exempeler Based Image Inpainting. *International Journal of Inventive Engineering and Sciences*, (13), pp.2319–9598. Available at: <http://citeseerx.ist.psu.edu/viewdoc/download?doi=10.1.1.684.5847&rep=rep1&type=pdf> [Accessed March 4, 2018].
- Shen, J. & Chan, T.F., 2002. Mathematical Models for Local Nontexture Inpaintings. *SIAM Journal on Applied Mathematics*, 62(3), pp.1019–1043. Available at: <http://epubs.siam.org/doi/10.1137/S0036139900368844> [Accessed February 16, 2018].
- Shi, Y. et al., 2009. Structure and Hue Similarity for Color Image Quality Assessment. In *2009 International Conference on Electronic Computer Technology*. IEEE, pp. 329–333. Available at: <http://ieeexplore.ieee.org/document/4795977/> [Accessed August 14, 2018].
- Smith, G.D. (Gordon D., 1985. *Numerical solution of partial differential equations : finite difference methods*, Clarendon Press. Available at: <https://global.oup.com/academic/product/numerical-solution-of-partial-differential-equations-9780198596509?cc=gb&lang=en> [Accessed July 9, 2018].
- Strobel, H., 1989. Strang, G., Introduction to Applied Mathematics. Wellesley, Mass. Wellesley-Cambridge Press 1986. IX, 758 pp. ISBN 0-9614088-0-4. *ZAMM - Journal of Applied Mathematics and Mechanics / Zeitschrift für Angewandte Mathematik und Mechanik*, 69(9), pp.311–312. Available at: <http://doi.wiley.com/10.1002/zamm.19890690917> [Accessed July 16, 2018].
- Sukho Lee et al., 2013. Colorization-Based Compression Using Optimization. *IEEE Transactions*

Reference

- on *Image Processing*, 22(7), pp.2627–2636. Available at: <http://ieeexplore.ieee.org/document/6482621/> [Accessed February 10, 2018].
- Suthar, R. et al., 2014. *A Survey on Various Image Inpainting Techniques to Restore Image*, Available at: www.ijera.com [Accessed January 28, 2019].
- T. Chan and J. Shen, 2001. Non-Texture Inpainting by Curvature-Driven Diffusions (CCD). *Journal of Visual Communication and Image Representation*, 12(4), pp.436–449. Available at: <https://conservancy.umn.edu/bitstream/handle/11299/3528/1743.pdf?sequence=1> [Accessed March 4, 2018].
- T.F. Chan, S.H. Kang, and J.S., 2002. Euler’s elastica and curvature-based inpainting. *SIAM J. Appl. Math.*, 63, pp.564–592.
- Takamichi Miyata et al., 2009. Novel inverse colorization for image compression. In *2009 Picture Coding Symposium*. IEEE, pp. 1–4. Available at: <http://ieeexplore.ieee.org/document/5167413/> [Accessed February 10, 2018].
- Tang, K.-T., 2007. Calculus of Variation. In *Mathematical Methods for Engineers and Scientists 3*. Berlin, Heidelberg: Springer Berlin Heidelberg, pp. 367–429. Available at: http://link.springer.com/10.1007/978-3-540-44697-2_7 [Accessed April 8, 2018].
- Tavakoli, A., Mousavi, P. & Zarmehi, F., 2018. Modified algorithms for image inpainting in Fourier transform domain. *Computational and Applied Mathematics*, 37(4), pp.5239–5252. Available at: <http://link.springer.com/10.1007/s40314-018-0632-4> [Accessed November 20, 2018].
- Telea, A., 2018. University of Groningen An Image Inpainting Technique Based on the Fast Marching Method An Image Inpainting Technique Based on the Fast Marching Method. Available at: <https://core.ac.uk/download/pdf/148284148.pdf> [Accessed July 12, 2018].
- Tikhonov, A.N., 2014. *Nonlinear Ill-posed Problems*, Springer Verlag.
- Torres-Méndez, L.A. & Dudek, G., 2008. Inter-Image Statistics for 3D Environment Modeling. *International Journal of Computer Vision*, 79(2), pp.137–158. Available at: <http://link.springer.com/10.1007/s11263-007-0108-2> [Accessed July 30, 2018].
- Tsai, A., Yezzi, A. & Willsky, A.S., 2001. Curve Evolution Implementation of the Mumford–Shah Functional for Image Segmentation, Denoising, Interpolation, and Magnification. *IEEE TRANSACTIONS ON IMAGE PROCESSING*, 10(8), pp.1169–1186. Available at: <https://pdfs.semanticscholar.org/035c/3e0009b5623505af55bc68129e1343b31f9b.pdf> [Accessed April 18, 2018].
- Vadhel, B. & Limbasiya, B., 2016. Survey on Different Techniques for Image Inpainting. *International Research Journal of Engineering and Technology*. Available at: www.irjet.net [Accessed January 28, 2019].
- Varga, D. & Szirányi, T., 2017. Convolutional Neural Networks for automatic image colorization. , pp.1–15. Available at: http://eprints.sztaki.hu/9292/1/Varga_1_3306455_ny.pdf [Accessed February 9, 2018].
- Vedaldi, M.C. and S.M. and I.K. and S.M. and and A., 2014. Describable Textures Dataset. Available at: <https://www.robots.ox.ac.uk/~vgg/data/dtd/index.html> [Accessed February 16, 2018].
- Veeravasarapu, V.S.R. & Sivaswamy, J., 2012. Fast and fully automated video colorization. In *2012 International Conference on Signal Processing and Communications (SPCOM)*. IEEE, pp. 1–5. Available at: <http://ieeexplore.ieee.org/document/6290028/> [Accessed February

Reference

- 9, 2018].
- Vese, L.A. & Osher, S.J., 2003. Modeling Textures with Total Variation Minimization and Oscillating Patterns in Image Processing. *Journal of Scientific Computing*, 19(1/3), pp.553–572. Available at: <http://link.springer.com/10.1023/A:1025384832106> [Accessed February 16, 2018].
- W. Rudin, 1976. PRINCIPLES OF MATHEMATICAL ANALYSIS. , Third edit. Available at: https://merounak.files.wordpress.com/2016/02/walter_rudin_principles_of_mathematical_analysisbookfi.pdf [Accessed July 9, 2018].
- Walden, S., 1985. The ravished image.
- Wang, Z. et al., 2004. Image Quality Assessment: From Error Visibility to Structural Similarity. *IEEE Transactions on Image Processing*, 13(4), pp.600–612. Available at: <http://ieeexplore.ieee.org/document/1284395/> [Accessed February 10, 2018].
- Wang, Z. & Bovik, A.C., 2006. Modern Image Quality Assessment. *Synthesis Lectures on Image, Video, and Multimedia Processing*, 2(1), pp.1–156. Available at: <http://www.morganclaypool.com/doi/abs/10.2200/S00010ED1V01Y200508IVM003> [Accessed August 15, 2018].
- Waykule, M. & Patil, M., 2012. Region Filling and Object Removal by Exemplar- Based Image Inpainting. *International Journal of Scientific & Engineering Research*, 3(1), pp.2229–5518. Available at: <http://www.ijser.org> [Accessed February 16, 2018].
- Wei Guo & Li-Hong Qiao, 2007. Inpainting based on total variation. In *2007 International Conference on Wavelet Analysis and Pattern Recognition*. IEEE, pp. 939–943. Available at: <http://ieeexplore.ieee.org/document/4420804/> [Accessed February 16, 2018].
- Wei, L.-Y. & Levoy, M., 2000. Fast Texture Synthesis using Tree-structured Vector Quantization. *In Proceedings of the 27th annual conference on Computer graphics and interactive techniques,, ACM Press*, pp.479–488. Available at: <http://graphics.stanford.edu/projects/texture/> [Accessed July 12, 2018].
- Weickert, J., 1996. *THEORETICAL FOUNDATIONS OF ANISOTROPIC DIFFUSION IN IMAGE PROCESSING*, Available at: <https://pdfs.semanticscholar.org/60b1/f3d452696feafd0fe54621ff015e688adcd2.pdf> [Accessed September 4, 2018].
- Weickert, J. & Stuttgart, B.G.T., 1998. *Anisotropic Diffusion in Image Processing*, Available at: http://www.lpi.tel.uva.es/muitic/pim/docus/anisotropic_diffusion.pdf [Accessed September 4, 2018].
- Winkler, S. & Mohandas, P., 2008. The Evolution of Video Quality Measurement: From PSNR to Hybrid Metrics. *IEEE Transactions on Broadcasting*, 54(3), pp.660–668. Available at: <http://ieeexplore.ieee.org/document/4550731/> [Accessed May 22, 2018].
- Xiang, Y., Zou, B. & Li, H., 2009. Selective color transfer with multi-source images. *Pattern Recognition Letters*, 30(7), pp.682–689. Available at: <https://www.sciencedirect.com/science/article/pii/S0167865509000191> [Accessed February 9, 2018].
- Xu, Z., Lian, X. & Feng, L., 2008. Image Inpainting Algorithm Based on Partial Differential Equation. In *2008 ISECS International Colloquium on Computing, Communication, Control, and Management*. IEEE, pp. 120–124. Available at: <http://ieeexplore.ieee.org/document/4609482/> [Accessed February 16, 2018].
- Yang, G. et al., 2017. A robust forgery detection algorithm for object removal by exemplar-

Reference

- based image inpainting. Available at: <https://www.researchgate.net/publication/317300165> [Accessed September 24, 2018].
- Yao_Wang, Jörn. Ostermann, Y.-Q.Z., 2001. Video Processing and Communications (Prentice-Hall Signal Processing Series). , pp.1–32.
- Yao Wang & Qin-Fan Zhu, 1998. Error control and concealment for video communication: a review. *Proceedings of the IEEE*, 86(5), pp.974–997. Available at: <http://ieeexplore.ieee.org/document/664283/> [Accessed May 11, 2018].
- Yatziv, L. & Sapiro, G., 2006. Fast image and video colorization using chrominance blending Chrominance Blending. *IEEE transactions on image processing*, 15, no. 5, pp.1120–1129. Available at: <http://www.ima.umn.edu> [Accessed February 9, 2018].
- Ye, J. & Shi, Y.-Q., 2017. A Hybrid Feature Model for Seam Carving Detection. In *International Workshop on Digital Watermarking*. Springer, Cham, pp. 77–89. Available at: http://link.springer.com/10.1007/978-3-319-64185-0_7 [Accessed March 22, 2018].
- You, Y.-L. & Kaveh, M., 2000. Fourth-order partial differential equations for noise removal. *IEEE Transactions on Image Processing*, 9(10), pp.1723–1730. Available at: <http://ieeexplore.ieee.org/document/869184/> [Accessed July 12, 2018].
- Zhang, R., Isola, P. & Efros, A.A., 2016. Colorful Image Colorization. In Springer, Cham, pp. 649–666. Available at: http://link.springer.com/10.1007/978-3-319-46487-9_40 [Accessed October 16, 2018].
- Zhang, Z. et al., 2009. A Colorization Method Based on Fuzzy Clustering and Distance Transformation. In *2009 2nd International Congress on Image and Signal Processing*. IEEE, pp. 1–5. Available at: <http://ieeexplore.ieee.org/document/5304487/> [Accessed February 9, 2018].
- Zhao, Y. et al., 2007. Colorizing Biomedical Images Based on Color Transfer. In *2007 IEEE/ICME International Conference on Complex Medical Engineering*. IEEE, pp. 820–823. Available at: <http://ieeexplore.ieee.org/document/4381855/> [Accessed February 9, 2018].
- Zhen, Z., Yan, G. & Lizhuang, M., 2012. An automatic image and video colorization algorithm based on pattern continuity. In *2012 International Conference on Audio, Language and Image Processing*. IEEE, pp. 531–536. Available at: <http://ieeexplore.ieee.org/document/6376674/> [Accessed November 14, 2018].
- Zhu, J.-Y. et al., 2016. Generative Visual Manipulation on the Natural Image Manifold. In *European Conference on Computer Vision, Springer, Cham*, pp.597–613. Available at: <https://arxiv.org/pdf/1609.03552.pdf> [Accessed March 22, 2018].
- Zongben Xu & Jian Sun, 2010. Image Inpainting by Patch Propagation Using Patch Sparsity. *IEEE Transactions on Image Processing*, 19(5), pp.1153–1165. Available at: <http://ieeexplore.ieee.org/document/5404308/> [Accessed February 16, 2018].

APPENDICES

A. Evaluation of performance of PDE algorithms

Experiment 1: Evaluation of performance of PDE algorithms using the TDA approach in the inpainted regions of natural images in ten inpainting domains in both spatial and frequency domains at threshold $T=10$, these algorithms described in chapter Chapter 4.

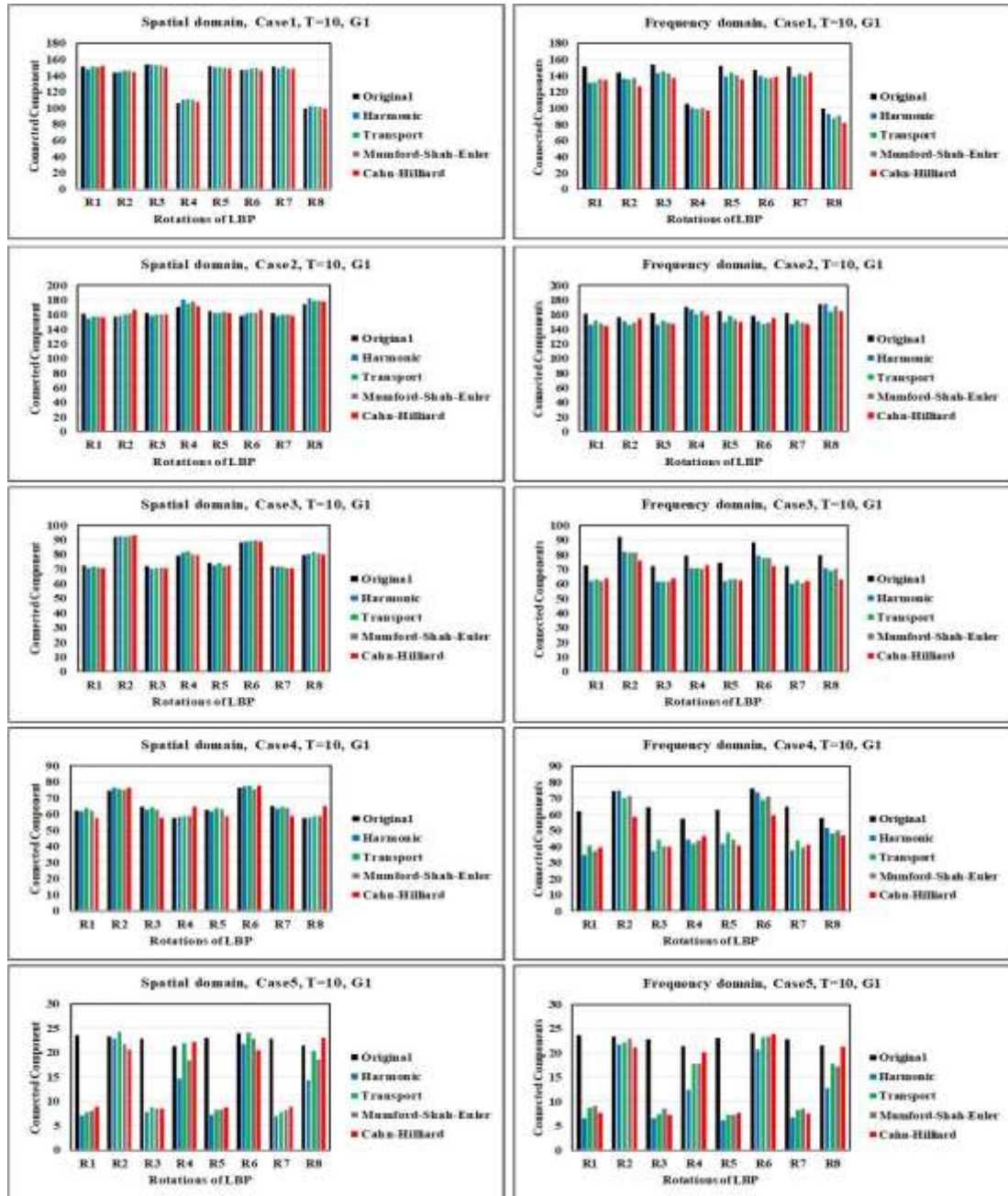


Figure A-1: Evaluation of performance of PDE algorithms using TDA approach at 8 iterations in G1 at threshold $T=10$ for 5 inpainting cases of natural images. Left column: Average of the number of CCs inpainted regions in the spatial domain Right column: Average of the number of CCs inpainted regions in the frequency domain.

Appendix

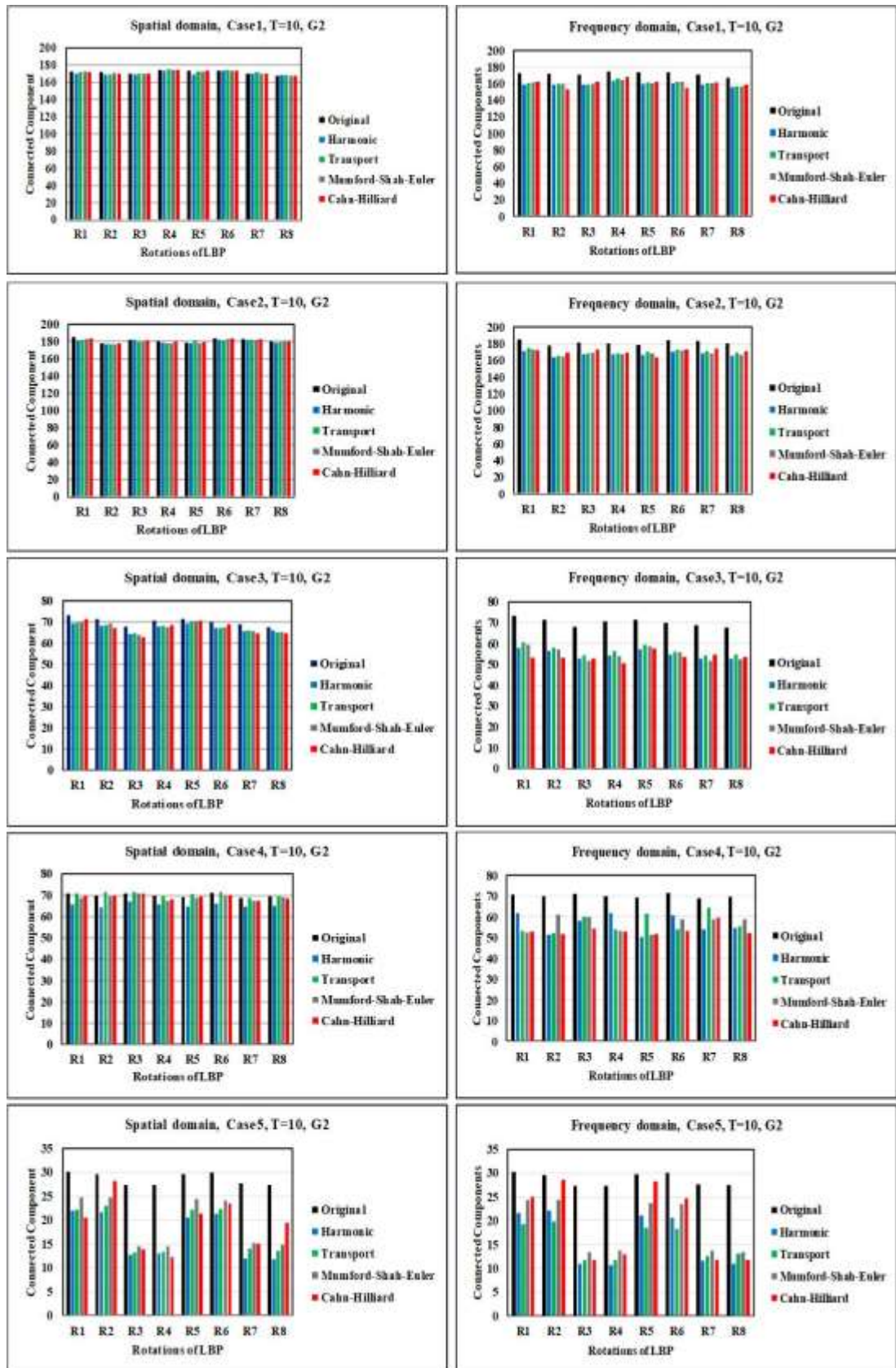


Figure A-2: Evaluation of performance of PDE algorithms using TDA approach at 8 iterations in G2 at threshold $T=10$ for 5 inpainting cases of natural images. Left column: Average of the number of CCs inpainted regions in the spatial domain Right column: Average of the number of CCs inpainted regions in the frequency domain.

Appendix

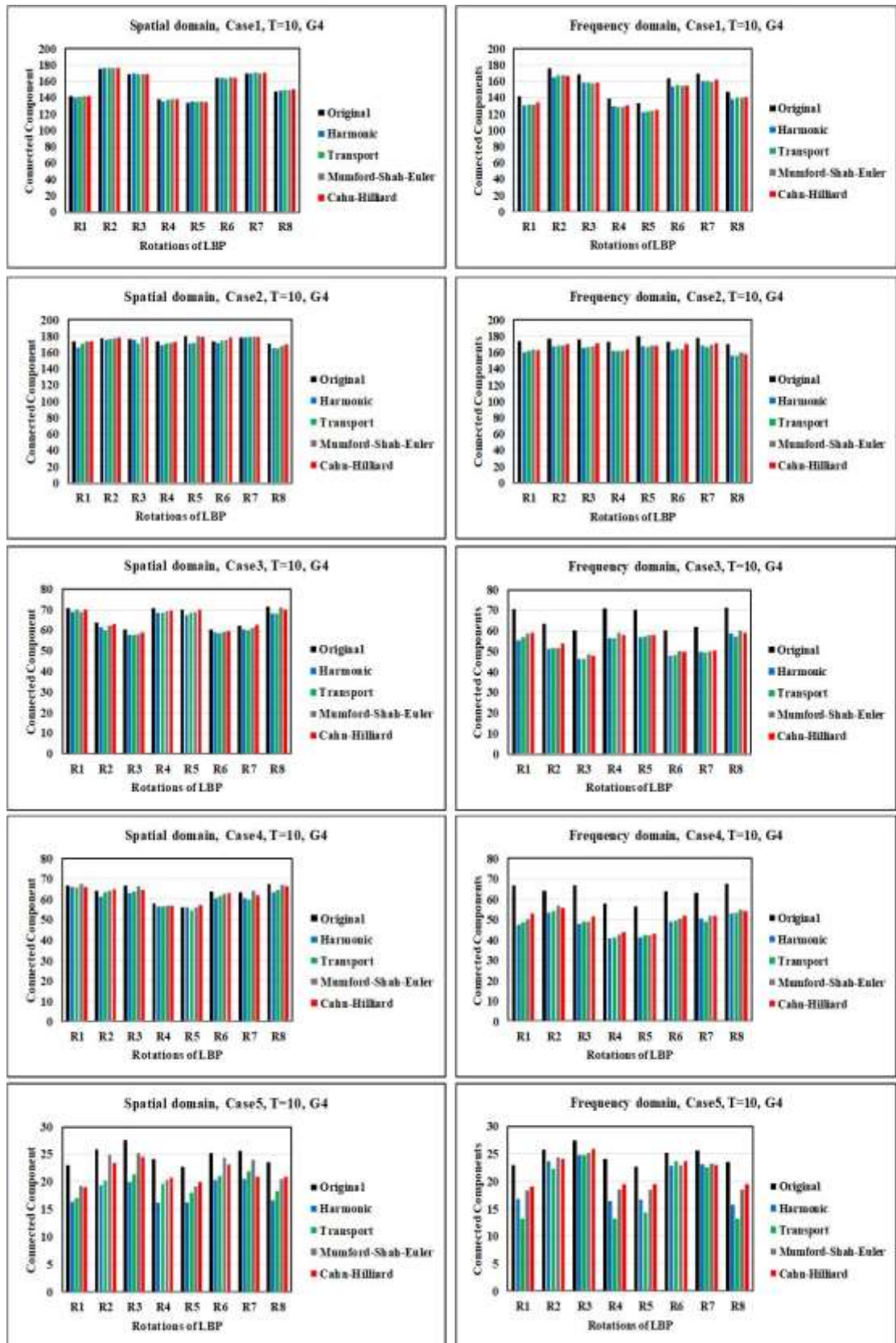


Figure A-3: Evaluation of performance of PDE algorithms using TDA approach at 8 iterations in G4 at threshold $T=10$ for 5 inpainting cases of natural images. Left column: Average of the number of CCs inpainted regions in the spatial domain Right column: Average of the number of CCs inpainted regions in the frequency domain.

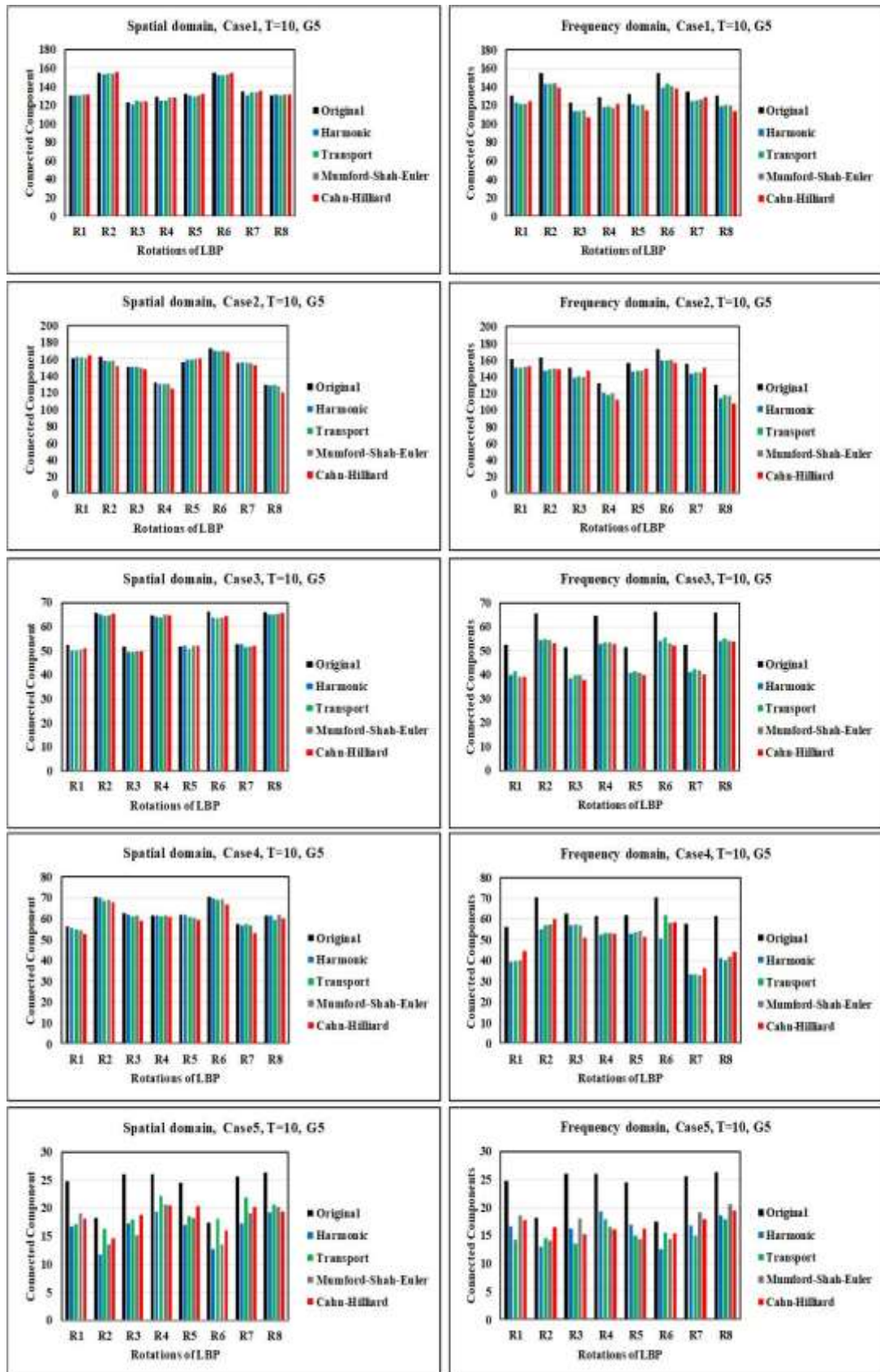


Figure A-4: Evaluation of performance of PDE algorithms using TDA approach at 8 iterations in G5 at threshold $T=10$ for 5 inpainting cases of natural images. Left column: Average of the number of CCs inpainted regions in the spatial domain Right column: Average of the number of CCs inpainted regions in the frequency domain.

Appendix

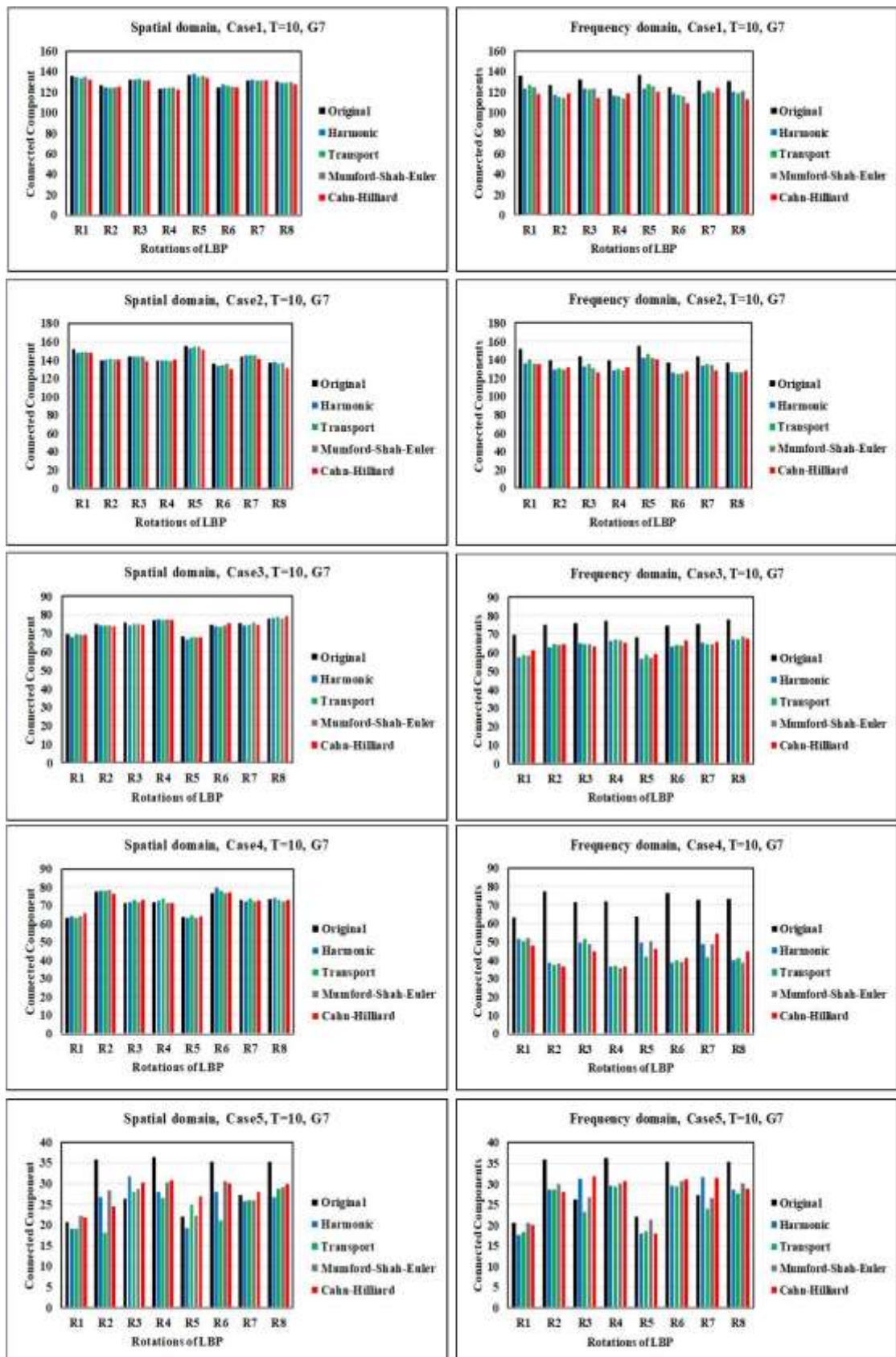


Figure A-5: Evaluation of performance of PDE algorithms using TDA approach at 8 iterations in G7 at threshold $T=10$ for 5 inpainting cases of natural images. Left column: Average of the number of CCs components inpainted regions in the spatial domain Right column: Average of the number of CCs inpainted regions in the frequency domain.

Appendix

Experiment 2: Evaluation of performance of PDE algorithms using the TDA approach in the inpainted regions of face images in ten inpainting domains in both spatial and frequency domains at threshold $T=10$, these algorithms described in chapter 4.

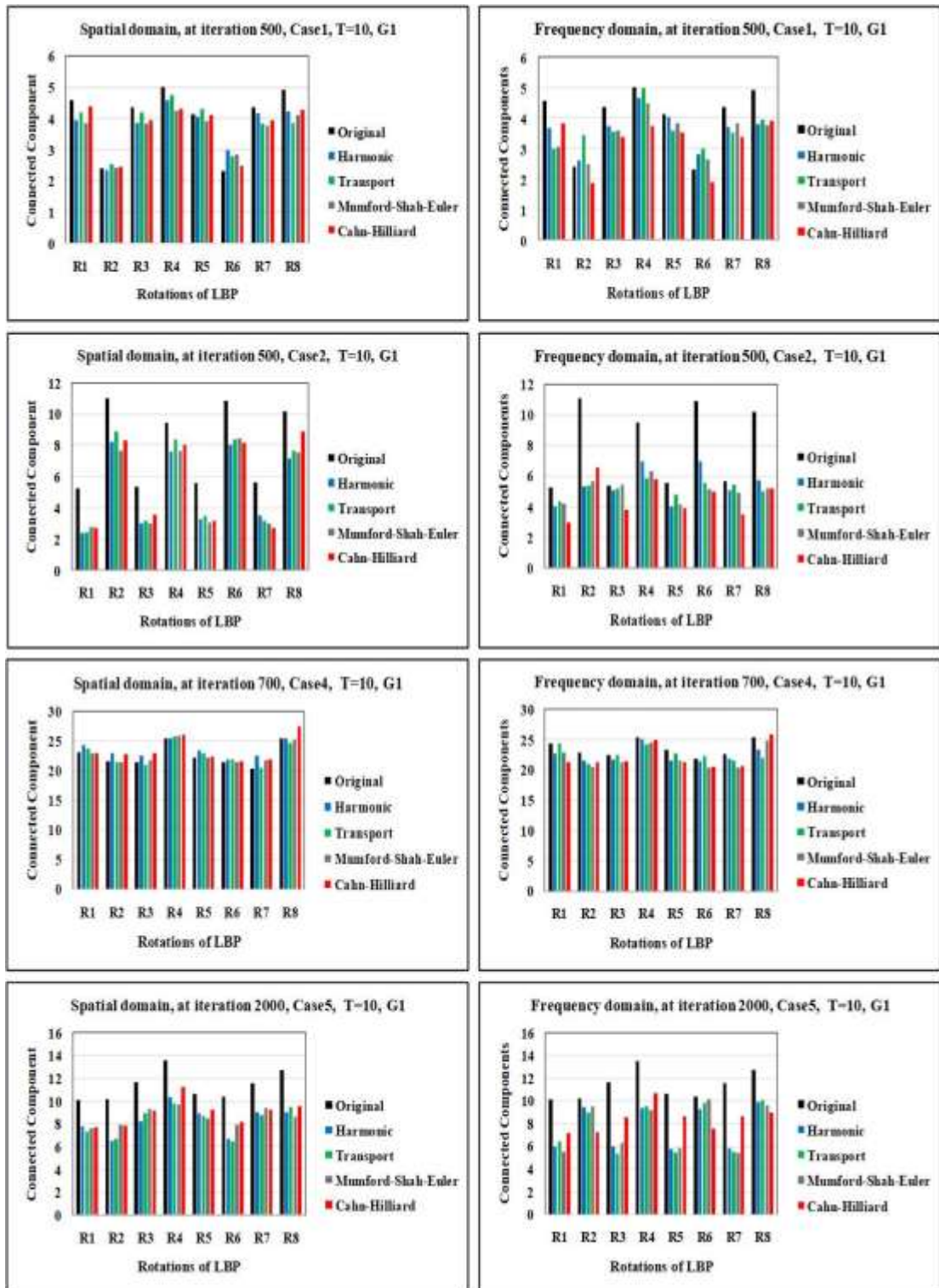


Figure A-6: Evaluation of performance of PDE algorithms using TDA approach at 8 iterations in G1 at threshold $T=10$ for 5 inpainting cases of face images. Left column: Average of the number of CCs inpainted regions in the spatial domain Right column: Average of the number of CCs inpainted regions in the frequency domain.

Appendix

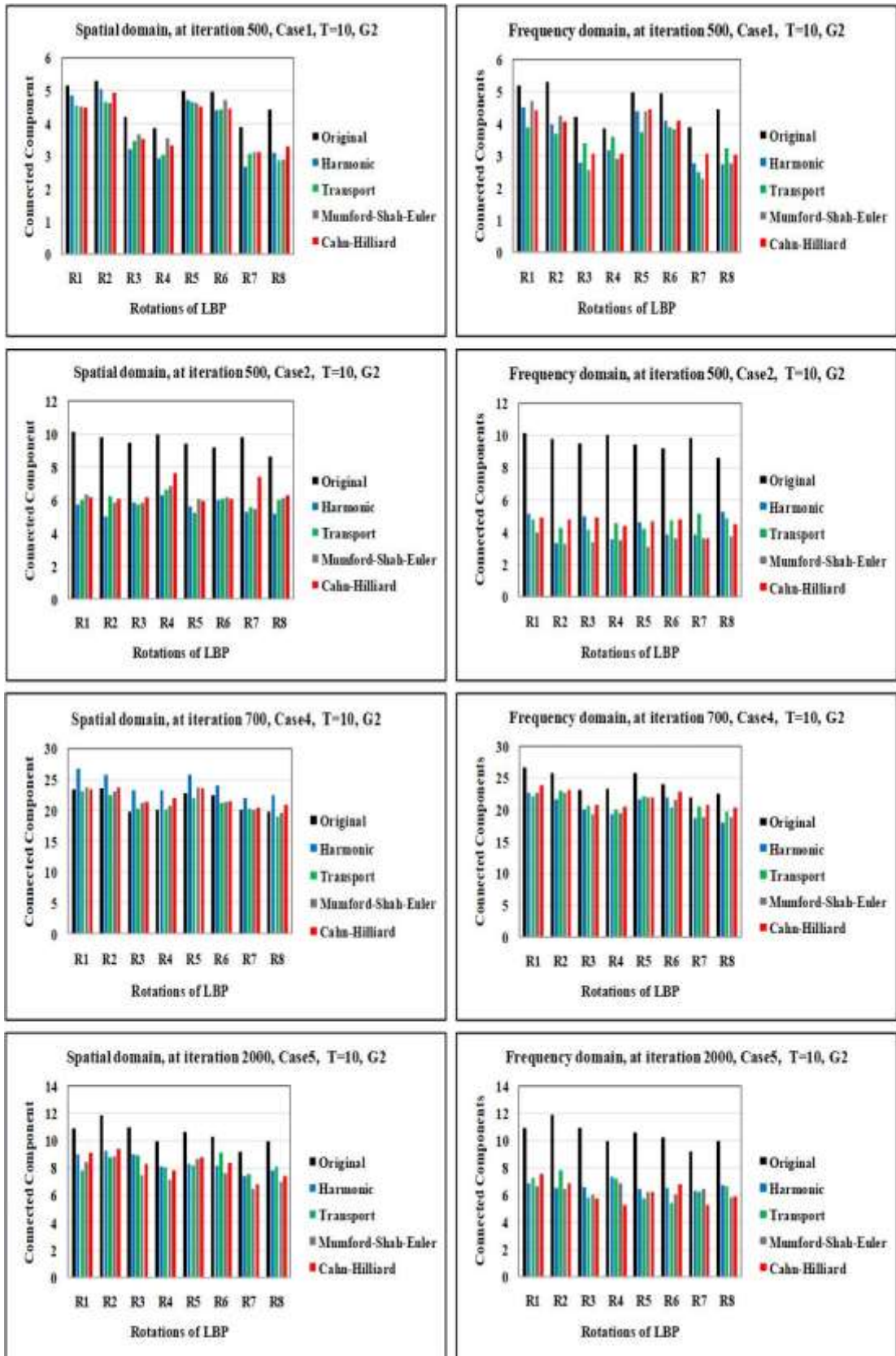


Figure A-7: Evaluation of performance of PDE algorithms using TDA approach at 8 iterations in G2 at threshold $T=10$ for 5 inpainting cases of face images. Left column: Average of the number of CCs inpainted regions in the spatial domain Right column: Average of the number of CCs inpainted regions in the frequency domain.

Appendix

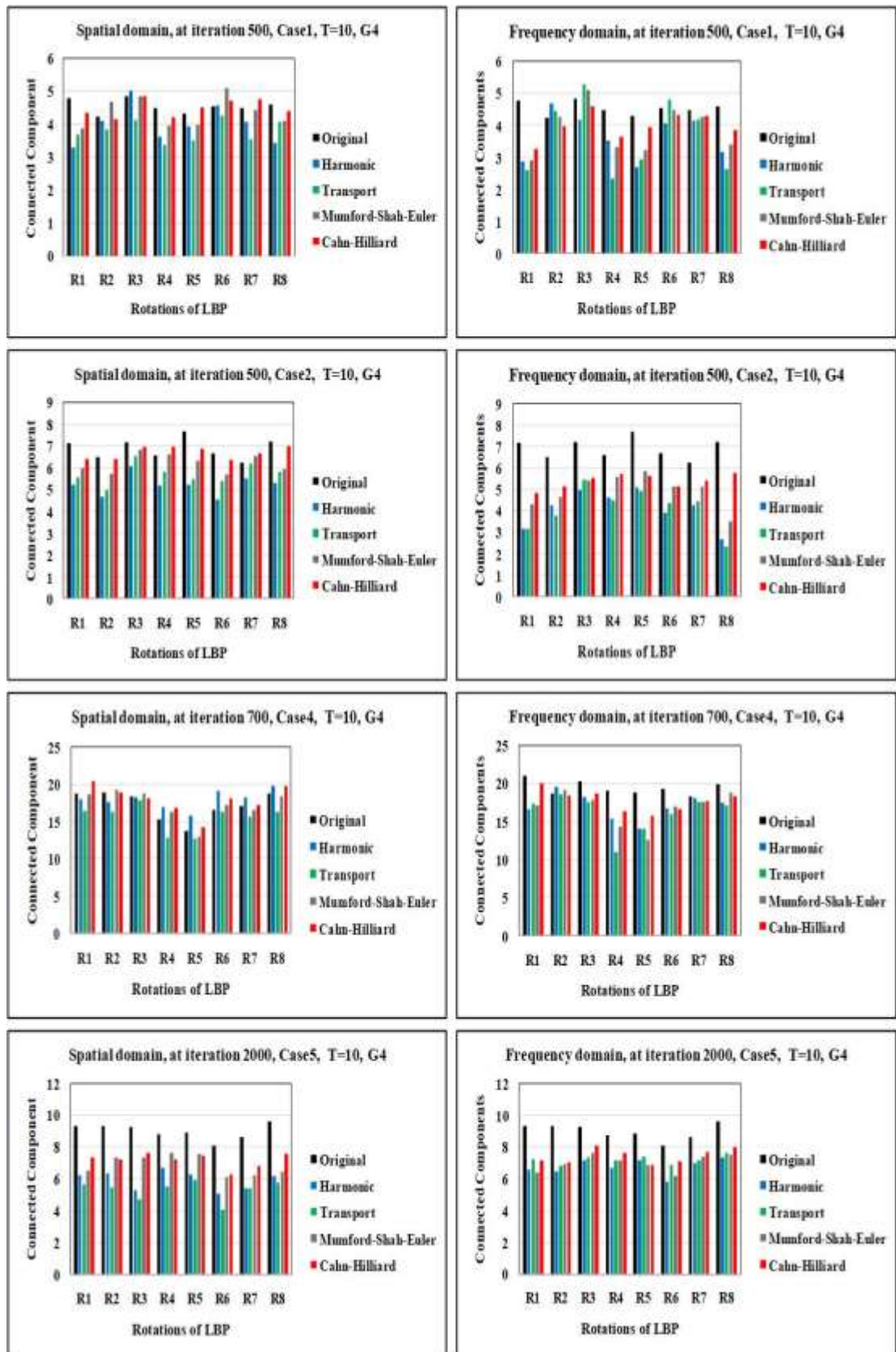


Figure A-8: Evaluation of performance of PDE algorithms using TDA approach at 8 iterations in G4 at threshold $T=10$ for 5 inpainting cases of face images. Left column: Average of the number of CCs inpainted regions in the spatial domain Right column: Average of the number of CCs inpainted regions in the frequency domain.

Appendix

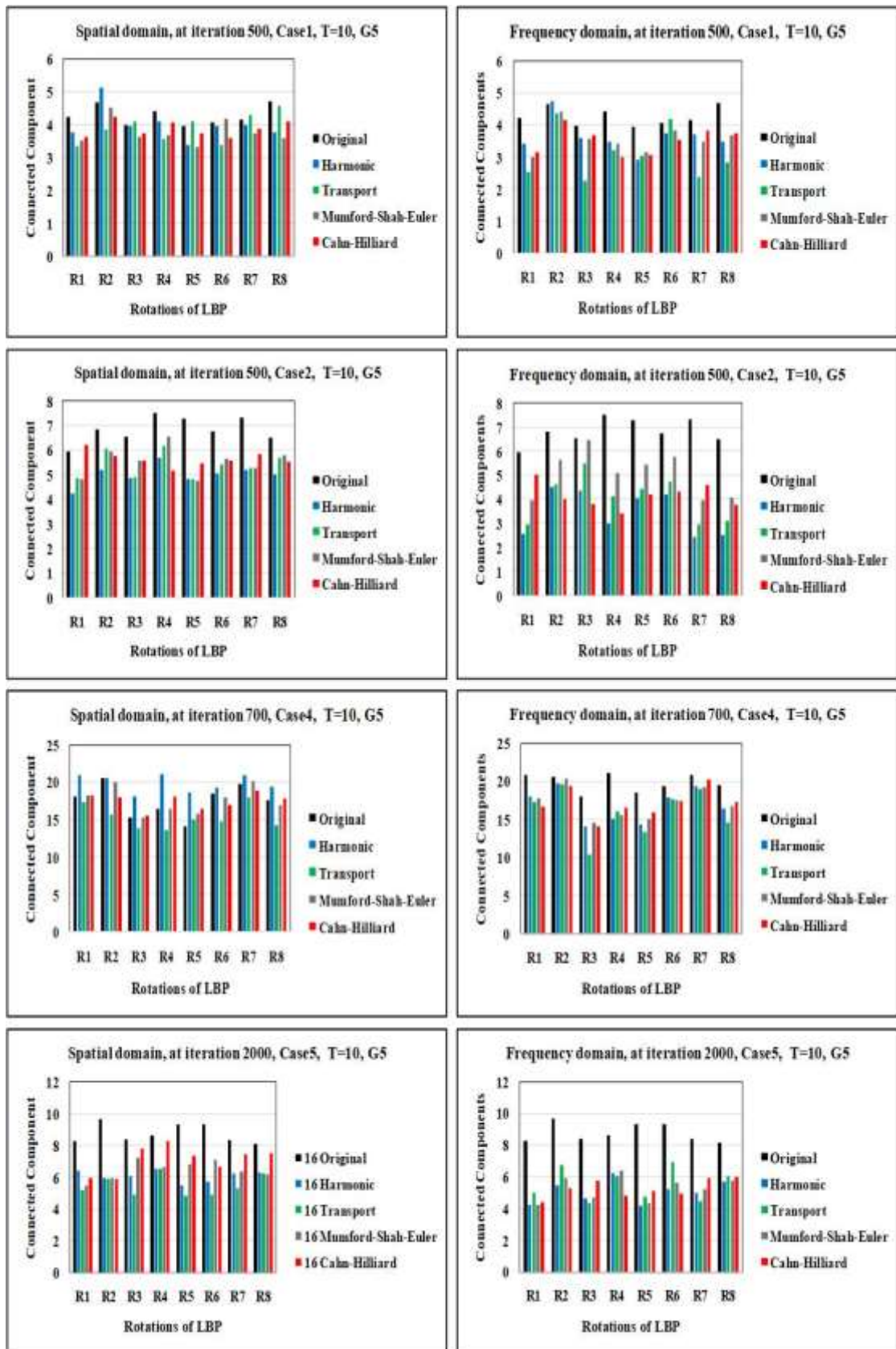


Figure A-9: Evaluation of performance of PDE algorithms using TDA approach at 8 iterations in G5 at threshold $T=10$ for 5 inpainting cases of face images. Left column: Average of the number of CCs inpainted regions in the spatial domain Right column: Average of the number of CCs inpainted regions in the frequency domain.

Appendix

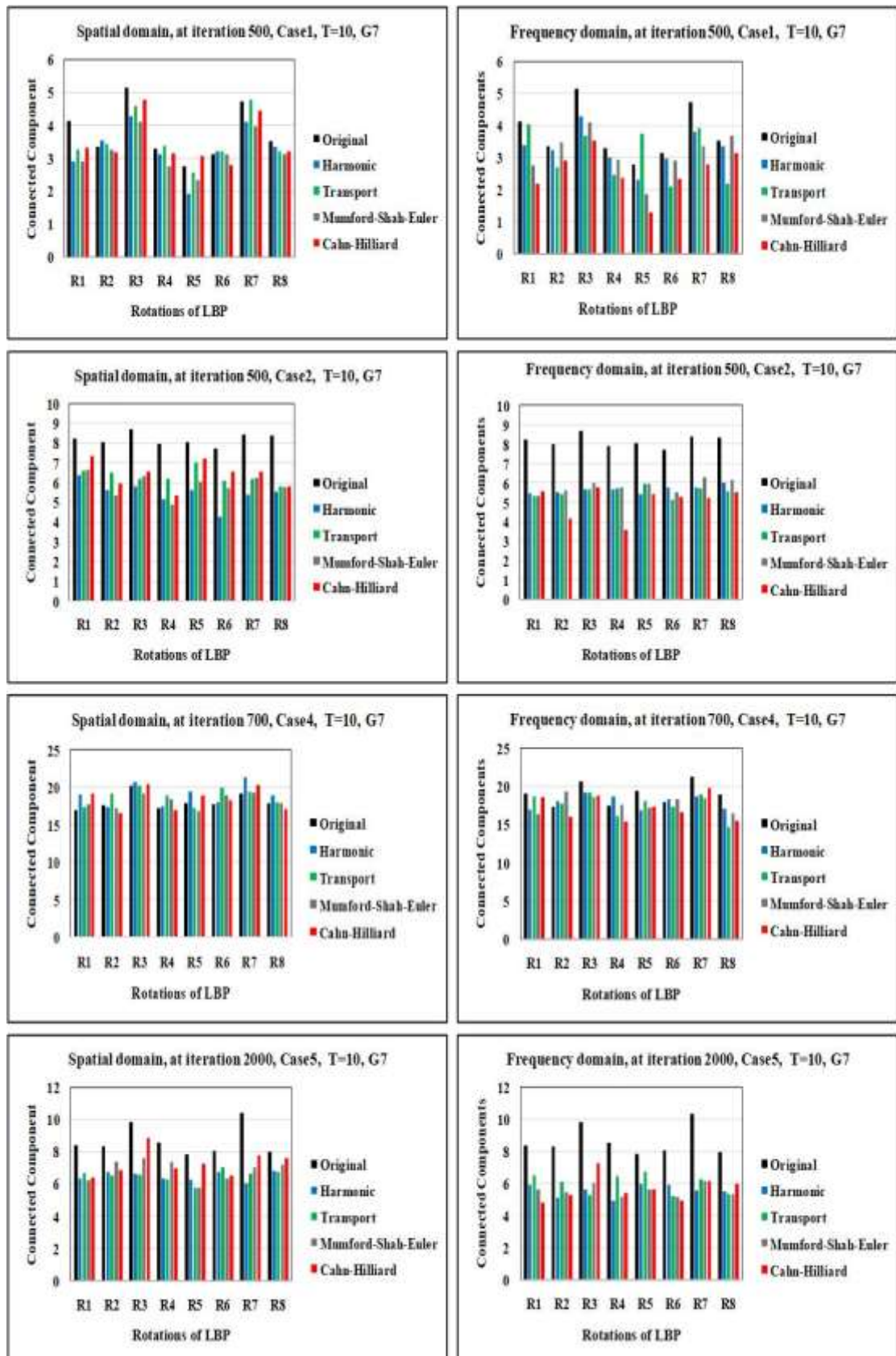


Figure A-10: Evaluation of performance of PDE algorithms using TDA approach at 8 iterations in G7 at threshold T=10 for 5 inpainting cases of face images. Left column: Average of the number of CCs inpainted regions in the spatial domain Right column: Average of the number of CCs inpainted regions in the frequency domain.

B. Evaluation of performance of EBI methods

Evaluation of performance of EBI methods using the TDA approach in the inpainted regions of high and low-information natural images in five inpainting domains at threshold $T=15$, these algorithms described in chapter 5.

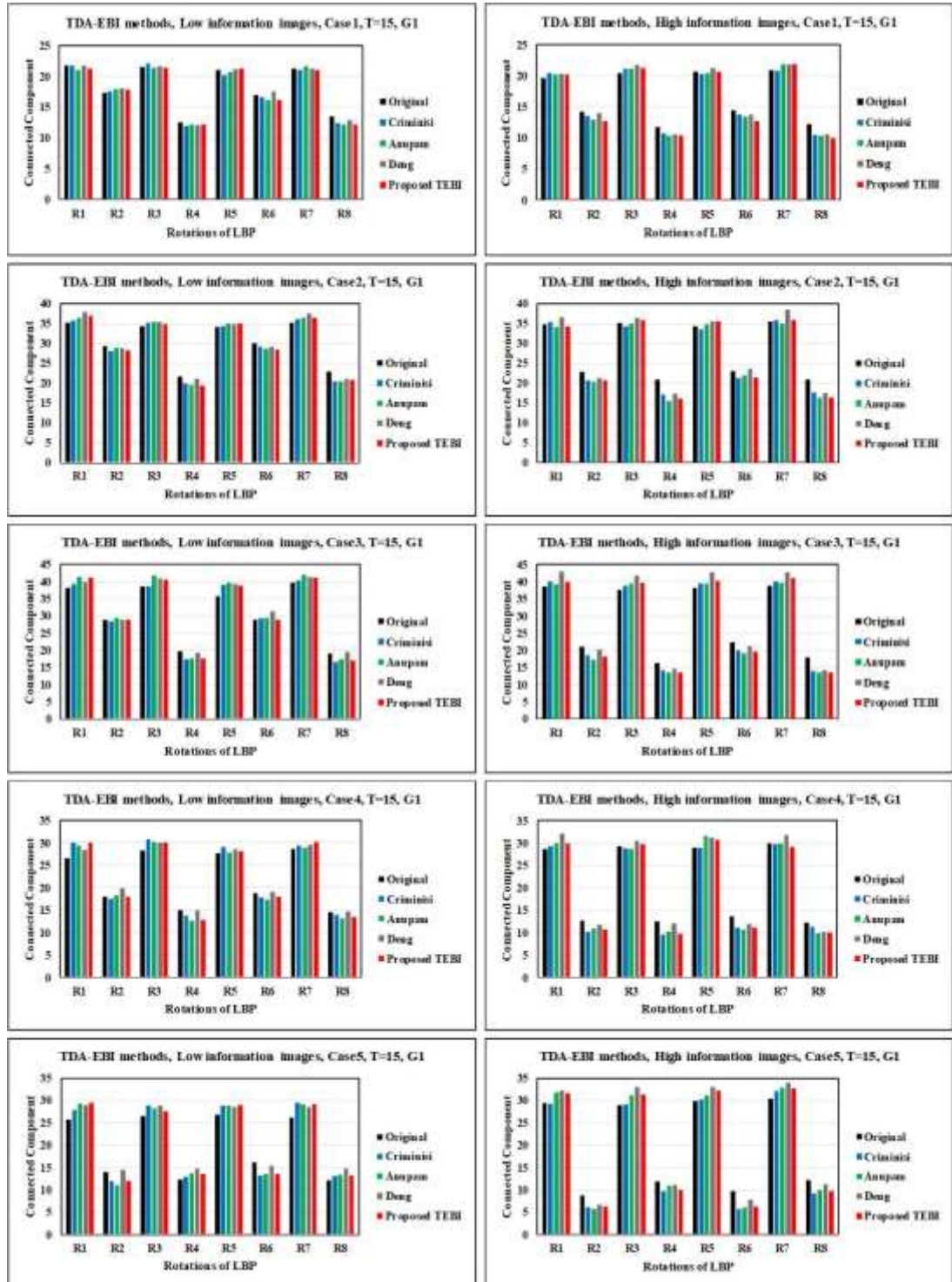


Figure B-1: Evaluation of performance of EBI techniques using TDA approach at 8 iterations in G1 at threshold $T=15$ for 5 inpainting cases of high and low-information natural images. Left column: Average of the number of CCs inpainted regions in low-information natural images. Right column: Average of the number of CCs inpainted regions in high-information natural images.

Appendix

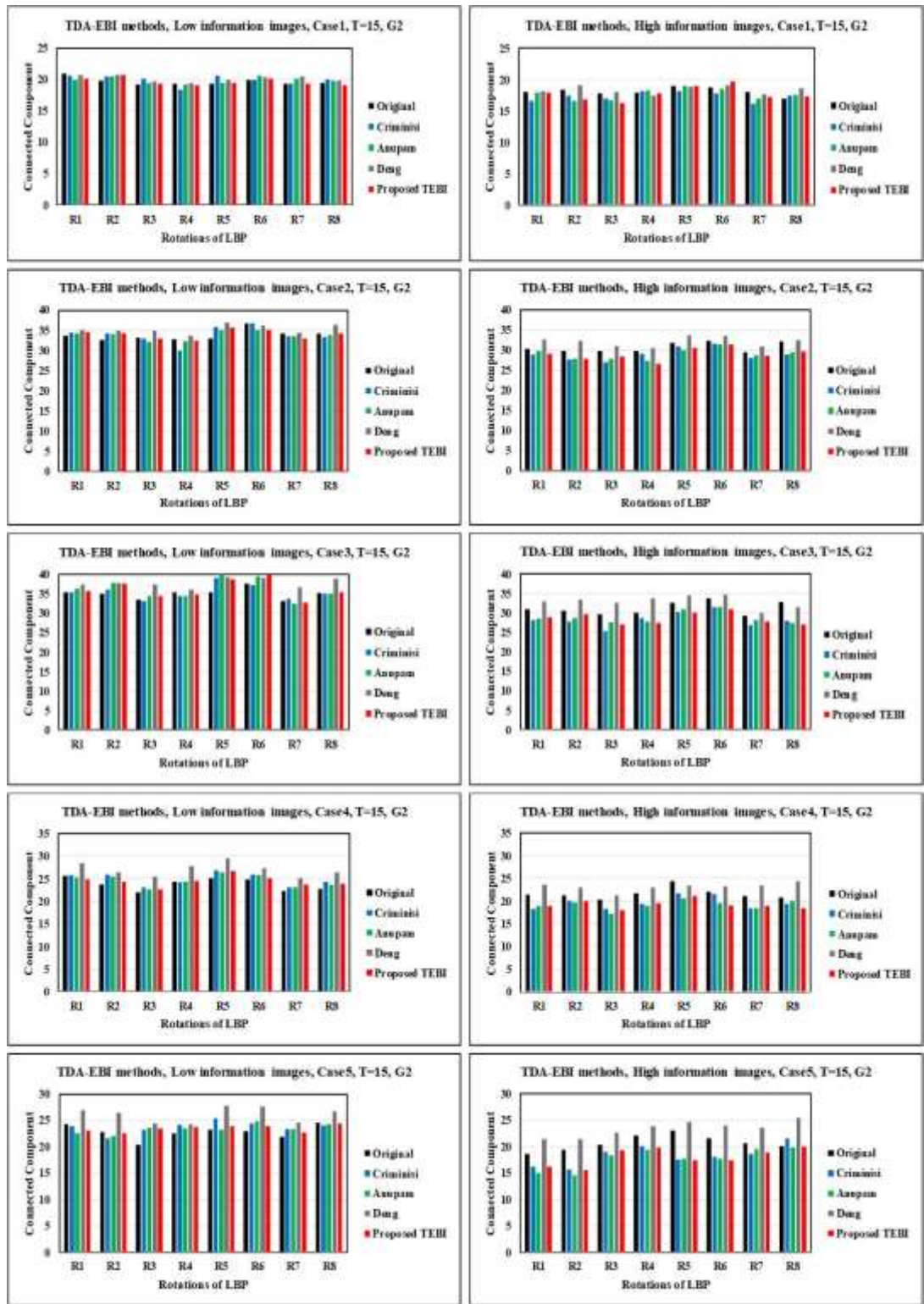


Figure B-2: Evaluation of performance of EBI techniques using TDA approach at 8 iterations in G2 at threshold $T=15$ for 5 inpainting cases of high and low-information natural images. Left column: Average of the number of CCs inpainted regions in low-information natural images. Right column: Average of the number of CCs inpainted regions in high-information natural images.

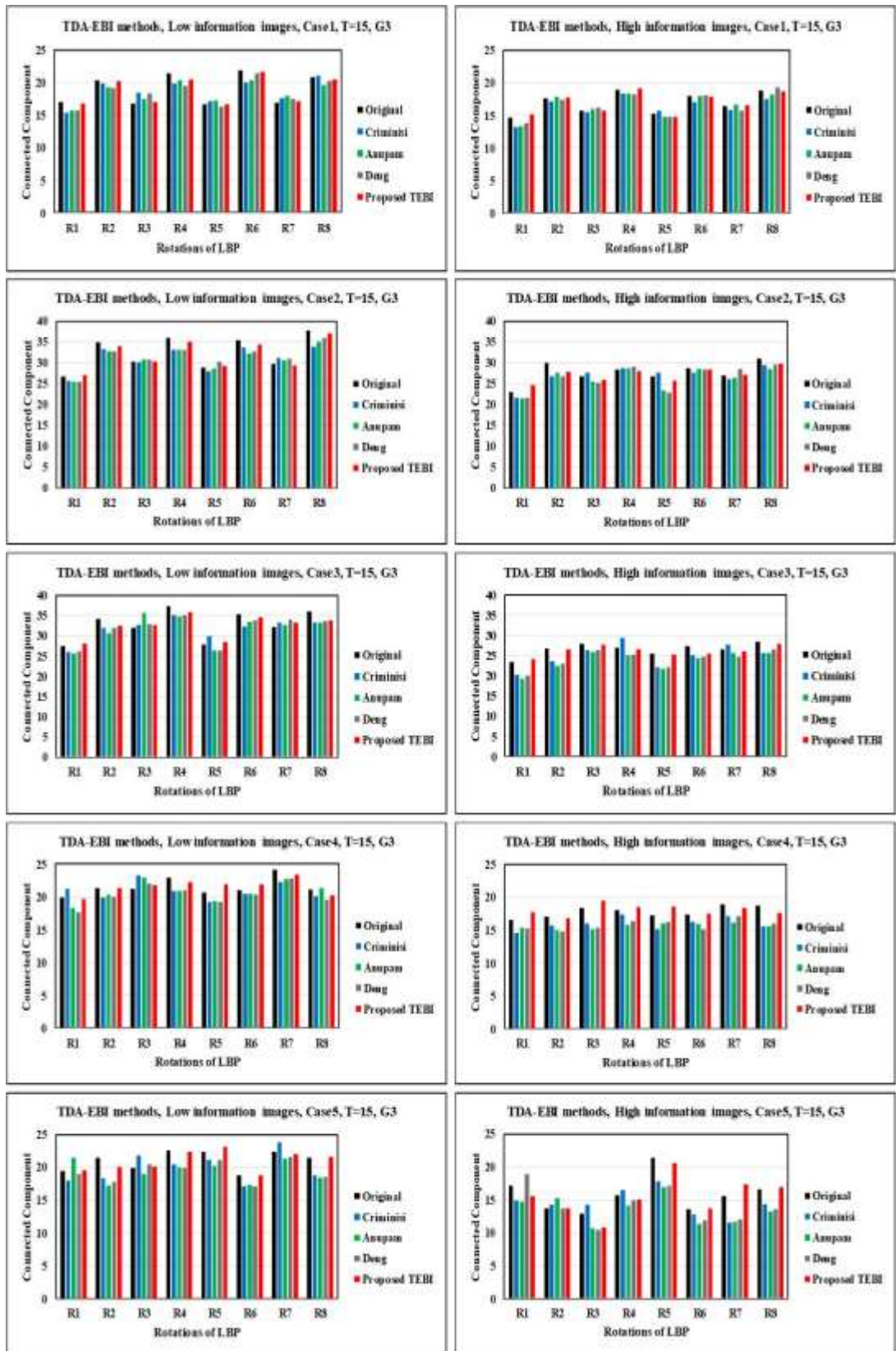


Figure B-3: Evaluation of performance of EBI techniques using TDA approach at 8 iterations in G3 at threshold $T=15$ for 5 inpainting cases of high and low-information natural images. Left column: Average of the number of CCs inpainted regions in low-information natural images. Right column: Average of the number of CCs inpainted regions in high-information natural images.

Appendix

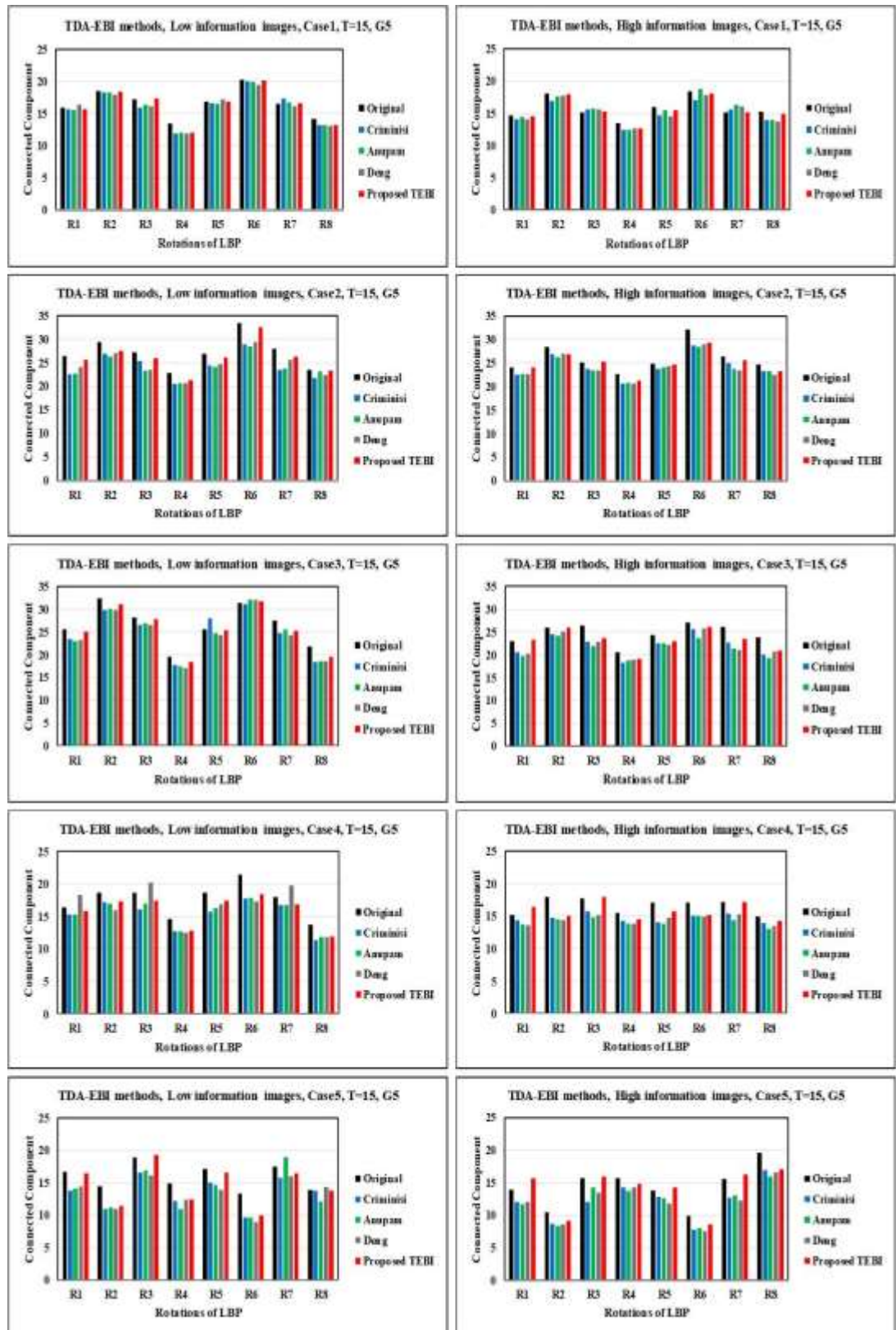


Figure B-4: Evaluation of performance of EBI techniques using TDA approach at 8 iterations in G5 at threshold T=15 for 5 inpainting cases of high and low-information natural images. Left column: Average of the number of CCs inpainted regions in low-information natural images. Right column: Average of the number of CCs inpainted regions in high-information natural images.

Appendix

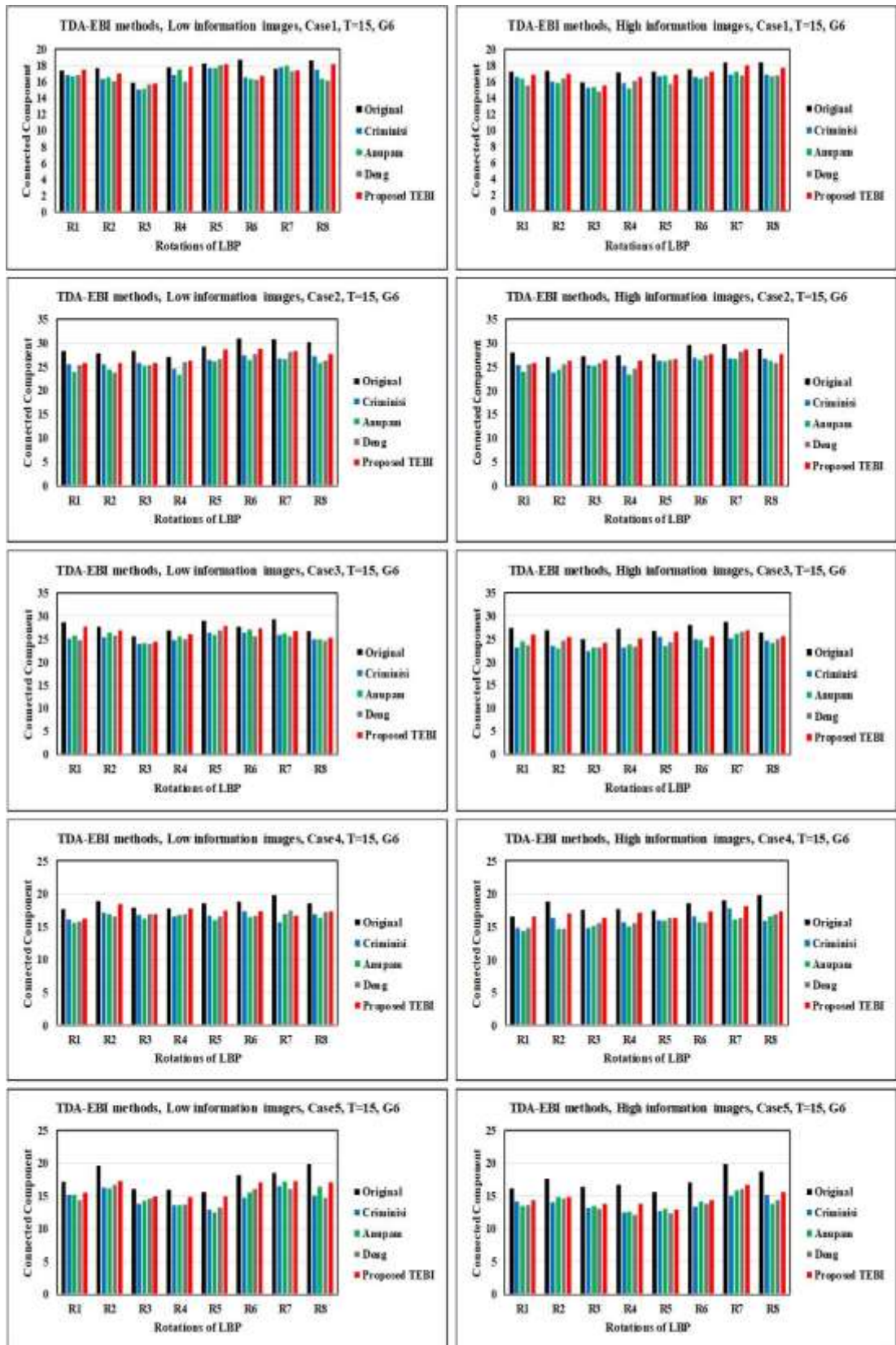


Figure B-5: Evaluation of performance of EBI techniques using TDA approach at 8 iterations in G6 at threshold T=15 for 5 inpainting cases of high and low-information natural images. Left column: Average of the number of CCs inpainted regions in low-information natural images. Right column: Average of the number of CCs inpainted regions in high-information natural images.

C. Evaluation of performance of Hybrid techniques

Evaluation of performance of hybrid techniques using the TDA approach in the inpainted regions of natural images in five inpainting domains in both spatial and frequency domains at threshold $T=10$, these algorithms described in chapter 6.

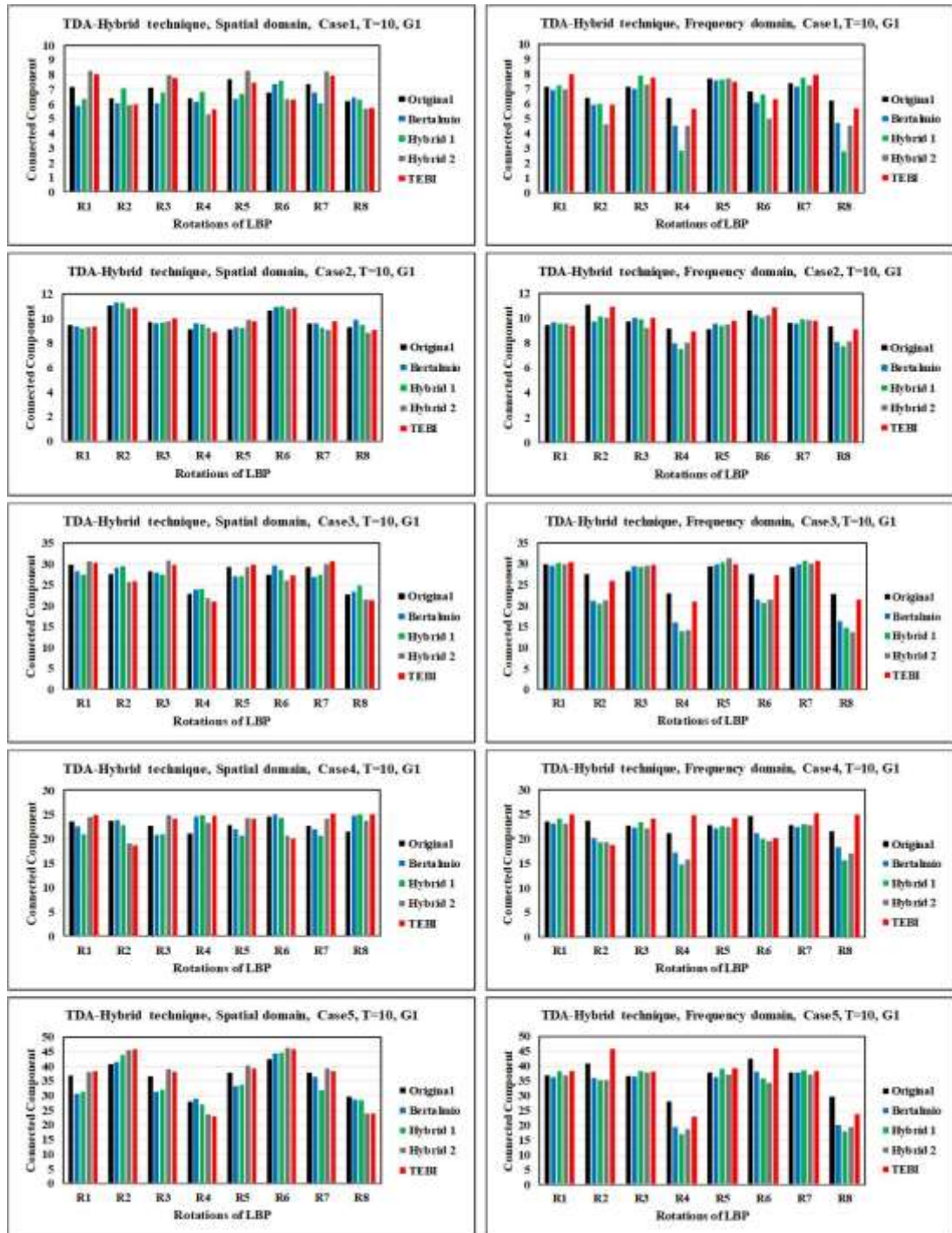


Figure C-1: Evaluation of performance of hybrid techniques using TDA approach at 8 iterations in G1 at threshold $T=10$, for 5 inpainting cases of natural images. Left column: Average of the number of CCs inpainted regions in the spatial domain. Right column: Average of the number of CCs inpainted regions in the Frequency domain.

Appendix

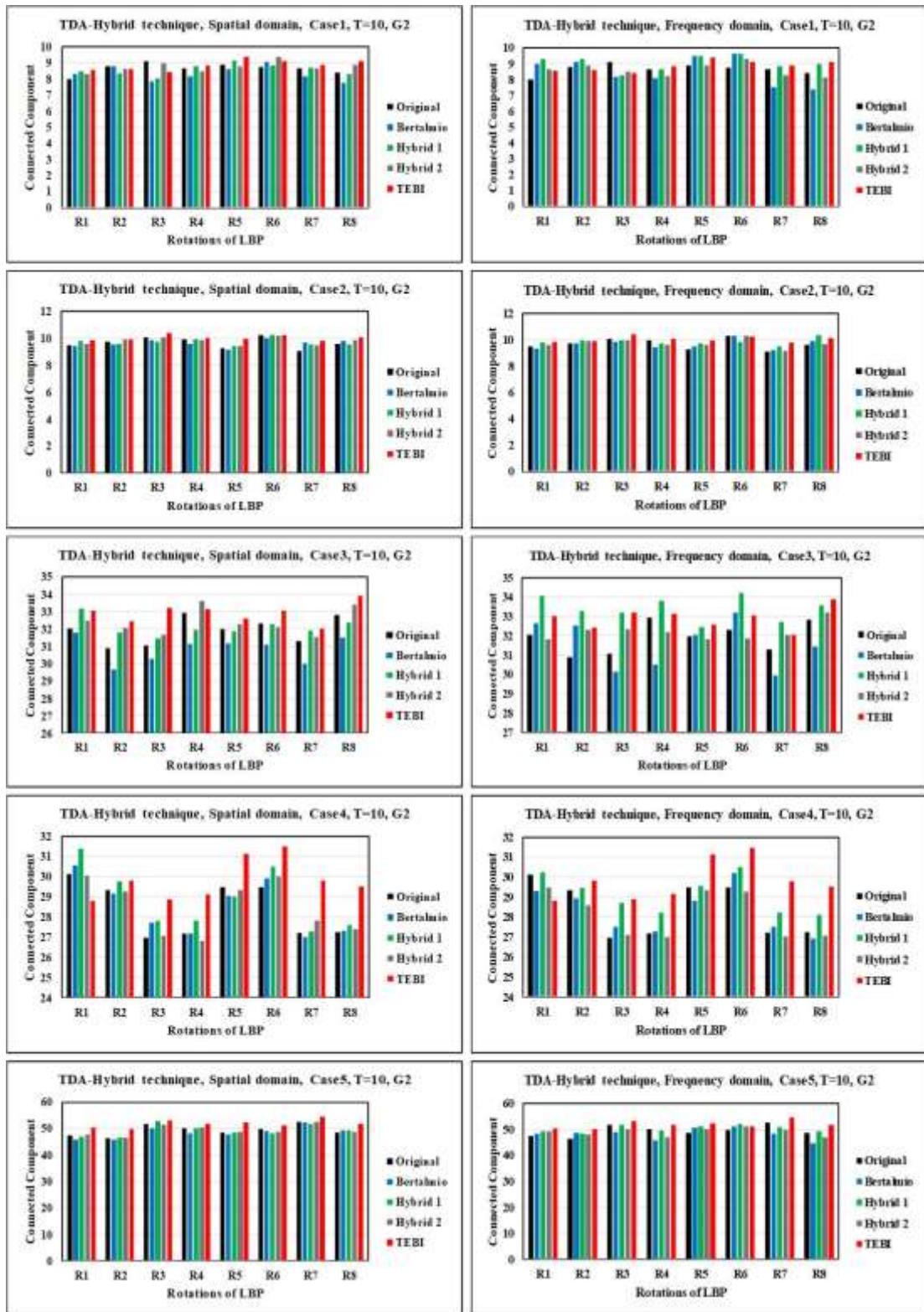


Figure C-2: Evaluation of performance of hybrid techniques using TDA approach at 8 iterations in G2 at threshold $T=10$ for 5 inpainting cases of natural images. Left column: Average of the number of CCs inpainted regions in the spatial domain. Right column: Average of the number of CCs inpainted regions in the Frequency domain.

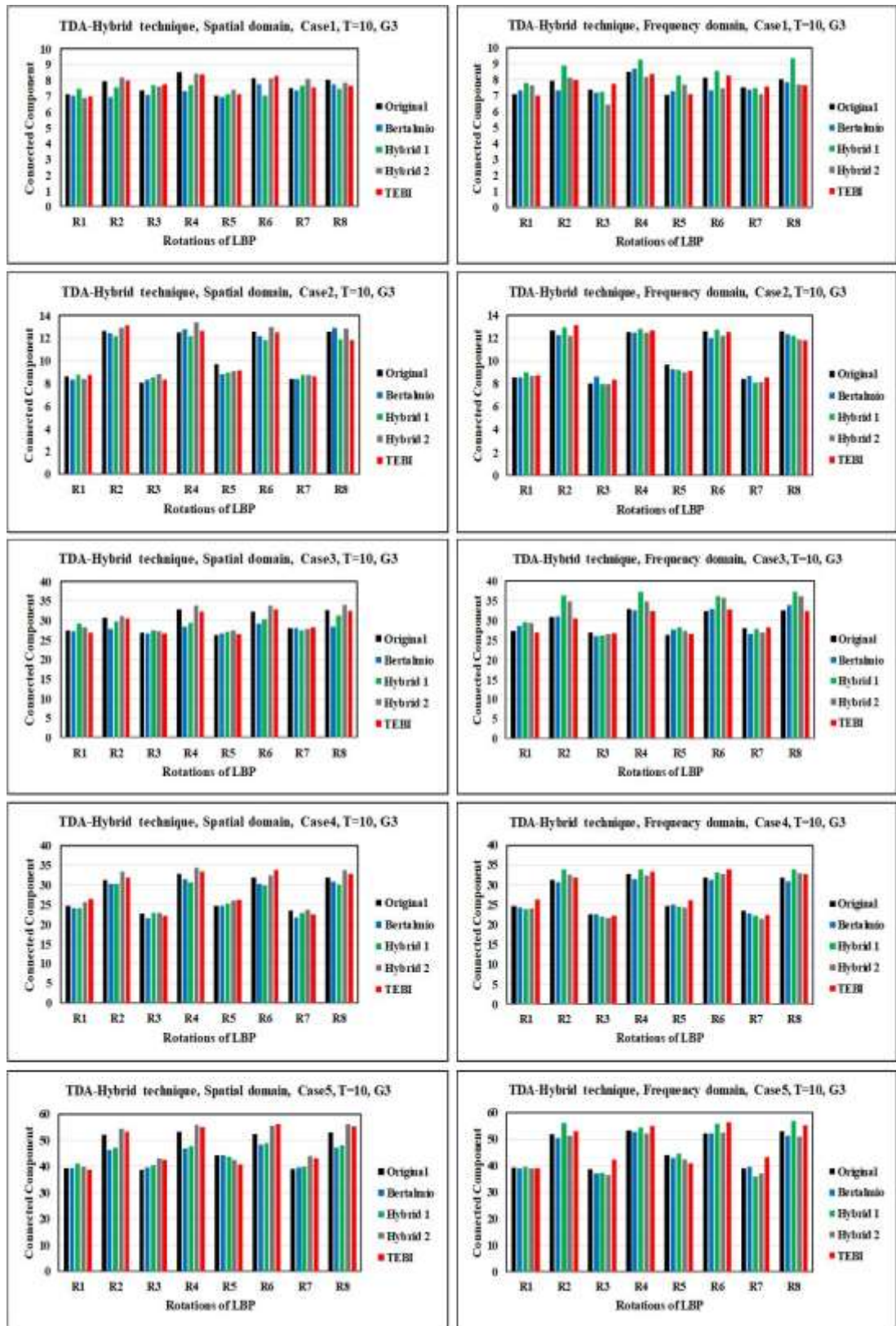


Figure C-3: Evaluation of performance of hybrid techniques using TDA approach at 8 iterations in G3 at threshold T=10 for 5 inpainting cases of natural images. Left column: Average of the number of CCs inpainted regions in the spatial domain. Right column: Average of the number of CCs inpainted regions in the Frequency domain.

Appendix

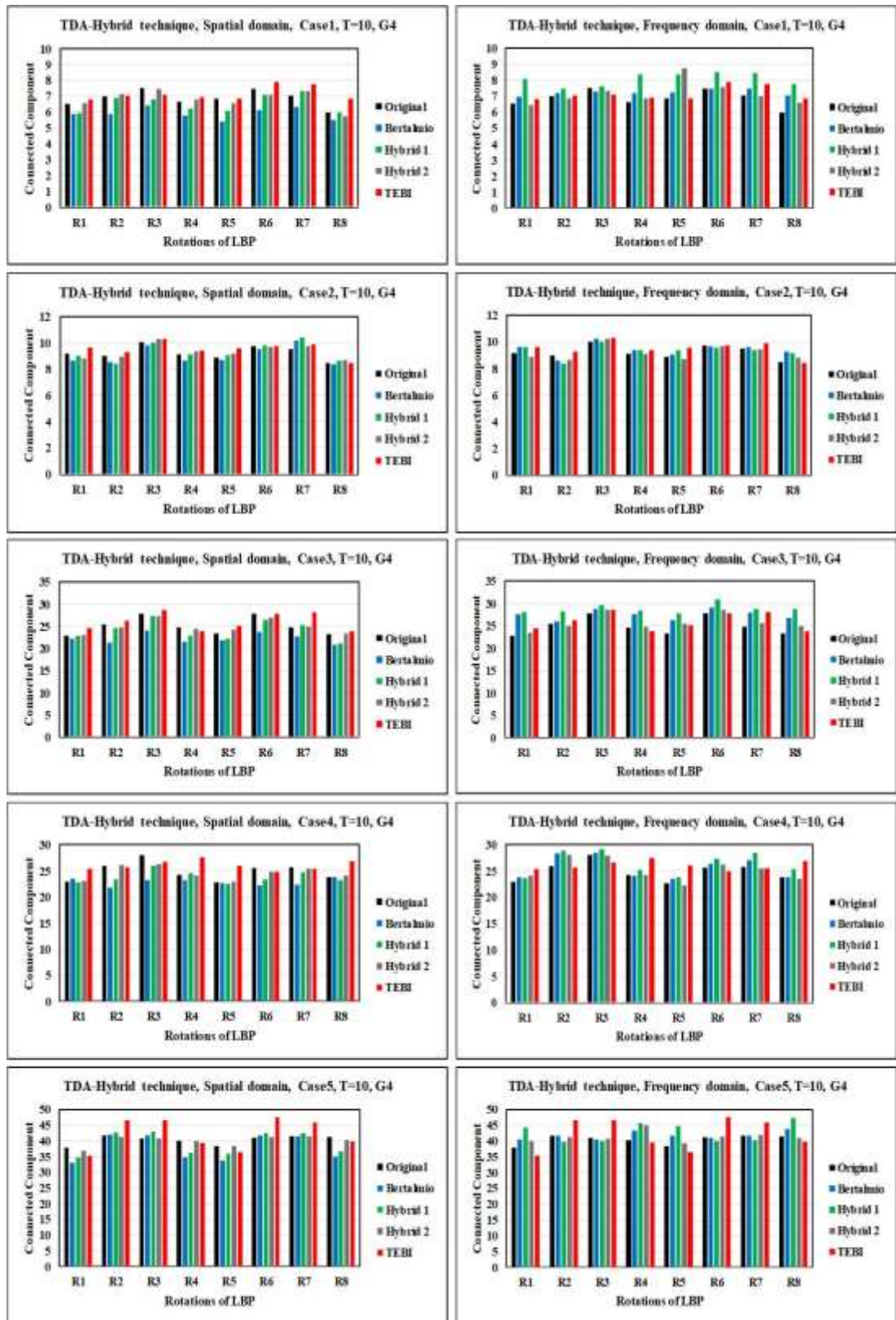


Figure C-4: Evaluation of performance of hybrid techniques using TDA approach at 8 iterations in G4 at threshold $T=10$ for 5 inpainting cases of natural images. Left column: Average of the number of CCs inpainted regions in the spatial domain. Right column: Average of the number of CCs inpainted regions in the Frequency domain.

Appendix

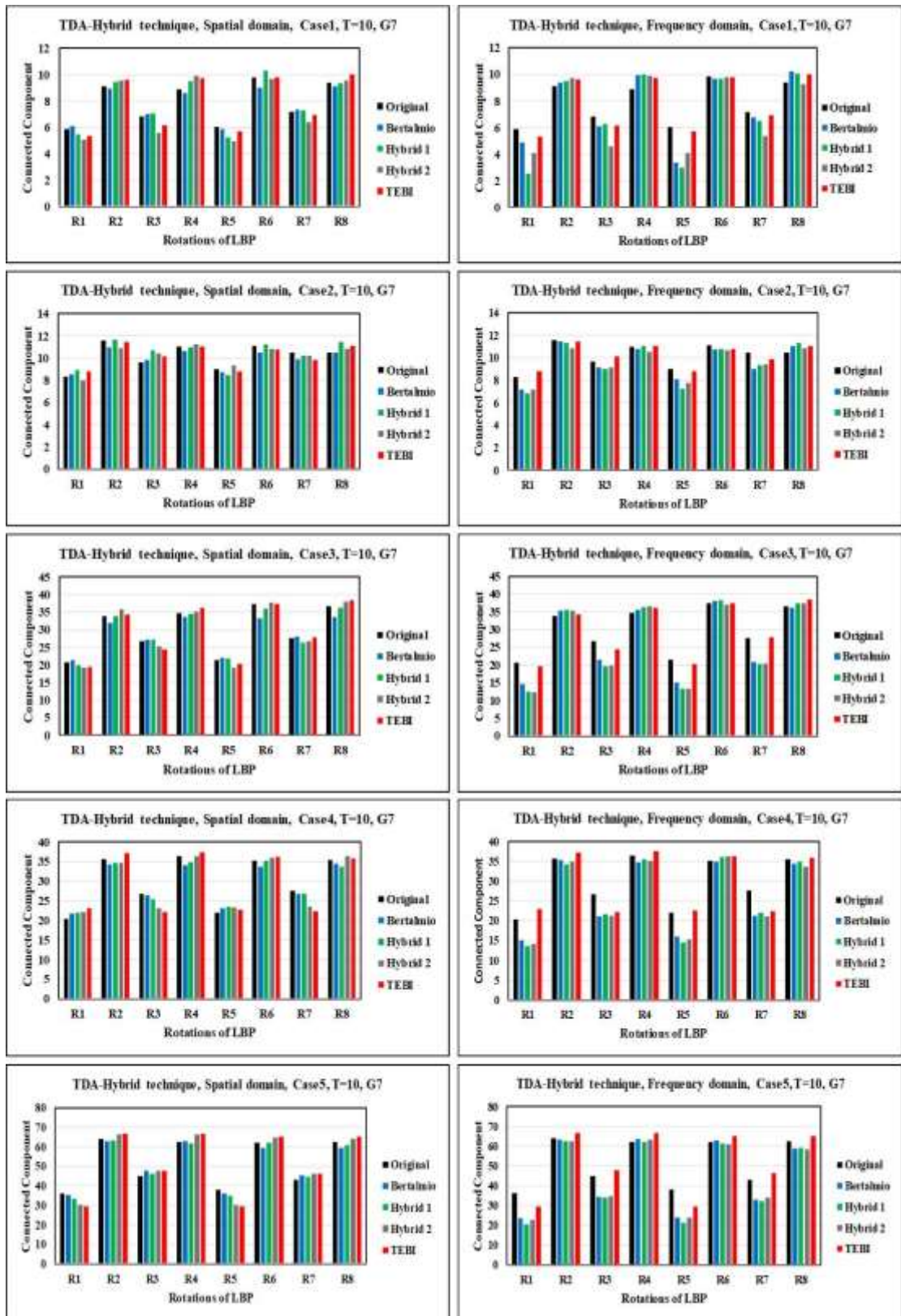


Figure C-5: Evaluation of performance of hybrid techniques using TDA approach at 8 iterations in G7 at threshold T=10 for 5 inpainting cases of natural images. Left column: Average of the number of CCs inpainted regions in the spatial domain. Right column: Average of the number of CCs inpainted regions in the Frequency domain.

D. Evaluation of performance of proposed technique based on seam carving

Evaluation of performance of proposed technique for large missing regions using the TDA approach in the inpainted regions of natural images in five inpainting domains at threshold $T=10$, these algorithms described in chapter 7.

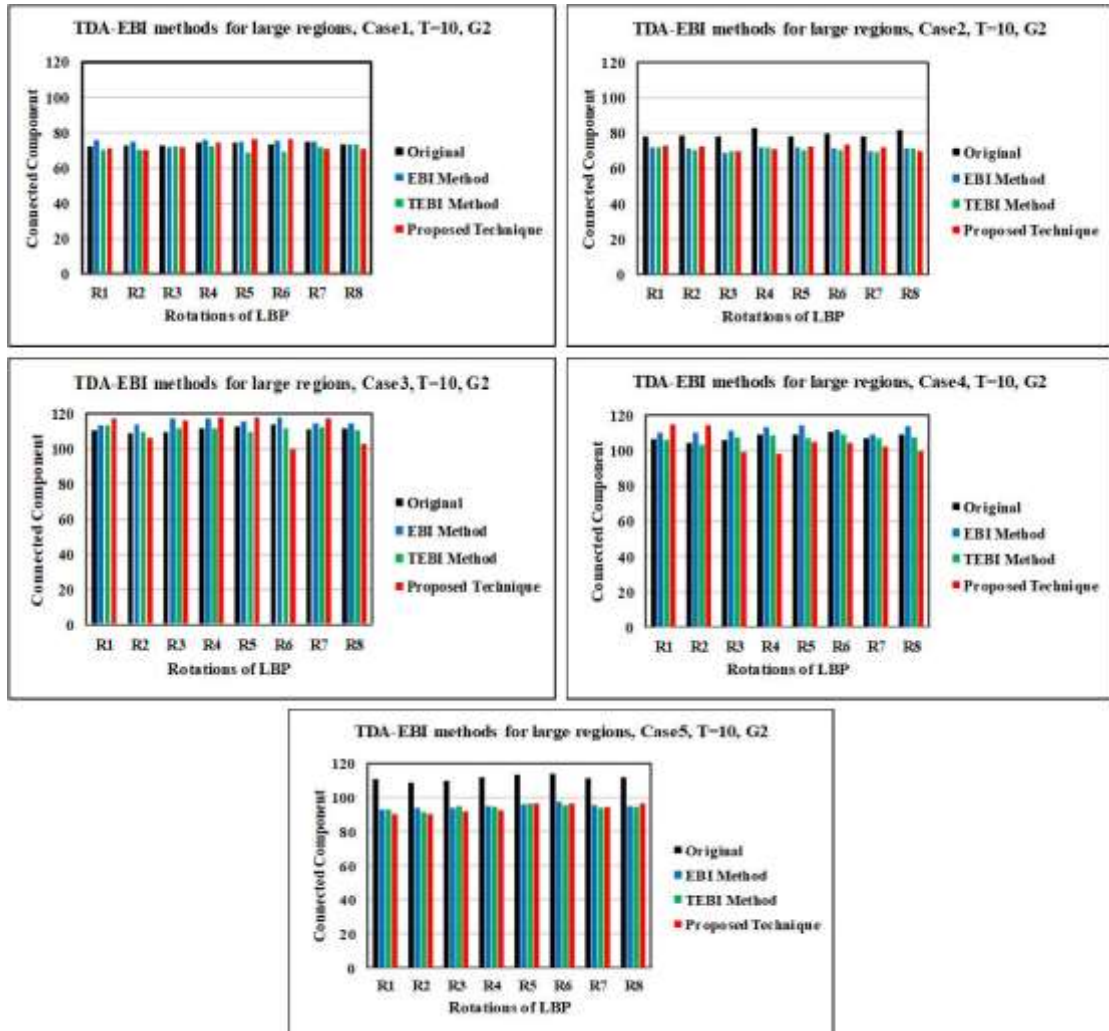


Figure D-1: Evaluation of performance of the proposed technique using the TDA approach at 8 iterations in G2 at threshold $T=10$ for 5 inpainting cases of natural images.

Appendix

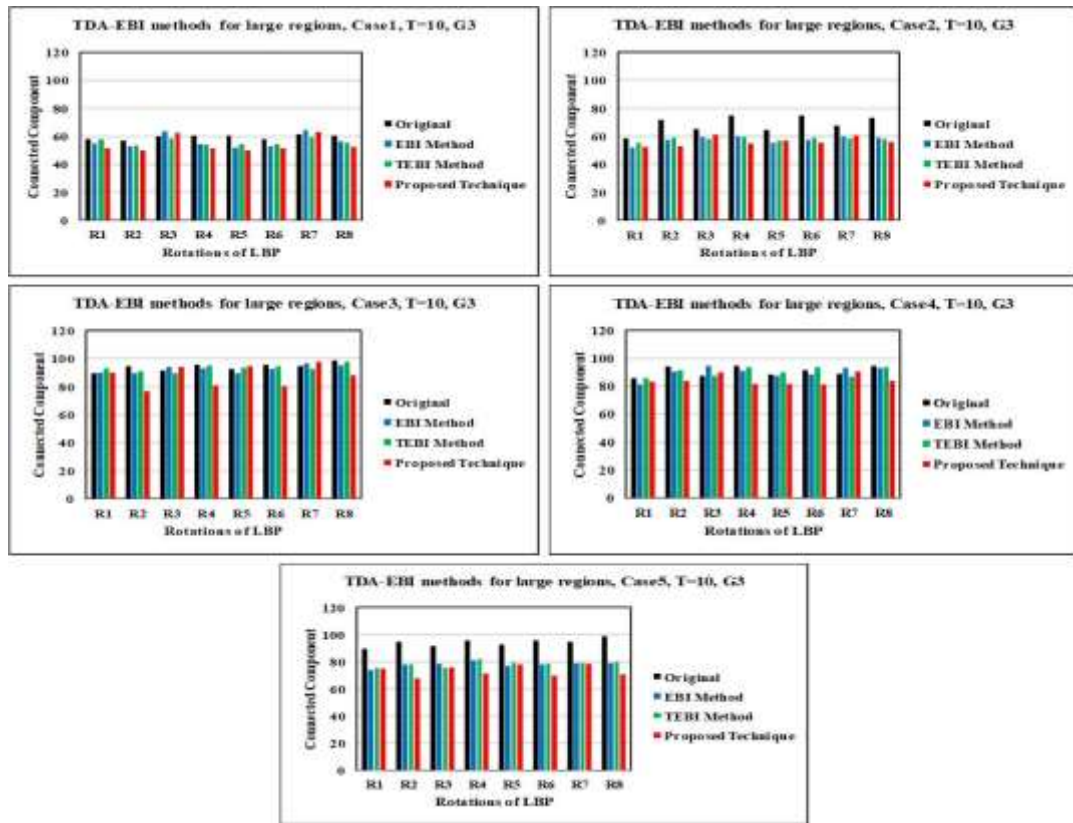


Figure D-2: Evaluation of performance of the proposed technique using the TDA approach at 8 iterations in G3 at threshold T=10 for 5 inpainting cases of natural images.

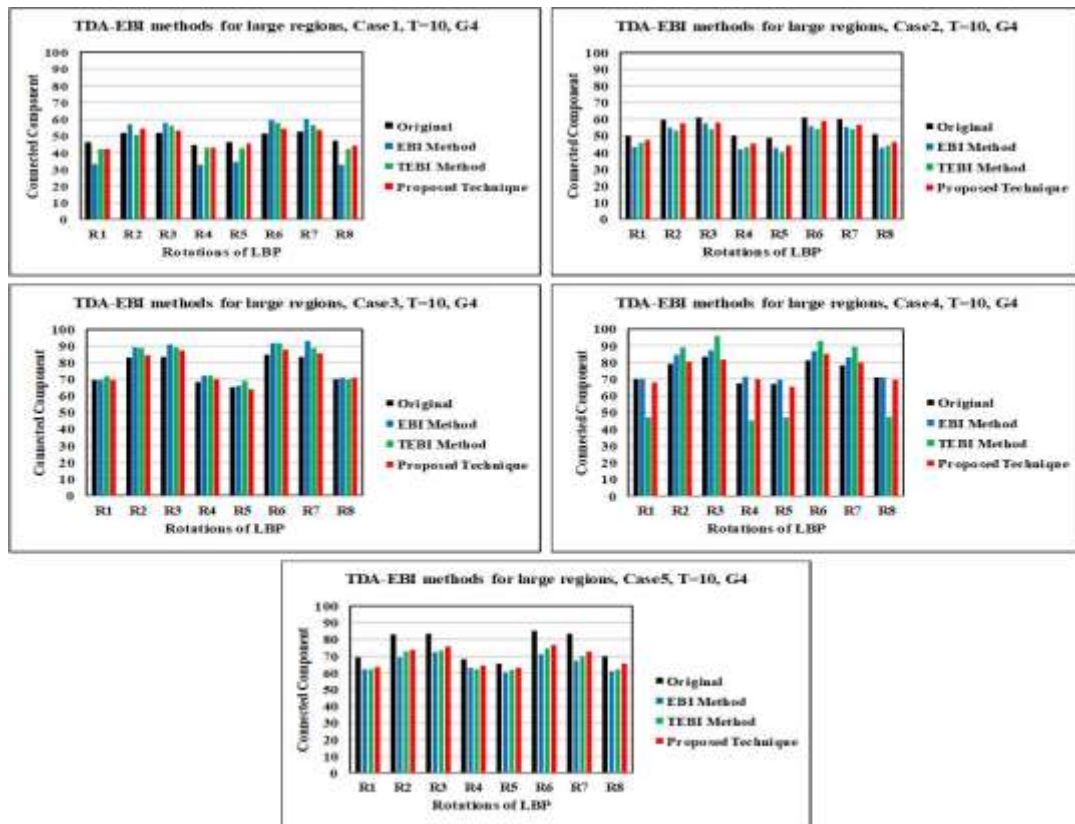


Figure D-3: Evaluation of performance of the proposed technique using the TDA approach at 8 iterations in G4 at threshold T=10 for 5 inpainting cases of natural images.

Appendix

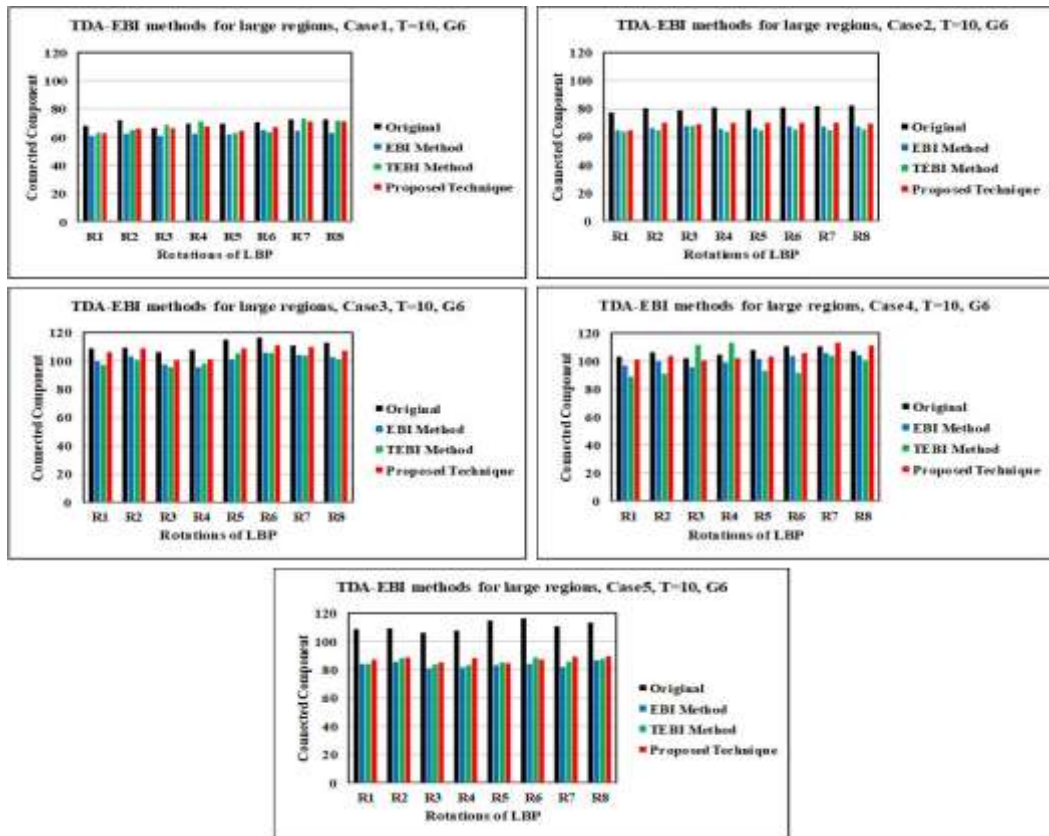


Figure D-4: Evaluation of performance of the proposed technique using the TDA approach at 8 iterations in G6 at threshold T=10 for 5 inpainting cases of natural images.

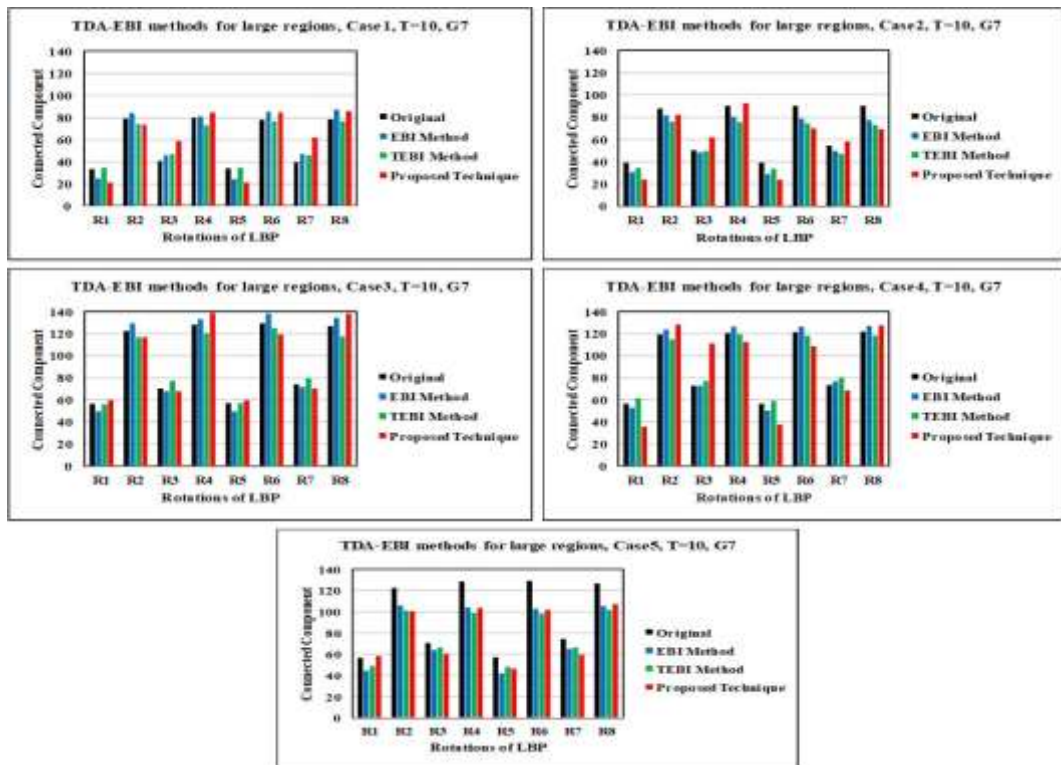


Figure D-5: Evaluation of performance of the proposed technique using the TDA approach at 8 iterations in G7 at threshold T=10 for 5 inpainting cases of natural images.